

School of Molecular and Life Sciences

**Harvesting DC current from friction and pressure on silicon-based diodes:
from micro to macro devices**

Carlos Hurtado Torres

This thesis is presented for the Degree of

Doctor of Philosophy

of

Curtin University

November 2024

Declaration

To the best of my knowledge, I declare that this thesis is the account of my research, and this thesis contains no materials previously published by any other person except where due acknowledgment has been made.

This thesis contains the main content of work not previously submitted for a degree or diploma at any university.

Date: 24/10/2024

Signature

Abstract

Integrating electrochemistry with semiconductor science and technology has helped revolutionize energy generation and storage technologies. Silicon, one of the most abundant semiconductors with a well-defined electrochemistry constitutes the foundation of many electronic devices whose functionalities span from energy conversion to energy storage, to sensors. Since Lindford and Chidsey's seminal work, combining silicon's sturdiness and richness with the complexities of organic molecules (i.e., self-assembled monolayers – SAMs) has opened new and exciting venues for surface chemistry science toward silicon electrodes broader adoption in consumables electronics. The essential components found in digital devices, rely on a consistent flow of direct current (DC) for operation, typically sourced from batteries storing chemical energy. Nevertheless, replacing a battery is often not possible when the device works in difficult access locations (i.e., medical implants, environmental remote sensors). In this sense, triboelectric nanogenerators (TENGs), have emerged as a promising technology to harness ubiquitous mechanical motion and convert it into a DC current output. The first TENGs device was reported by Z.L Wang in 2012 and consisted of a combination of polyester and Kapton, producing alternating current (AC-TENG). Most recently, an advanced version based on out-of-equilibrium Schottky diodes such as silicon–SAM functionalized-metal systems produced tuneable DC currents to power or replace the battery in conventional electronic devices (DC-TENGs).

Despite the tremendous effort to understand this class of energy harvesting devices, the scientific community still faces a lack of fundamental concepts behind the physics and chemistry of these hybrid devices, and this thesis aims to address some of them. For instance, since the working principle involves charge transport across the semiconductor surface, namely silicon–SAM–metal junction, **Chapter 2** is focused on linking the charge transport across the electrode–electrolyte interface with the charge transport in the “dry” out-of-equilibrium

silicon–SAM–Pt tip junctions (i.e. dry junctions analysed through an atomic force microscope, AFM, setup). There it is demonstrated that the electrochemistry of silicon surfaces functionalized with redox-active monolayers can be used as a diagnostic tool to predict the performance of these electrodes when incorporated as a TENG. Further, the etching of the highly conductive, but relatively underexplored, Si(211) crystal orientation was optimized, and the relevance of the etching route was also underscored towards the integration of the well-etched surfaces (i.e., surfaces with well-defined chemistry) on TENGs.

One of the most important challenges that DC-TENGs, and to some extent, the semiconductor industry in general, face is to develop strategies to limit surface wear under working conditions. **Chapter 3** explores this crucial drawback preventing broader adoption in the industry. Results revealed in Chapter 3 indicate that surface damage (i.e., oxide growth) is caused by large pressures and friction rather than the passage of a tribocurrent (i.e., current output caused by friction). Results obtained in Chapter 3 prompted the experiments of **Chapter 4**, which were aimed at investigating the replacement of the hard metal contact (i.e. the Pt AFM tip) with a softer metal (i.e., a drop of Galinstan, a common liquid metal). Unfortunately, as the Galinstan–electrode contact pressure against the silicon electrode is negligible compared to those found at the Pt tip–electrode junction (i.e., in the order of ~ 4 GPa vs ~ 2 Pa on a macroscopic contact), also tribocurrent measured with the soft junction was negligible. Nevertheless, Galinstan's usefulness in determining silicon's electrical characteristics when functionalized with different surface chemistries was demonstrated. The chapter also explores novel chemical routes to increase Galinstan surface tension to gain control over the junction area, hence improving the repeatability and reproducibility of the measurements.

The current output of TENGs is hard to correlate with sample conductivity or topographical features and, remarkably, **Chapter 5** provides experimental evidence proving that surface polarization is directly caused by changes in load (generation of a strain gradient). The chapter

focuses on how electrostatic effects between the Pt tip and the silicon surface reshape the charge transfer process at the interface leading to a directional surface polarization which needs to be added or subtracted from the nominal external bias (i.e., flexoelectric effect induced by electrostatic attraction). Results show that tip movements due to electrostatic attractive forces (tip–space charge) are causing an additional strain gradient. The relevance of Chapter 5 is to highlight that flexoelectricity is a missing term of triboelectricity, and sheds light on the long-standing question of the components of current generation based on mechanical motion.

This Ph.D. thesis expands our knowledge of out-of-equilibrium Schottky diodes based on oxide-free (monolayer-functionalised) silicon crystals and provides insights into the fundamental mechanisms of friction and wear in the context of dynamic nanoscale electrical junctions. These insights will impact the field of advanced semiconductor technologies, where precise control over material properties is critical. Furthermore, by improving our understanding of how flexoelectric and triboelectric effects can be harnessed, the work has the potential to guide the development of the next generation of DC-TENG devices, devices that will hopefully be more efficient and capable of harvesting energy from a wider range of mechanical stimuli than current options. The ability to effectively manage friction and wear in these devices will not only enhance their longevity and performance but also open new avenues for energy harvesting applications in areas such as wearable electronics, autonomous sensors, and sustainable energy solutions.

Acknowledgments

I believe one of the most beautiful things about completing a journey is looking back and appreciating the people who shared that adventure with you. A Ph.D. is exactly that, an adventure, a journey that wouldn't be possible without the support and collaboration of all the wonderful people who are part of the path.

First of all, I would like to sincerely thank A/Prof Simone Ciampi. Simone is not only an extraordinarily curious and intelligent person (qualities that are indispensable in science) but have also been a continuous guide and support in a relationship that is more mentor/friendship than simply a supervisor. Your infinite patience, wisdom, and help is the ground for all your students to develop as professionals.

I would also like to thank my co-supervisor, Nadim Darwish. Nadim has always made time to address my questions with a positive, approachable attitude, filled with wisdom.

Thanks to all my colleagues for the days we've shared and for helping me grow as a professional: Mattia, Harry, Malika, Essam, Soraya, Tiexin, Xin, Stuart, Wathsala, Viji (thanks for lending me your headphones every day I forgot mine), Shane and Chiara.

Thanks to our collaborators Anton P. Le Brun, Kai Chen, and Melanie McGregor, whose contributions have been essential in completing this thesis.

I would also like to thank Curtin University, and the Australian Research Council for the financial support that made this thesis possible.

Being extremely far from my beloved Cádiz has been particularly painful, but every one of my friends there, from afar, gave me the certainty that I will always have a place by the ocean, alongside them. Thank you.

Final thoughts are, of course, for Ingrid. I don't think English, or any language known to humankind can express what I feel when I wake up next to you every morning. Without you, this thesis would not exist, and the world would be a senseless place. I hope to read this many years from now and smile just as I am smiling now... t'estimu una mica.

List of publications

Publications included in this Thesis

[1] **Hurtado, C.**; Lyu, X.; Ferrie, S.; Le Brun, A. P.; MacGregor, M.; Ciampi, S. Organic Monolayers on Si(211) for Triboelectricity Generation: Etching Optimization and Relationship between the Electrochemistry and Current Output. *ACS Appl. Nano Mater.* 2022, 5, 14263–14274.

[2] **Hurtado, C.**; Andreoli, T.; Le Brun, A. P.; MacGregor, M.; Darwish, N.; Ciampi, S. Galinstan Liquid Metal Electrical Contacts for Monolayer-Modified Silicon Surfaces. *Langmuir* 2024, 40, 201–210.

[3] **Hurtado, C.**; Ciampi, S. Oxidative Damage during the Operation of Si(211)-Based Triboelectric Nanogenerators. *Surfaces* 2023, 6, 281–290.

[4] **Hurtado, C.**, MacGregor, M.; Kai, Chen Ciampi, S. Schottky Diode Leakage Current Fluctuations: Electrostatically Induced Flexoelectricity in Silicon. *Adv. Sci.*, 2024 2403524.

Publications not included in this Thesis

[5] Zhang, S.; Lyu, X.; **Hurtado, C.**; Darwish, N.; Ciampi, S. Non-Ideal Cyclic Voltammetry of Redox Monolayers on Silicon Electrodes: Peak Splitting is Caused by Heterogeneous Photocurrents and Not by Molecular Disorder. *Langmuir* 2022, 38, 743–750,

[6] Li, T.; Peiris, C. R.; Aragonès, A. C.; **Hurtado, C.**; Kicic, A.; Ciampi, S.; MacGregor, M.; Darwish, T.; Darwish, N. Terminal Deuterium Atoms Protect Silicon from Oxidation. *ACS Appl. Mater. Interfaces* 2023, 15, 47833–47844.

List of abbreviations

AC	alternate current
AFM	atomic force microscopy
C-AFM	conductive atomic force microscopy
CA	contact angle
CE	contact electrification
CI	charge induction
CuAAC	Copper-catalysed azide-alkyne coupling
CV	cyclic voltammetry
DC	direct current
DCM	dichloromethane
DMT	Derjaguin–Muller–Toporov
e^- -h	electron–hole
eV	electron volt
ESD	electrostatic discharge
E_c	conduction band
E_F	Fermi level
E_g	band gap
E_{redox}	redox potential
E_v	valence band
F/d	force/distance
FWHM	full width at half-maximum
I–V	current–potential
k	Boltzmann constant

KE	kinetic energy
PCM	photocurrent mapping
R_C	charge-transfer resistance
SC	semiconductor
S_{CL}	space charge layer
SPM	scanning probe microscopy
STM	scanning tunnelling microscopy
TENGs	triboelectric nanogenerators
XPS	x-ray photoelectron spectroscopy
XRR	x-ray reflectometry
Z_r	impedance, real component
Z_i	impedance, imaginary component
ρ	resistivity
Φ_b	Schottky barrier
ϕ_M	metal work function
χ	semiconductor electron affinity
μm	micrometer

Copyright statement

I, Carlos Hurtado, confirm that I have obtained the necessary permissions from copyright holders to use any third-party copyrighted materials included in this thesis. Additionally, I have secured authorization to incorporate any of my previously published work (such as journal articles) for which the copyright is held by another party (e.g., publisher, co-author). All documentation of copyright permissions is in *Appendices A & B*

Date: 24/10/2024

Signature

Statement of contribution to others

As the author of this thesis, I, Carlos Hurtado, have conducted most of the experimental works and data analysis under the guidance of my principal supervisor, A/Prof. Simone Ciampi. Contribution statements for each of the four published papers presented in this thesis are provided separately in *Appendix B*.

A/Prof Simone Ciampi provided project supervision, data analysis, and manuscript editing.

A/Prof Nadim Darwish provided project supervision.

Dr. Stuart P. Ferrie and Dr. Xin Lyu helped me extensively to master AFM measurements.

Table of Contents

Declaration.....	2
Abstract.....	3
Acknowledgments.....	6
List of publications	8
Publications included in this Thesis	8
Publications not included in this Thesis.....	8
List of abbreviations	9
Copyright statement.....	11
Statement of contribution to others.....	12
Table of Contents.....	13
Chapter 1. Thesis outline and introduction	15
1.1 Thesis outline	15
1.2 Introduction	18
1.2.1 Silicon electrodes physics	19
1.2.1.1 Band diagram theory overview.....	19
1.2.1.2 Photoelectric effect in silicon electrodes	22
1.2.1.3 Silicon–electrolyte contacts	24
1.2.1.4 Silicon–metal contacts	26
1.2.2 Silicon surface chemistry.....	28
1.2.2.1 Etching of silicon	28
1.2.2.2 Self-assembled monolayers (SAMs) on silicon.....	30
1.2.3 Electrochemical measurements.....	32
1.2.3.1 Cyclic voltammetry (CV)	32
1.2.3.2 Non–ideal voltammogram waves	35
1.2.3.3 Electrochemical impedance spectroscopy (EIS)	36
1.2.4 Spectroscopic measurements.....	38
1.2.4.1 X-ray photoelectron spectroscopy (XPS).....	38
1.2.4.2 X-ray reflectometry (XRR)	39
1.2.5 Atomic force microscopy (AFM) measurements	40
1.2.5.1 Topography measurements	40
1.2.5.2 Electrical measurements	42
1.2.6 Mechanically-induced DC outputs on silicon	43
1.2.6.1 Mechanism of triboelectricity.....	43
1.2.6.2 Mechanism of flexoelectricity	46

1.2.6.3 Triboelectric nanogenerators (TENGs)	48
Chapter 2. Organic monolayers on Si(211) for triboelectricity generation: etching optimization and relationship between the electrochemistry and current output.....	59
Chapter 3. Oxidative damage during the operation of Si(211)-based triboelectric nanogenerators	62
Chapter 4. Galinstan liquid metal electrical contacts for monolayer-modified silicon surfaces.....	64
Chapter 5. Schottky diode leakage current fluctuations: electrostatically induced flexoelectricity in silicon.....	67
Chapter 6. Summary and future outlook.....	69
6.1 Summary.....	69
6.2 Future outlook	71
<i>Appendix A.</i> Rights and permissions.....	74
<i>Appendix B.</i> Statement of contributions to others.....	86
<i>Appendix C.</i> Supplementary material of Chapter 2.....	91
<i>Appendix D.</i> Supplementary material of Chapter 3	92
<i>Appendix E.</i> Supplementary material of Chapter 4.....	93
<i>Appendix F.</i> Supplementary material of Chapter 5.....	94

Chapter 1. Thesis outline and introduction

1.1 Thesis outline

Chapter 1 provides an overview of key concepts that are crucial for the reader to understand the results and discussion of **Chapters 2 to 5**. First, a general introduction to semiconductor (SC) physics is provided, essential to understanding silicon electrode physics when it is contacting a metal or an electrolyte. Aspects such as the practical value of band diagrams, general features of Schottky diodes, electrical characteristics of p–n junctions, and the meaning and value of the photoelectric effect have been touched upon with the necessary level of details.

Given that this research has focused on silicon–monolayer functionalized (Si–SAMs) hybrid constructs as electrode platforms, basic concepts of semiconductor surface chemistry such as etching processes and monolayer attachment have also been presented in this chapter. Moreover, this chapter also addresses the main techniques used to characterize the systems. Therefore, a brief history and working principles of electrochemical, electrical, spectroscopic, and topographical measurements such as cyclic voltammetry (CV), electrochemical impedance spectroscopy (EIS), X-ray photoelectron spectroscopy (XPS), X-ray reflectometry (XRR), and atomic force microscopy (AFM) have been introduced. The chapter concludes with a brief introduction to the history and working mechanism of triboelectric nanogenerators (TENGs).

Chapter 2, in the form of paper 1, deals with autonomous power supplies that convert mechanical energy into electricity and proposes silicon as electrode material on which to build such devices. In this chapter, it is explored a new monolayer functionalization route (i.e., novel etching process) for Si(211), a highly conductive but largely underexplored silicon crystal cut. Results demonstrate that Si(211) electrodes substantially outperform Si(111) electrodes when incorporated into a TENG design and that the TENG performance can be predicted using

electrochemical screening prior to the electrical measurement. It can also be observed an enhancement of the current output when surface defects (i.e., substrate oxidation) are introduced. This enhancement is, nonetheless, transient and disappears over time.

Chapter 3, in the form of paper 2, builds upon and follows the findings of Chapter 2. The chapter is focused on how dynamic Schottky systems (namely, Si(211)–SAM–Pt tip dynamic junctions) that output significant direct current (DC), often suffer from limited durability, hence their practical scope remains uncertain. In the chapter it is revealed that surface wear is caused by mechanical motion (i.e., friction and pressure) and not by the flow of tribocurrent through the system. Results demonstrate that the current drop does not happen immediately and that the current output is maximised at those sample locations where the strain gradient is higher.

Chapter 4, in the form of paper 3, was conceptualised based on the results of surface damage presented in Chapter 3. It is attempted to substitute the metal contact used in the AFM measurements (i.e. a sharp Pt tip) with a softer metal contact for tribocurrent generation and electrical measurements. While the generation of tribocurrent based on sliding/pressing events was limited by the lack of a significant normal pressure (namely, negligible pressure in a macroscopic contact compared to large pressures on AFM) electrical measurements of Si–SAM systems were successfully performed by using Galinstan, the brand name for a low-melting gallium-based alloy. The chapter proposes solutions to maximize the repeatability and reproducibility in ambient air of SC–metal junctions by synthesizing magnetic Galinstan as top contact. A novel catalyst-free alkyne–alkyne homocoupling reaction is also explored and tested its electrical characteristics with Galinstan contacts.

Chapter 5, in the form of paper 4, explores to what extent the strain gradients observed contributed (and potentially governed) the triboelectric phenomena and have therefore the potential to influence/affect electrical measurements at the nanoscale. The same system

conditions as in prior chapters is reproduced (Si–SAM–Pt sliding diodes) and evaluated how the strain gradient generation at the tip–substrate junction affects the results. The experiments presented in this chapter revealed that the Pt tip experiences a significant rotation which is caused by a voltage-dependent adhesion force that is electrostatic in origin. This electrostatically induced tip (contact) rotation creates a strain gradient in the silicon surface, which in turn induces a parasitic flexoelectric bias. This additional bias, adds to the reverse bias (and subtracts from the forward bias) causing the flexoelectric-assisted breakdown to shift the forward current towards more positive values.

Chapter 6 summarises the main findings of this doctoral thesis and draws the conclusions relevant to each chapter. Further directions are also suggested for this promising class of energy-harvesting technology.

1.2 Introduction

Addressing the challenge of sustainable energy generation is a critical and global goal and will improve the quality of life in the modern era.¹ The urgent need to reduce dependency on fossil fuels has accelerated the development and adoption of renewable energy technologies. As the traditional centralised energy distribution model becomes less effective, there is a rising focus on distributed energy systems, including advanced solar technologies and energy storage solutions.² As we transition into the digital era, our reliance on electricity has grown to encompass a wide range of devices, from handheld cell phones and wearable electronics to electric vehicles, all integral to daily life.^{3, 4} Additionally, advanced sensors for health monitoring,⁵ personal medical networks,⁶ environmental and infrastructure monitoring,⁷ and security are now widely deployed across various fields. The rapid growth in electronic device development prioritises miniaturization, lightweight design, and enhanced portability. In this global technology race, finding power solutions that are sustainable, easily accessible, and maintenance-free has therefore become a key objective.⁸⁻¹⁰

Electronic devices typically operate on DC power and rely on batteries as a "non-regenerative" energy source. Batteries however have limitations, such as the need for regular recharging, as well as their reliance on costly or hazardous materials like lithium and cadmium.¹¹ Consequently, there is a growing interest in alternative and regenerative sources of energy, particularly in situations where replacing or recharging a battery is not feasible. Among the promising technologies emerging in this domain are nanogenerators which convert mechanical into electrical energy.¹²⁻¹⁴ Initial developments in this field were focused on piezoelectric nanogenerators,¹⁵ but their low power output limited these. An advanced variant, the triboelectric nanogenerator (TENG), functions through a combination of triboelectrification, electrostatics, and most recently pointed flexovoltage induced by strain gradients.^{16, 17} Since

their introduction in 2012,¹⁸ most TENGs presented in the recent literature are alternating-current, AC-TENGs.¹⁹ In the last five years there has however been a significant surge in research efforts dedicated to advancing the science of DC-TENGs, devices that produce direct current and voltage outputs in response to mechanical stimuli.^{20,21}

In this context, silicon emerges as a prime semiconductor (SC) candidate at the core of DC-TENGs.²² Silicon bulk and surface properties can be finely tuned through specific doping techniques and etching processes, which facilitate the creation of microstructures on silicon wafers, crucial for their electrical properties. However, silicon is a non-oxide SC and therefore faces the challenge of a thermodynamically favourable surface oxidation, an event that will impede charge transport. Addressing this shortcoming by surface engineering via self-assembled-monolayers (SAMs) emerged as a key tool,²³ allowing not only the mitigation of oxidation but also the tuning/enhancement of properties like friction, adhesion, and wettability, all of which are essential for the efficient operation of triboelectric nanogenerators.²⁴

1.2.1 Silicon electrodes physics

1.2.1.1 Band diagram theory overview

Given that this Ph.D. thesis integrates several fields such as electrochemistry, surface chemistry, and electrode physics, and given that the work is primarily intended for a chemical audience, a conceptual introduction to SC physics, is essential to the understanding of several SC properties, such as the meaning of a conduction band (E_C), valence band (E_V), and the operation of p-n and Schottky junctions will be briefly provided. This background knowledge will aid chemists in understanding concepts such as flexoelectricity, photocurrent decay, or triboelectricity, which constitute the core of **Chapters 2 to 5**.

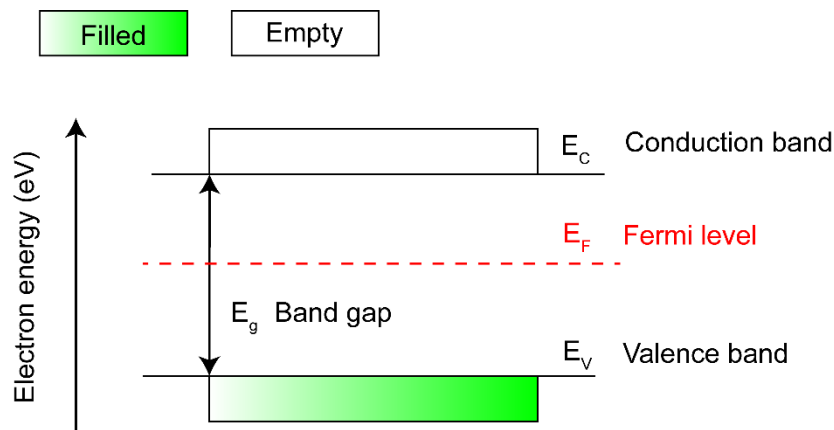


Figure 1. Scheme representing the energy band structure in a semiconductor. The valence band (E_V) is the energy band filled with electrons under normal conditions. These electrons can be excited to the conduction band (E_C), where they are free to move and conduct electricity. The energy difference between the valence and conduction bands is known as the band gap (E_g). The Fermi level (E_F), depicted as a red dashed line, is the energy level at which the probability of finding an electron is 50%. It does not mean that there is an energy level at the E_F , but if there was then the probability of occupancy would be 50%. In this illustration, the valence band is partially filled, indicating the presence of electrons, while the conduction band is empty, no electrons are available for conduction without external energy input.

In solids, energy levels available to electrons are grouped into bands.²⁵ The classification of materials into conductors, insulators, and SCs is primarily based on the band gap magnitude ($E_g = E_C - E_V$) namely, the energy difference between the E_V and the E_C (Figure 1). Conductors have overlapping E_V and E_C , allowing electrons to flow freely. Insulators have a wide band gap, typically greater than 5 eV, which prevents electron flow under normal conditions. SCs possess a moderate band gap, usually ranging from 0.1 to 4 eV, enabling controlled electron flow. Conductors typically have a resistivity (ρ) lower than $10^{-3} \Omega \text{ cm}$ while insulators exhibit a resistivity higher than $10^8 \Omega \text{ cm}$. SCs (i.e., silicon), which fall between these two categories, have resistivity values ranging from $10^{-3} \Omega$ to $10^8 \Omega \text{ cm}$ (Figure 2).²⁶

The electronic conductivity of SCs can be classified into two categories: intrinsic and extrinsic conductivity.²⁷ Intrinsic conductivity is produced by electrons originating from the atoms of the fundamental substance within the crystal lattice. At thermal equilibrium, electrons can be thermally excited from the valence band to the conduction band, creating electron–hole pairs (e^-h pair). In intrinsic (pure) SCs, the Fermi level (E_F) – the highest energy level that an

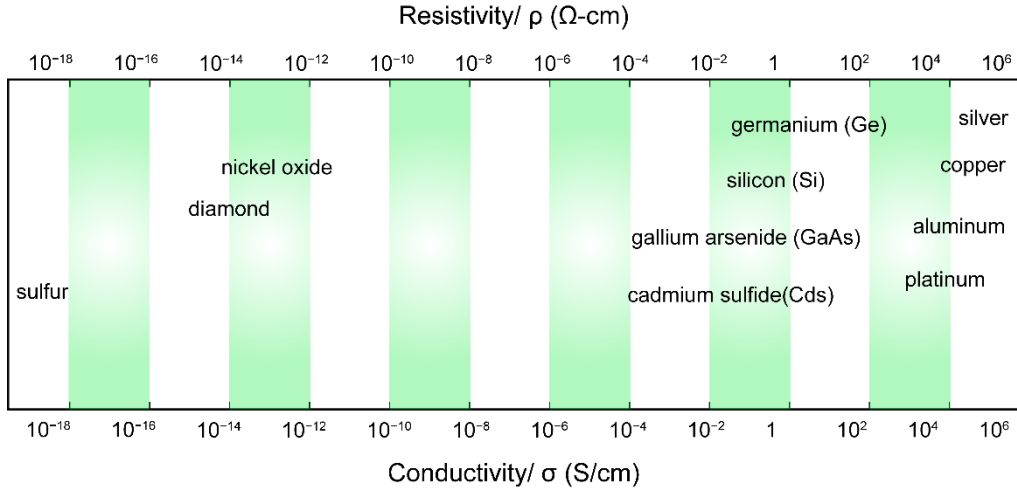


Figure 2. Relationship between resistivity and conductivity for various materials. Conductors, such as silver, copper, aluminum, and platinum, exhibit low resistivity and high conductivity. Insulators, like sulfur, nickel oxide, and diamond, have high resistivity and low conductivity. SCs, including germanium (Ge), silicon (Si), gallium arsenide (GaAs), and cadmium sulfide (CdS), display resistivity and conductivity values that lie between those of conductors and insulators.

electron can occupy—lies near the middle of the band gap as the number of electrons and holes are approximately even.

On the other hand, extrinsic conductivity is due to defects or added impurities (doping) in the lattice reducing the width of the E_g (~ 1.2 eV for silicon) (as well as by light or electric fields). There are two main types of doping: n-type and p-type. In n-type doping, donor atoms with more valence electrons than the host atoms, such as phosphorus in silicon, are added. This shifts the E_F closer to the conduction band, increasing the electron concentration and enhancing conductivity. Conversely, in p-type doping, acceptor atoms with fewer valence electrons than the host atoms, like boron in silicon, are introduced. The distribution of electron density in the SC was elucidated by Enrico Fermi and named in its honor the Fermi-Dirac equation (1).²⁸

$$P(E) = \frac{1}{1 + \exp\left(\frac{E - E_F}{kT}\right)} \quad (1)$$

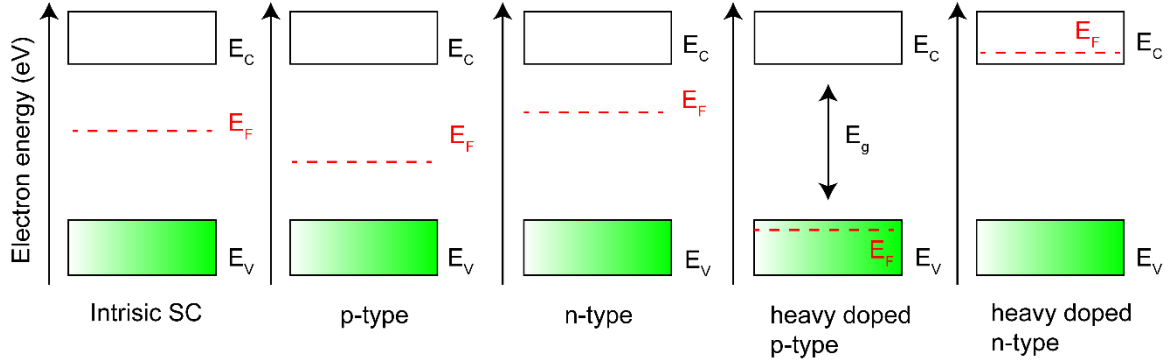


Figure 3. Energy band diagrams for different types of SCs. From left to right: intrinsic SC with the E_F near the middle of the E_g ; p-type SC with E_F closer to the E_V ; n-type SC with E_F closer to E_C ; heavily doped p-type SCs with E_F inside E_V due to high acceptor concentration; heavily doped n-type SCs with E_F inside E_C due to high donor concentration.

where E is the energy level, E_F is the Fermi level, k is the Boltzmann constant, and T is the absolute temperature in Kelvin.

The positioning of the E_F also varies with both the doping type and dopant concentration (Figure 3). In n-type SCs, the E_F is positioned above half the E_g (closer to the E_C) due to the abundance of free electrons in the E_C . On the contrary, in p-type SCs, the E_F is located below half the E_g (closer to the valence band) due to the prevalence of more free holes in the E_V .²⁹

In the case of silicon, the doping concentration can span from 10^{13} cm^{-3} to 10^{18} cm^{-3} . Beyond this doping level, the SC is classified as degenerate exhibiting properties similar to metals due to the high concentration of free charge carriers (i.e., heavy doping).

1.2.1.2 Photoelectric effect in silicon electrodes

While the photoelectric effect is not the main mechanism in DC-TENGs, its principles are closely related and will help the general audience to better understand the mechanism of the triboelectric phenomena. It is also of significant importance for **Chapter 3**, where photoconductivity measurements (PCM) will be employed to assess the degree of surface oxidation on silicon electrodes when working as TENGs.

At p–n junctions and Schottky interfaces (i.e., metal–silicon contacts), e^- – h pair generation and recombination reach a steady state in the absence of external factors. When light illuminates these junctions, it generates additional e^- – h pairs, disrupting this balance and initiating the photoelectric effect (first observed by Becquerel in 1839).³⁰ In this sense, optical transitions of electrons from the E_V to E_C occur through the absorption of photons with energy higher than the E_g energy.³¹ The nature of the E_g , defined by the crystal's band structure, can be direct or indirect. In direct E_g SCs, such as amorphous silicon, electronic transitions are fully allowed, meaning that an electron can move from the E_V to E_C directly by absorbing a photon. However, in indirect E_g SCs, like crystalline silicon, an additional phonon (a quantum of lattice vibration energy denoted by $h\omega$, where h is the Planck constant and ω is the phonon frequency) is required to facilitate the transition.³² This requirement for a simultaneous lattice vibration significantly decreases the absorption probability in indirect E_g SCs.

This distinction between direct and indirect bandgaps is reflected in the materials' absorption coefficients. Direct bandgap semiconductors (SCs), like GaAs, typically have higher absorption coefficients, allowing them to absorb light more efficiently. In contrast, indirect E_g SCs have lower absorption coefficients, and thicker material layers are needed to achieve the same level of light absorption.³³ For instance, crystalline silicon wafers used in photovoltaic solar cells usually have a thickness of several hundred μm to ensure sufficient light absorption, whereas thin layers of direct E_g materials like amorphous silicon can be used in low-power devices such as solar-powered calculators.³⁴ In the context of TENGs, this difference matters for charge transport properties rather than light absorption efficiency. Moreover, materials with direct band gaps, such as gallium arsenide (GaAs) and other III-V SCs, are often used in optoelectronic devices like LEDs and SC lasers due to their high radiative recombination rates.^{35, 36}

1.2.1.3 Silicon–electrolyte contacts

Although the main part of this work is focused on “dry junctions” such as silicon–metal contacts (section 1.2.1.4), silicon–electrolyte systems have been crucial in this work to determine the electrode surface properties (i.e., monolayer coverage, monolayer quality or electron transfer rate at the interface). Hence, a brief introduction of silicon–electrolyte physics is important to better understand the results presented in **Chapters 2** and **4** for instance, where silicon electrochemical characterization played a major role before the implementation of the electrode on different systems.

When an SC E_F , interfaces with an electrolyte (El) containing a dissolved redox couple and possessing its own Fermi level (E_F , El), equilibrium is established as E_F of both phases align.³⁷ In the case of an n-type SC, where E_F , SC is higher than E_F , El, equilibration involves a flow of electrons from the SC to the solution phase. The charge in excess is distributed within the space charge layer (S_{CL}), inducing band bending and the formation of a built-in electric field (Figure 4). As long as there is a difference in electrochemical potential between the SC and the electrolyte, electronic redistribution occurs primarily in the SC. Electrons migrate across the interface until the SCs' Fermi level aligns with the redox potential (E_{redox}) of the electrolyte species in the solution. In n-type SCs, when E_F exceeds E_{redox} , electrons transition from the SC into the solution. This movement generates a positive charge in the S_{CL} , forming an electric field. Consequently, a depletion region is created, which extends from the surface into the SCs' bulk.^{38, 39}

In an n-type SC, the S_{CL} consists of positively charged ionized donor atoms left behind after the electrons have moved toward the electrolyte. This region lacks free electrons, creating a depletion zone. The extent of this depletion region depends on the doping concentration and the applied bias.²⁵ The band-bending phenomenon in the depletion region is crucial for the

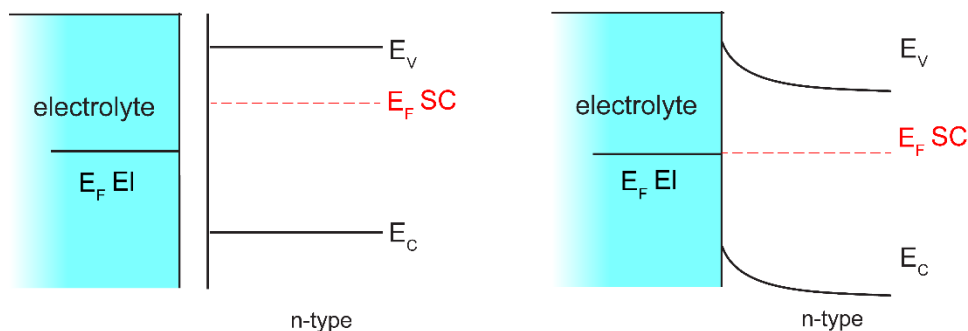


Figure 4. Energy band diagrams of an n-type SC and an electrolyte. The left diagram shows the initial condition before contact, where the Fermi level of the SC (E_F , SC) is higher than that of the electrolyte (E_F , EI). The right diagram illustrates the condition after contact, where electrons have moved from the SC to the electrolyte, resulting in upward band bending in the SC and the formation of a depletion region near the interface. This movement continues until the Fermi levels align, establishing equilibrium.

operation of various SCs devices, including diodes and transistors because it creates an electric field that controls the movement of charge carriers, enabling rectification in diodes and switching in transistors.⁴⁰

The magnitude of this band bending (also referred to as the built-in potential) depends on the difference between the SCs E_F and the redox potential of the electrolyte. As the E_F align, the built-in electric field forms a barrier that inhibits further electron flow from the SC to the electrolyte. This built-in field is crucial for the separation and transport of charge carriers, making it a key factor in the efficiency of devices such as photoelectrochemical cells and sensors.

In the presence of light, additional e^-h pairs are generated in the SC. The built-in electric field in the depletion region helps separate these photogenerated carriers, driving electrons toward the bulk of the SC and holes toward the surface (in a n-type material), where they can participate in redox reactions with the electrolyte. Essentially under illumination minority carriers become the majority carriers. This separation of charge carriers enhances the efficiency of photovoltaic and photoelectrochemical processes.

The equilibrium condition can be mathematically described using the Nernst equation, which relates the potential of the redox couple to the concentrations of the oxidised and reduced species.^{41, 42} The potential difference between the SC and the electrolyte, known as the flatband potential, is a critical parameter that indicates the potential at which the band bending is zero. Understanding and controlling the flatband potential is essential for optimising the performance of SC-based devices in various applications, from energy conversion to sensing technologies, and has been extensively explored in “dry junctions” with a novel Galinstan-based probe in **Chapter 4**.

1.2.1.4 Silicon–metal contacts

When a metal and a SC come into contact, a junction is formed, resulting in one of two types of behaviors: Schottky contacts (i.e., a significant difference between the SC E_F and metal work function (ϕ_M)) or ohmic contacts (i.e., the SC E_F and metal ϕ_M are aligned).⁴³ The work function is the minimum energy required to remove an electron from the metal's surface to a point immediately outside the material. For SCs, the electron affinity (χ) is the energy difference between the E_c and the vacuum energy level.

In an ideal scenario with no surface states or interfacial layers, the behavior of the junction is straightforward. When a metal with a high work function comes into contact with an n-type SC (where E_F , SC is closer to the conduction band), its E_F will align by a movement of negative carriers from SC to metal. This results in the upward bending of the energy bands in the SC and the formation of a depletion region near the interface.⁴⁴ The height of the resulting potential barrier, known as the Schottky barrier (ϕ_B), can be estimated by the difference between the metal's work function and the SC's electron affinity, $\phi_B = \phi_M - \chi$.⁴⁵

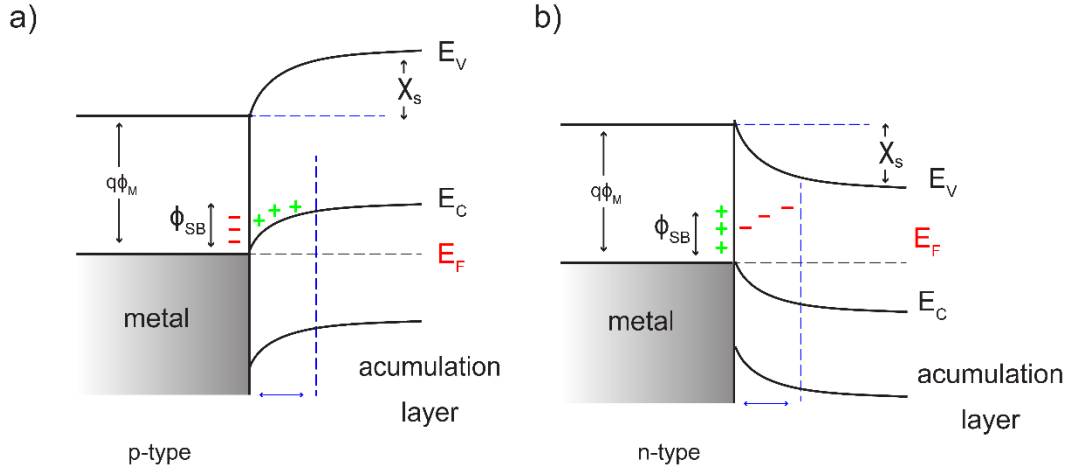


Figure 5. Energy band diagrams of metal-SC contacts. The left diagram illustrates a p-type SC in contact with a metal, forming an accumulation layer where the E_V bends downward near the interface. The right diagram shows an n-type SC in contact with a metal, forming an accumulation layer where the conduction band (E_C) bends upward near the interface. In both cases, the E_F aligns at the interface, the $q\phi_M$ and the ϕ_{SB} are indicated.

For an n-type SC, if the metal's ϕ_M is greater than the SC's E_F , the electrons will move from the SC into the metal, creating a positive charge in the S_{CL} and forming a depletion region. Conversely, if $\phi_M < E_F$, SC, an accumulation layer forms, and the contact exhibits Ohmic behavior, allowing current to flow easily in both directions (Figure 5). In the case of p-type SCs, the process is similar but involves the movement of holes rather than electrons.

Real-world metal–SC contacts often involve additional factors that need to be accounted for, such as surface states and interfacial layers, which can pin the E_F and affect the barrier height. Surface states are electronic states at the surface of the SC that can trap charge carriers, influencing the energy band structure at the interface. These states can result from imperfections in the crystal structure or from chemical reactions at the surface (i.e., substrate oxide growth). In such cases, the E_F at the surface can be pinned, meaning it does not move significantly with changes in the applied voltage. This pinning effect can alter the junction's expected barrier height and behavior. To prevent this, covalent bonding of organic molecules (i.e., 1,8-nonadiyne) to the SC surface can effectively control the surface states,⁴⁶ this has been used extensively in this thesis and will be considered in detail in the next section.

Another important aspect of metal–SC contacts is the method of contact formation. For instance, thermal annealing of metal contacts can change the interfacial properties and thus the barrier height. For example, annealing a Pt-Si diode can lead to the formation of a platinum silicide (PtSi) layer, which has different electrical properties compared to pure platinum and silicon.⁴⁷ The barrier height typically decreases with increasing annealing temperature due to improved interface quality and reduced defect density.

The electrical characteristics of the junction, whether it forms a rectifying (Schottky) or an Ohmic contact, are crucial for various SC devices.^{48, 49} Schottky diodes, for example, exploit the rectifying properties to allow current to flow more easily in one direction than the other. They are used in applications requiring fast switching speeds and low forward voltage drops, such as in radio frequency applications and power rectifiers. Ohmic contacts, on the other hand, are essential for ensuring efficient charge carrier injection in devices like transistors and light-emitting diodes (LEDs), where they serve as the connection between the active SC region and the external circuitry.

This analysis assumes a macroscopic and static contact such as that in **Chapter 4** where a macroscopic Galinstan-silicon junction was proposed to determine the electrical characteristics of the electrode. In microscopic contacts such as those described in **Chapter 5**, we will see that the presence of uncontrolled sliding events or induced loads will alter the charge transport characteristics of the junction.

1.2.2 Silicon surface chemistry

1.2.2.1 Etching of silicon

Silica (SiO_2) is one of the most common minerals on Earth and represents the natural form in which silicon is found and collected.⁵⁰ Chemical etching of silicon oxides is of significant

technological relevance, as it constitutes a key process for most silicon-based electronic devices.⁵¹ When manufactured, silicon wafers exhibit an unclean oxide layer (SiO_x) obtained from suppliers that need cleaning before etching. Harsh cleaning conditions (hot piranha solution, [1:3 H_2SO_4 , 30% H_2O_2]) are employed to remove any undesired organic compound that might be present on the surface.⁵² Thus, the initial step in integrating silicon into chips and related devices like TENGs and micromachining processes involves cleaning and dissolving the superficial oxide layer.

After cleaning, removing the oxide layer via chemical etching to expose a hydrogen-terminated (Si-H) surface comes into effect. Silicon etching has been extensively studied mainly through Alkaline and Fluoride-based solutions. HF-based solutions have been the most employed etchants for silicon oxide removal (Figure 6). Among them, NH_4F has been chosen in this Ph.D. thesis to minimize the hazards related to HF.⁵³

Despite the initial reliance on fluoride-based solutions, recent findings have shifted our understanding of surface passivation and stability mechanisms involving fluoride-based etching. The conventional assumption proposed that the chemical stability of the silicon lattice resulted from F^- passivation. This proposition was supported by the significantly higher Si-F bond strength (6.0 eV) compared to Si-H (3.5 eV).²⁶ However, it has been concluded that the chemical stability of these surfaces is, in reality, attributed to surface passivation by hydrogen.^{54,55} Furthermore, the etching mechanism of silica has been historically described as a pure chemical process, but in **Chapter 2** we will see that a strong electrochemical component is present in the removal of silicon oxides and different etching mechanisms to maximize electrical outputs of Si(211) when performing as a TENG will be further discussed in detail.

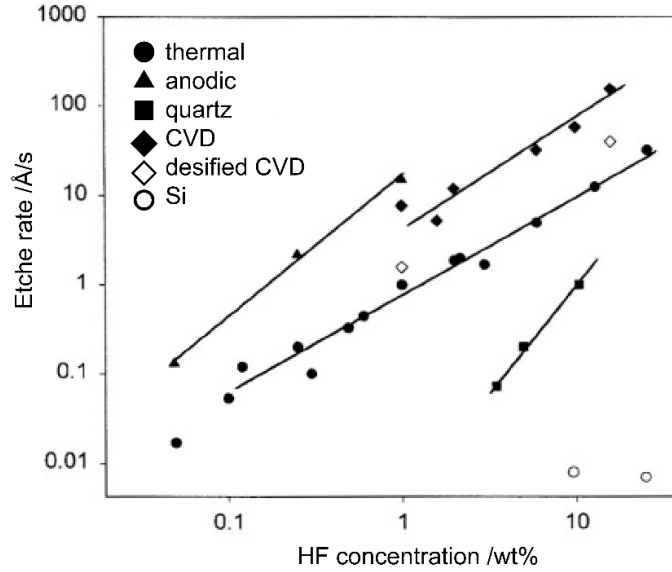


Figure 6. The etching rate of different silicon oxides as a function of HF concentration. Adapted with permission from Xiaoge Gregory Zhang, 2001, Springer New York, NY. © 2001 Springer (ref. 26).

1.2.2.2 Self-assembled monolayers (SAMs) on silicon

Even though the achieved Si–H layer is less prone to oxidation than a cleaved silicon surface (i.e., oxide formation implies in this case the breakup of Si–H bonds) it will unfortunately restore its oxide layer of around 2–4 Å when exposed to air.⁵⁶ To prevent this, the attachment of organic compounds to the hydrogen-terminated surface has been widely employed as Si–H is susceptible to be reacted with specific organic molecules to passivate and tune the properties of the silicon surface.^{57, 58}

This electrical and electrochemical characteristics tuning, is achievable through self-assembled monolayers (SAMs) attachment on the surface.⁵⁹ SAM bonding can tune different parameters such as conductivity,^{60, 61} roughness,⁶² adhesion,^{63, 64} and wettability,⁶⁵ and possesses the potential to influence the SC ϕ M.⁶⁶ These adjustments enable specific interactions with substrates, facilitating a deeper understanding of chemical thermodynamics and kinetics at interfaces advancing the surface science field toward molecular-scale resolution.⁶⁷

The development of carbon-based monolayers on silicon was pioneered by the seminal work of Linford and Chidsey in 1993.⁶⁸ This method involves the thermal decomposition of diacyl peroxides to generate alkyl radicals that bind to hydrogen-terminated Si(100) and Si(111) surfaces. Compared to silane-derived monolayers, these alkyl monolayers exhibit greater robustness. Further advancements have been made by employing 1-alkenes and 1-alkynes on hydrogen-terminated Si(111) surfaces, achieving high-quality monolayers through UV-catalyzed hydrosilylation. This synthetic mechanism, hydrosilylation of an α,ω -dialkyne molecule (1,8-nonadiyne, **1**, Figure 7), has been extensively exploited along the development of this Ph.D. to produce **Si-1** surfaces either on Si(111)-H or Si(211)-H.^{23, 24}

This process leaves an acetylene group at the distal end of the **Si-1** monolayer, offering a pathway for further derivatization, like copper-catalyzed azide-alkyne coupling (CuAAC) reactions by reacting azidomethylferrocene (**2**) with **Si-1** surfaces to generate **Si-2** surfaces (Figure 7).^{69, 70} This click chemistry approach facilitates the addition of various functionalities to the monolayer, including redox-active groups like ferrocenyl moieties.⁷¹ Incorporating a metallocene into the monolayer regulates the surface density of positively charged ferricenium tethers (as seen in **Si-2** samples); and provides the means to examine their electrochemical

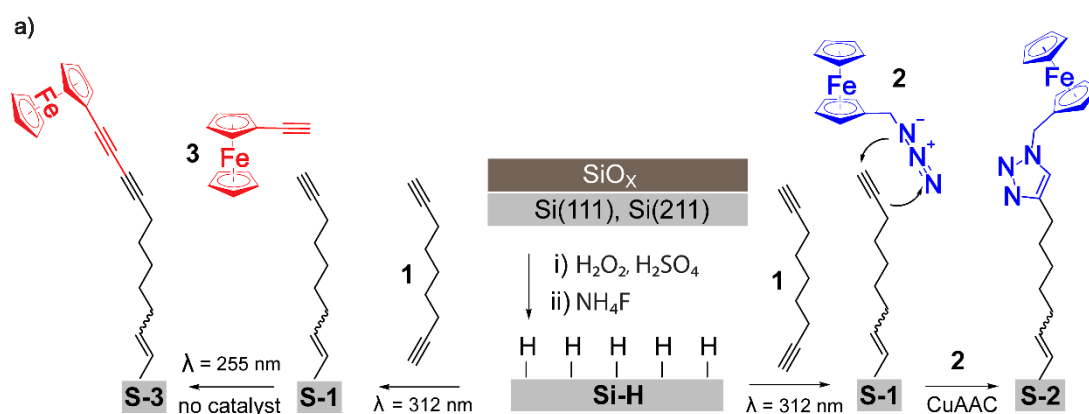


Figure 7. Schematic representation of the strategy used for the passivation and functionalization of the lowly doped Si(111) and Si(211) surfaces. Reprinted with permissions from ref. 78.

profiles to distinguish between electrostatic effects arising from molecule-to-molecule interactions and those due to molecule-to-space-charge interactions.⁷²

The CuAAC reaction offers several advantages, including minimal purification needs, the absence of protection and deprotection steps, high yields, and is compatible with a variety of solvents and offers a direct method to determine the monolayer surface coverage.^{73, 74} Nevertheless, the robustness of the CuAAC reaction comes at the cost of copper impurities on the surface which can greatly influence the electric surface properties.^{75, 76} Due to this association between copper contaminants and electronic defects that hinder charge transport across SAMs, I have also investigated an alkyne–alkyne photochemical homocoupling reaction as a copper-free method to attach ferrocenes following the method proposed by Sambhi.⁷⁷ This was achieved through UV-assisted coupling of alkyne **3** with **Si-1** surfaces to generate **Si-3** surfaces (Figure 7) and has been explored in detail in **Chapter 4**.⁷⁸

1.2.3 Electrochemical measurements

1.2.3.1 Cyclic voltammetry (CV)

Cyclic voltammetry (CV) is an indispensable technique in electrochemistry employed to investigate the reduction and oxidation processes (i.e., kinetic and thermodynamic properties, as well as mass transport for the case of diffusive systems) of electrode materials, including those of molecularly modified SC interfaces.^{79, 80} While all transient techniques theoretically can navigate the same current-potential-time space to gather the required information, CV offers a straightforward way to observe the impact of potential and time on the current within a singular experiment. Its simplicity and sensitivity make it an essential tool for the analysis of electrochemical reactions happening on the surface.⁸¹

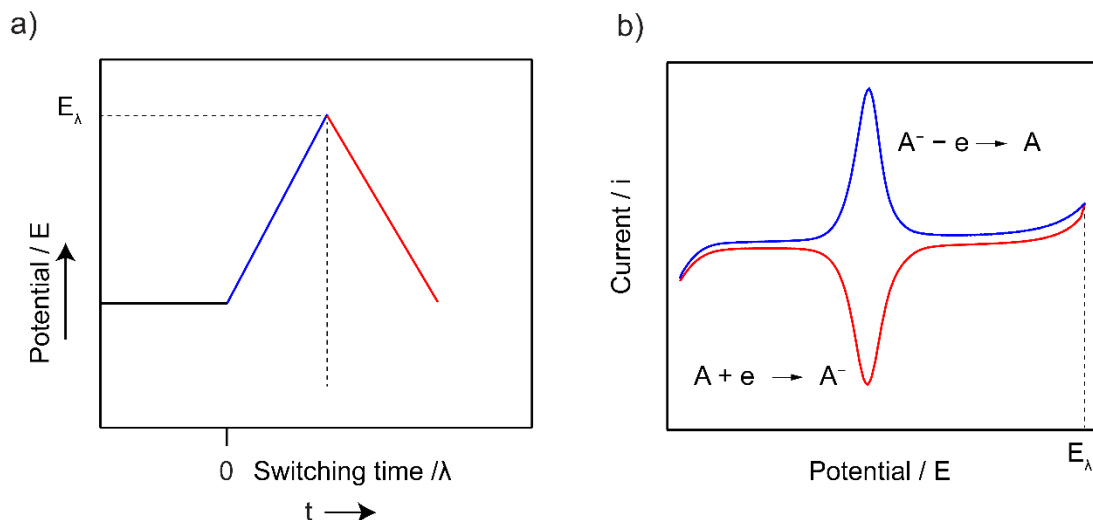


Figure 8. (a) Potential vs. time graph depicting the CV scan rate. The potential is swept linearly between two values and then reversed, with the switching time indicated. E_λ represents the switching potential. (b) Corresponding current vs. potential graph showing a typical cyclic voltammogram recorded on S-2 (surface confined) samples. The red and blue curves represent the anodic and cathodic sweeps, respectively, illustrating the oxidation (a) and reduction (b) reactions of a reversible redox couple. The peaks correspond to the redox processes occurring at the electrode surface.

CV operates on the principle of sweeping the potential of an electrode linearly over time within an electrochemical cell and measuring the resulting working electrode current (i.e., equivalent to a double potential step chronoamperometry) see Figure 8. The original potential of the working electrode is chosen to be a negligible current flow so the present chemical species in the electrode are not reduced or oxidized.⁸² This approach facilitates the analysis of redox reactions and electron transfer behaviors across interfaces, once the potential is swept linearly. The acquisition of the peak potential provides insights into the thermodynamics and kinetics of electrochemical processes, a feature that has been extensively exploited during my research to assess the charge transport characteristics of the functionalized silicon electrodes.⁸³

The redox reactions observed during CV can be described by the Nernst equation (2) (Walther Hermann Nerst 1889),⁸⁴ which relates the electrode potential to the concentrations of the oxidized and reduced species:

$$E = E^0 + \frac{RT}{nF} \ln \frac{[Ox]}{[Red]} \quad (2)$$

Where E is the electrode potential, E^0 is the standard electrode potential, R is the ideal gas constant, T is the temperature, n is the number of electrons transferred, and F is the Faraday constant.

Most of the information about the redox properties and the quality of the monolayer on the surface can be extracted from the voltammogram wave.⁸⁵ Essentially three important parameters must be considered while analyzing the voltammogram signal: the peak current ratio for the cathodic and anodic process, the full width at half-maximum (FWHM), and the shape of the wave. The ratio of the peak currents for the reduction (cathodic) and oxidation (anodic) processes is a vital indicator of the reversibility of the electrochemical reactions taking place on the electrode surface.⁸⁶ In an ideal reversible system, this ratio approaches unity, which indicates that the rates of the forward and reverse reactions are balanced. A deviation from unity suggests kinetic limitations, such as slow electron transfer rates, which can affect the efficiency of the redox process.⁸⁷ The FWHM of the peaks in a voltammogram directly reflects the homogeneity and the dynamic behavior of the electrochemical process. A narrow FWHM is indicative of a uniform and fast electron transfer process, often associated with well-organized and defect-free monolayers. Conversely, a broad FWHM suggests a distribution of electron transfer rates, possibly due to heterogeneities within the monolayer or the presence of different interacting species.⁸⁸ This parameter is crucial for assessing the quality of the monolayer and understanding the kinetics of the redox reactions. In this thesis, CV has been extensively used, particularly in **Chapters 2** and **4** to determine the etching outcome and monolayer quality, and as a diagnostic tool to predict how the surface will perform in a hypothetical TENG design system.

1.2.3.2 Non-ideal voltammogram waves

The voltammogram shape reveals details about the nature of the redox processes, the interaction of the analyte with the surface, and potential complications such as adsorption or competing side reactions.⁸⁹ Symmetrical waves with well-defined peaks suggest a smooth, reversible surface-confined process, while asymmetries or additional peaks may indicate complex reaction mechanisms or surface interactions affecting the redox behavior.⁹⁰

These deviations from ideal shapes manifest as broadened, split, or even multiple waves in voltammograms. The non-ideal behavior observed in SAMs has been commonly associated with diverse factors such as heterogeneous molecular interactions, disorder within the monolayer structure, odd-even effects in linker molecules between headgroups and substrates, repulsion functions of headgroups, and interactions between redox species and the electrolyte.⁹¹ Such non-ideal voltammetric responses have been thoroughly investigated in SAMs on gold substrates with these effects being well-documented.⁹² However, recent work by Song et al. has shown that in the case of SC photoelectrodes like silicon, multiple peaks, and peak broadening can be attributed to heterogeneous photocurrents rather than molecular disorder

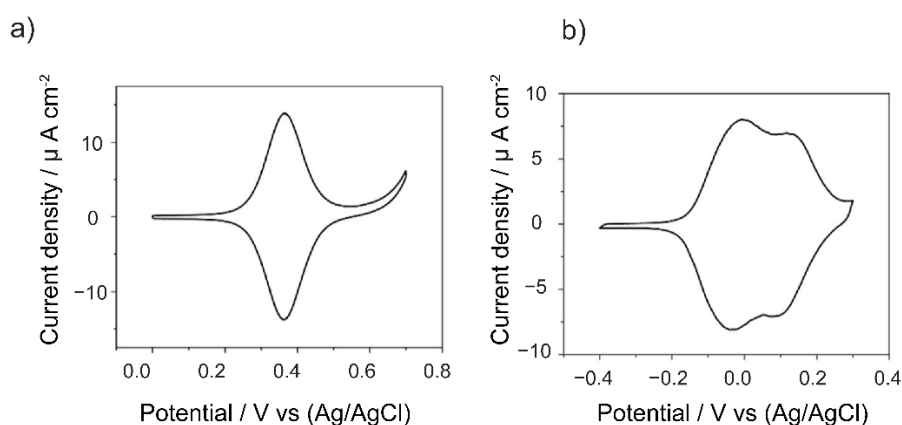


Figure 9. Doping level and type and ideality of the redox response. (a) Representative and close-to-ideal cyclic voltammogram recorded for a **S-2** (Figure 7) sample prepared on HD, p-type Si(111) (100 mV/s, 1.0 M HClO₄, dark). (b) Representative cyclic voltammogram for a **S-2** monolayer grafted on a Si(111), n-type, LD photoanode, showing an evident non-ideal peak splitting (100 mV/s, 1.0 M HClO₄, electrode illuminated at a light intensity of 1.0 mW m⁻²). Adapted from ref.88 with permission from the American Chemical Society, copyright (2022).

present in the monolayer attached (Figure 9).⁸⁸ Chapter 2 will explore and expand these often-overlooked features and probe that non-idealities such as multiple peaks are intimately linked to the substrate etching and can be potentially used to diagnose the performance of the system when forming part of a TENG.

1.2.3.3 Electrochemical impedance spectroscopy (EIS)

In the previous section, it has been considered the scenario where the system is perturbed through a potential sweep, driving the electrode far from equilibrium and measuring a transient signal. Electrochemical impedance spectroscopy (EIS) follows a different approach in which an alternating signal causes small perturbations in the system at a steady state across a broad frequency spectrum.^{80, 93} It is a highly effective technique used to measure the interfacial impedance or resistance present in a circuit element and is also commonly applied to assess the diffusion state of a solution, electrolyte movement towards the electrode, and charge transfer across the monolayer on the substrate.⁹⁴ It is particularly useful for distinguishing between the time constants of electrochemical reactions, with lower frequencies typically providing clearer differentiation than higher frequencies.⁹⁵

The impedance spectrum consists of a real component (Z_r), which does not vary with frequency, and an imaginary component (Z_i), which is frequency-dependent. The data gathered can be represented as "Nyquist " and "Bode" plots. In the Nyquist plot, the real part, Z' , is plotted on the X-axis, while the imaginary part, Z'' , appears on the Y-axis. Each curve point on the Nyquist plot indicates the impedance at a specific frequency and can be represented as a vector pointing from the coordinate origin to the impedance value.

In the Nyquist plots the critical parameter is the charge-transfer resistance (R_C), systems with a high R_C will demonstrate slow kinetic behavior (semicircular region Figure 10a). On the other hand, If R_C is relatively small mass transport will be a determining factor, and the semicircular

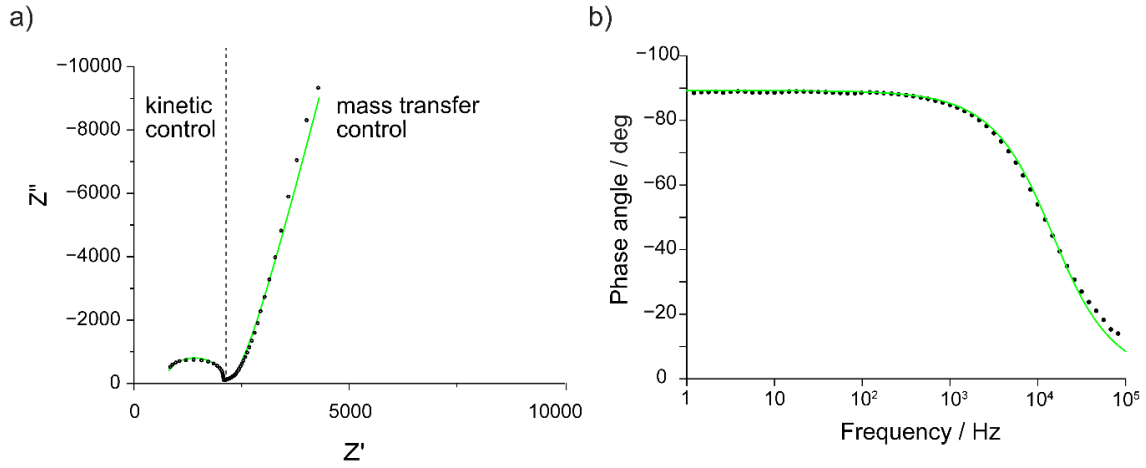


Figure 10. (a) Representative EIS Nyquist plot illustrating the real part of impedance (Z') versus the imaginary part of impedance (Z''). The plot distinguishes between kinetic control and mass transfer control regions. Systems with high charge-transfer resistance (R_C) are indicated by a steep slope in the kinetic control region. (b) Bode plot showing the phase angle as a function of frequency, the phase angle decreases with increasing frequency, indicating changes in the system's impedance characteristics.

region is not well defined. Conversely, the Bode plot (Figure 10b) features a logarithmic frequency scale on the X-axis and typically includes two Y-axes: one for the logarithmic magnitude of the impedance and another for the phase angle. The Nyquist plot is particularly useful for analyzing resistance characteristics, whereas the Bode plot is better suited for assessing capacitance features and, along with the formalism developed in 1979 by Pierre Laviron (3) has been extensively used in **Chapters 2** and **4** to estimate the charge transfer rate.⁹⁶

$$Z(\omega) = R_s + \frac{R_{ct}}{1 + j\omega R_{ct} C_{dl}} \quad (2)$$

Where $Z(\omega)$ is the impedance as a function of the angular frequency (ω) R_s is the solution resistance, R_{ct} is the charge transfer resistance, C_{dl} is the double-layer capacitance and j is the imaginary unit.

1.2.4 Spectroscopic measurements

1.2.4.1 X-ray photoelectron spectroscopy (XPS)

X-ray photoelectron spectroscopy (XPS) stands as the most prevalent technique for surface analysis, primarily because of its capability to provide detailed information about both the core-shell and valence electrons of the surface subjected to study. XPS relies on the photoelectric effect a phenomenon in which the material (i.e., atom) absorbs electromagnetic radiation and releases photoelectrons as a consequence of the excitation, described by Einstein (1987).⁹⁷⁻⁹⁹ XPS is distinguished from X-ray fluorescence (XRF), which involves the emission of secondary X-rays, and Auger electron spectroscopy (AES), which detects electrons emitted as a result of electron transitions within atoms (Figure 11).¹⁰⁰

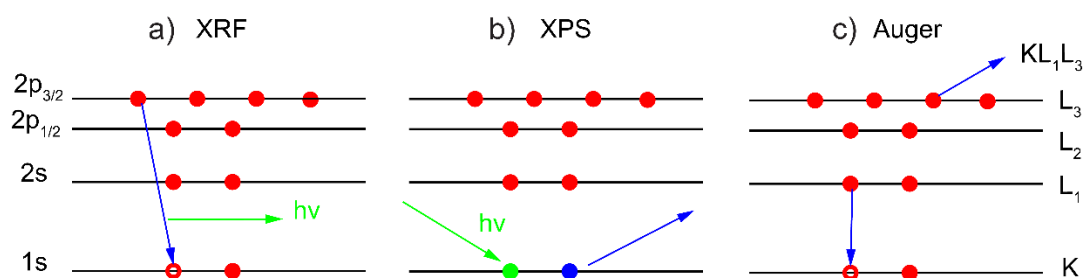


Figure 11. Processes associated with photon excitation. (a) Excitation resulting in fluorescence, (b), excitation of an electron from a core level, and (c) secondary excitation resulting in Auger emission.

The photoelectric effect was first observed with electronically isolated metals under vacuum that had an enhanced ability to spark when exposed to light. This led to the ability to derive the ratio of Planck's constant over electronic charge (h/e) and the work function (ϕ_M) of the metal object when altering the energy source of irradiation. XPS detection principle, thus, relies on the energy of the photoelectron that is ejected from the atom. Since photons lack mass, this energy transfer effectively absorbs the photon. If the energy is adequate, the electron is released from the atom and the solid. The remaining kinetic energy (K_E) of the electron is then measured,

representing the electron binding energy, which is unique to each element and its surrounding environment.^{101, 102} The process can be expressed as follows (4):

$$K_{E_{XPS}} = E_{ph} - \phi_{XPS} - BE_{XPS} \quad (4)$$

$K_{E_{XPS}}$ represents the energy of the electron that gets released, E_{ph} is the energy of the photon that starts the process, BE_{XPS} stands for the observed (or calculated) binding energy, and ϕ_{XPS} refers to the work function of the XPS instrument. XPS has been used during my Ph.D. to assess the atomic composition of the functionalized monolayers and to determine the degree of surface oxidation at silicon electrodes.

1.2.4.2 X-ray reflectometry (XRR)

The implementation of thin films in technological applications and, within the scope of this Ph.D thesis, of grafted SAMs on silicon, often requires precise control of film thickness because their properties tend to be thickness-dependent. X-ray reflectometry (XRR) offers a non-destructive, contact-free method for measuring thickness in the range of 2–200 nm with a precision ranging from 1–3 Å which is suitable for both crystalline and amorphous substances.^{103, 104}

Besides thickness measurement, XRR is also used to assess the density and surface roughness of films and multilayers with high accuracy.¹⁰⁵ The latter, surface roughness characterization, has been evaluated by combining XRR with AFM topography measurements (section 1.2.5.1) to shed light on the surface topographical properties of the monolayer-functionalized silicon electrodes and to correlate it with the performance of the system when working as a TENG (**Chapters 2 and 4**).

The working principle of XRR involves directing a monochromatic X-ray beam at a sample at grazing angles to measure the intensity of X-rays reflected from the surface.¹⁰⁶ As the X-rays

interact with the sample, variations in electronic density between different layers cause the X-rays to be reflected at various intensities, creating an interference pattern that can be analyzed to determine film thickness, density, and surface roughness according to Bragg's law for thin film analysis (5).

$$n\lambda = 2d \sin\theta \quad (5)$$

At very low angles of incidence, known as grazing angles, X-rays hitting a material's smooth surface will reflect below or at a small angle named the critical angle. This angle is minimal and varies based on the material's electronic density; denser materials have smaller critical angles. As the angle of the incident X-rays surpasses this critical threshold, the rays penetrate more deeply into the substance. On ideally flat surfaces, the reflectivity falls sharply when the angle exceeds the critical angle.

1.2.5 Atomic force microscopy (AFM) measurements

1.2.5.1 Topography measurements

AFM is an advanced imaging technique pioneered by Binnig and developed in the 1980s, expanding scanning probe microscopy (SPM) capabilities.^{107, 108} It significantly differs from scanning tunnelling microscopy (STM) as STM can only measure conductive samples in vacuum. AFM's primary application used in this thesis has been its ability to perform detailed surface analysis, allowing the study of the morphology and the mechanical properties of the silicon samples with atomic-scale resolution. Topography images extracted with AFM were also used to assess the surface roughness values in parallel with XRR measurements. Since the main research conducted during this thesis work has relied on AFM, it will be of significant relevance to introduce the working principles and main modes of this powerful technique.

SPM techniques in general rely on a sharp tip at one end that interacts with the sample's surface achieving high-resolution images, as they can precisely probe surface features at the nanoscale. For AFM, the probe is similar to a stylus profilometer that directly interacts with the sample surface. By detecting the repulsive and attractive forces between the probe and the surface, it generates a high-resolution, three-dimensional topographic image of the surface. The tip is mounted on a cantilever, visualized as a flexible beam that bends in response to forces between the tip and the sample surface. Cantilevers with low spring constants play a crucial role in AFM's functionality by enabling precise control over the forces exerted between the tip and the sample which causes the cantilever to deflect. A laser beam is placed at the back of the cantilever, actively monitoring the cantilever deflection. The reflection of this laser beam onto a sensitive photodetector (PSPD) captures the deflection changes (Figure 12) and provides the data needed to construct the topographic images of the surface.¹⁰⁷ These variations in the electric signal resulting from the laser spot's movement on the photodiode are harnessed within a feedback loop to ensure a consistent force is maintained on the AFM tip. This feedback loop

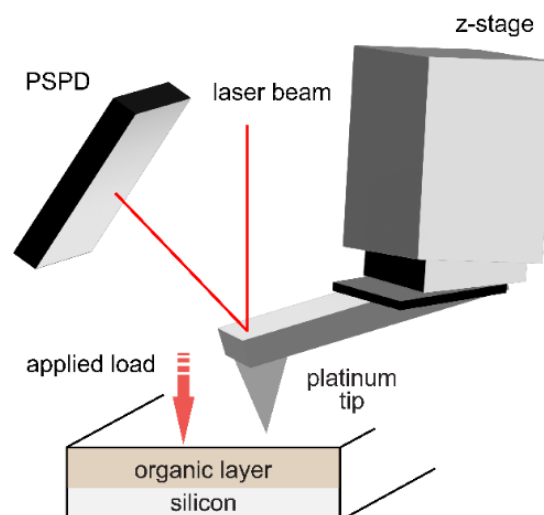


Figure 12. Schematic representation of an AFM setup. The setup includes a laser beam directed at a PSPD, a z-stage for vertical adjustments, and a platinum tip applying a load onto the sample. The sample consists of an organic layer on a silicon substrate. This configuration has been used to measure surface properties and interactions at the nanoscale.

controls the application of voltage to a piezoelectric scanner, enabling controlled vertical

movements of either the AFM tip or the sample. The vertical motions of the piezo are instrumental in its ability to construct the topography map. The level of precision we can get with AFM measurements is achieved through various imaging modes such as contact mode, tapping mode, and non-contact mode. While in contact mode the tip is contacting the surface at all times, in tapping mode the tip is on and off the surface as the cantilever oscillates a value close to its resonance frequency. This minimizes contact mode limitations such as lateral force interactions on steps or edges resulting in tip and/or surface damage. In non-contact mode, the cantilever oscillates at a much smaller amplitude minimizing the repulsive interactions regime, and tip/sample wear. This aspect, surface damage suffered by the sample due to tip sliding while operating AFM, has been evaluated in depth in **Chapter 3**.

1.2.5.2 Electrical measurements

Among the diverse AFM scanning functionalities, the capability to measure current outputs has been particularly exploited and used in all of the chapters of this thesis. Recent developments have further refined AFM techniques, enabling precise characterization of nanoscale surface interactions and their direct impact on triboelectric performance.

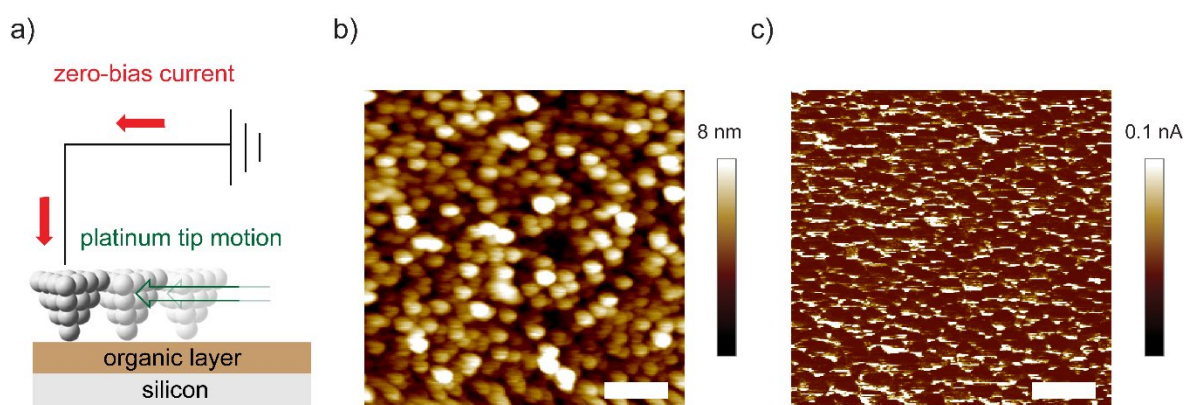


Figure 13. (a) Scheme of the AFM setup, a platinum tip slides across a monolayer-coated silicon wafer. (b) High-resolution AFM topography image of an S-1 monolayer on Si(211). Zero-voltage bias C-AFM map of an S-1 Si(211) sample. The horizontal scale bars in panels b and c represent 1 μm .

This has been effectively achieved through two primary modes: conductive mode (C-AFM) via Pt tip–silicon sliding events, and spectroscopy measurements (i.e., Current–Voltage (I–V) and Force/distance (F/d) modes), where the tip is pressed onto the surface.¹⁰⁹ Each method offers different insights and benefits, providing a deeper understanding of material properties at the nanoscale. C-AFM provides precise current measurements as the tip moves across the silicon substrate, allowing for the detailed mapping of electrical conductivity and topographical features (Figure 13). I–V measurements evaluate the current response while applying a voltage similar to traditional macroscopic probe methods but at the nanoscale,¹¹⁰ whereas force/distance (F/d) measurements assess the current response under strain gradients generated by applied loads. Local conductivity and current distribution at a specific bias (i.e., 0 V) are captured through a current amplifier.

C-AFM operates in contact mode because it requires a direct electrical connection between the conductive AFM tip and the sample to measure current. The force between the tip and the surface falls within the regime of short-range repulsive interactions. Hence, the tip experiences forces such as van der Waals attraction or electrostatic repulsion as it moves across the surface, causing the cantilever to bend subtly. The interaction of these forces and the direct implications regarding current outputs when scanning the sample's surface have been explored in depth in **Chapter 5** and will also be discussed in the next section.

1.2.6 Mechanically-induced DC outputs on silicon

1.2.6.1 Mechanism of triboelectricity

The concept of triboelectricity can be defined through the framework of charge induction (CI), contact electrification (CE), and electrostatic discharge (ESD), being the later detrimental in the current generation phenomena.^{111, 112} While CI and CE does not inherently require friction, triboelectricity involves both, CE and friction-related effects such as debris production and a

measurable friction coefficient.¹¹³ Friction can be dissipated in the form of phonons and e^- - h excitation, which is similar as previously mentioned, to the photoelectric effect causing them to transition from E_V to E_C resulting in the generation or movement of negative and positive charges (i.e., current output) through E_g .¹¹⁴ Within the scope of this thesis, triboelectricity and associated phenomena (i.e., flexoelectricity) have been investigated on a series of silicon-SAM-metal junctions (i.e., SC-insulator-metal junctions forming a Schottky diode).

The basic model describing friction between surfaces is Amontons' Law, which determines a direct proportionality between the friction force and the applied normal force, represented by (6):

$$F_{friction} = \mu F_{normal}. \quad (6)$$

From Amontons' law, it is inferred that the normal load plays a major role in determining the frictional force.¹¹⁵ However, the relationship between mechanical stress and electrical generation extends beyond basic friction. In this sense, tremendous efforts have been made to decouple triboelectric outputs from piezoelectric and flexoelectric contributions.^{116, 117} The role of flexoelectricity in the current generation will be expanded in the next section and **Chapter 5**. In this sense, comprehending and controlling the role of friction, loads and current outputs are essential for enhancing the performance of equipment, decreasing energy usage, and prolonging material durability.

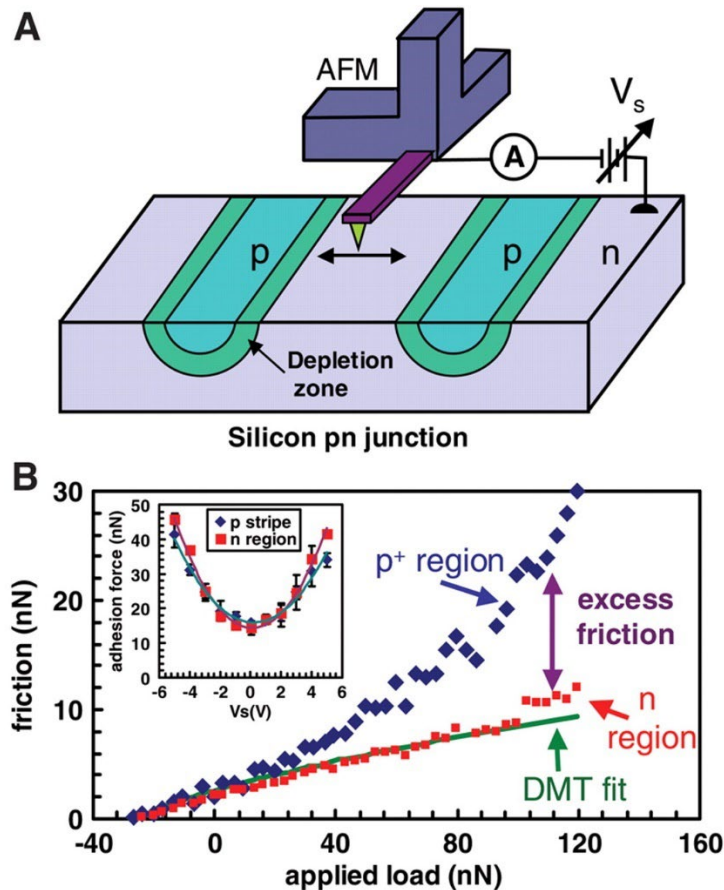


Figure 14. (a) Diagram illustrating AFM measurements on p-type stripes on n-type silicon bulk. (b) Graph depicting the relationship between friction force and applied load at a sample bias of +4V. Scanning speed was maintained at 5 $\mu\text{m/s}$. (Inset) The pull-off force as a function of sample bias is shown, with error bars representing the standard deviation from five separate measurements. Reprinted with permissions from ref. 115.

Understanding which factor governs the current generation mediated by mechanical stimulus has been a central motivation for researchers of the field. In 2006, Salmeron and co-workers conducted a study that observed a significant impact of silicon doping on friction.¹¹⁸ They implanted a highly doped p-type stripe onto an n-type doped substrate and measured the current and friction simultaneously at a +4 V applied bias, as depicted in **Figure 14**. This bias caused the p-type regions to undergo strong accumulation while the n-type regions experienced depletion or weak inversion. Interestingly, a substantial increase in friction was noted on the p-type regions compared to the n-type regions, without a corresponding rise in wear. This observation suggests that surface states induced by localized strain at the tip-silicon interface play a significant role. The relevance of these findings is such that attractive electronic forces

-electrostatic in origin- in the tip-silicon interface caused by a population of unbalanced ionized dopant atoms in the near-surface region of silicon, will cause an excess of friction or load. The direct implication is that an excess strain gradient will likely occur due to tip tilting/bending which will in contrast be reflected in an additional bias voltage. This will be the central point of **Chapter 5**, where the presence and relevance of the strain gradients (i.e., flexoelectric effect) to the triboelectric phenomena will be discussed.

1.2.6.2 Mechanism of flexoelectricity

Flexoelectricity refers to the electric polarization generated in a material due to a non-uniform mechanical strain resulting in the generation of an electric field ([Figure 15a](#)).¹¹⁹ The first report on flexoelectricity is likely from a 1910 paper by Walter Jamieson, who observed curvature-dependent surface charging in celluloid sheets.¹²⁰ Since then, flexoelectricity has been observed in several materials but the mechanism underlying the effect remained unclear. Unlike piezoelectricity, which occurs in materials without inversion symmetry and produces polarization proportional to the applied stress,¹²¹ flexoelectricity can be observed in centrosymmetric materials and is particularly significant at the nanoscale where strain gradients are pronounced.¹¹⁹

The mechanism of flexoelectricity involves the coupling of mechanical deformation and electric polarization, described by the flexoelectric coefficient (7).

$$P_i = u_{klmn} \frac{\partial \varepsilon_{lm}}{\partial x_k} \quad (7)$$

Where P_i is the polarization, u_{klmn} is the flexoelectric coefficient, $\partial \varepsilon_{lm}$ is the strain tensor, and ∂x_k denotes the spatial coordinates. Although the flexoelectric coefficient has been already determined for a wide range of materials,¹²² the experimental silicon flexoelectric coefficient remains unknown.

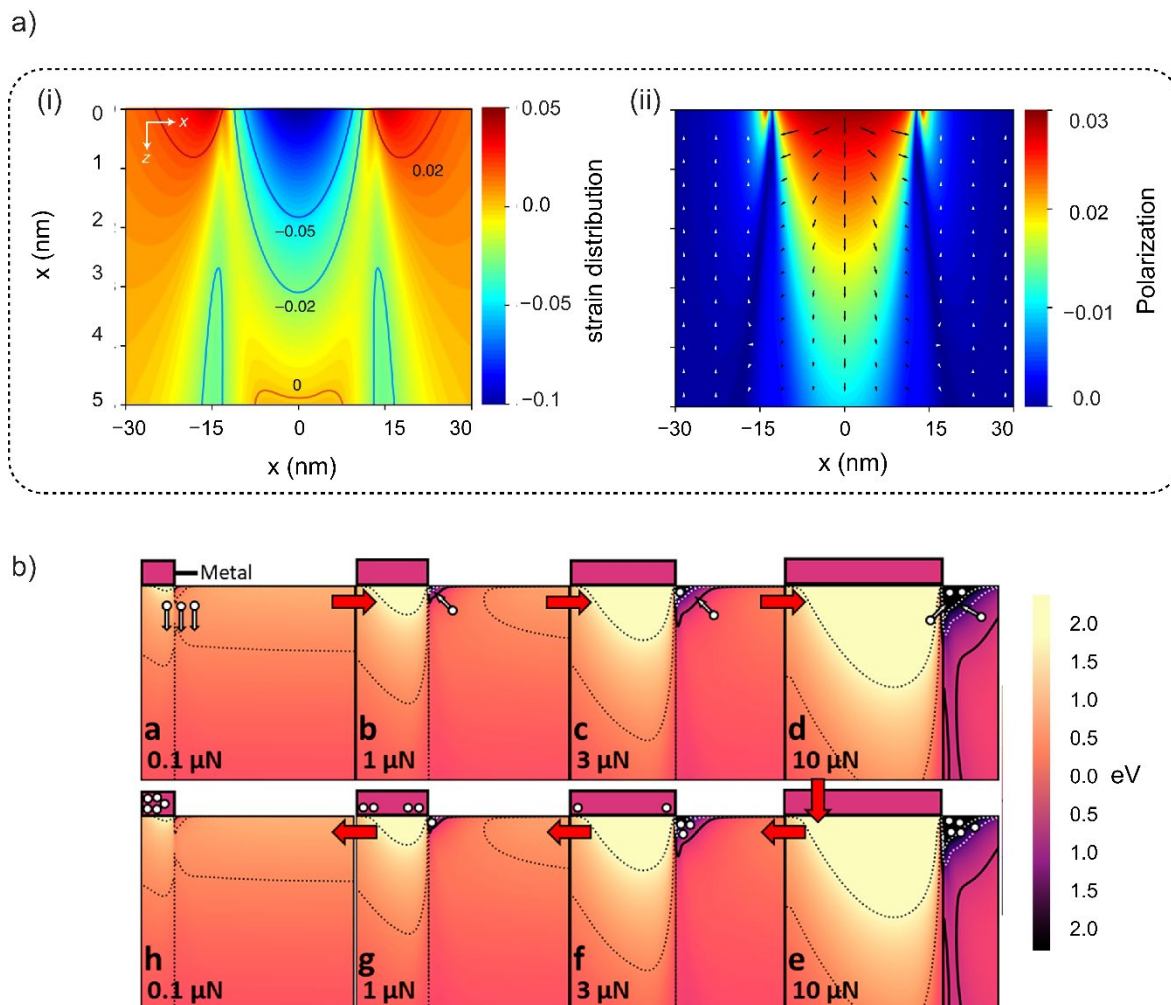


Figure 15. (a) Simulations of the flexoelectric effect in silicon, using a tip-force model (i) and the resulting flexoelectric polarization (ii) adapted with permission from ref. 119, *Copyright 2020 Springer Nature Limited*. (b) Ratcheting mechanism for charge transfer proposed by L. Marks for a PtIr–STO system. Adapted with permission from ref. 123, *Copyright 2022 American Chemical Society*.

Most recently, studies on n-type SrTiO₃ by L. Marks and co-workers have demonstrated that strain gradients can influence the height and width of the interface Φ_b impacting charge transport characteristics proposing the so-called Ratcheting mechanism to explain the phenomena [Figure 15b](#).¹²³ These reports become especially relevant within the scope of this thesis as flexoelectricity has been proposed as the “missing term” of triboelectricity. **Chapter 5** is entirely dedicated to exploring the effects of strain gradients triggered when a Pt AFM tip contacts the silicon surface (AFM contact mode) and the subsequent flexovoltage. The findings

are also focused to shed light on the factors that govern the performance of these systems when operating as TENGs.

1.2.6.3 Triboelectric nanogenerators (TENGs)

As one of the main goals of this thesis has been understanding the factors governing the performance of monolayer-functionalized silicon samples when incorporated as part of a TENG, the lector will benefit from a brief introduction to the history of these devices and how this thesis has approached the opening questions regarding the working mechanism.

The first report was made by Z. L. Wang in 2012, where the device was designed through a combination of polyester and Kapton, producing alternating current (AC-TENG), [Figure 16](#).¹⁸ However, in the past years, there has been a significant surge in research focused on developing DC-TENGs.¹²⁴ The initial design involved sharp metal wire slides across grains of molybdenum disulfide (MoS_2) and opened up the question of the feasibility of applying the DC-TENG design to other SCs like silicon, which has been the central motivation of this thesis.

As previously mentioned, TENGs operate on the principles of autonomous electricity generation by converting various forms of mechanical energy into electrical energy and its applications range from energy harvesting to sensing.¹²⁵⁻¹²⁷ They typically operate in four modes: contact-separation, sliding, single-electrode, and most recently discovered through electrical polarization due to strain gradients. Although the precise working mechanism of TENGs remains under debate, the main or dominant mechanism can be described on the basis of the photovoltaic effect (section 1.2.1.2). In this sense, adhesion and wear mechanisms at the frictional interface are critical factors influencing the performance of DC-TENGs.¹²⁸ Tribological behaviors such as material transfer, changes in the effective contact area, and surface charge modification can significantly affect charge density, thereby altering the device's output performance. Advances in understanding these interactions have reinforced the role of

surface characterisation in optimizing DC-TENGs by refining the surface design and material engineering. In sliding-mode DC-TENGs, where tangential forces induce relative motion between surfaces at kinetic friction, tribological phenomena become more pronounced, leading to dynamic changes in surface charge distribution and energy transfer efficiency.

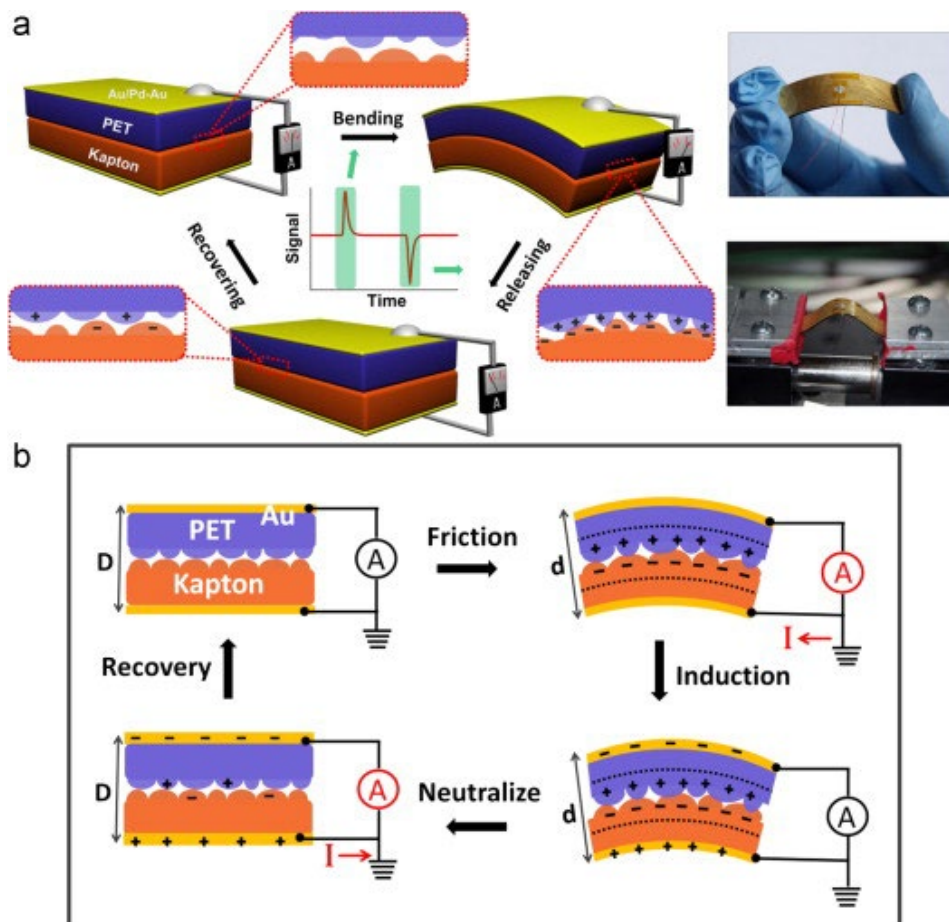


Figure 16. A schematic representation of the structure and operating principle of a triboelectric generator (TEG). (a) The configuration of an integrated TENG during the bending and release phases, along with corresponding electrical measurements. Photographs show a flexible TENG and a mechanical bending apparatus. (b) The suggested working mechanism of a TEG involves the generation of charges through friction between two polymer films, creating a triboelectric potential layer at the interface. Reproduced with permissions from ref. 18.

In the previous section, we discussed how flexoelectricity may also contribute to the mechanism of current generation (Figure 15). Theorization of this ratcheting effect has been performed on highly doped SC materials and remains uncertain whether these findings apply to dynamic junctions formed on lowly-doped SC, where the space charge region is significantly

thicker. In addition, most silicon-based DC-TENGs produce tribocurrents in the direction of leakage current, suggesting that the interfacial field formed during contact drives electrons through either avalanche breakdown or tunnelling. To determine which of these mechanisms is predominant in **Chapter 5** I conducted experiments where the temperature of the sliding junction was controlled.

The DC current density for metal–silicon TENGs is reported to be around 10^9 A/m²,¹²⁹ which was achieved by using the attachment of an organic layer that allows proton exchange introducing simultaneously a sufficiently high concentration of surface states, indicated by alterations in carrier recombination velocities, in combination with a pronounced surface dipole characterized by a surface alkoxide anion (Si–monolayer–O[−]). This is just an example but is extremely relevant, given that the interplay of chemical and electronic factors is not yet fully understood and surface chemistry control reveals itself as one of the dominant factors in DC TENG current generation (see section 1.6.2 and **Chapter 5**).¹³⁰

Therefore, to systematically leverage the performance of out-of-equilibrium diodes such as DC-TENGs, this Ph.D. thesis has addressed several key points that are critical to understanding the relationship between current output and mechanical motion which includes (but are not limited to): (i) the impact of the surface functionalization route (i.e., surface chemistry) (ii) the influence of surface conductivity, namely silicon crystal orientations, on current outputs (iii) to what extent does surface damage (i.e., oxide growth) determine the current output, and what causes it (iv) the implications of strain gradients in the current generation and how it can influence the measurements at the nanoscale.

References

- (1) Chu, S.; Cui, Y.; Liu, N. The path towards sustainable energy. *Nat. Mater.* **2017**, *16* (1), 16–22.
- (2) Lund, H.; Østergaard, P. A. Electric grid and heat planning scenarios with centralised and distributed sources of conventional, CHP and wind generation. *Energy (Oxford)* **2000**, *25* (4), 299–312.
- (3) Khan, S.; Kim, J.; Acharya, S.; Kim, W. Review on the operation of wearable sensors through body heat harvesting based on thermoelectric devices. *Appl. Phys. Lett.* **2021**, *118* (20).
- (4) Shariff, S. M.; Iqbal, D.; Saad Alam, M.; Ahmad, F. A State of the Art Review of Electric Vehicle to Grid (V2G) technology. *IOP Conf. Ser. Mater. Sci. Eng.* **2019**, *561* (1), 12103.
- (5) Pantelopoulos, A.; Bourbakis, N. G. A Survey on Wearable Sensor-Based Systems for Health Monitoring and Prognosis. *IEEE Trans. Syst. Man Cybern. C Appl. Rev.* **2010**, *40* (1), 1–12.
- (6) Varshney, U. Pervasive healthcare and wireless health monitoring. *Mob. Netw. Appl.* **2007**, *12* (2-3), 113–127.
- (7) Hart, J. K.; Martinez, K. Environmental sensor networks; a revolution in the earth system science? *Earth-science rev.* **2006**, *78* (3–4), 177–191.
- (8) Wang, M.; Zhang, J.; Wang, Y.; Lu, Y. Material and structural design of microsupercapacitors. *J. Solid State Electrochem.* **2022**, *26* (2), 313–334.
- (9) Zhang, P.; Wang, F.; Yu, M.; Zhuang, X.; Feng, X. Two-dimensional materials for miniaturized energy storage devices: from individual devices to smart integrated systems. *Chem. Soc. Rev.* **2018**, *47* (19), 7426–7451.
- (10) Da, Y.; Liu, J.; Zhou, L.; Zhu, X.; Chen, X.; Fu, L. Engineering 2D Architectures toward High-Performance Micro-Supercapacitors. *Adv. Mater.* **2019**, *31* (1).
- (11) Scrosati, B.; Aricò, A. S.; Bruce, P.; Tarascon, J.-M.; van Schalkwijk, W. Nanostructured materials for advanced energy conversion and storage devices. *Nat. Mater.* **2005**, *4* (5), 366–377.
- (12) Wang, Z. L. Triboelectric nanogenerators as new energy technology for self-powered systems and as active mechanical and chemical sensors. *ACS Nano* **2013**, *7* (11), 9533–9557.
- (13) Korkmaz, S.; Kariper, İ. A. Pyroelectric nanogenerators (PyNGs) in converting thermal energy into electrical energy: Fundamentals and current status. *Nano Energy* **2021**, *84*, 105888.
- (14) Mariello, M.; Guido, F.; Mastronardi, V.; Todaro, M.; Desmaële, D.; De Vittorio, M. Nanogenerators for harvesting mechanical energy conveyed by liquids. *Nano Energy* **2019**, *57*, 141–156.
- (15) Wang, X. Piezoelectric nanogenerators—Harvesting ambient mechanical energy at the nanometer scale. *Nano Energy* **2012**, *1* (1), 13–24.
- (16) Mizzi, C. A.; Marks, L. D. When flexoelectricity drives triboelectricity. *Nano Lett.* **2022**, *22* (10), 3939–3945.
- (17) Qiao, H.; Zhao, P.; Kwon, O.; Sohn, A.; Zhuo, F.; Lee, D. M.; Sun, C.; Seol, D.; Lee, D.; Kim, S. W. Mixed triboelectric and flexoelectric charge transfer at the nanoscale. *Adv. Sci.* **2021**, *8* (20), 2101793.

- (18) Fan, F.-R.; Tian, Z.-Q.; Lin Wang, Z. Flexible triboelectric generator. *Nano Energy* **2012**, *1* (2), 328–334.
- (19) Zhou, L.; Liu, D.; Wang, J.; Wang, Z. L. Triboelectric nanogenerators: Fundamental physics and potential applications. *Friction* **2020**, *8*, 481–506.
- (20) Song, Y.; Wang, N.; Wang, Y.; Zhang, R.; Olin, H.; Yang, Y. Direct current triboelectric nanogenerators. *Adv. Energy Mater.* **2020**, *10* (45), 2002756.
- (21) Zhao, Z.; Liu, D.; Li, Y.; Wang, Z. L.; Wang, J. Direct-current triboelectric nanogenerator based on electrostatic breakdown effect. *Nano Energy* **2022**, *102*, 107745.
- (22) Ferrie, S.; Darwish, N.; Gooding, J. J.; Ciampi, S. Harnessing silicon facet-dependent conductivity to enhance the direct-current produced by a sliding Schottky diode triboelectric nanogenerator. *Nano Energy* **2020**, *78*.
- (23) Ciampi, S.; Harper, J. B.; Gooding, J. J. Wet chemical routes to the assembly of organic monolayers on silicon surfaces via the formation of Si–C bonds: Surface preparation, passivation and functionalization. *Chem. Soc. Rev.* **2010**, *39* (6), 2158–2183.
- (24) Hurtado, C.; Lyu, X.; Ferrie, S.; Le Brun, A. P.; MacGregor, M.; Ciampi, S. Organic Monolayers on Si(211) for Triboelectricity Generation: Etching Optimization and Relationship between the Electrochemistry and Current Output. *ACS Appl. Nano Mater.* **2022**, *5* (10), 14263–14274.
- (25) Colinge, J. P.; Colinge, C. A. *Physics of Semiconductor Devices*; Springer US, 2002.
- (26) Zhang, X. G. *Electrochemistry of Silicon and Its Oxide*; Springer US, 2001.
- (27) Balkan, N.; Erol, A. Intrinsic and Extrinsic Semiconductors. In *Semiconductors for Optoelectronics: Basics and Applications*, Balkan, N., Erol, A. Eds.; Springer International Publishing, 2021; pp 37–78.
- (28) Srinivasan, G. Fermi–Dirac Distribution. In *Life and Death of the Stars*, Srinivasan, G. Ed.; Springer Berlin Heidelberg, 2014; pp 55–66.
- (29) Robertson, J.; Zhang, Z. Doping limits in p-type oxide semiconductors. *MRS Bull.* **2021**, *46* (11), 1037–1043.
- (30) Becquerel, M. Mémoire sur les effets électriques produits sous l'influence des rayons solaires. *C. R. Hebd. Seances Acad. Sci.* **1839**, *9*, 561–567.
- (31) Phillips, J. C. Introduction to the Physics of Electrons in Solids American Institute of Physics: New York, 1995; Vol. 48.
- (32) Neamen, D. A. *Semiconductor physics and devices : basic principles*; McGraw-Hill, 2012.
- (33) Rabe, K. M. Band Theory and Electronic Properties of Solids. **2002**, *55*, 61–62.
- (34) Green, M. A. High efficiency silicon solar cells. **1987**.
- (35) Kressel, H. *Semiconductor lasers and herterojunction LEDs*; Elsevier, 2012.
- (36) Blakemore, J. Semiconducting and other major properties of gallium arsenide. *J. Appl. Phys.* **1982**, *53* (10).
- (37) Zhao, Y.; Yu, J.; Xu, G.; Sojic, N.; Loget, G. Photoinduced electrochemiluminescence at silicon electrodes in water. *J. Am. Chem. Soc.* **2019**, *141* (33), 13013–13016.
- (38) Boddy, P. The structure of the semiconductor-electrolyte interface. *J. Electroanal. Chem.* **1965**, *10* (3), 199–244.

- (39) Memming, R. d. *Semiconductor electrochemistry*; Wiley-VCH, 2015.
- (40) Pierret, R. F. *Semiconductor device fundamentals*; Pearson Education India, 1996.
- (41) Schafer, F. Q.; Buettner, G. R. Redox environment of the cell as viewed through the redox state of the glutathione disulfide/glutathione couple. *Free Radic. Biol. Med.* **2001**, *30* (11), 1191–1212.
- (42) Vidal-Iglesias, F. J.; Solla-Gullón, J.; Rodes, A.; Herrero, E.; Aldaz, A. Understanding the Nernst equation and other electrochemical concepts: an easy experimental approach for students. *J. Chem. Educ.* **2012**, *89* (7), 936–939.
- (43) Card, H. C. Aluminum—Silicon Schottky barriers and ohmic contacts in integrated circuits. *IEEE Transactions on Electron Devices* **1976**, *23* (6), 538–544.
- (44) Zhang, Z.; Yates Jr, J. T. Band bending in semiconductors: chemical and physical consequences at surfaces and interfaces. *Chem. Rev.* **2012**, *112* (10), 5520–5551.
- (45) Lang, N.; Kohn, W. Theory of metal surfaces: work function. *Phys. Rev. B* **1971**, *3* (4), 1215.
- (46) Hurtado, C.; Ciampi, S. Oxidative Damage during the Operation of Si (211)-Based Triboelectric Nanogenerators. *Surfaces* **2023**, *6* (3), 281-290.
- (47) Taylor, J. C. Platinum metallization on silicon and silicates. *J. Mater. Res. Technol.* **2021**, *36*, 211–234.
- (48) Chen, C.-C.; Aykol, M.; Chang, C.-C.; Levi, A.; Cronin, S. B. Graphene-silicon Schottky diodes. *Nano Lett.* **2011**, *11* (5), 1863–1867.
- (49) Al-Ahmadi, N. A. Metal oxide semiconductor-based Schottky diodes: a review of recent advances. *Mater. Res. Express* **2020**, *7* (3), 032001.
- (50) Görlich, E. The structure of SiO₂—Current views. *Ceram. Int.* **1982**, *8* (1), 3–16.
- (51) Huang, Z.; Geyer, N.; Werner, P.; De Boor, J.; Gösele, U. Metal-assisted chemical etching of silicon: a review: in memory of Prof. Ulrich Gösele. *Adv. Mater.* **2011**, *23* (2), 285–308.
- (52) Sirghi, L.; Kylián, O.; Gilliland, D.; Ceccone, G.; Rossi, F. Cleaning and hydrophilization of atomic force microscopy silicon probes. *J. Phys. Chem. B* **2006**, *110* (51), 25975-25981.
- (53) Monk, D. J.; Soane, D. S.; Howe, R. T. A review of the chemical reaction mechanism and kinetics for hydrofluoric acid etching of silicon dioxide for surface micromachining applications. *Thin Solid Films* **1993**, *232* (1), 1–12.
- (54) Yablonovitch, E.; Allara, D. L.; Chang, C. C.; Gmitter, T.; Bright, T. B. Unusually low surface-recombination velocity on silicon and germanium surfaces. *Phys. Rev. Lett.* **1986**, *57* (2), 249–252.
- (55) Fenner, D.; Biegelsen, D.; Bringans, R. Silicon surface passivation by hydrogen termination: A comparative study of preparation methods. *J. Appl. Phys.* **1989**, *66* (1), 419–424.
- (56) Chabal, Y. J. Fundamental aspects of silicon oxidation. **2001**.
- (57) Gonçalves, V. R.; Lian, J.; Gautam, S.; Tilley, R. D.; Gooding, J. J. Functionalized silicon electrodes in electrochemistry. *Annu. Rev. Anal. Chem.* **2020**, *13* (1), 135–158.
- (58) Fabre, B.; Pujari, S. P.; Scheres, L.; Zuilhof, H. Micropatterned ferrocenyl monolayers covalently bound to hydrogen-terminated silicon surfaces: effects of pattern size on the cyclic voltammetry and capacitance characteristics. *Langmuir* **2014**, *30* (24), 7235–7243.

- (59) Aswal, D.; Lenfant, S.; Guérin, D.; Yakhmi, J.; Vuillaume, D. Self assembled monolayers on silicon for molecular electronics. *Anal. Chim. Acta* **2006**, *568* (1-2), 84–108.
- (60) Austin, M. D.; Chou, S. Y. Fabrication of a molecular self-assembled monolayer diode using nanoimprint lithography. *Nano Lett.* **2003**, *3* (12), 1687–1690.
- (61) O’Leary, L. E.; Rose, M. J.; Ding, T. X.; Johansson, E.; Brunschwig, B. S.; Lewis, N. S. Heck coupling of olefins to mixed methyl/thienyl monolayers on Si (111) surfaces. *J. Am. Chem. Soc.* **2013**, *135* (27), 10081–10090.
- (62) Wallart, X.; Henry de Villeneuve, C.; Allongue, P. Truly quantitative XPS characterization of organic monolayers on silicon: study of alkyl and alkoxy monolayers on H– Si (111). *J. Am. Chem. Soc.* **2005**, *127* (21), 7871–7878.
- (63) Wang, W.-Y.; Kala, K.; Wei, T.-C. Solvent-dependent adhesion strength of electroless deposited Ni–P layer on an amino-terminated silane compound-modified Si wafer. *Langmuir* **2018**, *34* (45), 13597–13602.
- (64) Ciampi, S.; James, M.; Le Saux, G.; Gaus, K.; Justin Gooding, J. Electrochemical “switching” of Si (100) modular assemblies. *J. Am. Chem. Soc.* **2012**, *134* (2), 844–847.
- (65) Sagiv, J. Organized monolayers by adsorption. 1. Formation and structure of oleophobic mixed monolayers on solid surfaces. *J. Am. Chem. Soc.* **1980**, *102* (1), 92–98.
- (66) Hiremath, R.; Rabinal, M.; Mulimani, B.; Khazi, I. Molecularly Controlled Metal–Semiconductor Junctions on Silicon Surface: A Dipole Effect. *Langmuir* **2008**, *24* (19), 11300–11306.
- (67) Ciampi, S.; Choudhury, M. H.; Ahmad, S. A. B. A.; Darwish, N.; Le Brun, A.; Gooding, J. J. The impact of surface coverage on the kinetics of electron transfer through redox monolayers on a silicon electrode surface. *Electrochim. Acta* **2015**, *186*, 216–222.
- (68) Linford, M. R.; Chidsey, C. E. Alkyl monolayers covalently bonded to silicon surfaces. *J. Am. Chem. Soc.* **1993**, *115* (26), 12631–12632.
- (69) Ciampi, S.; James, M.; Michaels, P.; Gooding, J. J. Tandem “click” reactions at acetylene-terminated Si (100) monolayers. *Langmuir* **2011**, *27* (11), 6940–6949.
- (70) Ziarani, G. M.; Hassanzadeh, Z.; Gholamzadeh, P.; Asadi, S.; Badiei, A. Advances in click chemistry for silica-based material construction. *RSC Adv.* **2016**, *6* (26), 21979–22006.
- (71) Fabre, B. Functionalization of oxide-free silicon surfaces with redox-active assemblies. *Chem. Rev.* **2016**, *116* (8), 4808–4849.
- (72) Zhang, L.; Vogel, Y. B.; Noble, B. B.; Goncales, V. R.; Darwish, N.; Brun, A. L.; Gooding, J. J.; Wallace, G. G.; Coote, M. L.; Ciampi, S. TEMPO monolayers on Si (100) electrodes: electrostatic effects by the electrolyte and semiconductor space-charge on the electroactivity of a persistent radical. *J. Am. Chem. Soc.* **2016**, *138* (30), 9611–9619.
- (73) Ciampi, S.; Le Saux, G.; Harper, J. B.; Gooding, J. J. Optimization of Click Chemistry of Ferrocene Derivatives on Acetylene-Functionalized Silicon (100) Surfaces. *Electroanalysis (N.Y.N.Y.)* **2008**, *20* (14), 1513–1519.
- (74) Ciampi, S.; Guan, B.; Darwish, N.; Reece, P. J.; Gooding, J. J. Redox-active monolayers in mesoporous silicon. *J. Phys. Chem. C* **2012**, *116* (30), 16080–16088.
- (75) Wu, F.; Zhang, D.-W.; Wang, J.; Watkinson, M.; Krause, S. Copper contamination of self-assembled organic monolayer modified silicon surfaces following a “Click” reaction characterized with LAPS and SPIM. *Langmuir* **2017**, *33* (13), 3170–3177.

- (76) Zoth, G.; Bergholz, W. A fast, preparation-free method to detect iron in silicon. *J. Appl. Phys.* **1990**, *67* (11), 6764–6771.
- (77) Colazzo, L.; Sedona, F.; Moretto, A.; Casarin, M.; Sambì, M. Metal-free on-surface photochemical homocoupling of terminal alkynes. *J. Am. Chem. Soc.* **2016**, *138* (32), 10151–10156.
- (78) Hurtado, C.; Andreoli, T.; Le Brun, A. P.; MacGregor, M.; Darwish, N.; Ciampi, S. Galinstan Liquid Metal Electrical Contacts for Monolayer-Modified Silicon Surfaces. *Langmuir* **2024**, *40* (1), 201–210.
- (79) Nicholson, R. S. Theory and application of cyclic voltammetry for measurement of electrode reaction kinetics. *Anal. Chem.* **1965**, *37* (11), 1351–1355.
- (80) Bard, A. J.; Faulkner, L. R. *Electrochemical methods : fundamentals and applications*; John Wiley, 2001.
- (81) Compton, R. G.; Banks, C. E. *Understanding voltammetry*; World Scientific, 2018.
- (82) Ge, M.; Cao, C.; Biesold, G. M.; Sewell, C. D.; Hao, S. M.; Huang, J.; Zhang, W.; Lai, Y.; Lin, Z. Recent advances in silicon-based electrodes: from fundamental research toward practical applications. *Adv. Mater.* **2021**, *33* (16), 2004577.
- (83) Gonzalez, J.; Sequí-Castellano, J. Electrochemical determination of kinetic parameters of surface confined redox probes in presence of intermolecular interactions by means of Cyclic Voltammetry. Application to TEMPO monolayers in gold and platinum electrodes. *Electrochim. Acta* **2021**, *365*, 137331.
- (84) Nernst, W. Zur Kinetik der in Lösung befindlichen Körper. *Z. Phys. Chem.* **2009**, *2*, 613–637.
- (85) Vogel, Y. B.; Molina, A.; Gonzalez, J.; Ciampi, S. Quantitative analysis of cyclic voltammetry of redox monolayers adsorbed on semiconductors: isolating electrode kinetics, lateral interactions, and diode currents. *Anal. Chem.* **2019**, *91* (9), 5929–5937.
- (86) Darwish, N.; Eggers, P. K.; Ciampi, S.; Tong, Y.; Ye, S.; Paddon-Row, M. N.; Gooding, J. J. Probing the effect of the solution environment around redox-active moieties using rigid anthraquinone terminated molecular rulers. *J. Am. Chem. Soc.* **2012**, *134* (44), 18401–18409.
- (87) Li, T.; Peiris, C. R.; Aragonès, A. C.; Hurtado, C.; Kicic, A.; Ciampi, S.; MacGregor, M.; Darwish, T.; Darwish, N. Terminal Deuterium Atoms Protect Silicon from Oxidation. *ACS Appl. Mater. Interfaces.* **2023**, *15* (40), 47833–47844.
- (88) Zhang, S.; Lyu, X.; Hurtado Torres, C.; Darwish, N.; Ciampi, S. Non-Ideal Cyclic Voltammetry of Redox Monolayers on Silicon Electrodes: Peak Splitting is Caused by Heterogeneous Photocurrents and Not by Molecular Disorder. *Langmuir* **2022**, *38* (2), 743–750.
- (89) Heinze, J. Cyclic Voltammetry-"Electrochemical Spectroscopy". *New Analytical Methods* (25). *Angew. Chem. Int. Ed.* **1984**, *23* (11), 831–847.
- (90) Laviron, E. General expression of the linear potential sweep voltammogram in the case of diffusionless electrochemical systems. *J. Electroanal. Chem. Interf. Electrochem.* **1979**, *101* (1), 19–28.
- (91) Wong, R. A.; Yokota, Y.; Wakisaka, M.; Inukai, J.; Kim, Y. Probing consequences of anion-dictated electrochemistry on the electrode/monolayer/electrolyte interfacial properties. *Nat. Commun.* **2020**, *11* (1), 4194–4194.

- (92) Vericat, C.; Vela, M. E.; Benitez, G.; Carro, P.; Salvarezza, R. C. Self-assembled monolayers of thiols and dithiols on gold: new challenges for a well-known system. *Chem. Soc. Rev.* **2010**, *39* (5), 1805–1834.
- (93) Chang, B. Y.; Park, S. M. Electrochemical impedance spectroscopy. *Annu. Rev. Anal. Chem. (Palo Alto Calif.)* **2010**, *3* (1), 207–229.
- (94) Pajkossy, T.; Jurczakowski, R. Electrochemical impedance spectroscopy in interfacial studies. *Curr. Opin. Electrochem.* **2017**, *1* (1), 53–58.
- (95) Eckermann, A. L.; Feld, D. J.; Shaw, J. A.; Meade, T. J. Electrochemistry of redox-active self-assembled monolayers. *Coord. Chem. Rev.* **2010**, *254* (15), 1769–1802.
- (96) Laviron, E. ChemInform Abstract: A.C. Polarography and faradaic impedance of strongly adsorbed electroactive species. Part i. Theoretical and experimental study of a quasi-reversible reaction in the case of a langmuir isotherm. *Chem. Inform.* **1979**, *10* (23).
- (97) Lacki, J. The Collected Papers of Albert Einstein, vol 10: The Berlin Years: Correspondence, May-December 1920, and Supplementary Correspondence, 1909-1920. Univ. Chicago Press.: CHICAGO, 2008; Vol. 99, pp 850–851.
- (98) Hofmann, S. *Auger- and X-Ray Photoelectron Spectroscopy in Materials Science: A User-Oriented Guide*; Springer Nature, 2012.
- (99) Seah, M. The quantitative analysis of surfaces by XPS: A review. *J. Surf. Interfac.* **1980**, *2* (6), 222–239.
- (100) Stevie, F. A.; Donley, C. L. Introduction to x-ray photoelectron spectroscopy. *J. Vac. Sci. Technol.* **2020**, *38* (6).
- (101) Van der Heide, P. *X-ray photoelectron spectroscopy: an introduction to principles and practices*; John Wiley & Sons, 2011.
- (102) Greczynski, G.; Hultman, L. A step-by-step guide to perform x-ray photoelectron spectroscopy. *J. Appl. Phys.* **2022**, *132* (1).
- (103) Zhou, X.-L.; Chen, S.-H. Theoretical foundation of X-ray and neutron reflectometry. *Phys. Rep.* **1995**, *257* (4-5), 223–348.
- (104) Yasaka, M. X-ray thin-film measurement techniques. *Rigaku J.* **2010**, *26* (2), 1–9.
- (105) Su, H.-C.; Lee, C.-H.; Lin, M.-Z.; Huang, T.-W. A comparison between X-ray reflectivity and atomic force microscopy on the characterization of a surface roughness. *Chin. J. Phys.* **2012**, *50* (2), 291–300.
- (106) Drenth, J. *X-ray Diffraction: Principles*. John Wiley & Sons, Ltd: Chichester, UK, 2005; Vol. 19, pp 595–601.
- (107) Bowen, W. R.; Hilal, N. *Atomic Force Microscopy in Process Engineering: Introduction to AFM for Improved Processes and Products*. Elsevier Science & Technology, 2009.
- (108) Binnig, G.; Quate, C. F.; Gerber, C. Atomic force microscope. *Phys. Rev. Lett.* **1986**, *56* (9), 930–933.
- (109) Lanza, M. *Conductive atomic force microscopy: applications in nanomaterials*; John Wiley & Sons, 2017.
- (110) Yanev, V.; Erlbacher, T.; Rommel, M.; Bauer, A.; Frey, L. Comparative study between conventional macroscopic IV techniques and advanced AFM based methods for electrical characterization of dielectrics at the nanoscale. *Microelectron. Eng.* **2009**, *86* (7-9), 1911–1914.

- (111) Pan, S.; Zhang, Z. Fundamental theories and basic principles of triboelectric effect: A review. *Friction* **2019**, *7*, 2–17.
- (112) Leon, R. T.; Sherrell, P. C.; Michel, J. I.; Bullock, J.; Berry, J. D.; Ellis, A. V. Understanding and Controlling Electrostatic Discharge in Triboelectric Nanogenerators. *ChemSusChem* **2024**, *17* (17).
- (113) Wang, Z. L. From contact electrification to triboelectric nanogenerators. *Rep. Prog. Phys.* **2021**, *84* (9), 096502.
- (114) Park, J. Y.; Salmeron, M. Fundamental aspects of energy dissipation in friction. *Chem. Rev.* **2014**, *114* (1), 677–711.
- (115) Gao, J.; Luedtke, W.; Gourdon, D.; Ruths, M.; Israelachvili, J.; Landman, U. Frictional forces and Amontons' law: from the molecular to the macroscopic scale. ACS Publications: 2004; Vol. 108, pp 3410–3425.
- (116) Leon, R. T.; Sherrell, P. C.; Šutka, A.; Ellis, A. V. Decoupling piezoelectric and triboelectric signals from PENGs using the fast fourier transform. *Nano Energy* **2023**, *110*, 108445.
- (117) Mizzi, C. A.; Lin, A. Y. W.; Marks, L. D. Does flexoelectricity drive triboelectricity? *Phys. Rev. Lett.* **2019**, *123* (11), 1. DOI: 10.1103/PhysRevLett.123.116103.
- (118) Park, J. Y.; Ogletree, D.; Thiel, P.; Salmeron, M. Electronic control of friction in silicon pn junctions. *Science* **2006**, *313* (5784), 186–186.
- (119) Wang, L.; Liu, S.; Feng, X.; Zhang, C.; Zhu, L.; Zhai, J.; Qin, Y.; Wang, Z. L. Flexoelectronics of centrosymmetric semiconductors. *Nat. Nanotechnol.* **2020**, *15* (8), 661–667.
- (120) Jamieson, W. The electrification of insulating materials. *Nature* **1910**, *83* (2111), 189–189.
- (121) Akbarinejad, A.; Fiedler, H.; Nguyen, J.; Li, Z.; Gito, D. A.; Sherrell, P. C.; Ellis, A. V.; Aw, K.; Malmstrom, J. Stretching, Tapping, or Compressing—What Role Does Triboelectricity Play in the Signal Output from Piezoelectric Nanogenerators? *Adv. Electron. Mater.* **2024**, *10* (9). DOI: 10.1002/aelm.202400019.
- (122) Shu, L.; Wei, X.; Pang, T.; Yao, X.; Wang, C. Symmetry of flexoelectric coefficients in crystalline medium. *J. Appl. Phys.* **2011**, *110* (10).
- (123) Olson, K. P.; Mizzi, C. A.; Marks, L. D. Band bending and ratcheting explain triboelectricity in a flexoelectric contact diode. *Nano Lett.* **2022**, *22* (10), 3914–3921.
- (124) Liu, D.; Zhou, L.; Wang, Z. L.; Wang, J. Triboelectric nanogenerator: from alternating current to direct current. *IScience* **2021**, *24* (1).
- (125) Kim, W.-G.; Kim, D.-W.; Tcho, I.-W.; Kim, J.-K.; Kim, M.-S.; Choi, Y.-K. Triboelectric nanogenerator: Structure, mechanism, and applications. *ACS Nano* **2021**, *15* (1), 258–287.
- (126) Cheng, T.; Gao, Q.; Wang, Z. L. The current development and future outlook of triboelectric nanogenerators: a survey of literature. *Adv. Mater. Technol* **2019**, *4* (3), 1800588.
- (127) Cheng, T.; Shao, J.; Wang, Z. L. Triboelectric nanogenerators. *Nat. Rev.* **2023**, *3* (1), 39.
- (128) Xiao, K.; Wang, W.; Wang, K.; Zhang, H.; Dong, S.; Li, J. Improving triboelectric nanogenerators performance via interface tribological optimization: a review. *Adv. Funct. Mater.* **2024**, *34* (39), 2404744.

- (129) Lyu, X.; Ferrie, S.; Pivrikas, A.; MacGregor, M.; Ciampi, S. Sliding Schottky diode triboelectric nanogenerators with current output of 109 A/m² by molecular engineering of Si (211) surfaces. *Nano Energy* **2022**, *102*, 107658.
- (130) Lyu, X.; Ciampi, S. Improving the performances of direct-current triboelectric nanogenerators with surface chemistry. *Curr. Opin. Colloid Interface Sci.* **2022**, *61*, 101627.

Chapter 2. Organic monolayers on Si(211) for triboelectricity generation: etching optimization and relationship between the electrochemistry and current output

Introduction to Chapter 2

Chapter 2, adapted from paper 1, deals with autonomous power supplies that take on a vital role when it is not possible to replace or recharge a battery, such as in life-critical medical implants or sensors in remote/dangerous places. The environment provides a broad range of mechanical energy sources, but converting mechanical energy into direct current remains challenging in a nanoscale setting.

Recent reports (J. Liu, et al., Direct-Current Triboelectricity Generation by a Sliding Schottky Nanocontact on MoS₂ Multilayers, *Nat. Nanotechnol.* 13 (2018) 1120) showed for the first time that a sliding metal–semiconductor contact converts small movements into direct current, which can power electronic circuitry, without the need of electrical rectification. Without any externally applied bias, a fine metal wire sliding across a semiconductor surface outputs a “tribocurrent” that can recharge or supplement a battery.

By achieving molecular precision control on the surface chemistry of Si(211) – an highly conductive Si facets, more conductive than the more common Si(111) and Si(100) cuts – this chapter demonstrates a new path for the design of metal–semiconductor dynamic junctions that efficiently harvest electricity from mechanical energy. The etching and surface modification of Si(211), an underexplored but readily available and highly conductive crystallographic cut of silicon have been optimized and lead to prove that TENGs made on Si(211) achieve tribocurrent outputs significantly greater than equivalent devices made on Si(111).

Results presented in this chapter demonstrate that engineering the surface chemistry of Si(211) is effective in maximizing current without the need to increase the applied normal force. This is a path towards limiting device wear, potentially opening the way to the widespread adoption of this technology. Another important and counterintuitive finding that emerged from the

research presented in this chapter is that introducing surface defects (namely, the presence of traces of SiO_x) leads to a significant enhancement of the tribocurrent output. Interestingly, the chapter also discusses the usefulness of electrochemistry as a diagnostic tool to anticipate whether or not a given surface will perform satisfactorily when used in a TENG design. The results obtained in this chapter will start a new debate among physicists, chemists, and nanotechnologists whose interests span from autonomous power sources, control of friction and wear, electrostatic actuation, and interfacial charge transport.

The supporting information for this chapter can be found in *Appendix C*.

Organic Monolayers on Si(211) for Triboelectricity Generation: Etching Optimization and Relationship between the Electrochemistry and Current Output

Carlos Hurtado, Xin Lyu, Stuart Ferrie, Anton P. Le Brun, Melanie MacGregor, and Simone Ciampi*

Cite This: *ACS Appl. Nano Mater.* 2022, 5, 14263–14274

Read Online

ACCESS |



Metrics & More



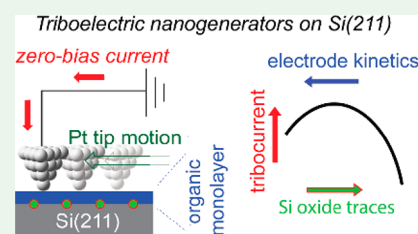
Article Recommendations



Supporting Information

ABSTRACT: Triboelectric nanogenerators (TENGs) based on sliding silicon–organic monolayer–metal Schottky diodes are an emerging autonomous direct-current (DC) current supply technology. Herein, using conductive atomic force microscopy and electrochemical techniques, we explore the optimal etching conditions toward the preparation of DC TENGs on Si(211), a readily available, highly conductive, and underexplored silicon crystallographic cut. We report optimized conditions for the chemical etching of Si(211) surfaces with subnanometer root-mean-square roughness, explore Si(211) chemical passivation, and unveil a relationship between the electrochemical charge-transfer behavior at the silicon–liquid interface and the zero-applied bias current output from the corresponding dynamic silicon–organic monolayer–platinum system. The overall aim is to optimize the etching and functionalization of the relatively underexplored Si(211) facet, toward its application in out-of-equilibrium Schottky diodes as autonomous power supplies. We also propose the electrochemical behavior of surface-confined redox couples as a diagnostic tool to anticipate whether or not a given surface will perform satisfactorily when used in a TENG design.

KEYWORDS: triboelectricity, silicon, surface chemistry, organic monolayers, electrochemistry



1. INTRODUCTION

Semiconducting materials have revolutionized society and are the foundation of our digitized technologies. Silicon-based components are at the core of devices whose functions range from energy storage to energy conversion,¹ to data processing and storage,² to sensing.³

Prompted by the pioneering work of Lindford and Chidsey,⁴ expanding our ability to merge the complexity of the molecular world^{5,6} with the sturdiness of an inorganic silicon substrate has been a central motivation behind 4 decades of surface chemistry, electrochemistry, and molecular electronics research.^{7–12} The ongoing quest of predictably tuning the performance and function of silicon-based devices has made tremendous progress. For instance, silicon–molecule–metal diodes have been realized experimentally,¹³ and such hybrid constructs are now at the core of new autonomous power technologies, such as triboelectric nanogenerators (TENGs) harvesting mechanical vibrations and friction into electrical energy.^{14,15}

The operation of such hybrid organic–inorganic devices relies on a complete and correct understanding of how electrons cross the interface formed between silicon and either a metal or a liquid electrolyte contact.^{13,16} Being able to engineer the interfacial properties of silicon can therefore expand the performance of semiconductor devices,^{17,18} and specific monolayer chemistries can maximize the direct-current (DC) current output of out-of-equilibrium silicon diodes used as TENGs.¹⁵

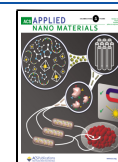
Despite being readily available, silicon wafers of orientation other than $\langle 111 \rangle$ and $\langle 100 \rangle$ have received little attention by the surface science community. This point is of particular importance because 4 years have already elapsed since the discovery by Huang and co-workers¹⁹ of the surprisingly high electrical conductivity of Si(211). Since then, a limited number of follow-up works have demonstrated that for silicon, surface conductivity decreases in the order $\langle 211 \rangle \gg \langle 100 \rangle > \langle 111 \rangle$.²⁰ These works have also highlighted some of the practical consequences of this facet-dependent conductivity, such as the silica–silicon redox couple becoming reversible on Si(110) defects, which are ubiquitous even on a nominal and well-prepared Si(111) surface.¹⁶

We believe that one of the reasons still hindering a broader adoption, in both the electrochemistry and energy conversion fields (e.g., TENGs), of commercially available and highly conductive Si(211) and Si(110) wafers is the lack of suitable etching and surface chemistry modification procedures. Equally poorly documented are their electrical and electrochemical responses, that is, whether solid and liquid junctions made on

Received: May 8, 2022

Accepted: September 15, 2022

Published: September 28, 2022



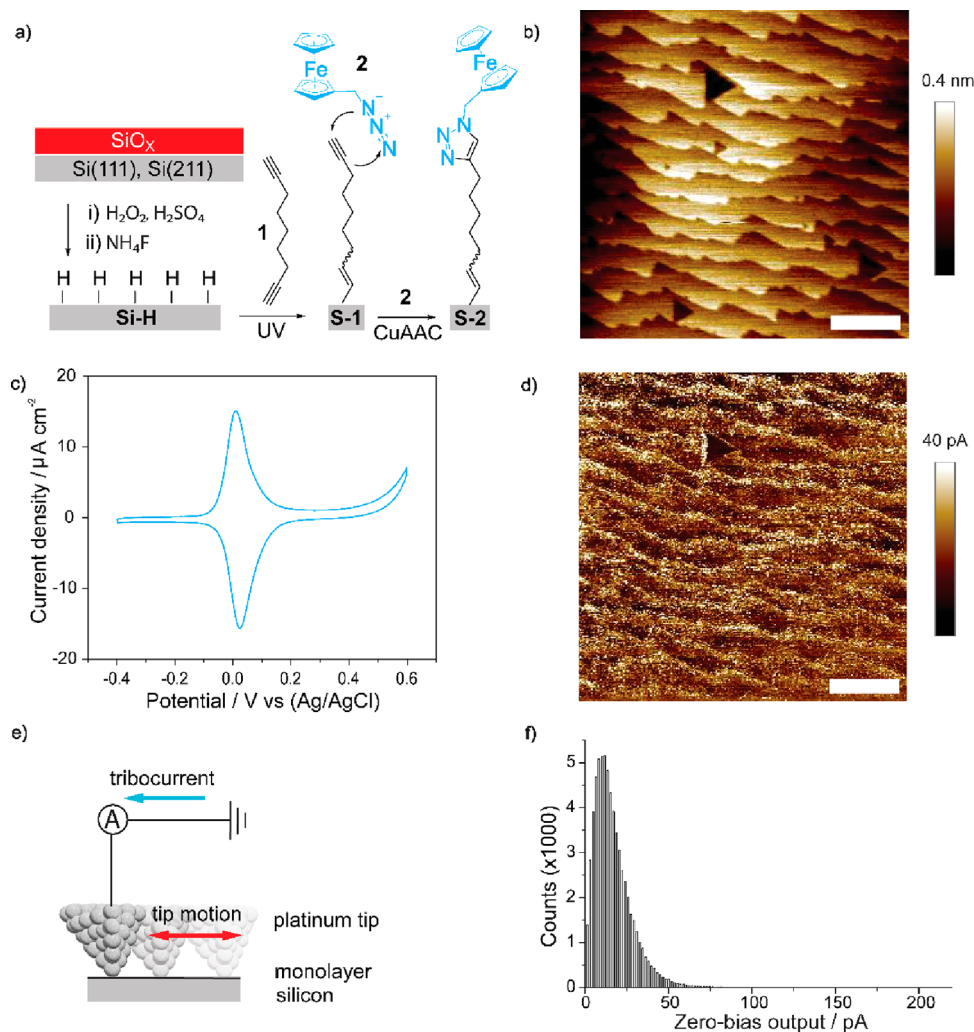


Figure 1. (a) Schematics of the chemical strategy for silicon surface passivation and functionalization. Etching of the native oxide layer was followed by the UV-assisted hydrosilylation of diyne **1** on the hydrogen-terminated silicon (Si-H) surface. The resulting alkyne-terminated monolayer (**S-1**) is then reacted with azide **2** via a CuAAC reaction, to yield a redox-active monolayer (**S-2**). (b) High-resolution AFM topography image for a **S-1** monolayer on $\text{Si}(111)$. The etching time was 13 min [40% aqueous NH_4F under ambient light (0.2 mW cm^{-2})]. (c) Representative cyclic voltammogram for a **S-2** sample made on a $\text{Si}(111)$ photoanode (100 mV s^{-1} , 1.0 M HClO_4). The electrode was illuminated at a light intensity of 1.7 mW cm^{-2} . (d) Zero-voltage bias C-AFM map of a **S-1** $\text{Si}(111)$ sample. The horizontal scale bars in parts b and d are $1 \mu\text{m}$. (e) Schematic representation of the TENG design, made up of an AFM platinum tip sliding over a monolayer-coated silicon wafer. (f) Histogram plot of the current output of the C-AFM map in part d, where the counts indicate the number of pixels (sample locations) of a given current, with a total of $\sim 65\text{K}$ pixels making up a C-AFM map.

these alternative silicon crystallographic cuts behave close or far from ideality.²¹

The purpose of this paper is to define the optimal conditions for the preparation and functionalization of oxide-free and monolayer-modified $\text{Si}(211)$ surfaces, an underexplored but readily available silicon crystallographic cut. We seek to expand the applicability of monolayer-modified $\text{Si}(211)$ surfaces in miniaturized sliding Schottky-diode TENGs, devices aimed at converting mechanical into electrical energy.

2. RESULTS AND DISCUSSION

The focus of this paper is on chemically modified phosphorus-doped $\text{Si}(211)$ because the n type is the preferred choice for DC TENGs that rely on relatively soft metal contacts of large work function, such as platinum.^{15,22,23} The precise charge separation mechanism for this and similar DC TENGs is still unclear, but it most likely involves the formation of electron-hole pairs in response to a mechanical stimulus. These charges

are then separated by the built-in electric field of the Schottky diode and/or by static electricity. It is possible that negative charges generated on the platinum tip²⁴ and flexoelectricity²⁵ of the junction are also contributing to the enhancement of the junction's electric field. Particular emphasis is placed on trying to unveil the presence (or absence) of a relationship between electrochemical charge transfer of the silicon-liquid interface and the zero-applied bias current output of the corresponding dynamic silicon-platinum system.

The expectation is to develop a diagnostic electrochemical test to help predicting which surface is more likely to perform well in a TENG setup. All silicon samples were first etched to expose a hydrogen-terminated surface (Si-H ; Figure 1a), which is reactive toward unsaturated organic molecules^{4,26,27} and therefore amenable to chemical passivation to limit anodic decomposition of the electrode. Chemical passivation was achieved via hydrosilylation of a symmetrical α,ω -dialkyne molecule [1,8-nonadiyne (**1**); Figure 1a]. This chemical

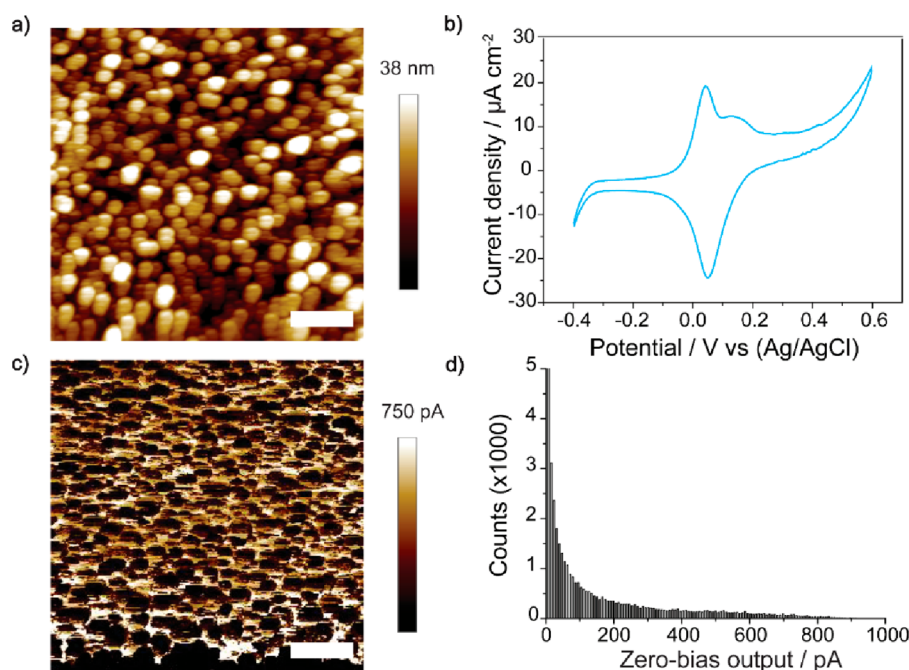


Figure 2. (a) AFM topography image of a S-1 sample made on Si(211). (b) Representative CV curve for a S-2 sample [Si(211), 100 mV s^{-1} , 1.0 M HClO_4 , red light at 1.7 mW cm^{-2}] etched following conditions identical with those of Si(111). (c) Zero-bias C-AFM map of a S-1 sample–platinum junction. The horizontal scale bars in parts a and c are 1 μm . (d) Histogram plot of the current output of data in part c. Counts indicate the number of pixels of a given current bin, with a total of $\sim 65\text{K}$ pixels being sampled in a single C-AFM map. The data in the figure are for Si(211) wafers etched for 13 min in aqueous 40% ammonium fluoride under ambient light (0.2 mW cm^{-2}) and then chemically modified.

reaction generates an alkyne-terminated monolayer (S-1; Figure 1a),²⁸ which can be further modified via a copper(I)-catalyzed azide–alkyne cycloaddition (CuAAC) reaction (S-2; Figure 1a).²⁹ The latter point, further derivatization of the alkyne film with a redox probe [azidomethylferrocene (2)], is of central importance to the electrochemical experiments used to study the electrochemical heterogeneity and charge-transport characteristics of the semiconductor–liquid junction.

This study involves a systematic screening of the etching conditions to generate a Si–H surface from oxide-coated commercial Si(211) wafers. The goal is to define the etching conditions yielding near-to-ideal voltammetry (S-2 samples), along with a smooth surface on which to test the current outputs of sliding Si(211)–monolayer–platinum Schottky-diode TENGs (S-1 and S-2 samples). Throughout this report, we have benchmarked our results for Si(211) against those for monolayer systems prepared on Si(111) (Figure 1b–d,f). As mentioned in the Introduction, unlike Si(211), the surface chemistry and electrochemistry of Si(111) have been explored extensively.^{30,31}

Because silica and silicon are etched by ammonium fluoride solutions at significantly different rates,^{32,33} etching experiments were preceded by ellipsometric measurements to estimate the thickness of the native oxide in the commercial wafer. In our Si(111) wafers, the oxide layer was generally ~ 1 nm, while it is only slightly thicker (~ 2 nm, vide infra) for Si(211). Figure 1b gives an example of a topography map for a S-1 sample made on hydrogen-terminated Si(111). The surface is an ensemble of flat $\langle 111 \rangle$ terraces separated by small vertical steps (~ 3 Å).³⁴ The surface is very smooth, with a root-mean-square (rms) roughness of only 0.2 ± 0.7 nm. The high surface quality is also reflected in the lack of phase angle dispersion at low frequency in electrochemical impedance spectroscopy (EIS) measurements (Figure S1).³⁵ At low

alternating-current (AC) frequencies the EIS phase angle for S-1 samples approaches -90° , which is an indication of negligible monolayer imperfections.³⁶ As shown in Figure 1c, the cyclic voltammetry (CV) response of S-2 samples prepared on Si(111) is close to ideal.^{37–39} The full width at half-maximum (fwhm hereafter) of the CV current waves is 90.6 ± 3.9 mV. This fwhm is an excellent match of the value expected from a Langmuir isotherm of a Nernstian process. Because of its photoanodic nature, n-type silicon is in depletion, and sample illumination with visible light is required to remove a kinetic barrier and allow the ferrocene redox chemistry to take place within a solvent-accessible potential window.^{40,41} Unlike analogous systems prepared on highly doped p-type silicon, hence operating under accumulation, the CV curves of the illuminated n-type photoanodes display a marked cathodic shift in the ferrocene apparent formal potential (Figure S2). The surface coverage of ferrocene units in S-2 samples prepared on Si(111), obtained from the CV-derived faradaic charge, was $(2.1 \pm 0.3) \times 10^{-10}$ mol cm^{-2} . This coverage is lower than the maximum value for a packed ferrocene monolayer (4.5×10^{-10} mol cm^{-2})⁴² but as expected for a two-step derivatization procedure.^{26,43}

Furthermore, as immediately appreciable from the negligible voltammetric peak-to-peak separation (Figure 1c), the electrode kinetics for S-2 samples on Si(111) is fast. The peak-to-peak separation for the CV curves recorded at 100 mV s^{-1} (Figure 1c) becomes more significant at faster voltage sweep rates (Figure S3). The electron-transfer rate constant, k_{et} extracted from EIS experiments carried out at a DC bias equal to the ferrocene apparent formal potential (Figure S4, Supporting Information) was $(3.6 \pm 1.4) \times 10^2$ s^{-1} .

Moving now to “dry” sliding junctions, Figure 1d shows a representative zero-voltage-bias conductive atomic force microscopy (C-AFM) map for a S-1 sample made on

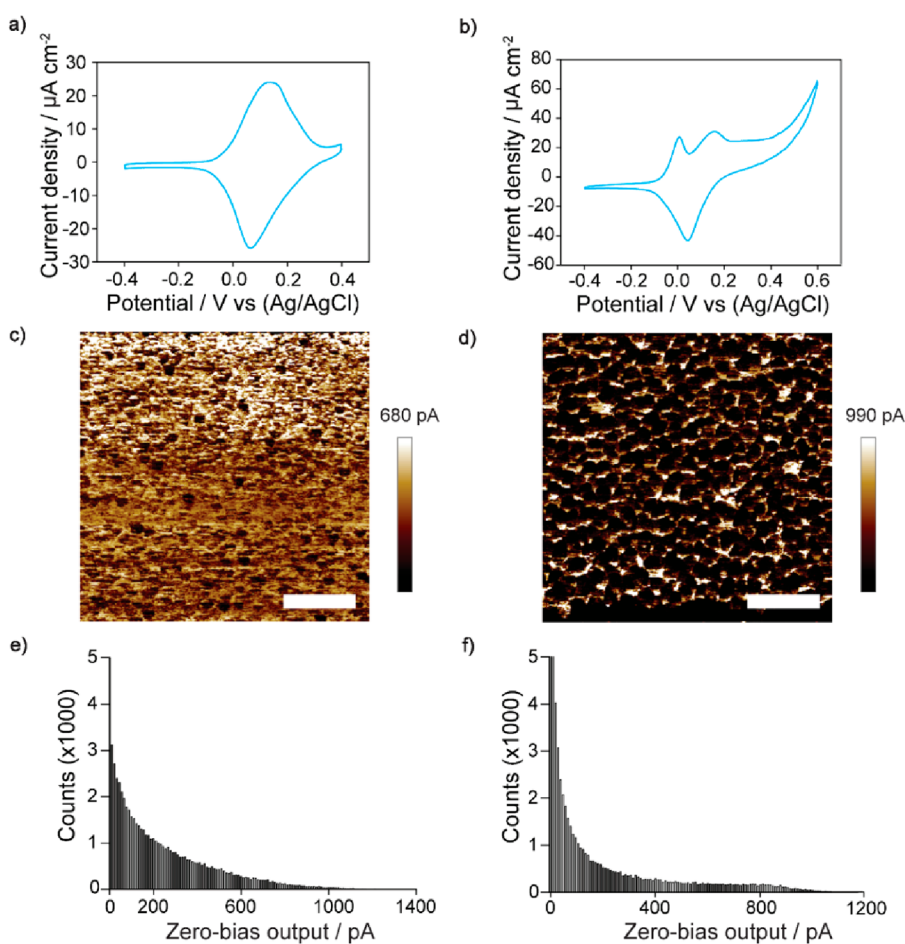


Figure 3. (a and b) Representative CV curves for Si(211) S-2 photoanodes (100 mV s^{-1} , 1.0 M HClO_4 , 1.7 mW cm^{-2} red light electrode illumination). Samples were etched in a mixture of MeOH and 40% NH_4F (1:10) under ambient light (0.2 mW cm^{-2}). The etching time varied between (a) 2 and (b) 13 min. (c and d) Zero-bias C-AFM experiments carried out on S-1 samples etched for (c) 2 and (d) 13 min. The horizontal scale bars in parts c and d are $1 \mu\text{m}$. (e and f) Histograms of the current output of the C-AFM maps in parts c and d. Counts are in pixels ($\sim 65\text{K}$ total image pixels).

Si(111). In this experiment the solid platinum AFM tip moves along the S-1 surface and generates a DC output,^{14,15} that is, a sliding Schottky diode that outputs a DC tribocurrent without an external voltage bias (Figure 1e). A histogram of the DC, mapped in Figure 1d, reveals a skewed shape (Figure 1f), where the most frequent output is around 20 pA, the current range from noise level ($\sim 120 \text{ fA}$) to $\sim 220 \text{ pA}$, with the 99th percentile of the DC output being 54 pA.

This tribocurrent has the sign of a leakage current (electrons flowing from the metal to the n-type silicon) and is distributed within a relatively narrow range (Figure 1f). The measurable current increase, present near the edges of the Si(111) terraces (Figure 1d), is of unclear origin, but it may be linked to the presence of highly conductive $\langle 211 \rangle$ steps separating the $\langle 111 \rangle$ terraces.¹⁶ This localized increment in the tribocurrent output is, however, not reflected in the narrow dispersion (fwhm) of the macroscopic CV measurements, which, as discussed above, is close to ideal.

Following this initial electrochemical and electrical benchmarking of Si(111), we then moved to the focus of this study: Si(211), both as an electrode as well as a TENG substrate. To ensure the reproducibility of our etching conditions, especially with regard to experiments using shorter etching times, we performed ellipsometric measurements on commercial Si(211) wafers to measure the thickness of the native oxide layer. The

oxide on Si(211) was $\sim 2 \text{ nm}$ thick, hence prompting us to initially adopt the same etching times as those used for Si(111). Immersion of Si(211) wafers in degassed 40% aqueous ammonium fluoride for 13 min led, however, to a rms surface roughness of $7.8 \pm 3.2 \text{ nm}$ (Figure 2a, S-1 samples), which is significantly greater than that for Si(111). In addition, X-ray photoelectron spectroscopy (XPS) data (Figure S5) reveal minor traces of substrate oxidation.

The poor etching outcome is probably caused by the sizable evolution of hydrogen gas on Si(211). The evolution of hydrogen gas during silicon etching is well-known.^{44,45} The etching reaction is affected by several factors, such as the presence of a voltage bias, electrode illumination, and doping level,⁴⁶ but under identical etching conditions, gas evolution is much more evident on Si(211) than on Si(111), resulting in a significantly faster etching rate for the former. This is possibly linked to the higher surface energy of high Miller index silicon surfaces, namely, $\langle 211 \rangle$, $\langle 311 \rangle$, and $\langle 331 \rangle$,⁴⁷ as well as to the lower work function of Si(211) compared to Si(111) and Si(100).¹⁹

The issue of surface-pinned gas bubbles is probably also exacerbated by a rough surface, further slowing the desorption kinetics of bubbles.⁴⁸ We note that roughening of Si(211) during fluoride etching is not a significant problem in p-type substrates,²⁰ indicating that etching rates (hence, hydrogen

evolution) are probably augmented by the electron-donor nature of the n-type samples of this study.⁴⁹

Surface derivatization of these Si(211) rough surfaces, to generate ferrocene-terminated electrodes (S-2), led to a relatively large coverage, $(2.9 \pm 0.9) \times 10^{-10}$ mol cm⁻², as well as to nonideal CV shapes with evident multiple peaks (Figure 2b). Peak multiplicity may be triggered by heterogeneous photocurrent effects or by molecular disorder.^{50,51} The unusual onset of a Faradaic current below -0.3 V (Figure 2b) is attributed to the minor presence of oxide, introducing energy levels in the gap.⁵² It is at first counterintuitive to link an increase in the current with silica-related defects. However, despite being counterintuitive, transient increases in the conductivity for minor levels of silicon oxidation are known.^{24,53}

Figure 2c shows the corresponding zero-bias C-AFM map. On Si(211), there is a dramatic increase in the current output compared to Si(111), with an output average of ~ 250 pA and 1% of the sampled locations showing DC with values above 870 pA. The distribution of the current output (Figure 2d) indicates, however, a high frequency of sample locations with output close to the noise level. This is significantly different from Si(111), where the most frequent output was around 20 pA.

What followed was an attempt to mitigate the formation of surface-pinned bubbles on Si(211), first by reducing the surface tension of the etchant. Figure S6 shows the effect of adding 10% methanol (MeOH) to the aqueous 40% NH₄F, with the etching still carried out for 13 min and under ambient light. The addition of MeOH to aqueous NH₄F led to a significant roughness reduction: from ~ 8 to 3.2 ± 0.3 nm. This can be explained by a reduction in the liquid surface tension, preventing the nucleation and growth of surface-pinned gas bubbles (Figure S6). Further improvement was obtained by shortening the etching time to 2 min, resulting in a rms roughness of only 0.9 ± 0.1 nm (Figure S7).

Such improvements in the topography were, however, not paralleled by a reduction in the electrochemical nonidealities. The CV curves for Si(211) S-2 photoanodes prepared under the above (partially improved) etching conditions are shown in Figure 3a,b. For the shorter etching time (2 min), there is no peak multiplicity, but the CV waves are broad (fwhm ~ 208 mV; Figure 3a). This indicates a negative value of the Frumkin G parameter. Negative G values are an indication of net repulsive forces between the redox units,^{54–56} but this is surprising because the ferrocene coverage of $(2.8 \pm 0.7) \times 10^{-10}$ mol cm⁻² is comparable to that of Si(111) samples. Roughness factors could be behind the increased repulsions between ferrocene units. Longer etching times (13 min) lead once again, despite the smoother surface relative to the results for samples etched in the absence of MeOH (Figure 2), to multiple CV peaks (Figure 3b). As mentioned above, a heterogeneous redox population can manifest as multiple peaks.⁵⁰

Ferrocene coverages scaled with etching times, reaching values as high as $(4.9 \pm 0.2) \times 10^{-10}$ mol cm⁻² (13 min). This is probably not a true increase in the surface coverage but more likely due to an increase in the actual electrode area with increased roughness (Figure S7). The XPS data (Figure S8) for samples prepared when MeOH is added to the etchant indicate small traces of silicon oxide.

C-AFM performed on these samples (Figure 3c,d) revealed again large maximum tribocurrent outputs, but the most

frequent value is still close to the noise level. Despite the significant improvement in the surface smoothness, histograms in Figure 3e,f show a current distribution very similar to that of samples etched in the absence of MeOH (Figure 2d). The 99th percentile of the current output is 1.2 nA for the 2 min etching and 915 pA for samples etched for 13 min. Further, for both the data of Figures 2 and 3, nonideal CV responses seem to be linked to the likelihood of having a large fraction of the sample outputting tribocurrent close to noise. Whether electrochemical nonidealities could be used to predict if a given surface will perform poorly in a TENG design is what we next tried to clarify.

Considering the anodic nature of the etching process and because we are focusing on n-type electrodes (photoanodes), we attempted to slow the etching rate by shielding the electrodes from light. Under darkness, adding MeOH to the etching bath and further adjusting the etching times, we were able to reduce the presence of surface-pinned bubbles and improve the surface smoothness. Samples etched for 13 min in a mixture of MeOH and 40% NH₄F (1:10), while protected from light, had a rms roughness of only 2.6 ± 0.1 nm (Figure S9). This is a significant improvement compared to our initial results (Figure 2), and closer to the quality of the Si(111) benchmark (Figure 1). The outcome (surface roughness) of the various etching conditions explored in this work is summarized in Table S1. Again, samples etched for 2 min were very smooth, with an average roughness of only 0.7 ± 0.4 nm.

The quality of the carbonaceous monolayer on Si(211) is also comparable to what can be achieved on Si(111). C 1s and Si 2p XPS data, such as those of Figure 4a,b, suggest that, in Si(211) S-1 samples, $\sim 27\%$ (13 min etching) of the silicon surface atoms bear a monolayer-forming molecule (25% for the 2 min etching),⁵⁷ with no clear traces of substrate oxidation.

A satisfactory fitting of the C 1s XPS emission (S-1 samples) required three contributions: one for carbon bound to silicon at 283.6 eV,⁵⁸ a carbon-bound carbon envelope at 284.9 eV,⁵⁹ and a high-binding-energy band at 286.9 eV, ascribed to C \equiv C and/or C–OH.⁶⁰ Elemental silicon emissions are found at 99.5 eV for Si 2p_{3/2} and at 100.1 eV for Si 2p_{1/2}. The high-binding-energy Si 2p signal shifted by 0.40 eV from the bulk Si 2p_{1/2} peak, discernible in the high-resolution Si 2p scans (Figure 4b), is a common XPS feature even in oxide-free samples and is tentatively ascribed to silicon bound to hydrogen.⁶¹

Ferrocene-terminated (S-2) samples prepared on Si(111) and Si(211) electrodes returned similar XPS spectral features, including similar levels of oxidation (Figure S10). The successful attachment of the ferrocene unit was reflected by the appearance of Fe 2p signals at ~ 710 – 720 eV and N 1s at ~ 401 eV. The experimental binding energies are in good agreement with those reported for other immobilized triazoles.²⁸ The XPS narrow scan of the Fe 2p region (Figure S10c,d) shows two main spin–orbit-split components, Fe 2p_{3/2} and Fe 2p_{1/2}, located at 708.6 and 721.5 eV, respectively, indicating a predominant iron(II) population. There are traces of high-binding-energy satellite signals indicating the presence of iron(III) species, hence a nonnegligible level of oxidation of ferrocene to ferricenium units. The N 1s signal was fitted in two contributions assigned to N–N=N (400.7 eV) and N–N=N (402.3 eV), with the area ratio of the two envelopes being $\sim 2:1$, as expected for a triazole moiety. Deconvolution of the N 1s signals is supported by data for nitrogen atoms of aromatic compounds.⁶² Absent from the N 1s spectra is the

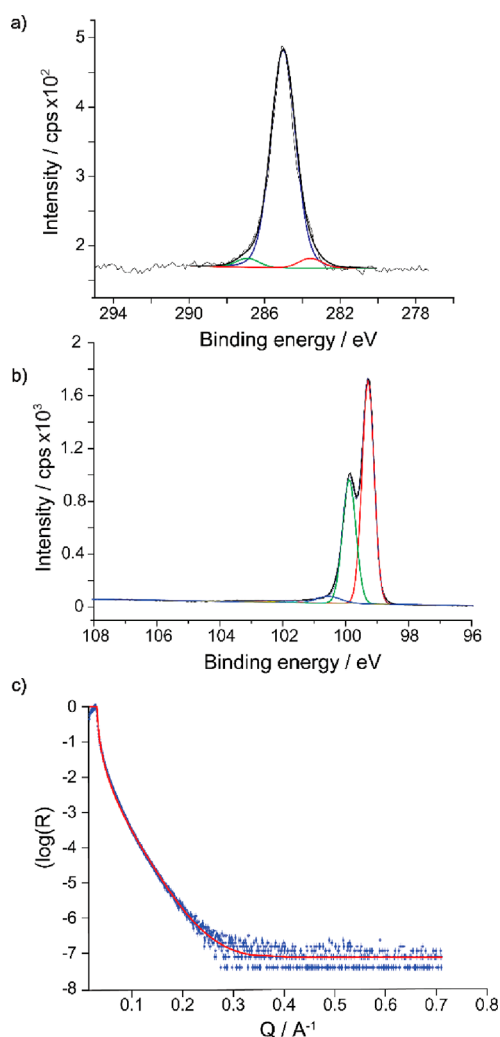


Figure 4. (a and b) High-resolution XPS C 1s and Si 2p scans of S-1 samples grafted on Si(211) [dark etching in 1:10 (v/v) MeOH/ NH_4F , 13 min]. (c) XRR spectra for S-1 samples [Si(211), etching as in parts a and b]. The refined data (red solid line; $\chi^2 = \sim 30$) is plotted over the experimental data (solid blue symbols).

high-binding-energy emission (~ 405 eV) from the central and electron-deficient nitrogen atom of unreacted **2**, hence supporting negligible physical adsorption of the unreacted azide in the S-2 film.

The electron density (ρ_{el}) of the organic monolayer [S-1 film made on Si(211)], inferred from refinement of the X-ray reflectometry (XRR) data (Figure 4c), was $0.35 \text{ e}^-/\text{\AA}^3$, which is not drastically lower than the $0.44 \text{ e}^-/\text{\AA}^3$ for the same film prepared on Si(111) (Figure S11 and Table S2). Literature values for ρ_{el} of high-quality carbon-based films made on oxide-free silicon range, in general, between 0.32 and $0.46 \text{ e}^-/\text{\AA}^3$.^{63,64} The XRR-derived roughness of the monolayer–air interface was ~ 3.1 nm and very close to the AFM-derived value (13 min etch).

S-2 samples made on dark-etched Si(211) wafers showed a nearly ideal voltammetric fwhm (Figure 5a,b). Furthermore, for samples etched for 13 min, the ferrocene coverage was $(2.0 \pm 0.2) \times 10^{-10} \text{ mol cm}^{-2}$, a value comparable to that of the Si(111) benchmark (Figure 1) but likely to reflect an actually lower molecular density because the Si(211) roughness (13 min etching time) is significantly higher than that of Si(111)

samples. Lower coverages were obtained for the smooth Si(211) surfaces (2 min etch), which were on average $(1.2 \pm 0.1) \times 10^{-10} \text{ mol cm}^{-2}$, roughly half the Si(111) value. We are at present unsure on the cause of the lower ferrocene coverage because the nonadiyne coverage (vide supra, XPS data) of the base acetylene layer appears to be comparable between the 2 and 13 min samples. Furthermore, etching times of 6 and 10 min led to qualitatively similar CV curves, with the ferrocene coverage per geometric area scaling with the etching time (Figure S12). As expected, the anodic and cathodic peak currents scaled with the scan rate and not with the square root of the scan rate, indicating a surface-confined (diffusionless) redox process (Figure S13).

Notably, as is evident in Figure 5a,b, the CV curves of S-2 samples made on etching-optimized Si(211) are characterized by a peak inversion: at low-voltage sweep rates, the anodic wave peaks at voltages more negative than those of the cathodic wave maxima. This unusual feature is not an artifact but an indication of electrostatic interactions between the positively charged ferricenium units and the semiconductor space-charge layer (SCL). CV inverted peak positions disappear at larger voltage sweep rates (Figure S14) as the peak inversion becomes masked by kinetic factors.^{37,38} The CV current is always the net sum of the anodic and cathodic currents, but the appearance of this peak inversion indicates that dynamic charges in S-2 samples (the positive Fc^+ surface tethers formed upon Fc oxidation) transiently remove a barrier (the upward SCL band bending) sensed by electrons crossing from the silicon to the electrolyte, hence transiently favoring the photogenerated cathodic current. As a result, the cathodic wave peaks at more positive voltages than the anodic wave. Interestingly, the peak inversion is much more evident on Si(211) than on Si(111), where it manifests only occasionally. Although a complete explanation is still lacking, this electrostatic effect is possibly linked to disorder in the molecular film and/or to the presence of low levels of oxide not detectable by XPS. The oxide may decrease the dielectric barrier (relative to a well-packed organic monolayer), which possibly favors the electrostatic interactions behind the inversion. In support of disorder in the monolayer being linked to the inverted peak positions is the consistent appearance of such a phenomenon in amorphous silicon.³⁷

When the voltage sweep rate is increased (Figure S14), or upon substrate oxidation when the charge-transfer kinetics is irreversibly slowed,⁶⁵ such a peak inversion is no longer detectable (Figures S15 and S16). We propose that such a disappearance can be turned into a simple diagnostic tool of substrate oxidation, and as discussed below, it has an immediate implication in anticipating the performance of a TENG made on these substrates.

The outcomes of C-AFM experiments on Si(211) S-1 samples are shown in Figure 5c–f. TENGs made on S-1 samples etched for 2 min led to excellent outputs, with the mode of the zero-bias tribocurrent being at 1.1 nA (equivalent to a current density of $1.2 \times 10^7 \text{ A m}^{-2}$; Figure 5e). As is clearly visible in the current histogram of Figure 5f, S-1 samples made on Si(211) etched for 13 min had a large fraction of spots with tribocurrent close to the noise level but also an almost equally large population of locations with very high current output (~ 320 pA) and with a satisfactory homogeneity across the macroscopic sample (Figure S17). This is a remarkable improvement over Si(211) etched under ambient light. The 99th percentile of the current output is 1.2

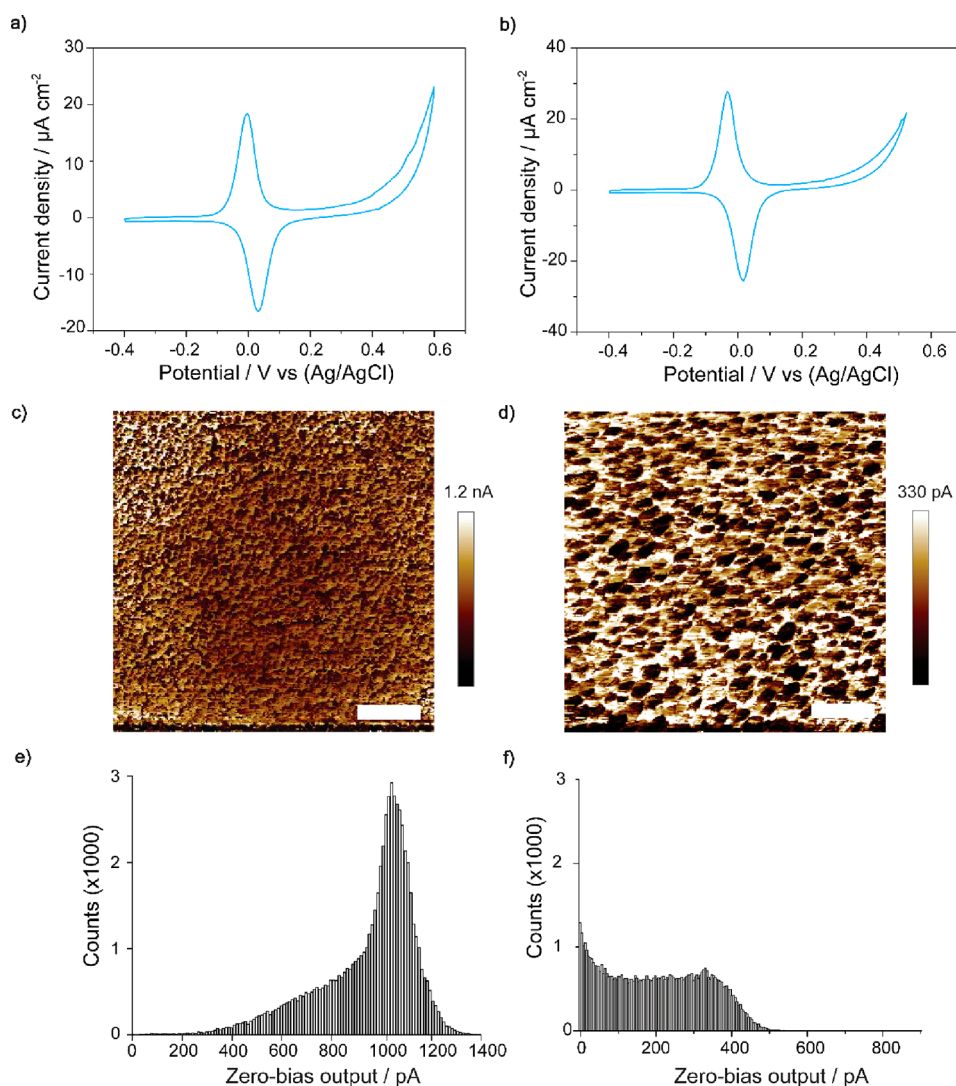


Figure 5. (a and b) Representative CV curves for Si(211) S-2 photoanodes (100 mV s^{-1} , 1.0 M HClO_4 , 1.7 mW cm^{-2} red light electrode illumination). Samples were etched in a mixture of MeOH and aqueous 40% NH_4F (1:10, v/v) in the dark. The etching times were (a) 2 and (b) 13 min. (c and d) Zero-bias C-AFM maps [S-1, etching times of (c) 2 and (d) 13 min]. The horizontal scale bars in parts c and d are $1 \mu\text{m}$. (e and f) Histograms of the tribocurrent output from the C-AFM experiments (2 and 13 min, respectively). Counts are in pixels ($\sim 65\text{K}$ total image pixels).

nA and 528 pA for the 2 and 13 min samples, respectively. Such high current outputs, along with well-defined voltammetric responses (Figure 5a,b), are a significant improvement against more widespread Si(111) systems, which we initially took as our benchmark (Figure 1).

Further, the current output of the sliding junction was tested under prolonged operations (Figure S18), as well as under different scan speeds (Figure S19). There is a substantial drop in the mean zero-bias current with consecutive cycling ($\sim 90\%$ after three full scans). This is probably caused by deterioration of the monolayer and anodic damaging of the substrate.

Changes to the platinum sliding velocity revealed that the output current increases with the scan speed (Figure S19). We are unsure of the reason for such a positive correlation between the sliding velocity and current, but we believe it may be linked to a not-yet-explored flexoelectric time factor, such as electrons accumulating on one side of the junction, inside a well created by bands that are being bent under pressure, eventually drifting away anisotropically before being transferred directionally from the metal to the semiconductor. This point will need further

investigation. Furthermore, as shown in Figure S20, we found a direct correlation between the force and DC current output. Changes to the applied load have recently been demonstrated to influence the DC output of similar metal–semiconductor systems.²³ We believe this increase not only reflects increased friction due to increased normal force but also is a response to dynamic changes to the band bending upon inevitable fluctuations to the vertical load. The contribution of flexoelectric effects to the triboelectricity has recently been demonstrated and explained by Marks and co-workers.²⁵ For a contact between a platinum–iridium ($\text{Pt}_{0.8}\text{Ir}_{0.2}$) AFM tip and a niobium-doped strontium titanate surface, the flexoelectricity is rationalized as a band-bending ratcheting mechanism cyclically moving electrons from the semiconductor to the metal under cyclic changes to the contact pressure. It is likely that a similar mechanism will hold for silicon–platinum junctions, but a direct test of this hypothesis is still lacking.

Because formation of the triazole moiety has been shown to cause a reduction in the work function, to increase leakage current, and to enhance tribocurrents,¹⁵ we also tested the

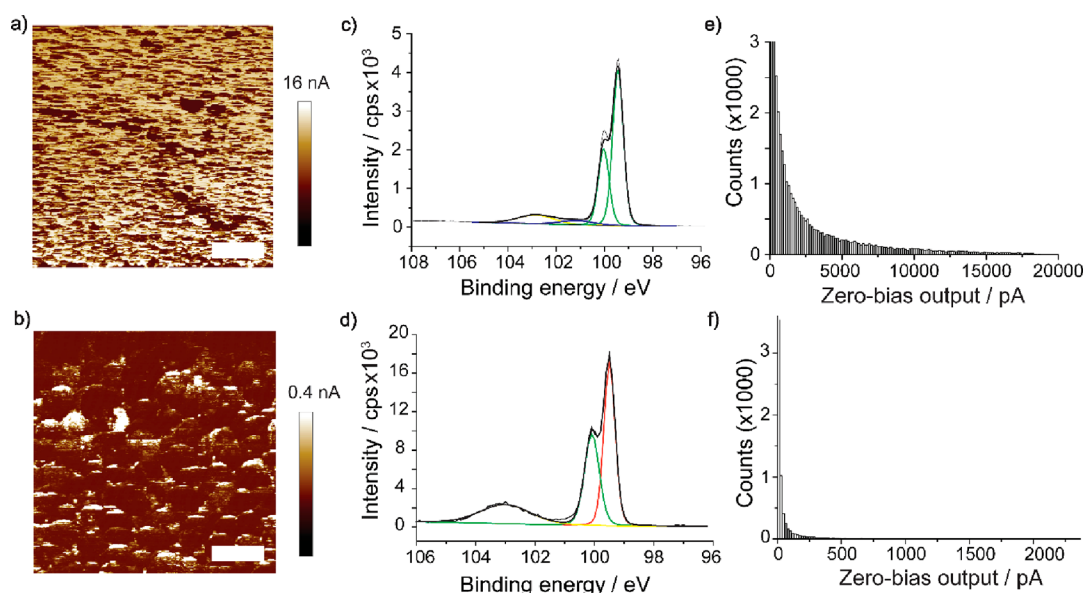


Figure 6. (a and b) Zero-bias C-AFM maps for Si(211) S-1 samples etched for 13 min in a mixture of MeOH and aqueous 40% NH_4F (1:10, v/v) under darkness. Samples were subjected to 10 (a, c, and e) and 40 (b, d, and f) CV cycles from -0.4 to 0.6 V, at 100 mV s^{-1} , 1.0 M HClO_4 , and 1.7 mW cm^{-2} red light electrode illumination, and the horizontal scale bars in parts a and b are $1 \mu\text{m}$. (c and d) High-resolution XPS Si 2p scans of the anodically damaged samples (10 and 40 CV cycles, respectively). The broad band between 101 and 104 eV are photoelectrons from $\text{Si}^{(1)}$ to $\text{Si}^{(4)}$ oxides. (e and f) Histograms of the current output from the C-AFM experiments of parts a and b. The counts are in pixels ($\sim 65\text{K}$ total image pixels).

zero-bias current output of sliding junctions made on S-2 samples. C-AFM experiments performed on S-2 surfaces revealed for both facets an increase in the current outputs relative to S-1 samples. Outputs were as high as 8 nA for Si(111) (99th percentile of 3.8 nA; Figure S21) and 10 nA for Si(211) (99th percentile of 9.8 nA; Figure S22).

To clarify further why such a large TENG current exists and why bimodal distributions occur, we focused on the impact of oxide growth on these surfaces. We therefore performed C-AFM experiments on deliberately oxidized samples. Figure 6a is a C-AFM map recorded on a sample first subjected to 10 CV cycles. The 99th percentile of the tribocurrent output was as high as 14 nA (current average ~ 2.8 nA). There is oxidative damage (Figure 6b) and yet significant tribocurrent enhancement relative to freshly prepared samples (Figure 5). After 40 CV cycles (Figure 6b), the TENG performances drop drastically. As oxide grows beyond trace levels, as shown in Figures 6d and S23, the value of the 99th percentile current output drops to 1.8 nA (the average current decreases to ~ 287 pA).

Upon sample oxidation, there is an increase in the fraction of sample locations that have very low or negligible zero-bias tribocurrent (Figure 6e,f), but while this is not surprising because silica is an electrical insulator, what is notable is that minor silica growth results in an increase of the maximum TENG output. The explanation is probably that low levels of silica introduce energy levels in the band gap, causing a counterintuitive increase in the conductivity, which is, however, not unprecedented. For example, minor silicon oxidation accounts for an initial and transient drop in the anodization voltage required for the constant-current growth of silica adlayers over a silicon electrode.⁵³

3. CONCLUSIONS

In this work, we have optimized the etching and surface modification of Si(211)—an underexplored but highly conductive silicon crystal cut. The overall goal is to facilitate the uptake of silicon as a platform for DC TENGs. Silicon is a cheap and readily available semiconductor, and a promising substrate for out-of-equilibrium Schottky-diode TENGs for autonomous power supplies converting microscopic sliding motion into DC electricity.^{66–68} We have shown that the etching of Si(211) in aqueous ammonium fluoride can yield surfaces as smooth as high-quality Si(111) surfaces, which are taken as the benchmark. The key to achieving this was to reduce the etching rates to a minimum by means of complete shielding from light and to simultaneously prevent the formation of surface-pinned hydrogen bubbles by reducing the etchant surface tension. Such an optimized Si(211) system can be monolayer-modified and, when rubbed with sharp metal contacts, yields tribocurrent outputs significantly greater than those of equivalent sliding Schottky diodes made on Si(111). We found that monolayer-modified Si(211) systems that, upon attachment of a redox tether, give broad and multiple voltammetric waves are generally poor TENG performers, while surfaces with well-behaved electrochemistry are the best performers, with a negligible fraction of sample locations having tribocurrent outputs close to the noise level. Introducing defects in the band gap (namely, traces of silica) significantly enhanced the tribocurrent output. This enhancement is, however, temporary because further substrate oxidation leads to an increase of the sample's locations with negligible current outputs. The work highlights the scope of noncanonical silicon crystallographic cuts in both TENGs and electrochemistry and reveals the scope of engineering defects in the gap to boost DC TENG outputs.

4. EXPERIMENTAL SECTION

Chemicals and Materials. Unless stated otherwise, all chemicals were of analytical grade and used as received. Sulfuric acid (95–97%, Honeywell), aqueous hydrogen peroxide (30% w/w, Honeywell), and aqueous ammonium fluoride (40% w/w, Honeywell) were of semiconductor grade or equivalent purity grade. Methanol (MeOH; HPLC grade, >99.9%) and ammonium sulfite monohydrate (92%) were purchased from Sigma-Aldrich. Hydrochloric acid (35–37%, Ajax Finechem) and 2-propanol (>99.8%, Ajax Finechem) were supplied by Thermo Fisher Scientific. Redistilled dichloromethane (DCM) and Milli-Q water (>18 M Ω cm resistivity) were used for wafer-cleaning and surface-modification procedures. Si(111) and Si(211) prime grade single-side polished silicon wafers ($\pm 0.05^\circ$, 500 μ m thick), n-type with a resistivity of 7–13 Ω cm, were obtained from Siltronix, S.A.S. (Archamps, France). 1,8-Nonadiyne (**1**; 98%, Sigma-Aldrich) was used as received. Azidomethylferrocene (**2**) was prepared according to literature procedures.²⁸

Surface Modification Procedures. Silicon wafers were first cut into either 10 \times 10 mm (AFM measurements), 15 \times 15 mm (electrochemical measurements and ellipsometry), or 15 \times 35 mm (XRR measurements) pieces and then washed sequentially with DCM, 2-propanol, and water before being immersed for 30 min in a hot (100 $^\circ$ C) piranha solution [a 3:1 mixture (v/v) of concentrated sulfuric acid and hydrogen peroxide (30%)]. Samples were then rinsed three times with water and then immediately etched, with the polished side facing up, in a deoxygenated (by means of bubbling argon for at least 15 min) aqueous 40% solution of ammonium fluoride. A small amount of ammonium sulfite was added as an oxygen scavenger to the etching bath. The etching times, presence or absence of MeOH, and degree of illumination of the sample during the etching were varied and are specified separately. Control Si(111) samples were etched for 13 min under ambient light with the polished side facing up (fluorescent tubes, 0.2 mW cm⁻²). Hydrogen-terminated samples (Si–H) were then rinsed once with Milli-Q water and twice with DCM and then blow-dried under a stream of nitrogen gas. The Si–H surfaces were immediately reacted with a small sample of **1** (Figure 1a), following minor modifications of a previously reported hydrosilylation procedure. A brief account of the hydrosilylation procedure is as follows: the liquid diyne stock was bubbled with argon for at least 15 min, and then ~ 0.1 mL of **1** was used to cover a Si–H sample, which was then rested for 2 h under nitrogen at approximately 20 cm from a 312 nm light source (Vilber, VL-215.M, nominal power output of 30 W). The surface of the liquid sample was covered with a 1-mm-thick quartz plate (part 01031-AB, SPI Supplies) to limit its evaporation. The reaction was stopped by removing the acetylene-terminated monolayer (**S-1**) from the UV chamber, followed by extensive sample rinsing with DCM. **S-1** samples were stored for 24 h under DCM at +4 $^\circ$ C prior to analysis or further derivatization. The CuAAC reaction used to prepare a ferrocene-functionalized silicon surface (**S-2**) was performed following previous procedures.²⁸ **S-1** samples were rinsed with 2-propanol and then placed in a reaction tube containing 4 mL of **2** in 2-propanol (0.5 mM), 1 mL of aqueous copper sulfate (20 mol % relative to **2**), and 1 mL of aqueous sodium ascorbate (100 mol % relative to **2**). The reaction tube was stoppered and the CuAAC reaction carried out at room temperature with gentle agitation while being shielded from ambient light. The reaction was stopped after 30 min by removing the ferrocene-modified electrode (**S-2**) from the vial. Samples were rinsed thoroughly with 2-propanol, water, HCl (0.5 M), and DCM. Finally, the samples were dried under a stream of nitrogen gas before being analyzed.

Atomic Force Microscopy (AFM). AFM measurements of the surface topography and zero-bias tribocurrent were carried out on a Park NX10 (Park Systems Corp., Korea). The instrument is fitted with a variable enhanced conductive (VECA) probe holder for conductive AFM (C-AFM). The AFM tips were solid platinum tips (25Pt300B, Rocky Mountain Nanotechnology, Holladay) with a resonance frequency of 14 kHz, a spring constant of 18 N m⁻¹, and a tip radius of ~ 18.20 nm. The experimental contact area (tip–sample) was in the range of 2.4–5.5 nm² and was calculated as described in

the Section S1. All measurements were performed at room temperature and under ambient air (relative humidity of $\sim 76\%$). The topography and current images were obtained simultaneously. The C-AFM sample routing is such that a positive-sign electric current indicates a tip-to-silicon electron flow (i.e., a leakage current for n-type silicon with a platinum top contact). Samples were secured on the AFM stage by carbon tape after having ensured ohmic contact between the sample and stage by scratching the back of the silicon with SiC emery paper and applying on the abraded surface a small amount of gallium–indium eutectic (99.9% Alfa Aesar). Unless otherwise specified, the imaging size was set to 5 \times 5 μ m, the imaging resolution to 256 points/line, the scan rate to 1.0 Hz, and the applied normal force to 360 nN. All data were analyzed with XEI processing software (Park Systems), and the average and maximum current output results are the average of at least three independent measurements. Maximum zero-bias current at the 99th percentile sampled points at zero bias, states for current outputs higher than 99% of the total sampled points.⁶⁹ The vertical palette color legend (scale bar) for the AFM height and current maps does not cover the full scale. The scale bar maximum was selected to better visualize lateral changes in the current and height images. The residual output (noise level) is situated around ~ 120 fA.

Electrochemical Measurements. All electrochemical measurements were carried out on a CHI650D electrochemical workstation (CH Instruments) using a three-electrode and single-compartment poly(tetrafluoroethylene) cell. Monolayer-modified **S-1** and **S-2** surfaces (10 \times 10 mm) served as working electrodes, a platinum coil served as the counter electrode, and Ag/AgCl (in a 3.0 M aqueous NaCl solution) served as a potential reference. The geometric area of the working electrode was set to 0.28 cm² by means of a circular rectilinear cross-sectional Kalrez gasket. The electrical contact of the working electrode to a copper plate was obtained as described for the C-AFM experiments. The electrolyte was aqueous 1.0 M perchloric acid, and all measurements were carried out in air at room temperature (22 \pm 2 $^\circ$ C) and under illumination. The red light illuminating the silicon electrode, through the electrolyte compartment, was a light-emitting diode (660 nm, nominal power output 940 mW, Thorlabs part M660L4) coupled to a collimator adapter (SM1P25-A, Thorlabs). The collimator–sample distance was approximately 10 cm. A meter from Amprobe (model IC-LM-200) was used to measure the illuminance. Electrode illumination was measured in lx but reported in mW cm⁻² (1 lx approximated to 0.0024 mW cm⁻²). The light intensity at the electrode surface was generally ~ 1.7 mW cm⁻². Surface coverages of ferrocene molecules on **S-2** samples are reported in mol cm⁻². Coverage values are calculated from the CV-derived faradaic charge, taken as the average of the anodic and cathodic scans' background-subtracted integrated current. The reported data are the average of at least three independently prepared and analyzed samples, with values averaged over at least 10 different voltage sweep rates. The 99% confidence limit of the mean coverage was calculated following literature procedures. The apparent electron-transfer rate constants (k_{et}) for the electron-transfer reaction between ferrocenes and substrates (**S-2** samples) was estimated from EIS measurements using the formalism developed by Laviron.⁷⁰ The EIS data to estimate k_{et} were obtained at a working electrode DC bias, E_{dc} , equal to the midpoint between the potential of the anodic and cathodic current peaks from CV experiments. k_{et} was calculated as $1/(2R_{et}C_{ads})$. The potential amplitude of the AC perturbation was set to 15 mV. The EIS data were collected between 10⁵ and 10⁰ Hz. The data were analyzed with ZView (version 4.0c, Scribner Associates) using the equivalent circuits shown in Section S2. The reported values are the average of at least three independently prepared and analyzed samples.

X-ray Photoelectron Spectroscopy (XPS). XPS was used to analyze the atomic composition and chemical state of elements in the monolayers. An AXIS Ultra DLD spectrometer (Kratos Analytical Inc., Manchester, U.K.) with monochromic Al K α radiation (1486.6 eV) and a hemispherical analyzer (165 mm radius) was operated in fixed analyzer transmission mode at 2 \times 10⁻⁸ Torr. The analysis area

was $300 \times 700 \mu\text{m}$, and the photoelectron take-off angle was perpendicular to the sample. Survey spectra were obtained from the accumulation of five scans using 160 eV pass energy over a 0–1100 eV range in 0.5 eV steps. High-resolution spectra (10 scan accumulations) were collected at a pass energy of 20 eV, with step sizes of 0.05 eV for Si 2p (96–108 eV) and 0.1 eV for C 1s (278–295 eV). High-resolution narrow scans for O 1s (520–545 eV), N 1s (395–407 eV), and Fe 2p (700–735 eV) were collected in normal emission with a monochromatic Kratos Axis Supra, using Al K-alpha excitation (1486.7 eV) at 225 W. The pass energy was set to 20 eV, the step size to 0.05 eV, and the dwell time to 200 ms. The XPS data were processed using the CasaXPS software. Analysis of the spectra involved background subtraction using the U2 Tougaard routine and Lorentzian-Asymmetric (LA, 1.53,243) line shape. All of the reported energies are binding energies (eV) and are corrected by applying a rigid shift to bring the Si $2p_{3/2}$ emission to 99.5 eV.

X-ray Reflectometry (XRR). Specular XRR of the monolayer-modified sample was measured on a Panalytical X'Pert Pro instrument. The instrument uses an X-ray wavelength of 1.54 Å (Cu K α) from a tube source and a Göbal mirror and fixed slit of 0.1 mm to create a parallel beam. Samples had an average size of $15 \times 30 \text{ mm}^2$, and a $10 \times 10 \text{ mm}^2$ illuminated footprint was used. Data were collected over a time frame of 2 h and taken from an angle of incidence of 0.05–5.0° in 0.01° steps with a counting time of 15 s step⁻¹. The collected data were reduced so the reflectivity at the critical edge is scaled to unity and the angle of incidence converted to momentum transfer ($Q = 4\pi \sin \theta / \lambda$, where θ is the angle of incidence and λ the wavelength). The prepared organic-thin-layer structural parameters were fitted and refined using the *refnx* analytical software. The data were fitted to a model that describes the monolayer as a single slab with the parameters of thickness, scattering length density (SLD), and roughness. These three parameters were varied along with the background value and substrate roughness using a differential evolution routine until a global minimum in χ^2 was reached. The SLD of the substrate (silicon) was set at $2.01 \times 10^{-5} \text{ \AA}^{-2}$ during the fitting routines. The experimental data are represented as points, and the theoretical reflectivity developed with the structural models is presented in the form of solid lines.

Ellipsometry Measurements. The thickness of the oxide layer (post piranha wash, prior to the fluoride etching) was measured by ellipsometry on a M-2000XI ellipsometer (J. A. Woollam Co.). The samples were irradiated with a FLS-300, 75 W xenon arc lamp light source working in the UV–visible–near-IR range (245–1690 nm) at a fixed angle of 65°. Spectral analysis was performed with the CompleteEASE software (J. A. Woollam Co.).

■ ASSOCIATED CONTENT

SI Supporting Information

The Supporting Information is available free of charge at <https://pubs.acs.org/doi/10.1021/acsnm.2c02006>.

Additional experimental procedures, AFM data under different scan velocities, different loads, with different organic terminal groups, and scans over large areas, XPS data for alternative etching conditions and surface chemistries, XRR data for large-area roughness measurements and a tabled summary of the outcome from alternative etching conditions, and EIS data (PDF)

Special Issue Paper

This paper was intended for the Forum Focused on Australian Authors special issue [ACS Appl. Nano Mater. 2022, 5 (9)].

■ AUTHOR INFORMATION

Corresponding Author

Simone Ciampi – School of Molecular and Life Sciences, Curtin University, Bentley, Western Australia 6102,

Australia; orcid.org/0000-0002-8272-8454;

Email: simone.ciampi@curtin.edu.au

Authors

Carlos Hurtado – School of Molecular and Life Sciences, Curtin University, Bentley, Western Australia 6102, Australia

Xin Lyu – School of Molecular and Life Sciences, Curtin University, Bentley, Western Australia 6102, Australia;

orcid.org/0000-0002-6506-0392

Stuart Ferrie – School of Molecular and Life Sciences, Curtin University, Bentley, Western Australia 6102, Australia

Anton P. Le Brun – Australian Centre for Neutron Scattering, Australian Nuclear Science and Technology Organization, Lucas Heights, New South Wales 2234, Australia;

orcid.org/0000-0003-2431-6985

Melanie MacGregor – Flinders Institute for Nanoscale Science and Technology, Flinders University, Bedford Park, South Australia 5042, Australia

Complete contact information is available at:

<https://pubs.acs.org/10.1021/acsnm.2c02006>

Author Contributions

The manuscript was written with contributions by all authors. All authors have approved the final version of the manuscript.

Notes

The authors declare no competing financial interest.

■ ACKNOWLEDGMENTS

This work was financially supported by the Australian Research Council (Grants DP190100735, FT190100148, and FT200100301). The authors acknowledge the instruments and expertise of Microscopy Australia at the Future Industries Institute, University of South Australia, enabled by NCRIS, university, and state government support.

■ REFERENCES

- (1) Peng, K.-Q.; Wang, X.; Li, L.; Hu, Y.; Lee, S.-T. Silicon nanowires for advanced energy conversion and storage. *Nano Today* 2013, 8, 75–97.
- (2) Fabre, B. Ferrocene-Terminated Monolayers Covalently Bound to Hydrogen-Terminated Silicon Surfaces. Toward the Development of Charge Storage and Communication Devices. *Acc. Chem. Res.* 2010, 43, 1509–1518.
- (3) Michaels, P.; Alam, M. T.; Ciampi, S.; Rouesnel, W.; Parker, S. G.; Choudhury, M. H.; Gooding, J. J. A robust DNA interface on a silicon electrode. *Chem. Commun.* 2014, 50, 7878–7880.
- (4) Linford, M. R.; Chidsey, C. E. Alkyl monolayers covalently bonded to silicon surfaces. *J. Am. Chem. Soc.* 1993, 115, 12631–12632.
- (5) Vogel, Y. B.; Zhang, J.; Darwish, N.; Ciampi, S. Switching of Current Rectification Ratios within a Single Nanocrystal by Facet-Resolved Electrical Wiring. *ACS Nano* 2018, 12, 8071–8080.
- (6) Ciampi, S.; Darwish, N.; Aitken, H. M.; Díez-Pérez, I.; Coote, M. L. Harnessing electrostatic catalysis in single molecule, electrochemical and chemical systems: a rapidly growing experimental tool box. *Chem. Soc. Rev.* 2018, 47, 5146–5164.
- (7) Fabre, B.; Pujari, S. P.; Scheres, L.; Zuilhof, H. Micropatterned Ferrocenyl Monolayers Covalently Bound to Hydrogen-Terminated Silicon Surfaces: Effects of Pattern Size on the Cyclic Voltammetry and Capacitance Characteristics. *Langmuir* 2014, 30, 7235–7243.
- (8) Lattimer, J. R. C.; Brunschwig, B. S.; Lewis, N. S.; Gray, H. B. Redox Properties of Mixed Methyl/Vinylferrocenyl Monolayers on Si(111) Surfaces. *J. Phys. Chem. C* 2013, 117, 27012–27022.
- (9) Mukhopadhyay, A.; Bernard, B.; Liu, K.; Paulino, V.; Liu, C.; Donley, C.; Olivier, J.-H. Molecular Strategies to Modulate the

- Electrochemical Properties of P-Type Si(111) Surfaces Covalently Functionalized with Ferrocene and Naphthalene Diimide. *J. Phys. Chem. C* **2019**, *123*, 11026–11041.
- (10) Zhang, X. G. *Electrochemistry of Silicon and Its Oxide*; Springer: Boston, MA, 2007.
- (11) Ciampi, S.; James, M.; Le Saux, G.; Gaus, K.; Justin Gooding, J. Electrochemical “Switching” of Si(100) Modular Assemblies. *J. Am. Chem. Soc.* **2012**, *134*, 844–847.
- (12) Fabre, B. Functionalization of Oxide-Free Silicon Surfaces with Redox-Active Assemblies. *Chem. Rev.* **2016**, *116*, 4808–4849.
- (13) Aragonès, A. C.; Darwish, N.; Ciampi, S.; Sanz, F.; Gooding, J. J.; Diéz-Pérez, I. Single-molecule electrical contacts on silicon electrodes under ambient conditions. *Nat. Commun.* **2017**, *8*, 15056–15056.
- (14) Ferrie, S.; Darwish, N.; Gooding, J. J.; Ciampi, S. Harnessing silicon facet-dependent conductivity to enhance the direct-current produced by a sliding Schottky diode triboelectric nanogenerator. *Nano Energy* **2020**, *78*, 105210.
- (15) Ferrie, S.; Le Brun, A. P.; Krishnan, G.; Andersson, G. G.; Darwish, N.; Ciampi, S. Sliding silicon-based Schottky diodes: Maximizing triboelectricity with surface chemistry. *Nano Energy* **2022**, *93*, 106861.
- (16) Zhang, S.; Ferrie, S.; Peiris, C. R.; Lyu, X.; Vogel, Y. B.; Darwish, N.; Ciampi, S. Common Background Signals in Voltammograms of Crystalline Silicon Electrodes are Reversible Silica–Silicon Redox Chemistry at Highly Conductive Surface Sites. *J. Am. Chem. Soc.* **2021**, *143*, 1267–1272.
- (17) Zhang, J.; Ferrie, S.; Zhang, S.; Vogel, Y. B.; Peiris, C. R.; Darwish, N.; Ciampi, S. Single-Electrode Electrochemistry: Chemically Engineering Surface Adhesion and Hardness To Maximize Redox Work Extracted from Tribocharged Silicon. *ACS Appl. Nano Mater.* **2019**, *2*, 7230–7236.
- (18) Zhao, Y.; Bouffier, L.; Xu, G.; Loget, G.; Sojic, N. Electrochemiluminescence with semiconductor (nano)materials. *Chem. Sci.* **2022**, *13*, 2528–255.
- (19) Tan, C. S.; Hsieh, P. L.; Chen, L. J.; Huang, M. H. Silicon Wafers with Facet-Dependent Electrical Conductivity Properties. *Angew. Chem. Int. Ed.* **2017**, *129*, 15541–15545.
- (20) Zhang, S.; Ferrie, S.; Lyu, X.; Xia, Y.; Darwish, N.; Wang, Z.; Ciampi, S. Absence of a Relationship between Surface Conductivity and Electrochemical Rates: Redox-Active Monolayers on Si(211), Si(111), and Si(110). *J. Phys. Chem. C* **2021**, *125*, 18197–18203.
- (21) Waelder, J.; Vasquez, R.; Liu, Y.; Maldonado, S. A Description of the Faradaic Current in Cyclic Voltammetry of Adsorbed Redox Species on Semiconductor Electrodes. *J. Am. Chem. Soc.* **2022**, *144*, 6410–6419.
- (22) Sharov, V. A.; Alekseev, P. A.; Borodin, B. R.; Dunaevskiy, M. S.; Reznik, R. R.; Cirilin, G. E. InP/Si Heterostructure for High-Current Hybrid Triboelectric/Photovoltaic Generation. *ACS Appl. Energy Mater.* **2019**, *2*, 4395–4401.
- (23) Liu, J.; Goswami, A.; Jiang, K.; Khan, F.; Kim, S.; McGee, R.; Li, Z.; Hu, Z.; Lee, J.; Thundat, T. Direct-current triboelectricity generation by a sliding Schottky nanocontact on MoS₂ multilayers. *Nat. Nanotechnol.* **2018**, *13*, 112–116.
- (24) Lyu, X.; Ferrie, S.; Pivrikas, A.; MacGregor, M.; Ciampi, S. Sliding Schottky diode triboelectric nanogenerators with current output of 10⁹A/m² by molecular engineering of Si(211) surfaces. *Nano Energy* **2022**, *102*, 107658.
- (25) Olson, K. P.; Mizzi, C. A.; Marks, L. D. Band Bending and Ratcheting Explain Triboelectricity in a Flexoelectric Contact Diode. *Nano Lett.* **2022**, *22*, 3914–3921.
- (26) Gooding, J. J.; Ciampi, S. The molecular level modification of surfaces: From self-assembled monolayers to complex molecular assemblies. *Chem. Soc. Rev.* **2011**, *40*, 2704–2718.
- (27) Linford, M. R.; Fenter, P.; Eisenberger, P. M.; Chidsey, C. E. D. Alkyl Monolayers on Silicon Prepared from 1-Alkenes and Hydrogen-Terminated Silicon. *J. Am. Chem. Soc.* **1995**, *117*, 3145–3155.
- (28) Ciampi, S.; Le Saux, G.; Harper, J. B.; Gooding, J. J. Optimization of Click Chemistry of Ferrocene Derivatives on Acetylene-Functionalized Silicon(100) Surfaces. *Electroanalysis* **2008**, *20*, 1513–1519.
- (29) Meldal, M.; Tornøe, C. W. Cu-Catalyzed Azide–Alkyne Cycloaddition. *Chem. Rev.* **2008**, *108*, 2952–3015.
- (30) Rohde, R. D.; Agnew, H. D.; Yeo, W.-S.; Bailey, R. C.; Heath, J. R. A Non-Oxidative Approach toward Chemically and Electrochemically Functionalizing Si(111). *J. Am. Chem. Soc.* **2006**, *128*, 9518–9525.
- (31) Hauquier, F.; Ghilane, J.; Fabre, B.; Hapiot, P. Conducting Ferrocene Monolayers on Nonconducting Surfaces. *J. Am. Chem. Soc.* **2008**, *130*, 2748–2749.
- (32) Ouyang, J. H.; Zhao, X. S.; Li, T.; Zhang, D. C. Direct measurement of the etching rates on Si (111) and silicon dioxide surfaces in 40% ammonium fluoride aqueous solution via atomic force microscopy. *Int. J. Appl. Phys.* **2003**, *93*, 4315–4320.
- (33) Williams, K. R.; Muller, R. S. Etch rates for micromachining processing. *J. Microelectromech. Syst.* **1996**, *5*, 256–269.
- (34) Baski, A. A.; Erwin, S. C.; Whitman, L. J. The structure of silicon surfaces from (001) to (111). *Surf. Sci.* **1997**, *392*, 69–85.
- (35) Nikolov, V.; Lin, J.; Merzlyakov, M.; Hristova, K.; Searson, P. C. Electrical Measurements of Bilayer Membranes Formed by Langmuir–Blodgett Deposition on Single-Crystal Silicon. *Langmuir* **2007**, *23*, 13040–13045.
- (36) Chilcott, T. C.; Wong, E. L. S.; Böcking, T.; Coster, H. G. L. Electrical characterizations of biomimetic molecular layers on gold and silicon substrates. *Physiol. Meas.* **2008**, *29*, S307–S319.
- (37) Vogel, Y. B.; Zhang, L.; Darwish, N.; Gonçalves, V. R.; Le Brun, A.; Gooding, J. J.; Molina, A.; Wallace, G. G.; Coote, M. L.; Gonzalez, J.; Ciampi, S. Reproducible Flaws Unveil Electrostatic Aspects of Semiconductor Electrochemistry. *Nat. Commun.* **2017**, *8*, 2066.
- (38) Vogel, Y. B.; Molina, A.; Gonzalez, J.; Ciampi, S. Quantitative Analysis of Cyclic Voltammetry of Redox Monolayers Adsorbed on Semiconductors: Isolating Electrode Kinetics, Lateral Interactions, and Diode Currents. *Anal. Chem.* **2019**, *91*, S929–S937.
- (39) Gonçalves, V. R.; Lian, J.; Gautam, S.; Tilley, R. D.; Gooding, J. J. Functionalized Silicon Electrodes in Electrochemistry. *Annu. Rev. Anal. Chem.* **2020**, *13*, 135–158.
- (40) Choudhury, M. H.; Ciampi, S.; Yang, Y.; Tavallaie, R.; Zhu, Y.; Zarei, L.; Gonçalves, V. R.; Gooding, J. J. Connecting Electrodes with Light: One Wire, Many Electrodes. *Chem. Sci.* **2015**, *6*, 6769–6776.
- (41) Vogel, Y. B.; Gooding, J. J.; Ciampi, S. Light-addressable electrochemistry at semiconductor electrodes: redox imaging, mask-free lithography and spatially resolved chemical and biological sensing. *Chem. Soc. Rev.* **2019**, *48*, 3723–3739.
- (42) Chidsey, C. E. D.; Bertozzi, C. R.; Putvinski, T. M.; Mujsce, A. M. Coadsorption of ferrocene-terminated and unsubstituted alkanethiols on gold: electroactive self-assembled monolayers. *J. Am. Chem. Soc.* **1990**, *112*, 4301–4306.
- (43) Ciampi, S.; Choudhury, M. H.; Ahmad, S. A. B. A.; Darwish, N.; Brun, A. L.; Gooding, J. J. The impact of surface coverage on the kinetics of electron transfer through redox monolayers on a silicon electrode surface. *Electrochim. Acta* **2015**, *186*, 216–222.
- (44) Gerischer, H.; Mindt, W. The mechanisms of the decomposition of semiconductors by electrochemical oxidation and reduction. *Electrochim. Acta* **1968**, *13*, 1329–1341.
- (45) Allongue, P.; Kieling, V.; Gerischer, H. Etching mechanism and atomic structure of H-Si(111) surfaces prepared in NH₄F. *Electrochim. Acta* **1995**, *40*, 1353–1360.
- (46) Palik, E. D.; Glembocki, O. J.; Heard, I. H. Study of bias-dependent etching of Si in aqueous KOH. *J. Electrochem. Soc.* **1987**, *134*, 404–409.
- (47) Chadi, D. J. Theoretical study of the atomic structure of silicon (211), (311), and (331) surfaces. *Phys. Rev., B Condens.* **1984**, *29*, 785–792.
- (48) Vaziri Hassas, B.; Caliskan, H.; Guven, O.; Karakas, F.; Cinar, M.; Celik, M. S. Effect of roughness and shape factor on flotation characteristics of glass beads. *Colloids Surf. A Physicochem. Eng. Asp.* **2016**, *492*, 88–99.

(49) Thong, J. T. L.; Choi, W. K.; Chong, C. W. TMAH etching of silicon and the interaction of etching parameters. *Sens. Actuator A Phys.* **1997**, *63*, 243–249.

(50) Zhang, S.; Lyu, X.; Hurtado Torres, C.; Darwish, N.; Ciampi, S. Non-Ideal Cyclic Voltammetry of Redox Monolayers on Silicon Electrodes: Peak Splitting is Caused by Heterogeneous Photocurrents and Not by Molecular Disorder. *Langmuir* **2022**, *38*, 743–750.

(51) Rudnev, A. V.; Yoshida, K.; Wandlowski, T. Electrochemical characterization of self-assembled ferrocene-terminated alkanethiol monolayers on low-index gold single crystal electrodes. *Electrochim. Acta* **2013**, *87*, 770–778.

(52) Madou, M. J.; Loo, B. H.; Frese, K. W.; Morrison, S. R. Bulk and surface characterization of the silicon electrode. *Surf. Sci.* **1981**, *108*, 135–152.

(53) Uritsky, V. X. Role of Electron/Hole Processes in the Initial Stage of Silicon Anodization. *Mater. Sci. Forum* **1995**, *185–188*, 115–118.

(54) Gonzalez, J.; Sequi, J.-A. Analysis of the Electrochemical Response of Surface-confined Bidirectional Molecular Electro-catalysts in the Presence of Intermolecular Interactions. *ChemCatChem* **2021**, *13*, 747–762.

(55) Gonzalez, J.; Sequi-Castellano, J. A. Electrochemical determination of kinetic parameters of surface confined redox probes in presence of intermolecular interactions by means of Cyclic Voltammetry. Application to TEMPO monolayers in gold and platinum electrodes. *Electrochim. Acta* **2021**, *365*, 137331.

(56) Zhang, L.; Vogel, Y. B.; Noble, B. B.; Gonçales, V. R.; Darwish, N.; Brun, A. L.; Gooding, J. J.; Wallace, G. G.; Coote, M. L.; Ciampi, S. TEMPO Monolayers on Si(100) Electrodes: Electrostatic Effects by the Electrolyte and Semiconductor Space-Charge on the Electroactivity of a Persistent Radical. *J. Am. Chem. Soc.* **2016**, *138*, 9611–9619.

(57) Cicero, R. L.; Linford, M. R.; Chidsey, C. E. D. Photoreactivity of Unsaturated Compounds with Hydrogen-Terminated Silicon(111). *Langmuir* **2000**, *16*, 5688–5695.

(58) Bashouti, M. Y.; Paska, Y.; Puniredd, S. R.; Stelzner, T.; Christiansen, S.; Haick, H. Silicon nanowires terminated with methyl functionalities exhibit stronger Si–C bonds than equivalent 2D surfaces. *Phys. Chem. Chem. Phys.* **2009**, *11*, 3845–3848.

(59) Wallart, X.; Henry de Villeneuve, C.; Allongue, P. Truly Quantitative XPS Characterization of Organic Monolayers on Silicon: Study of Alkyl and Alkoxy Monolayers on H–Si(111). *J. Am. Chem. Soc.* **2005**, *127*, 7871–7878.

(60) Scheres, L.; Arafat, A.; Zuilhof, H. Self-Assembly of High-Quality Covalently Bound Organic Monolayers onto Silicon. *Langmuir* **2007**, *23*, 8343–8346.

(61) Cerofolini, G. F.; Galati, C.; Renna, L. Accounting for anomalous oxidation states of silicon at the Si/SiO₂ interface. *Surf. Interface Anal.* **2002**, *33*, 583–590.

(62) Ito, E.; Oji, H.; Araki, T.; Oichi, K.; Ishii, H.; Ouchi, Y.; Ohta, T.; Kosugi, N.; Maruyama, Y.; Naito, T.; Inabe, T.; Seki, K. Soft X-ray Absorption and X-ray Photoelectron Spectroscopic Study of Tautomerism in Intramolecular Hydrogen Bonds of N-Salicylideneaniline Derivatives. *J. Am. Chem. Soc.* **1997**, *119*, 6336–6344.

(63) Böcking, T.; James, M.; Coster, H. G. L.; Chilcott, T. C.; Barrow, K. D. Structural Characterization of Organic Multilayers on Silicon(111) Formed by Immobilization of Molecular Films on Functionalized Si–C Linked Monolayers. *Langmuir* **2004**, *20*, 9227–9235.

(64) Sieval, A. B.; Demirel, A. L.; Nissink, J. W. M.; Linford, M. R.; van der Maas, J. H.; de Jeu, W. H.; Zuilhof, H.; Sudhölter, E. J. R. Highly Stable Si–C Linked Functionalized Monolayers on the Silicon (100) Surface. *Langmuir* **1998**, *14*, 1759–1768.

(65) Li, T.; Dief, E. M.; Lyu, X.; Rahpeima, S.; Ciampi, S.; Darwish, N. Nanoscale Silicon Oxide Reduces Electron Transfer Kinetics of Surface-Bound Ferrocene Monolayers on Silicon. *J. Phys. Chem. C* **2021**, *125*, 27763–27770.

(66) Ren, L.; Yu, A.; Wang, W.; Guo, D.; Jia, M.; Guo, P.; Zhang, Y.; Wang, Z. L.; Zhai, J. p-n Junction Based Direct-Current Triboelectric

Nanogenerator by Conjunction of Tribovoltaic Effect and Photo-voltaic Effect. *Nano Lett.* **2021**, *21*, 10099–10106.

(67) Zheng, Q.; Peng, M.; Liu, Z.; Li, S.; Han, R.; Ouyang, H.; Fan, Y.; Pan, C.; Hu, W.; Zhai, J.; Li, Z.; Wang, Z. L. Dynamic real-time imaging of living cell traction force by piezo-phototronic light nano-antenna array. *Sci. Adv.* **2021**, *7*, eabe7738.

(68) Peng, M.; Liu, Y.; Yu, A.; Zhang, Y.; Liu, C.; Liu, J.; Wu, W.; Zhang, K.; Shi, X.; Kou, J.; Zhai, J.; Wang, Z. L. Flexible Self-Powered GaN Ultraviolet Photoswitch with Piezo-Phototronic Effect Enhanced On/Off Ratio. *ACS Nano* **2016**, *10*, 1572–1579.

(69) Miller, J. N. A. In *Statistics and Chemometrics for Analytical Chemistry*, 7th ed.; Miller, J. N., Miller, J. C., Miller, R. D., Eds.; Pearson Education Ltd.: Harlow, U.K., 2018.

(70) Laviron, E. A.C. Polarography and faradaic impedance of strongly adsorbed electroactive species: Part III. Theoretical complex plane analysis for a surface redox reaction. *J. Electroanal. Chem. Interface Electrochem.* **1979**, *105*, 35–42.

Recommended by ACS

Thermopower Modulation Analyses of High-Mobility Transparent Amorphous Oxide Semiconductor Thin-Film Transistors

Hui Yang, Hiromichi Ohta, *et al.*

SEPTEMBER 29, 2022

ACS APPLIED ELECTRONIC MATERIALS

READ 

Retention Improvement of HZO-Based Ferroelectric Capacitors with TiO₂ Insets

Aleksandra A. Koroleva, Andrey M. Markeev, *et al.*

DECEMBER 07, 2022

ACS OMEGA

READ 

Role of Hydrogen in Suppressing Secondary Nucleation in Chemical Vapor-Deposited MoS₂

Sayema Chowdhury, Sanjay K. Banerjee, *et al.*

DECEMBER 13, 2022

ACS APPLIED ELECTRONIC MATERIALS

READ 

Structural and Electrical Response of Emerging Memories Exposed to Heavy Ion Radiation

Tobias Vogel, Lambert Alff, *et al.*

SEPTEMBER 16, 2022

ACS NANO

READ 

Get More Suggestions >

Chapter 3. Oxidative damage during the operation of Si(211)-based triboelectric nanogenerators

Introduction to Chapter 3

With the increasing integration of portable electronic devices and the Internet of Things (IoT) into everyday life, the demand for self-sustaining power sources has intensified leading to a growing interest in Triboelectric nanogenerators (TENGs). As we have seen in **Chapter 2**, hybrid constructs such as Si-SAM electrodes have the potential to harness mechanical energy to generate electricity, for a continuous power supply. However, their widespread application is limited by challenges related to surface wear and oxidation, which can significantly degrade device performance over time.

Chapter 3, in the form of paper 2, provides a comprehensive analysis of the factors contributing to surface degradation in silicon-based DC-TENGs, focusing on Schottky diodes with organic monolayer modifications. These modifications are intended to enhance TENG performance by improving surface properties such as wettability, friction, and work function. Despite these enhancements, silicon-based TENGs still face durability issues, particularly due to the high pressures and current densities involved in their operation.

Results reveal that the main surface damage is caused by oxide growth, but this oxide growth is not caused by the passage of current but rather by the applied load (the surface experiences large pressures $\sim 4\text{GPa}$).

Interestingly, as we will see in the chapter, the drop in current occurs with a certain delay during the operation (sliding events). This could be one of the causes explaining why the device wear is often not considered or neglected.

The supporting information for **Chapter 3** can be found in *Appendix D*

Oxidative damage during the operation of Si(211)-based triboelectric nanogenerators

Carlos Hurtado¹ and Simone Ciampi^{1*}

¹ School of Molecular and Life Sciences, Curtin University, Bentley, Western Australia 6102, Australia

* Correspondence: simone.ciampi@curtin.edu.au

Abstract: Triboelectric nanogenerators (TENGs) based on sliding metal–semiconductor junctions are an emerging technology that can efficiently harvest mechanical into electrical energy. These miniature autonomous power sources can output large direct current (DC) densities, but often suffer from limited durability hence their practical scope remains uncertain. Herein, through a combination of conductive atomic force microscopy (C-AFM) and photocurrent decay (PCM) experiments we have explored the underlying cause of the surface wear during the operation of DC-TENGs. Using monolayer-functionalized Si(211) surfaces as the model system, we demonstrate the extent to which surface damage develops during TENG operation. We reveal that introduction of surface defects (oxide growth) during TENG operation is not caused by the passage of the rather large output current densities (on average $\sim 2 \times 10^6$ A/m²) but it is instead mainly caused by the large pressure (\sim GPa) required for the sliding Schottky diode to output a measurable zero-bias current. We also discovered that the drop in output during operation occurs with a delay from the friction/pressure event, which partially explains why such deterioration of DC-TENG performances is often underestimated or not reported.

Keywords: Silicon; triboelectric nanogenerators, Schottky diodes; conductive atomic force microscopy; silicon oxidation, organic monolayers

1. Introduction

The rapid growth of the Internet of Things and the surging demand for portable electronic devices have fueled the need for autonomous power sources.[1, 2] Conventional batteries, while a common and widespread solution to power up electronics, are non-regenerative power sources, hence need frequent recharging or replacing. While other energy harvesting technologies, such as piezoelectric nanogenerators (PENGs) and solar cells, have made significant strides in converting mechanical and solar energy into electricity, they often face limitations in terms of efficiency, scalability, and compatibility with various operating environments.[3] Triboelectric nanogenerators (TENGs) based on the contact electrification (CE) phenomena,[4, 5] have emerged as a promising solution, offering a means to convert ubiquitous mechanical energy into electrical power.[6, 7]

The output of conventional TENGs is alternating current,[8, 9] but recently there have been a series of breakthroughs towards the development of direct current (DC) TENGs (DC-TENGs),[10-12] which is an important step forward since most of microelectronic components rely on a DC source. For instance, in 2018 Liu et al. succeeded in showing that friction of an out-of-equilibrium Schottky contact (between Pt and MoS₂) can be efficiently converted into DC.[13] This report prompted the search for cheaper and more readily accessible alternatives to MoS₂. In this context, silicon represents a promising material for the further development of DC-TENGs.[14-16].

Citation: To be added by editorial staff during production.

Academic Editor: Firstname Last-name

Received: date

Revised: date

Accepted: date

Published: date



Copyright: © 2023 by the authors. Submitted for possible open access publication under the terms and conditions of the Creative Commons Attribution (CC BY) license (<https://creativecommons.org/licenses/by/4.0/>).

The mechanism for the mechanic-to-electric energy conversion occurring in a sliding Schottky diode is undoubtedly a surface process dominated by several properties of the metal–semiconductor interface.[17] Consequently, the manipulation of the silicon surface chemistry, for example via hydrosilylation reactions to graft organic monolayers on the surface [18, 19] offers a path to maximize TENGs performances by controlling wettability, friction, adhesion, and work function.[20, 21] Despite the undisputed anodic protection that the attachment of an organic monolayer imparts to the silicon surface when the contact is a (soft) liquid,[18, 19, 22, 23] silicon-based Schottky TENGs have so far shown only a limited lifespan, severely restricting their viability.[24] Previous studies have highlighted that the generation of DC current in Schottky TENGs requires substantial pressure and small contacts,[25, 26] and that large current densities, up to 10^9 A/m², can be obtained.[15] These operational conditions, both the mechanical pressure and localized heating from the flow of a large current density even under zero external bias, can undoubtedly lead to substrate oxidation, hence limiting the durability of Si-based DC-TENGs. Therefore, while minor oxide growth can lead to a temporary enhancement of the DC output,[15, 27] extensive silicon oxidation results in a complete loss of the triboelectric output.[28] Notably, the passage of current, regardless of the current direction, plays a major role in oxide growth.[29] Here we present a detailed analysis of the underlying causes of surface wear/oxidation during the operation of DC silicon-based triboelectric nanogenerators (DC-TENGs) based on sliding metal-semiconductor junctions. Our study focuses on monolayer-modified Si(211) surfaces, which have demonstrated superior TENG performances in a previous work.[28] We aim to clarify whether surface damage and oxide growth in silicon-based TENGs are primarily caused by pressure and friction or by current-related effects. To address this, we utilized a combination of conductive atomic force microscopy (C-AFM) and photocurrent decay (PCM) experiments. We begin by discussing the characteristics of the model system used in our study, followed by an exploration of the progressive surface damage during sliding events. Subsequently, we present our findings related to surface defects, carrier life-times, and current behavior under various conditions. We also discuss the unexpected observations at damaged regions and provide insights into the potential role of flexovoltage. By exploring the progressive surface damage during sliding events and its (detrimental) impact on current generation we aim to clarify the actual durability of silicon-based TENGs.

2. Materials and methods

2.1 Chemicals and materials

Ammonium fluoride (semiconductor grade, 40 wt%, Honeywell), hydrogen peroxide (MOS Puranal™, 30 wt% in water, Honeywell), sulfuric acid (VLSI Puranal™, 95–97 %, Honeywell) and Milli-Q water (>18 MΩ cm) were used for sample etching and cleaning procedures. 1,8-Nonadiyne (98%, **1**), sodium ascorbate (98%), and methanol (MeOH; HPLC grade, >99.9%) were obtained from Sigma–Aldrich and used without further purification. Si(211) wafers ($\pm 0.05^\circ$, prime grade) were purchased from Siltronic, S.A.S (Archamps, France). Wafers were 500 μ m thick, one-side polished and N-type (phosphorus-doped) with resistivity of 7–13 Ω cm. Gallium–indium (Galn) eutectic (99.99 %, Sigma–Aldrich) was used to establish an electrical contact between the non-polished side (back side) of the silicon sample and the AFM sample holder.

2.2 Surface modification procedures

Silicon wafers were cut into wafers of approximately 1 \times 1 cm. Samples were first rinsed with dichloromethane (3 \times 50 mL), 2-propanol (3 \times 50 mL) and Milli-Q water (5 \times 50 mL) and subsequently immersed for 30 min in a hot piranha solution (100 $^\circ$ C, consisting in a 3:1 v/v mixture of concentrated sulfuric acid and 30% hydrogen peroxide). After the

piranha bath, samples were rinsed with water (3 × 50 mL) and etched for 13 min in a mixture of deoxygenated ammonium fluoride solution (22.5 mL) and methanol (1 mL) while shielded from ambient light, following reported procedures.[28] Ammonium sulfite was added as oxygen scavenger to the etching mixture and the etching bath was degassed by bubbling argon gas for 15 min before adding the silicon sample. During the etching (13 min) the polished side of the silicon sample was faced upwards. After the etching, the silicon samples were rinsed with water (1 × 50 mL), dichloromethane (2 × 50 mL), and then covered by a deoxygenated sample of **1**. The silicon-hydride diyne-coated samples were then placed inside a UV chamber (312 nm UV source, Vilber, VL-215. M, nominal power output of 30 W) and held for 2 h at approximately 20 cm from the UV source. The hydrosilylated product (the **S-1** surface, Figure 1a) was rinsed with dichloromethane (1 × 50 mL) and stored overnight at +4 °C under dichloromethane in a sealed sample tube prior to analysis.

2.3 Atomic force microscopy characterization

Atomic force microscopy (AFM) topography maps, zero-bias current maps, and lateral force (friction) scans were performed using a NX10 microscope (Park Systems Corporation, Suwon, Korea). Measurements were performed using a single solid platinum tip (25PT300B, Rocky Mountain Nanotechnology, Holladay, UT) with a nominal resonance frequency of 14 kHz, a spring constant of 18 N/m, and a tip radius of ~20 nm, set points were either 50 or 360 nN. The silicon samples–Pt tip contact area was estimated against the Derjaguin, Muller and Toporov (DMT) model (described in the Supporting Information).[30] The imaging resolution was set to 256 points/line, the scan rate to 1 Hz, and scan size ranged from 2 × 2 μm to 5 × 5 μm. Reverse currents have a positive sign and are indicative of an electron flow from the Pt tip to the silicon sample. The maximum zero-bias current output is taken as the output of the 99th percentile.[31] The vertical height and current scale bars (color coded) for the AFM measurements do not cover the full scale. The color range was arbitrarily set so to maximize the visual clarity of topographic and current features. The instrument current noise is around ~120 fA. AFM data were processed with the XEI software (Park Systems). Transient photocurrent measurements (PCM) were recorded at 10 separate sample locations, the laser wavelength is 635 nm and the nominal laser power output is 5 mW. Current transients decay curves were fitted in Origin 9.0™ software. Statistical analysis was performed in Python. Ohmic contact between the AFM stage and the silicon samples was ensured by applying a small amount of GaIn eutectic to the silicon non-polished side and gently rubbing it with sandpaper. Samples were further secured on the AFM stage with conductive copper tape. All measurements were conducted in air at ambient temperature (24±2 °C)

3. Results and discussion

Our research focuses on Si(211) crystals, a choice based on the fact that the surface conductivity of Si(211) is greater than that of both Si(100) and Si(111).[32, 33] This makes Si(211) an excellent candidate for DC-TENGs. The native oxide needs first to be removed to ensure sufficient electrical conductivity, and the resulting (hydride) surface needs to be chemically passivated to allow handling the samples under ambient air without significant oxidation. To this end, Si–C-bound monolayers of 1,8-nonadiyne, **1**, were prepared following published procedures (Figure 1a).[19, 34, 35] Silicon oxide samples were first etched to expose a Si–H surface, which is reactive towards 1-alkynes such as the α,ω -dialkyne molecule **1**. This chemical strategy (**S-1**) prevents spontaneous semiconductor oxidation and enhances the generation of DC output in response to mechanical stimuli such as vibrations and friction.[20]

Wet etched Si(211) has a rougher surface as compared to other Si crystal cuts, such as for example Si(111) and Si(100).[28, 34] Figure 1b shows an AFM topography map of a Si(211) S-1 sample, with evident rounded features, and a root-mean-square (RMS) roughness of ~3 nm, a value that comparable to published results,[28] and which is at present the smoother Si(211) surface achievable by wet chemistry methods. We then performed a zero-bias current (C-AFM) map ($2 \times 2 \mu\text{m}$) to measure the current generation upon lateral movement of the solid platinum AFM tip across the semiconductor surface (Figure 1c). Figure 1d shows the DC distribution for the map in Figure 1c and reveals that the current ranged from noise level up to 750 pA. The average output was ~120 pA, and 1% of the sampled points returned current values above 700 pA. The average current density is in the order of $\sim 2 \times 10^6 \text{ A/m}^2$.

141
142
143
144
145
146
147
148
149
150
151
152

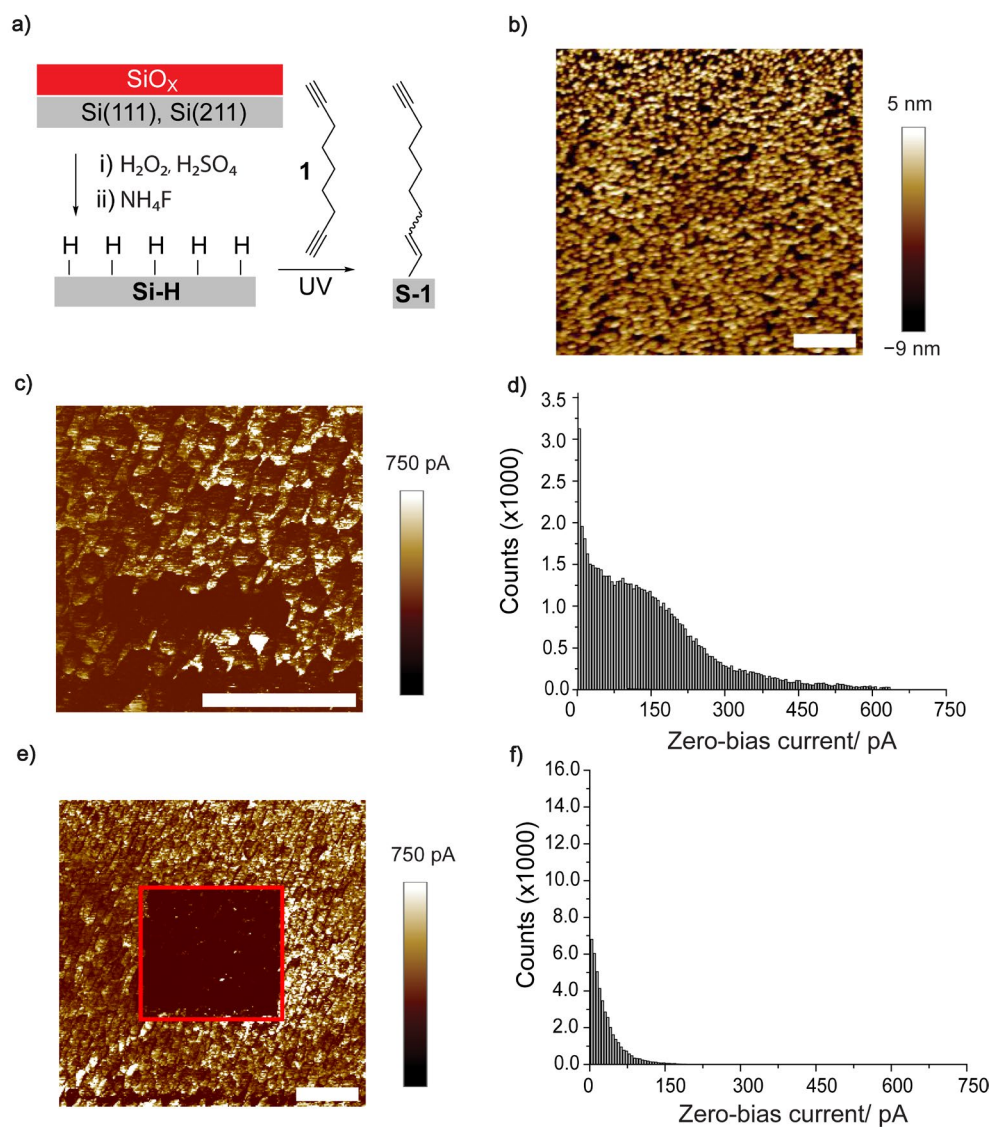


Figure 1. (a) Chemical strategy used for the cleaning, etching and passivation of silicon samples. Hydrogen-terminated Si(211) samples were reacted under an UV-assisted hydrosilylation reaction with dyne **1** to yield the covalent, monolayer-modified, **S-1** surface. (b) AFM topography image ($5 \times 5 \mu\text{m}$ scan size) of a Si(211) **S-1** sample. (c) Zero-voltage bias C-AFM map of **S-1** sample obtained in a $2 \times 2 \mu\text{m}$ region. The applied normal load was 360 nN, and the contact area (Pt-Si contact) was estimated to be $\sim 80 \text{ nm}^2$, hence the normal pressure was $\sim 4.5 \text{ GPa}$ (d) Current distribution histogram plot obtained from the C-AFM map shown in panel (c). (e) Wide zero-voltage bias C-AFM map ($5 \times 5 \mu\text{m}$) of the **S-1** sample. The area marked as a red square corresponds to region where the C-AFM scan of panel (c) was performed. (f) Current distribution histogram for the C-AFM map of panel (e). The histogram counts refer to the number of pixels (sample locations) of a given current value/bin, with a total of $\sim 65\text{K}$ pixels making up an entire C-AFM map ($5 \times 5 \mu\text{m}$). The horizontal scale bars in panels (b), (c) and (e) indicate $1 \mu\text{m}$.

This tribocurrent is measured under zero external bias, and it bears the sign of a reverse current, that is, electrons flowing from the Pt tip to the silicon surface. Notably in our C-AFM experiments the pressure reaches a pressure of $\sim 4.5 \text{ GPa}$. To evaluate the surface damage, if any, induced after the initial current map scan ($2 \times 2 \mu\text{m}$) we repeated the C-AFM measurement expanding the scan area to a $5 \times 5 \mu\text{m}$ region (Figure 1e). Interestingly, the surface area previously scanned (region marked by a red square in Figure 1e) returned a significantly reduced current output. The average current decreased to $\sim 20 \text{ pA}$

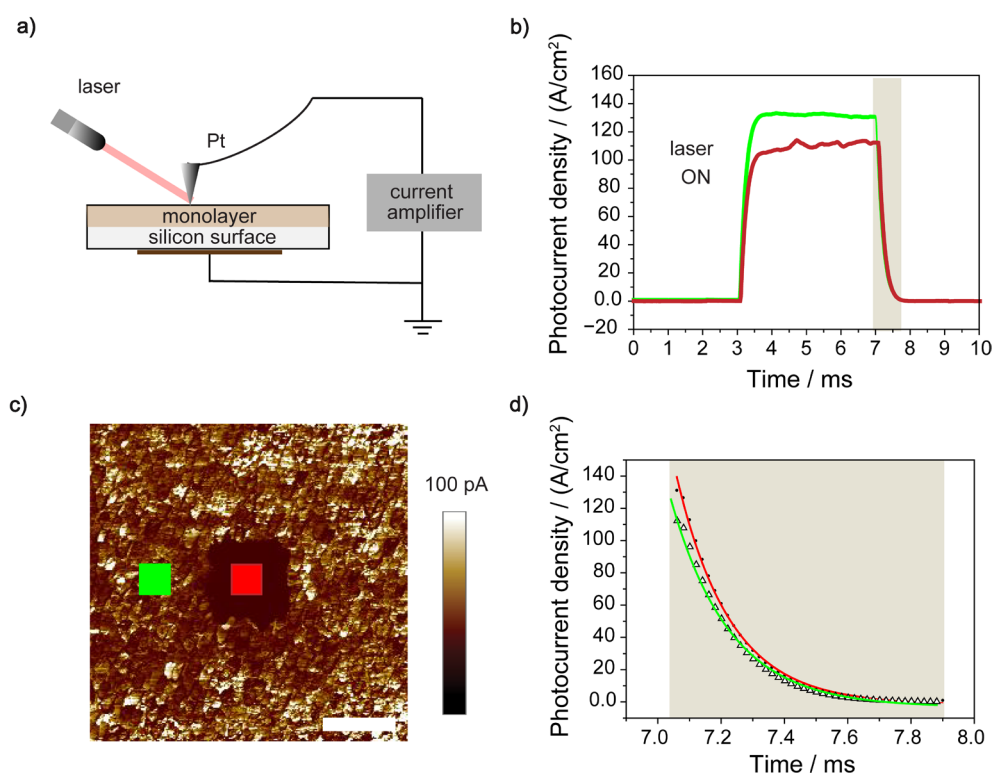


Figure 2. Spatially and time-resolved photoconductivity (PCM) measurements (AFM-based) conducted on S-1 surfaces. (a) Schematic representation of the PCM measurement performed to calculate the carrier lifetime from the transient photocurrent response. (b) Representative PCM traces on S-1 surfaces. The shaded grey colored area indicates the region of the curve where the exponential fit was conducted. (c) C-AFM map of a S-1 sample conducted at zero-voltage bias in a $5 \times 5 \mu\text{m}$ area after a previous scan conducted in a $1 \times 1 \mu\text{m}$ scan area (center of the image). The horizontal scale bar in panel (c) indicates $1 \mu\text{m}$. (d) Exponential fits for photocurrent curve response sampled inside and outside the square shown in panel (c).

(current density $\sim 3 \times 10^5 \text{ A/m}^2$, Figure 1f). In terms of percentage, the observed wear-induced degradation led to an approximate 83.3% reduction in current density within the scanned area. This quantified decay underscores the sensitivity of DC-TENG performance to wear-related effects. Similar current attenuations have been previously reported for AFM experiments on silicon surfaces under an external bias and were linked to oxide growth.[29] We also tested the system under lower set points ($\sim 50 \text{ nN}$) to qualitatively evaluate the surface damage (Figure S1, Supporting Information). Interestingly, C-AFM maps revealed that the loss of spots returning DC output is only partial when performing the scan under lower force, but this comes at a cost of lower tribocurrent outputs.

It is technically hard to acquire an XPS spectra to verify the presence of oxide inside a $2 \times 2 \mu\text{m}$ region, hence we opted for a spatially resolved measurement of surface defects rather than a direct spectroscopic evidence of silicon oxidation. We conducted spatially and time-resolved photoconductivity (PCM) experiments to evaluate the recombination velocities of charge carriers, hence trying to assess the introduction of surface defects during TENG operation. Figure 2a depicts a PCM measurement, and Figure 2b displays representative transient photocurrent decay traces for static Pt-S-1 junctions, inside and outside the putatively oxidized square (Figure 2c).

Unfortunately, a stable and strong photocurrent response is not always present and approximately half of the sampled locations did not return traces as those in Figure 2b but rather resembled those shown in Figure S2 (Supporting Information). The “non-ideal” transients shown in Figure S1 are characterized by a capacitive charging/discharging behavior and could not be used to extract information on recombination velocities. The fit-

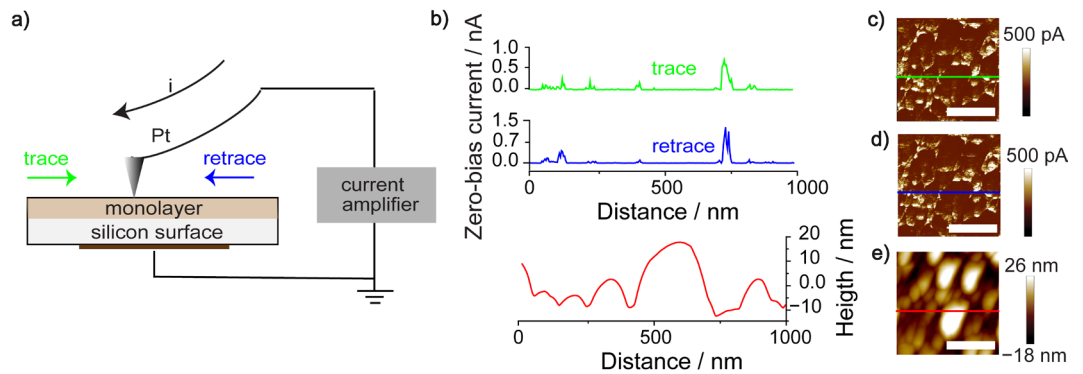


Figure 3. (a) Schematic representation of the C-AFM measurement, the platinum tip is sliding in both, trace and retrace direction, through a silicon (S-1) sample. (b) Zero-bias DC current and topography profiles obtained during C-AFM experiments. The green and blue color coding indicates the direction of the scan: first a trace (green, left to right) and then a retrace (blue, right to left) over the same line. The topographic (height) profile is indicated by the red trace. (c-e) C-AFM and topography maps indicating the location of the line along which the current trace (green), current retrace (blue) and topography (red) data of panel (b) were acquired.

ting of the more ideal photoconductive locations (Figure 2d) returned significantly different carrier lifetimes inside versus outside the square. The average carrier's lifetime inside the square was $147.9 \pm 10.7 \mu\text{s}$ (the uncertainty is the 99% confidence limit of the mean; the lower and upper bound were $137.2 \mu\text{s}$ and $158.6 \mu\text{s}$ respectively). The average carrier's lifetime outside the square was 188.1 ± 15.7 (lower and upper bound of $172.4 \mu\text{s}$ and $203.8 \mu\text{s}$ respectively). The confidence limit was calculated as $t_{n-1}/n^{1/2}$, where t_{n-1} is 3.01 for 10 different samples, where n is the number of measurements and s the standard deviation.[31] In summary, sample locations within the initially scanned area returned a higher surface recombination velocity (i.e., lower time constant), which suggests the introduction of electronic defects, most likely linked to the onset of substrate oxidation, during TENG operations.

The reason why such a drastic drop in TENGs performances is often unnoticed is perhaps because it is customary to screen for such current changes by comparing outputs of sequential trace and retrace scans. This point warrants a further explanation. A conventional C-AFM measurement, as for those shown in Figure 3a and S3 (Supporting Information), allows to simultaneously measure current and map topography (Figure 3b). The sliding Pt tip scans the same topographical feature, sequentially, in both the trace and retrace directions. What is indeed very surprising is that the oxidative damage and corresponding drop in TENG output discussed above (Figure 1 and Figure 2) for microscopic regions has no parallel drop in current output when one tries to detect specifically this based on a single line of trace/retrace measurement (Figure 3c,d). In fact, retrace currents can even reach slightly higher DC outputs than those for trace scans (Figure 3b). The data in Figure 3 show just this, as well as showing that the zero-bias current peaks at concave locations of the Si(211) surface. This effect has been previously reported by Ferrie et al. for Si(111)/(100) pyramids generated via anisotropic etching of Si(100) substrates with potassium hydroxide solutions.[14] The same authors also did not observe an oxidative damage when conducting trace/retrace scans and stressed that tribocurrent discharging happened at the base of the pyramid rather than at its apex. This was explained tentatively as the space charge region becoming thinner at concave sites.[36]

Furthermore, it did not escape our attention that the AFM tip is twisting (based on lateral deflection data) at the edge of the protrusions (Figure S4, Supporting Information). This point will require further investigation and the electronic component of friction remains debated.[37] Recently, Marks and co-workers have suggested that flexoelectricity (i.e. linear coupling between strain gradients and voltage) to be the "missing term" in the

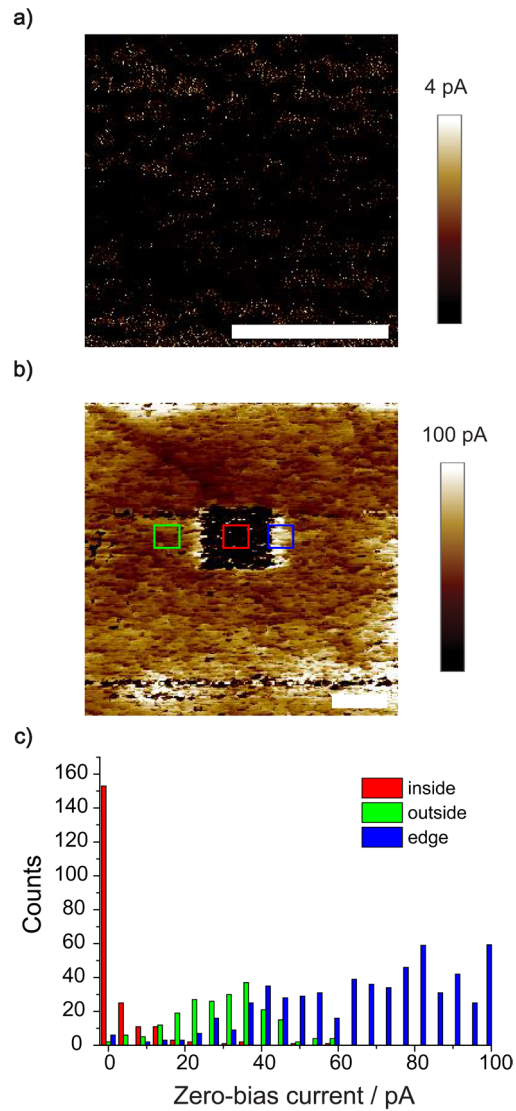


Figure 4. (a) Nullifying-bias DC current output C-AFM experiments with a current reading close to noise level. (b) C-AFM current map obtained at zero-bias scan in a $2 \times 2 \mu\text{m}$ area after the experiment of panel (a). In the study, a load of 360 nN was applied to the sample, and the estimated contact area was on the order of 80 nm^2 . (c) Current distribution histogram plot obtained from the C-AFM map the yellow square corresponds to C-AFM scan conducted at nullifying voltage, green square corresponds to tribospots outside the square and blue square tribospots close to the edge of the square. On the histograms the counts indicate the number of pixels (sample locations) of a given current, with a total of $\sim 65\text{K}$ pixels making up a C-AFM map. The horizontal scale bars in parts a and b are $1 \mu\text{m}$.

contact electrification process.[38] We propose that the presence of flexovoltage may be responsible for the occurrence of current peaks at the base of the pyramid. This hypothesis is rooted in the understanding that a reduction in the thickness of the space charge layer is recognized to take place at Si N-type concave sites, a phenomenon often associated with flexoelectric effects.[39, 40]

Finally, in order to separate the impact of friction/pressure on surface damage from damage caused by the very high current densities of a DC-TENG, we conducted C-AFM experiments with an external DC bias of such magnitude and direction to nullify the flow of current, while introducing no changes to the normal load and friction of the sliding platinum tip (Figure 4a). Results depicted in Figure 4b,c indicate that the drop in DC-TENG output is not caused by the passage of a tribocurrent. A further note which may

stimulate future investigations is that we very often observed large tribocurrents near the edge of previously oxidized regions (Figure 4b,c). The reason for such (localized) enhancement of DC output is at present unclear.

4. Conclusion

We have quantified the extent of operational damage for DC-TENGs based on sliding Si(211)–organic monolayer–platinum Schottky diodes and attempted to define the relative importance of friction/pressure-induced wear versus oxidative damages to the semiconductor due to the flow of the large current densities ($\sim 2 \times 10^6$ A/m²) reached during the operation of these miniature autonomous power sources. Using conductive atomic force microscopy (C-AFM) experiments and photocurrent decay measurements (PCM) we revealed that oxide growth and loss of TENG performances upon operation are not primarily caused by the passage of current, but rather more strictly linked to pressure and friction-induced surface wear. Results revealed current density drops from $\sim 2 \times 10^6$ A/m² to $\sim 3 \times 10^5$ A/m² representing a current decay of $\sim 83\%$. The carrier lifetime within damaged regions was found to be 147.9 ± 10.7 μ s, compared to 188.1 ± 15.7 μ s outside damaged areas, emphasizing the impact of surface defects on charge recombination. We also bring evidence of a time delay between the friction/pressure event and the manifestation of the surface damage (drop in TENG output). Further, which we believe will stimulate future studies, i) zero-bias DC outputs are significantly higher at the edge of damaged areas, an observation for which we currently lack an explanation, and ii) outputs are generally greater at concave semiconductor locations, which may be the result of a localized thinning of the space charge layer (i.e., enhanced flexoelectric effect).

References

- (1) Xiang, S.; Wang, Y.; Zhang, C.; Zhao, Z.; Wang, B.; Zou, W.; Wu, J. Smart Contact Lenses for the New Era of IoT: Integrated Biosensors, Circuits, and Human–Machine Interface Systems. *Adv. Mater. Technol.* **2023**, *8*,
- (2) Le, X.; Guo, X.; Lee, C. Evolution of Micro-Nano Energy Harvesting Technology—Scavenging Energy from Diverse Sources towards Self-Sustained Micro/Nano Systems. *Nanoenergy Adv.* **2023**, *3*, 101–125
- (3) Mariello, M.; Guido, F.; Mastronardi, V. M.; Todaro, M. T.; Desmaële, D.; De Vittorio, M. Nanogenerators for harvesting mechanical energy conveyed by liquids. *Nano Energy* **2019**, *57*, 141–156
- (4) Zheng, M.; Lin, S.; Xu, L.; Zhu, L.; Wang, Z. L. Scanning Probing of the Tribovoltaic Effect at the Sliding Interface of Two Semiconductors. *Adv. Mater.* **2020**, *32*, e2000928-n/a
- (5) Lin, S.; Lin Wang, Z. The tribovoltaic effect. *Mater. today* **2023**, *62*, 111–128
- (6) Song, Y.; Wang, N.; Wang, Y.; Zhang, R.; Olin, H.; Yang, Y. Direct Current Triboelectric Nanogenerators. *Adv. Energy Mater.* **2020**, *10*,
- (7) Wu, C.; Wang, A. C.; Ding, W.; Guo, H.; Wang, Z. L. Triboelectric Nanogenerator: A Foundation of the Energy for the New Era. *Adv. Energy Mater.* **2019**, *9*,
- (8) Seol, M.-L.; Woo, J.-H.; Jeon, S.-B.; Kim, D.; Park, S.-J.; Hur, J.; Choi, Y.-K. Vertically stacked thin triboelectric nanogenerator for wind energy harvesting. *Nano Energy* **2015**, *14*, 201–208
- (9) Wang, Z. L. Triboelectric nanogenerator (TENG)—sparking an energy and sensor revolution. *Adv. Energy Mater.* **2020**, *10*,
- (10) Liu, D.; Zhou, L.; Wang, Z. L.; Wang, J. Triboelectric nanogenerator: from alternating current to direct current. *Isience* **2021**, *24*,

- (11) You, Z.; Wang, S.; Li, Z.; Zou, Y.; Lu, T.; Wang, F.; Hu, B.; Wang, X.; Li, L.; Fang, W.; Liu, Y. High current output direct-current triboelectric nanogenerator based on organic semiconductor heterojunction. *Nano Energy* **2022**, *91*, 272–273
- (12) Naval, S.; Jain, A.; Mallick, D. Direct current triboelectric nanogenerators: A review. *J. Micromech. Microeng.* **2022**, 274
- (13) Liu, J.; Goswami, A.; Jiang, K.; Khan, F.; Kim, S.; McGee, R.; Li, Z.; Hu, Z.; Lee, J.; Thundat, T. Direct-current triboelectricity generation by a sliding Schottky nanocontact on MoS₂ multilayers. *Nat. Nanotechnol.* **2018**, *13*, 112–116 275–276
- (14) Ferrie, S.; Darwish, N.; Gooding, J. J.; Ciampi, S. Harnessing silicon facet-dependent conductivity to enhance the direct-current produced by a sliding Schottky diode triboelectric nanogenerator. *Nano Energy* **2020**, *78*, 277–278
- (15) Lyu, X.; Ferrie, S.; Pivrikas, A.; MacGregor, M.; Ciampi, S. Sliding Schottky diode triboelectric nanogenerators with current output of 109 A/m² by molecular engineering of Si (211) surfaces. *Nano Energy* **2022**, *102*, 279–280
- (16) Lyu, X.; MacGregor, M.; Liu, J.; Darwish, N.; Ciampi, S. Direct-current output of silicon–organic monolayer–platinum Schottky TENGs: Elusive friction-output relationship. *Nano Energy* **2023**, *114*, 281–282
- (17) Liu, J.; Ciampi, S.; Antony, A., The Origins of Solid-Solid Contact Electrification. In *Handbook of Triboelectric Nanogenerators*, Wang, Z. L.; Yang, Y.; Zhai, J.; Wang, J., Eds. Springer International Publishing: Cham, 2023; pp 1–37. 283–284
- (18) Fabre, B. Functionalization of Oxide-Free Silicon Surfaces with Redox-Active Assemblies. *Chem. Rev.* **2016**, *116*, 4808–4849 285
- (19) Ciampi, S.; Harper, J. B.; Gooding, J. J. Wet chemical routes to the assembly of organic monolayers on silicon surfaces via the formation of Si-C bonds: surface preparation, passivation and functionalization. *Chem. Soc. Rev.* **2010**, *39*, 2158–2183 286–287
- (20) Ferrie, S.; Le Brun, A. P.; Krishnan, G.; Andersson, G. G.; Darwish, N.; Ciampi, S. Sliding silicon-based Schottky diodes: Maximizing triboelectricity with surface chemistry. *Nano Energy* **2022**, *93*, 288–289
- (21) Lyu, X.; Ciampi, S. Improving the performances of direct-current triboelectric nanogenerators with surface chemistry. *COCIS* **2022**, *61*, 290–291
- (22) Fabre, B. Ferrocene-Terminated Monolayers Covalently Bound to Hydrogen-Terminated Silicon Surfaces. Toward the Development of Charge Storage and Communication Devices. *Acc. Chem. Res.* **2010**, *43*, 1509–1518 292–293
- (23) Vogel, Y. B.; Zhang, L.; Darwish, N.; Gonçalves, V. R.; Le Brun, A.; Gooding, J. J.; Molina, A.; Wallace, G. G.; Coote, M. L.; Gonzalez, J.; Ciampi, S. Reproducible flaws unveil electrostatic aspects of semiconductor electrochemistry. *Nat. Commun.* **2017**, *8*, 294–295
- (24) Deng, S.; Xu, R.; Seh, W.; Sun, J.; Cai, W.; Zou, J.; Zhang, Q. Current degradation mechanism of tip contact metal-silicon Schottky nanogenerator. *Nano Energy* **2022**, *94*, 296–297
- (25) Park, S. M.; Wang, B.; Chen, L.-Q.; Noh, T. W.; Yang, S. M.; Lee, D. Flexoelectric control of physical properties by atomic force microscopy. *Appl. Phys. Rev.* **2021**, *8*, 298–299
- (26) Qiao, H.; Zhao, P.; Kwon, O.; Sohn, A.; Zhuo, F.; Lee, D. M.; Sun, C.; Seol, D.; Lee, D.; Kim, S. W. Mixed triboelectric and flexoelectric charge transfer at the nanoscale. *Adv. Sci* **2021**, *8*, 300–301
- (27) Uritsky, V. In *Role of electron/hole processes in the initial stage of silicon anodization*, Materials Science Forum, Trans Tech Publ: 1995; pp 115–118. 302–303
- (28) Hurtado, C.; Lyu, X.; Ferrie, S.; Le Brun, A. P.; MacGregor, M.; Ciampi, S. Organic Monolayers on Si(211) for Triboelectricity Generation: Etching Optimization and Relationship between the Electrochemistry and Current Output. *ACS Appl. Nano Mater.* **2022**, *5*, 14263–14274 304–306
- (29) Peiris, C. R.; Ferrie, S.; Ciampi, S.; Rickard, W. D. A.; Darwish, N. Memristor Arrays Formed by Reversible Formation and Breakdown of Nanoscale Silica Layers on Si-H Surfaces. *ACS Appl. Nano Mater.* **2022**, *5*, 6609–6617 307–308
- (30) Park, J. Y.; Salmeron, M. Fundamental Aspects of Energy Dissipation in Friction. *Chem. Rev.* **2014**, *114*, 677–711 309
- (31) Miller, J. N.; Miller, J. C.; Miller, R. D., *Statistics and chemometrics for analytical chemistry*. Seventh edition ed.; Pearson Education Limited: Harlow, United Kingdom, 2018. 310–311
- (32) Zhang, S.; Ferrie, S.; Lyu, X.; Xia, Y.; Darwish, N.; Wang, Z.; Ciampi, S. Absence of a Relationship between Surface Conductivity and Electrochemical Rates: Redox-Active Monolayers on Si(211), Si(111), and Si(110). *J. Phys. Chem. C* **2021**, *125*, 18197–18203 312–313

- (33) Tan, C. S.; Hsieh, P. L.; Chen, L. J.; Huang, M. H. Silicon Wafers with Facet - Dependent Electrical Conductivity Properties. *Angew. Chem. Int. Ed.* **2017**, *129*, 15541 - 15545 314
315
- (34) Ciampi, S.; Böcking, T.; Kilian, K. A.; James, M.; Harper, J. B.; Gooding, J. J. Functionalization of Acetylene-Terminated Monolayers on Si(100) Surfaces: A Click Chemistry Approach. *Langmuir* **2007**, *23*, 9320–9329 316
317
- (35) Ng, A.; Ciampi, S.; James, M.; Harper, J. B.; Gooding, J. J. Comparing the reactivity of alkynes and alkenes on silicon 100 surfaces. *Langmuir* **2009**, *25*, 13934–13941 318
319
- (36) Zhang, X. Mechanism of pore formation on n - type silicon. *J. Electrochem. Soc.* **1991**, *138*, 320
- (37) Park, J. Y.; Ogletree, D. F.; Thiel, P. A.; Salmeron, M. Electronic Control of Friction in Silicon pn Junctions. *science* **2006**, *313*, 186–186 321
322
- (38) Mizzi, C. A.; Lin, A. Y. W.; Marks, L. D. Does flexoelectricity drive triboelectricity? *Phys. Rev. Lett.* **2019**, *123*, 1 323
- (39) Zhang, X. G.; Collins, S. D.; Smith, R. L. Porous silicon formation and electropolishing of silicon by anodic polarization in HF solution. *Journal of the Electrochemical Society* **1989**, *136*, 1561–1565 324
325
- (40) Olson, K. P.; Mizzi, C. A.; Marks, L. D. Band Bending and Ratcheting Explain Triboelectricity in a Flexoelectric Contact Diode. *Nano Lett.* **2022**, *22*, 3914–3921 326
327

328

Chapter 4. Galinstan liquid metal electrical contacts for monolayer-modified silicon surfaces

Introduction to Chapter 4

Chapter 4 is presented as paper 3 and was conceptualized as part of an attempt to replace the hard metal tip used in AFM nanoscale electrical measurements with a softer metal contact, in this case a liquid metal drop. This chapter therefore follows from the previous chapter (Chapter 3) as it is an attempt to reduce the surface damage with hard contacts and large normal forces. Although the tribocurrent the system generated when replacing the Pt tip with liquid metal (see section 6.1) was minimal, the soft systems still performed extremely well in terms of electrical measurements of silicon-based junctions.

Specifically, in this chapter, a drop of Galinstan, a promising non-toxic alternative to mercury, is proposed as a probe to monitor changes in the rectification ratios of different surface chemistries. It compares the electrical characteristics of **S-1** and **S-2** surfaces exploited in **Chapters 2** and **3** and explores a novel monolayer functionalization via homocoupling reaction. The chapter also explores the effect of surface chemistry over junction leakage to make qualitative predictions on the DC outputs when the electrode works as a TENG.

Importantly, as soon as exposed to air, Galinstan forms a self-limiting oxide layer which alters the drop conductivity and surface tension. Changes in the shape and size of the junction during operation, as well as the lack of unambiguous data on the oxide skin on conductivity, have hindered a broader approach of Galinstan as top contact. The effect of contact size on the quality and reproducibility of current–voltage and capacitance–voltage traces becomes extremely relevant. The Chapter proposes chemical means to increase the liquid metal surface tension to gain finer control over the junction size, shape, and stability (i.e., synthesis of magnetic Galinstan by iron particle addition).

Supporting information for Chapter 4 can be found in *Appendix E*.

Galinstan Liquid Metal Electrical Contacts for Monolayer-Modified Silicon Surfaces

Carlos Hurtado, Tony Andreoli, Anton P. Le Brun, Melanie MacGregor, Nadim Darwish, and Simone Ciampi*



Cite This: *Langmuir* 2024, 40, 201–210



Read Online

ACCESS |



Metrics & More

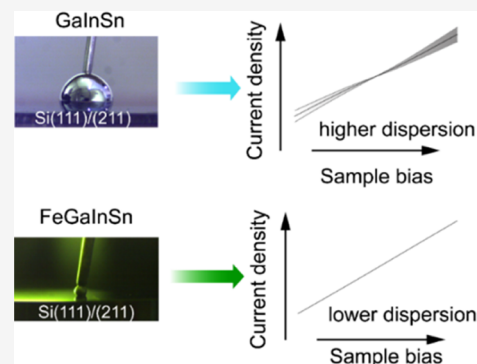


Article Recommendations



Supporting Information

ABSTRACT: Galinstan is the brand name for a low-melting gallium-based alloy, which is a promising nontoxic alternative to mercury, the only elemental metal found in the liquid state at room temperature. Liquid alloys such as Galinstan have found applications as electromechanical actuators, sensors, and soft contacts for molecular electronics. In this work, we validate the scope of Galinstan top contacts to probe the electrical characteristics of Schottky junctions made on Si(111) and Si(211) crystals modified with Si–C-bound organic monolayers. We show that the surface-to-volume ratio of the Galinstan drop used as a macroscopic contact defines the junction stability. Further, we explore chemical strategies to increase Galinstan surface tension to obtain control over the junction area, hence improving the repeatability and reproducibility of current–voltage (I – V) measurements. We explore Galinstan top contacts as a means to monitor changes in rectification ratios caused by surface reactions and use these data, most notably the static junction leakage, toward making qualitative predictions on the DC outputs recorded when these semiconductor systems are incorporated in Schottky-based triboelectric nanogenerators. We found that the introduction of iron particles leads to poor data repeatability for capacitance–voltage (C – V) measurements but has only a small negative impact in a dynamic current measurement (I – V).



INTRODUCTION

To predictably combine the functionality of molecular organic components with the sturdiness of inorganic semiconductors is the aim at the core of most molecular electronic research.^{1,2} Hybrid diodes such as semiconductor–molecules–metal junctions harvest the richness of organic chemistry,^{3,4} and their scope and limitations have been explored extensively.^{5–9} For instance, the attachment of a self-assembled monolayer (SAM) on the surface of a semiconductor, such as oxide-free silicon, can both mitigate surface electronic defects and modify charge transport characteristics.¹⁰ Silicon–SAM–metal rectifying junctions are at the heart of devices whose function ranges from sensing¹¹ to energy storage,¹² and recently found application in the conversion of friction into direct current. These junctions are contributing to the development of triboelectric nanogenerators (TENGs), a class of out-of-equilibrium diodes with scope as autonomous power sources.^{13,14}

Despite such a wide range of applications, the characterization of Si–SAM–metal junctions through seemingly simple current–voltage and capacitance–voltage measurements remains challenging, particularly with regard to methods to realize a nondamaging top metal contact. Evaporated macroscopic metal contacts such as Au and Pd islands can penetrate and damage the organic SAM,^{15,16} while measurements with nanoscopic electrical probes, such as a conductive tip used in

atomic force microscopy (AFM), often carry the additional disadvantage of poorly repeatability and reproducibility.¹⁷ van der Waals metal contacts¹⁸ overcome most of these issues, but their deposition is technically challenging.¹⁹ A drop of mercury has therefore remained, for decades, the preferred metallic contact for the electrical characterization (conductance and capacitance) of hybrid macroscopic junctions.^{20–22} However, regulations and increased awareness toward mercury toxicity have prompted a search for liquid alloy alternatives.^{23,24}

Liquid metals such as gallium–indium eutectic (EGaIn hereafter) and Galinstan (GaInSn hereafter) alloys have a high electrical conductivity of $\sim 3 \times 10^6$ S/m²⁵ and are flexible and self-healing.^{26,27} GaInSn has a lower melting point than EGaIn²⁸ and is used in sensors,²⁹ soft robotics,³⁰ autonomous power sources such as TENGs,³¹ and as electrode material in electrochemistry.³² Since the pioneering 2007 work by Whitesides and co-workers on EGaIn,³³ several other research groups have explored liquid metals for the electrical characterization of molecular systems based on both semiconductors³⁴

Received: August 13, 2023

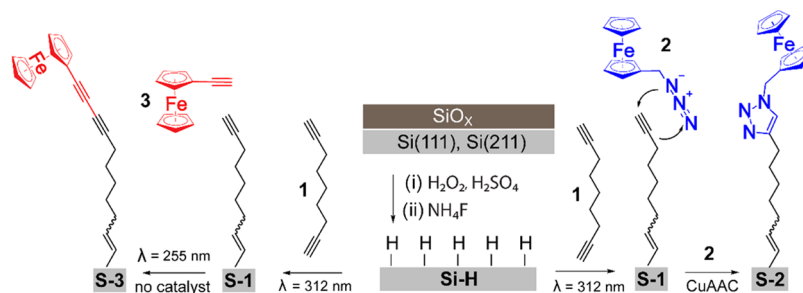
Revised: November 29, 2023

Accepted: November 29, 2023

Published: December 15, 2023



Scheme 1. Schematic Representation of the Strategy Used for the Passivation and Functionalization of the Lowly Doped Si(111) and Si(211) Surfaces



and metals.³⁵ Very recently, Jurchescu and co-workers have used EGaIn to electrically wire silane-based (oxygen-bridged) monolayers on silica, creating highly efficient SAM-based rectifiers.³⁶ Nevertheless, the scope of GaInSn for the electrical characterization of rectifying junctions based on silicon-carbon-bound monolayers is still largely unexplored.

Herein, we investigate the use of GaInSn droplets as soft contacts to probe charge transport characteristics (current-voltage and capacitance-voltage) of Si(111) and Si(211) crystals modified with Si-C-bound SAMs. Si(111) is an established platform for electrochemical and molecular electronics research,^{3,37} while Si(211) remains relatively underexplored despite being readily available. Si(211) has recently attracted interest as an electrode material,^{9,38} as well as a substrate for TENGs that convert friction and pressure into direct current.³⁹ We also explored the scope of GaInSn junctions to detect transport changes upon monolayer derivatization reactions (Scheme 1).

EXPERIMENTAL SECTION

Chemicals and Materials. If not specified otherwise, all chemicals were of analytical grade and used without further purification. Aqueous ammonium fluoride (40% w/w, Honeywell), sulfuric acid (95–97%, Honeywell), and aqueous hydrogen peroxide (30% w/w, Honeywell) were of semiconductor grade. Methanol ($\geq 99.8\%$), ammonium sulfite monohydrate (92%), aqueous hydrochloric acid (HCl, 35–37%), 1,8-nonadiyne (**1**, 98%), and ethynylferrocene (**3**, 97%) were purchased from Sigma-Aldrich. 2-Propanol ($>99.8\%$) was purchased from Ajax Finechem. Redistilled dichloromethane (DCM), Milli-Q water (>18 M Ω cm resistivity), and acetonitrile ($>99.9\%$, Honeywell) were used for substrate-cleaning and surface modification procedures. Phosphorus-doped (N-type, 7–13 Ω cm) prime grade single-side polished Si(111) and Si(211) wafers ($\pm 0.05^\circ$, 500 μ m thick) were purchased from Siltronix, S.A.S (Archamps, France). High-purity glassy carbon planchets (25 mm diameter) were purchased from Ted Pella, Inc. (part n. 16526). Azidomethylferrocene (**2**) was prepared according to literature procedures.⁴⁰ Commercial GaInSn (Ga/In/Sn, 62:22:16 wt %) was purchased from Thermo Fisher Scientific and stored under an inert atmosphere prior to use. Magnetic GaInSn was synthesized following the procedure of Chen and co-workers.⁴¹ In brief, commercial GaInSn (2 g) was gently mixed with 0.2 g of iron powder (diameter of ~ 0.5 μ m, 99.98%, Alfa Aesar) inside a Pyrex glass bottle (150 mL). The magnetic GaInSn sample was then washed five times with 20 mL of aqueous 0.5 M HCl and then stored in the dark under HCl (0.5 M) prior to use.

Surface Modification Procedures. Silicon wafers were cut into samples of either 10 \times 10 mm (AFM, current-capacitance, current-voltage, and XPS measurements) or 15 \times 15 mm (electrochemical measurements) and rinsed sequentially with DCM (3 \times 50 mL), 2-propanol (3 \times 50 mL), and water (3 \times 50 mL) before being washed for 30 min in a heated (100 $^\circ$ C) 3:1 mixture (v/v) of concentrated

sulfuric acid (98%) and hydrogen peroxide (30%) [*caution: Piranha solution reacts violently with any organic material*]. After the Piranha wash, the samples were rinsed with water (3 \times 50 mL) and then etched (polished side facing upward) for 13 min in a 40% aqueous solution of ammonium fluoride, which had previously been deoxygenated by means of 15 min argon bubbling ($>99.99\%$, Coregas). Ammonium sulfite (~ 50 mg) was added to the etching bath (~ 50 mL) as an oxygen scavenger. Si(111) samples were etched under ambient light (fluorescent tubes, ~ 4.1 mW cm $^{-2}$), while Si(211) samples were etched in the dark. Both Si(111) and Si(211) were etched under an inert atmosphere (N $_2$).¹⁴ The hydrogen-terminated samples (Si-H) were rinsed first with water (1 \times 50 mL) and then with DCM (2 \times 50 mL) and finally blow-dried under a stream of nitrogen gas ($>99.99\%$, Coregas).

The UV-assisted hydrosilylation of 1,8-nonadiyne (**1**) on the Si-H surface was carried out following previous procedures.⁴² In brief, a small sample of **1** (~ 0.1 mL) was dropped over the Si-H sample (polished side). The liquid-covered sample was then transferred to a nitrogen-filled reaction chamber and placed at a distance of ~ 20 cm from a 312 nm light source (Vilber, VL-215.M, nominal power output of 30 W). To ensure equal distribution and limit the evaporation of **1** during the hydrosilylation, the liquid sample was contacted with a 1 mm thick quartz plate (part no. 01031-AB, SPI Supplies). After 2 h, the monolayer-modified surface (**S-1**) was removed from the UV chamber and rinsed with DCM (3 \times 50 mL). **S-1** samples were stored for 24 h under DCM at +4 $^\circ$ C prior to analysis or further modification.

For the preparation of **S-2** surfaces, azidomethylferrocene (**2**) was covalently attached to **S-1** samples through a copper(I)-catalyzed azide-alkyne cycloaddition (CuAAC) reaction following previous procedures.⁴⁰ In brief, **S-1** samples were washed with 2-propanol (3 \times 50 mL) and then loaded into a glass reaction tube containing 4 mL of a 4 mM solution of **2** in 2-propanol. To the azide solution were then added 1 mL of aqueous copper sulfate solution (20 mol % relative to **2**) and 1 mL of aqueous sodium ascorbate (100 mol % relative to **2**). The CuAAC reaction was carried out in the dark at room temperature (24 ± 2 $^\circ$ C) and with gentle agitation. After 30 min, the reaction was stopped by rinsing the silicon samples sequentially with 2-propanol (3 \times 50 mL), water (3 \times 50 mL), 0.5 M HCl (3 \times 50 mL), water (3 \times 50 mL), 2-propanol (3 \times 50 mL), and DCM (3 \times 50 mL). Finally, the samples were dried under a stream of nitrogen gas before being analyzed. To prepare **S-3** surfaces, an alkyne homocoupling reaction between **S-1** and ethynylferrocene (**3**) was performed by adapting reported procedures for homocoupling reactions.⁴³ In brief, **S-1** surfaces were rinsed with 2-propanol (3 \times 10 mL), covered with ~ 0.2 mL of a 1.0 mM solution of **3** in acetonitrile, and placed with the sample polished side facing upward and toward a UV LED (~ 255 nm, UV-C). The sample-LED distance was ~ 10 cm. After 5 min of reaction time, the samples were removed from the LED light and rinsed with 2-propanol (3 \times 50 mL) and water (3 \times 50 mL).

Electrochemical Measurements. All electrochemical measurements were carried out in air at room temperature (24 ± 2 $^\circ$ C) in aqueous 1.0 M perchloric acid using a CH Instruments Inc. potentiostat (model CHI650D). Ohmic contact between the back of the sample and a copper plate was ensured by first gently rubbing

the back of the silicon sample with silicon carbide abrasive paper (800 grit) and then covering the clean abraded silicon surface with a small amount of gallium–indium eutectic. Electrochemical experiments were conducted using a single-compartment and three-electrode custom polytetrafluoroethylene cell (Figure S1 in the Supporting Information). S-2 and S-3 monolayer-modified surfaces served as the working electrode, a platinum coil as the counter electrode, and an aqueous Ag/AgCl (3.0 M aqueous NaCl) electrode as a potential reference. The geometric area of the working electrode was defined by a rectangular Kalrez gasket to 0.28 cm². During the cyclic voltammetry experiments, the surface of the silicon working electrode was illuminated through the electrolyte (the thickness of the electrolyte layer was ~1.5 cm) with a red LED (660 nm, nominal power output of 940 mW, Thorlabs, part n. M660L4) fitted with a collimating lens system (SM1P25-A, Thorlabs). The overall distance between the collimator and the electrode was ~10 cm. The electrode illumination intensity was ~0.12 mW cm⁻² as measured with a meter from Amprobe (model IC-LM-200, 1 lx = 0.0001708 mW cm⁻²).

The surface coverage of the ferrocene molecules (2 and 3) on S-2 and S-3 samples was extracted from the faradaic charge measured from the integration of cyclic voltammetry (CV) traces. Ferrocene coverages (mol cm⁻²) are the average of the cathodic and anodic charges (background-subtracted) from at least three independent samples and averaged over at least five different voltage sweep rates per sample.

The electron transfer rate constant of the S-2 and S-3 samples ($k_{\text{et}} = 1/2R_{\text{et}}C_{\text{ads}}$) was estimated from electrochemical impedance spectroscopy (EIS) experiments (data collected between 10⁵ and 10⁰ Hz) using the formalism developed by Laviron.⁴⁴ Capacitance and resistance values were obtained by refining experimental EIS data to fit the equivalent circuit shown in Section S1 (Supporting Information) through ZView software (Version 4.0c, Scribner Associates). The EIS DC offset (E_{dc}) was set equal to the midpoint between the potentials of the anodic and cathodic CV current maxima ($E_{1/2}$), and the AC amplitude was set to 15 mV.

Electrical Characterization. Current density–voltage and capacitance–voltage (J – V , C – V) measurements were performed inside a grounded and light-proof Faraday cage using a source measure unit (SMU, B2902A, Keysight) for J – V measurements and a precision LCR meter (E4980A, Keysight) for C – V measurements (Figure S2 in the Supporting Information). C – V characteristics were measured at an AC frequency of 1 kHz and with an AC amplitude of 20 mV. The E4980A does not have the DC bias enhancement option, so the DC offset was introduced by a potential ramp supplied by the SMU. The SMU was interfaced to the LCR via an external bias adapter (16065C, Keysight), which was in turn fitted with and 4-wire Kelvin clip (BK precision, TLKB1 model). LCR and SMU were synchronized by means of a square waveform trigger supplied by a function generator (DG-1022, RIGOL). GaInSn top contacts were dispensed on silicon samples from a threaded plunger syringe (Gilmont, model GS-1200A, 2 mL capacity, 0.002 mL graduation intervals, 24 G). A steel needle blunt tip (~0.49 mm radius) in contact with the GaInSn drop was used to establish electrical contact. The positioning of the needle contacting the GaInSn was controlled by a three-axis micromanipulator (three DTS25 linear translation stages, Thorlabs). The junction voltage was ramped cyclically between –2.0 and 2.0 V in steps of 55 mV for J – V measurements and from 1.0 to 0.0 V in steps of 10 mV for C – V measurements (the duration of each step is 370 ms). The bias is applied from the sample (glassy carbon or silicon) to the GaInSn top contact, and the terminal was configured to be grounded internally (sensing type set to four wires). A minimum of 10 samples were analyzed for each surface chemistry type, and the uncertainty of each chemistry was reported as the 95% confidence level of the mean.⁴⁵ The contact area of the GaInSn–silicon junction was estimated from an optical image acquired with a CMOS camera (model DCC1240C from Thorlabs) fitted with a machine vision lens (Model MVL133A and 1.5× lens attachment, Thorlabs) and analyzed using the Fiji package.⁴⁶ The size of the liquid metal drop was estimated by using the diameter of the needle contact

as an internal reference. All experiments were carried out under dark conditions.

Surface Tension Measurements. Surface tension measurements of the GaInSn drops were conducted in air, at room temperature and using the pendant drop method.⁴⁷ The analysis of the shape of an asymmetric drop was performed with a right-angle clamp (RA/90 model, Thorlabs) and a threaded plunger syringe (GS-1200 model, Gilmont instruments) coupled with a point H style needle (1.2 mm × 28 mm from Terumo) used to generate the drops. Surface tension data were processed with ImageJ software. The reported surface tension values are the average of three measurements on five drops, and the uncertainty is quoted as the 95% confidence limit of the mean.

Atomic Force Microscopy. Atomic force microscopy (AFM) measurements for surface topography and current maps (C-AFM) were carried out on a Park NX10 microscope (Park Systems Corp., Korea) using solid platinum tips (25Pt300B, Rocky Mountain Nanotechnology). The AFM tip resonance frequency was 14 kHz, the tip radius was ~10 nm, and the spring constant was 18 N m⁻¹. Reverse currents exhibited a positive polarity, indicating the movement of electrons from the Pt tip toward the silicon sample. Ohmic contact between the Si sample and the AFM stage was ensured by gently scratching the Si nonpolished side with sandpaper and applying a small amount of EGaIn. Data were analyzed with XEI processing software (Park Systems). The scale bars for vertical height and current (color-coded) employed in the AFM measurements did not span the complete spectrum. The selection of color range was done arbitrarily in order to optimize the visualization of topographic and current features. The size of the scan was set to 5 μm × 5 μm, the resolution to 256 points/line, the scan rate to 1.0 Hz, and the applied normal force to 360 nN.

X-ray Photoelectron Spectroscopy (XPS). XPS measurements were performed on an AXIS Ultra DLD spectrometer (Kratos Analytical Inc., Manchester, UK). The spectrometer was fitted with a monochromatic Al K α radiation source (1486.6 eV) and a hemispherical analyzer (165 mm radius) and operated in Fixed Analyzer Transmission (FAT) mode at ~2 × 10⁻⁸ Torr. Emitted photoelectrons (takeoff angle 90°) were collected from a 300 μm × 700 μm analysis area, setting the pass energy to 20 eV and the step size to 0.05 eV for Si 2p (96–108 eV) and 0.1 eV for C 1s (278–295 eV), accumulating 10 scans). Survey spectra were obtained over the 0–1100 eV range in 0.5 eV steps, accumulating 5 scans and with a pass energy of 160 eV. CasaXPS software was used to process XPS data. The background subtraction routine was U 2 Tougaard, and the spectral lines were a combination of 95% Gaussian and 5% Lorentzian line shapes.⁴⁸ All of the reported energies are binding energies (eV), which were corrected by applying a rigid shift to bring the Si 2p_{3/2} emission to 99.5 eV.

X-ray Reflectometry (XRR). X-ray reflectometry data were acquired on a Rigaku Smart Lab instrument equipped with a thin film measuring setup. The source was a rotating anode with a wavelength (λ) of 1.54 Å (Cu K α). X-ray collimation was achieved by cross-beam optics with a 0.5° Soller collimator pre- and postsample and a Hypix-3000 2D detector. Specular measurements were taken at angle of incidence (θ) values ranging from 0.05 to 5.00° in steps of 0.01° (total measuring time of ~20 min). XRR data were reduced so that the angle of incidence was converted to the scattering vector, Q , according to (1)

$$Q = \frac{4\pi \sin \theta}{\lambda} \quad (1)$$

and reflectivity was scaled so that the critical edge was equal to a reflectivity of 1. Data were fitted in the *reflx* software package,⁴⁹ where the monolayer was defined as a single slab where fit parameters for the monolayer were thickness (τ), scattering length density (SLD), and roughness (σ). The SLD for X-rays is determined by multiplying the electron density of the material (e⁻/Å³) by a constant factor of 2.82 × 10⁻⁵ Å.⁴⁸ The number of molecules per unit area is determined by multiplying the volume fraction (ratio of the

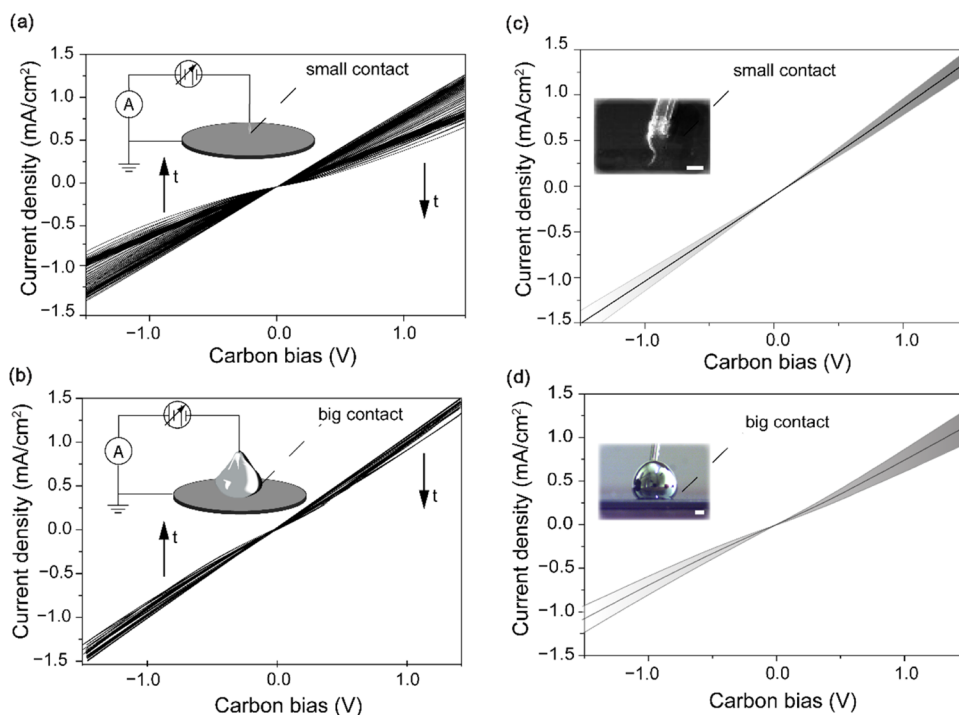


Figure 1. Current density–voltage (J – V) curves recorded on glassy carbon with a GaInSn top contact of variable size. (a, b) Evolution of the J – V traces during 50 continuous voltage cycles (-1.5 to 1.5 V) in ambient air over a period of ~ 1.5 h (sweep rate of 55 mV/s) for (a) small contacts (1.25×10^{-3} cm 2) and (b) big contacts (0.03 cm 2). The insets are schematic representations of the measurement circuit. (c, d) J – V curves (10 cycles) recorded at 10 separate locations for (c) small contacts and (d) big contacts, where the black central line is the calculated mean, and the shaded areas represent the standard deviation. The insets show optical images of the junction. The scale bars in the insets represent 0.5 mm.

determined SLD to the theoretical SLD), the thickness, and Avogadro's number and dividing by the molecular volume.

RESULTS AND DISCUSSION

Although the electrical conductivity of GaInSn is 3 times that of mercury,²⁸ this alloy rapidly develops an oxidized skin (0.5 – 2.5 nm thick) when exposed to air.⁵⁰ If GaInSn is used to establish an electrical contact, this oxidation reaction will most likely affect the junction conductivity.^{51,52} To assess the impact of Ga_xO_y formation on the repeatability of electrical measurements done in ambient air, we first conducted controls with GaInSn serving as the top contact on an unmodified glassy carbon surface rather than on silicon. The chemical stability of glassy carbon is greater than that of silicon,⁵³ thereby allowing to distinguish electrical changes due to oxidation of the liquid metal from changes due to oxidation of the semiconductor. To assess the stability and repeatability of the current density–voltage (J – V) traces of the GaInSn–glassy carbon junctions, a small drop of GaInSn was deposited on the electrode through a setup consisting of a stainless steel needle mounted on a three-axis positioning stage (Figure S3 in the Supporting Information). The tip of the needle was immersed in a large GaInSn drop that had been previously dispensed on a clean PTFE surface by using a threaded plunger syringe, and the GaInSn-coated needle was then brought into contact with the glassy carbon surface (insets in Figure 1a,c). J – V curves acquired with freshly dispensed GaInSn contacts (junctions ~ 0.02 cm in radius) are repeatable, but for each data set, there is a progressive current drop (from ~ 0.8 to ~ 0.4 mA/cm 2 , measured at a bias of 1.0 V) during 50 consecutive cycles of bias ramping (Figure 1a). The $\sim 100\%$ increase in junction resistance is unlikely to be caused by a change in junction area

(Figure 1c),⁵⁴ but more likely a consequence of an oxide layer (Ga_xO_y) formed upon prolonged cycling.^{55,56} If the increase in junction resistance is a consequence of oxide skin formation from the periphery of the contact and moving inward (i.e., from the substrate–GaInSn–air contact toward the bulk of the liquid metal), then such an increase would be relatively less pronounced for larger junctions, as it is reasonable to assume the oxide growth to be self-limiting. To clarify this point, we tested junctions of larger size, ranging from 0.1 to 0.2 cm in radius. As shown in Figure 1b, larger junctions are relatively more stable, and after 50 consecutive voltage cycles, the resistance only increased by $\sim 30\%$. However, although for large GaInSn drops (millimeter scale), stability is no longer an issue, a new problem emerges; that is, the contact does not have a well-defined circular shape, rendering uncertain the measurement of the GaInSn–sample contact area. This is reflected in a lower reproducibility of current density measurements (Figure 1d). As shown in Figure 1d, the current density standard deviation is higher for the larger junctions rather than for the smaller junctions. We attribute this to errors made in estimating the contact area, which becomes a significant issue in terms of reporting charge transport characteristics.⁵⁷ Issues in controlling and reproducing the shape and size of large GaInSn drops are probably rooted in the decrease of the GaInSn surface tension upon its oxidation,^{58,59} a problem which affects mainly larger droplets (optical image in Figure 1d).

In order to enhance the reproducibility of the J – V traces, we therefore attempted to increase the surface tension of the metal droplet to gain a better control on its shape and size. To achieve this, we synthesized magnetic GaInSn (FeGaInSn) through a method developed by Chen and co-workers.⁴¹ The

method is illustrated schematically in Figures 2a and S4 (Supporting Information). The procedure was successful in

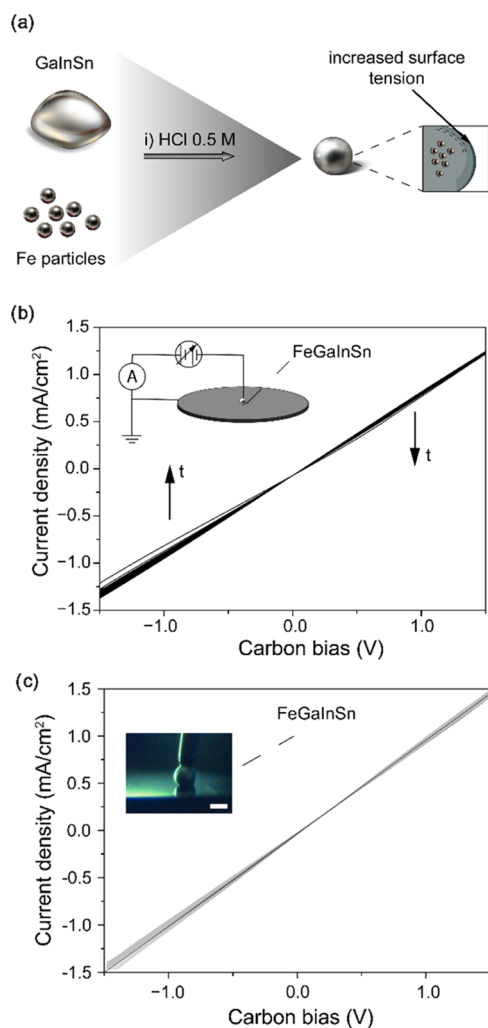


Figure 2. (a) Schematics of the procedure used to synthesize magnetic GaInSn (FeGaInSn). (b) J - V curves (50 cycles, sweep rate of 55 mV/s) for glassy carbon-FeGaInSn junctions recorded over a period of ~ 1.5 h. (c) Mean (solid black trace) and standard deviation (shaded gray area) for 10 independent J - V curves. The insets in (b,c) are the circuit used for the measurement and an optical image of the junction, respectively. The scale bar for the inset in (c) is 0.5 mm. The junction is ~ 0.02 cm in radius.

increasing the surface tension of the liquid metal from 0.47 ± 0.03 N/m for GaInSn to 0.56 ± 0.02 N/m for FeGaInSn (Figure S5 and Table S1 in the Supporting Information). The increase in surface tension improved the spherical symmetry of the droplet. The droplet radius ranged from 0.01 to 0.02 cm. The stability during potential cycling of the FeGaInSn contacts was satisfactory, as also observed above for large GaInSn contacts, but with FeGaInSn, there is the additional advantage of increased reproducibility of the current traces (Figure 2b).

We then moved to prepare a series of covalently bound SAMs on silicon, with the overall aim of ascertaining whether or not FeGaInSn contact may replace Hg to test for the transport characteristics of Si-C-bound SAMs. Bare silicon samples were first etched to generate a hydrogen-terminated surface (Si-H, Scheme 1), which is reactive toward unsaturated organic molecules.^{37,60} A symmetrical α,ω -

dialkyne molecule (1,8-nonadiyne, **1**) was then grafted on Si-H via a UV-assisted (312 nm) hydrosilylation reaction to yield **S-1** surfaces.⁶¹ Further derivatization of the acetylene-terminated **S-1** surface with an azide-tagged ferrocene molecule (**2**) through a copper-catalyzed cycloaddition reaction led to a redox-active film (**S-2** surfaces),^{62,63} and the presence of the metallocene can also potentially augment the rectification ratio of the monolayer system.⁶⁴ Since copper contaminations have been linked with electronic defects that affect charge transport across SAMs,^{13,65} we also explored alkyne-alkyne homocoupling reactions as a catalyst-free route toward tethered ferrocenes. Sambhi and co-workers have recently developed a mechanism for the metal-free photochemical coupling of terminal alkynes on solid samples,⁴³ and as depicted in Scheme 1, we adapted this reaction to generate **S-3** surfaces through the UV-assisted coupling of alkyne **3** with **S-1** surfaces. Before performing any electrical characterization of these monolayer systems (**S-1**, **S-2**, and **S3**) we conducted a surface analysis (topography, ferrocene surface coverage, and surface chemical composition). AFM-derived surface root-mean-square (rms) roughness values for **S-1** samples made on Si(111) and Si(211) crystals were 0.1 and 1.2 nm, respectively (Figure S6 in the Supporting Information), values that are in line with previous reports.¹⁴ As shown in Figure S7 (Supporting Information), roughness values for **S-2** samples were 0.2 and 1.4 nm (Si(111) and Si(211), respectively), whereas the roughness of **S-3** samples was as high as 1.6 and 3.4 nm (Si(111) and Si(211), respectively).

To explain the increase in surface roughness observed after the homocoupling ferrocene attachment, we first measured electrochemically the surface coverage of the metallocene (Figure 3). As the time scale of the experiment decreases (faster sweeps), peak broadening is observed, affecting the linearity of peak current versus scan rate (Figures S8 and S9 in the Supporting Information). As studied in detail recently by Gonzalez,⁶⁶ this can be explained by both Laviron and Marcus-Hush-Chidsey theories. We also checked the stability of the new **S-3** surface, which indirectly confirms a diffusion-free (surface-confined) redox process (Figure S10 in the Supporting Information).⁶⁷

The ferrocene surface coverages of **S-2** samples made on Si(111) and Si(211) (Figure 3a,b) were $(2.2 \pm 0.6) \times 10^{-10}$ and $(2.4 \pm 0.7) \times 10^{-10}$ mol cm⁻², respectively. These coverages are below the theoretical maximum coverage expected for a close-packed ferrocene monolayer (4.5×10^{-10} mol cm⁻²)^{68,69} and comparable to previously reported data.¹⁴ As discussed above, the surface roughness does not increase significantly upon moving from the base layer (**S-1**) to the “clicked” ferrocene samples (**S-2**). On the contrary, **S-3** surfaces obtained through the alkyne-alkyne photocoupling reaction (Figure 3c,d) had coverages well above the theoretical limit, $5.1 \pm 0.2 \times 10^{-10}$ mol cm⁻² for Si(111) and $7.0 \pm 1.1 \times 10^{-10}$ mol cm⁻² for Si(211), as well as large full width at half-maximum (fwhm) values (~ 140 and ~ 180 mV for Si(111) and Si(211), respectively).

Values of fwhm were close-to-ideal for **S-2** surfaces (~ 100 and ~ 90 mV, for Si(111) and Si(211), respectively) but as mentioned above larger for **S-3** samples, indicating a negative value of the Frumkin G parameter and hence predominant repulsive forces in the **S-3** adsorbate.^{70,71} We are at present unsure as to the exact relationship between the large **S-3** surface roughness (AFM-derived) and ferrocene surface coverages above the monolayer limit, but one explanation

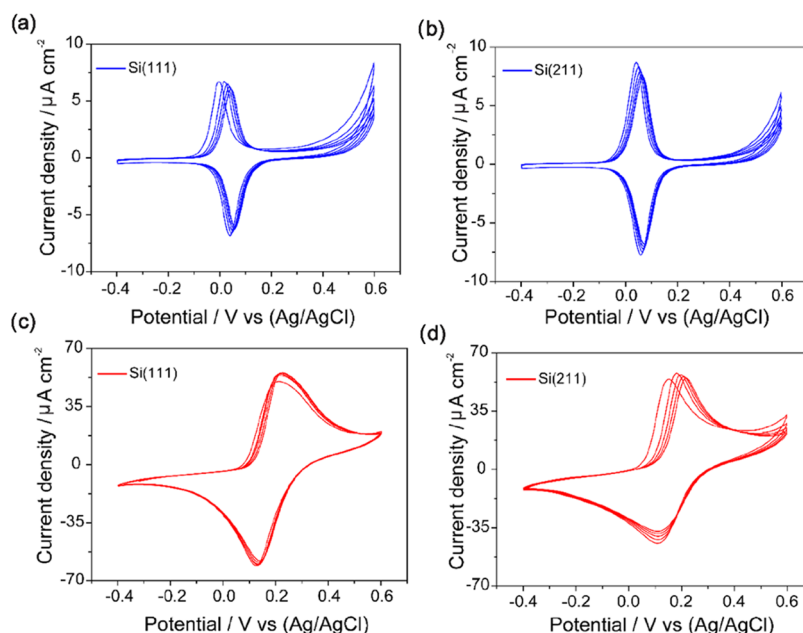


Figure 3. Representative cyclic voltammograms (CVs) for S-2 (a, b) and S-3 (c, d) samples prepared on Si(111) and Si(211) photoanodes. The electrode was illuminated at a light intensity of 0.12 mW cm^{-2} . The voltage scan rate was 50 mV/s .

can be that exposure to UV light is triggering side reactions aside from the intended homocoupling path depicted in Scheme 1.

As can be seen in the CVs of S-2 samples, at low voltage sweep rates, the anodic wave peaks at voltages more negative than those of the cathodic peak. This so-called “peak inversion” is not an artifact but rather the manifestation of electrostatic interactions between the positively charged ferricenium units and the semiconductor’s space-charge layer (SCL). It is worth emphasizing that at sufficiently fast voltage sweep rates (Figure S11 in the Supporting Information), the inversion is masked by kinetic factors.^{42,72}

X-ray photoelectron spectroscopy (XPS) and X-ray reflectometry (XRR, Figure S12 in the Supporting Information) helped to reveal other contributing factors to the large roughness of the S-3 samples. XPS analysis of S-3 reveals oxide growth, which we tentatively attributed to the exposure to UV light during sample derivatization (Figure S12a,b, Supporting Information). Elemental silicon peak signals were fitted at 99.5 eV for Si $2p_{3/2}$ and at 100.1 eV for Si $2p_{1/2}$.⁷³ There was a high binding energy shoulder, at 0.4 eV from Si $2p_{1/2}$, assigned to Si–H species.⁷³ In the $101.1\text{--}104.0 \text{ eV}$ region, we merged photoelectron contributions from Si⁽²⁾, Si⁽³⁾, and Si⁽⁴⁾ oxides into a single band. Emissions at 708.5 and 721.5 eV (Figure S13 in the Supporting Information) confirmed the presence of ferrocene units in the S-3 film. The presence of oxide correlates with a notable reduction of the electron transfer kinetics as inferred from the electron transfer rate constant (k_{et}) measured by EIS (Figure S14 in the Supporting Information). XRR-derived roughness revealed values in line with those reported on AFM (2.7 and 3.0 nm for Si(111) and Si(211), respectively). Data refinement returned a monolayer thickness value of $\sim 12 \text{ \AA}$, which is not drastically different from literature values for ferrocene monolayers of similar carbon length.⁷⁴ Electron density values (ρ_e) of the S-3 organic layer were 0.59 and $0.54 \text{ e}^-/\text{\AA}^3$ for Si(111) and Si(211), respectively (Figure S12c,d). Literature values of ρ_e in the order of $0.52\text{--}0.57 \text{ e}^-/\text{\AA}^3$ have been reported for highly

packed monolayers of length similar to that of S-3 surfaces.^{75,76} The volume fraction inferred from ρ_e indicates coverages in the order of $3.8 \times 10^{-10} \text{ mol cm}^{-2}$ for Si(111) and $4.4 \times 10^{-10} \text{ mol cm}^{-2}$, which are not drastically different from the electrochemical estimate.

We next evaluated the potential of the improved FeGaInSn method (vide supra) by testing the tunneling dynamics of S-1, S-2, and S-3 surfaces (Figure 4). We started by comparing the current density characteristics of Si(111) S-1 surfaces (gray trace) against freshly etched silicon surfaces (Si–H). As shown in Figure 4a, satisfactory rectification is observed for FeGaInSn junctions made on S-1 surfaces. The RR estimated at $\pm 0.5 \text{ V}$ was ~ 24 for S-1 samples but only ~ 1 for Si–H. We are at present unsure of the underlying cause of the lack of rectification by Si–H-based junctions, but similar data have been reported,¹⁰ and a plausible cause is the lack of chemical passivation; hence, the likelihood of a significant level of band gap defects was introduced during the handling of the samples under ambient air. Figure 4a,b presents $J\text{--}V$ traces for S-1, S-2, and S-3 samples made on Si(111) and Si(211) surfaces, respectively. We found that the ferrocene-terminated surfaces (S-2 and S-3) had a larger RR (95 and 130 for S-2 surfaces prepared on Si(111) and Si(211), respectively, and 53 and 70 for S-3 samples prepared on Si(111) and Si(211)), respectively, compared to those of S-1 surfaces (RR values of 24 and 28 for Si(111) and Si(211) samples, respectively). In addition, we observed that S-3 samples made on Si(111) substrates, compared to analogous systems made on Si(211), generally returned a higher current density, particularly under a reverse bias. This observation raises the question as to whether or not static Schottky junctions made with a soft contact can be used to predict the output of out-of-equilibrium (sliding) junctions, specifically as to whether or not static junctions characterized by a large leakage current will be top performers when part of a TENG, noting that tribocurrent outputs (i.e., the zero-bias current output of a sliding Schottky diode under large normal pressure) generally take the sign of a reverse-bias current. It has been previously shown that Schottky junctions

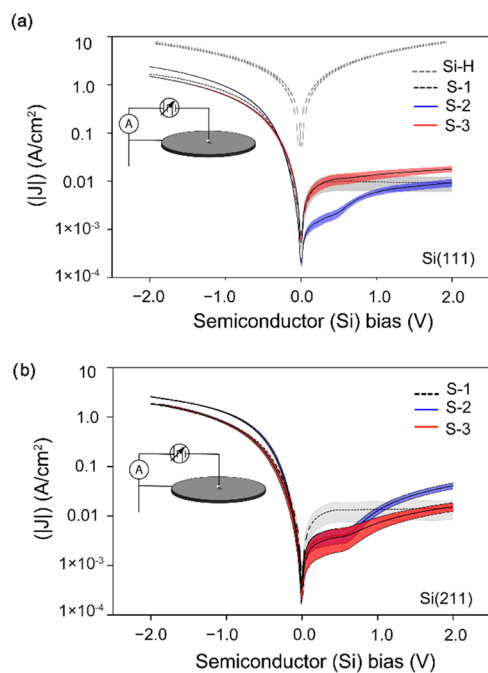


Figure 4. (a) Current–voltage ($\log(|J|)$ – V) curves acquired on moderately doped Si(111) Si–H (dashed gray line), S-1 (dashed black trace), S-2 (blue trace), and S-3 (red trace) samples using a FeGaInSn top contact. (b) $\log(|J|)$ – V data (FeGaInSn top contact) for S-1 (dashed black trace), S-2 (blue trace), and S-3 (red trace) samples made on Si(211). The solid or dashed lines in the plots are the mean current of 10 different curves (recorded on 10 S-1, S-2, or S-3 samples), while the shadowed areas indicate the standard deviation of the mean. The voltage sweep rate was 55 mV/s, and the junctions were ~ 0.02 cm in radius.

(platinum–monolayer–silicon) that are under large normal and lateral forces, that is, operating as sliding Schottky TENGs, output large current densities that bear the sign of a leakage current, even under no external bias.^{13,14,77}

We therefore assessed the TENG performances of S-3 systems, since for this surface chemistry, we observed the largest difference in leakage current between Si(111) and Si(211) samples under moderate reverse bias (~ 0.3 V). This bias is of similar magnitude (but opposite polarity) to the voltage generally required to nullify the TENG output.⁷⁸ As shown in Figure S15 (Supporting Information), zero external bias C-AFM maps recorded on S-3 samples returned current outputs as high as ~ 6 and ~ 10 nA, with the 99th percentile of the DC output being 1.3 and 9.6 nA for Si(111) and Si(211) samples, respectively. We suggest that the generation of tribocurrent in a centrosymmetric material such as silicon possibly involves mechanical aspects such as material polarization due to a large strain gradient⁷⁹ rather than just the generation of electron/hole pairs due to friction.⁸⁰ The possibility of predicting TENG outputs from the leakage of static FeGaInSn junctions therefore appears, at least for our systems, not a viable approach.

Finally, when performing capacitance–voltage (C – V) experiments, for instance to extract values of flat-band potential, we found that FeGaInSn-based junctions did not yield reproducible and physically meaningful results (Figure S16 in the Supporting Information). Changes to the number of surface states such as upon variations in iron oxide thickness are known to impact Mott–Schottky plots.^{81,82} C – V data

acquired with large GaInSn junctions (Mott–Schottky plots in Figure 5) were generally of satisfactory quality. The

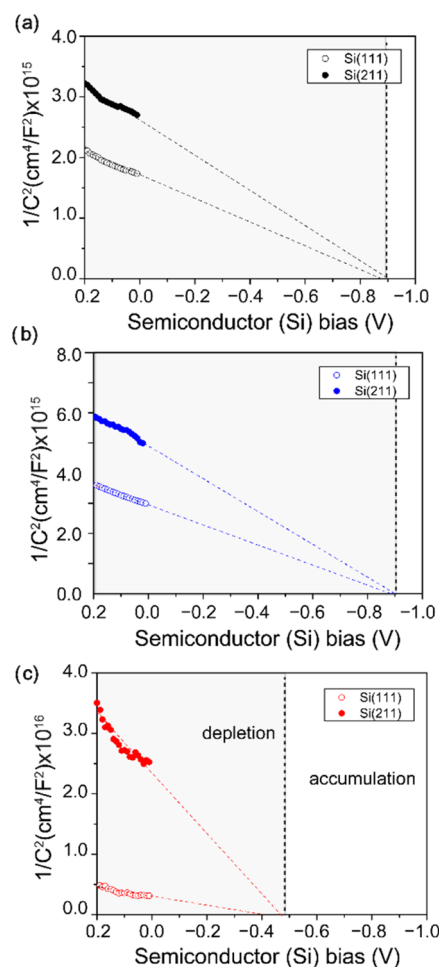


Figure 5. Mott–Schottky plots of capacitance–voltage data acquired on Si(111)- and Si(211)-based GaInSn junctions at an AC frequency of 1 kHz. The surface chemistry is S-1 (a), S-2 (b), and S-3 (c). Capacitance data are plotted as $1/C^2$ against the semiconductor bias.

experimentally determined flat-band potential (extrapolation of the semiconductor bias for which $(1/C^2) = 0$) was ~ -0.89 V for both S-1 and S-2 surfaces (Figure 5a,b). Interestingly, the flat band shifted at less negative biases (~ -0.55 V) for S-3 surfaces (Figure 5c). XPS data (vide supra) suggest non-negligible substrate oxidation, but while the positive shift of the flat band (i.e., less negative biases required to reach accumulation) would suggest the presence of positively charged surface states, it is hard to reconcile this scenario with the very low pK_a of silica (~ 2).⁸³ Shifts of the flat band with the level of substrate oxidation are however very complex, and as demonstrated before, substrate oxidation can shift the flat band in either direction.⁸⁴

CONCLUSIONS

In this work, we have explored the scope of GaInSn as a nontoxic alternative to mercury to make soft electrical contacts to monolayer systems grafted on Si(111) and Si(211). The growth of insulating oxide skins causes poor electrical stability in small junctions. Junctions made with relatively large GaInSn drops have stable current–voltage traces but poor data reproducibility, mainly due to irreproducible/hard-to-control

spreading of the liquid alloy on the substrate being contacted. This issue can be addressed by increasing the top contact surface tension through the addition of iron powder to GaInSn. The use of magnetic FeGaInSn is an effective strategy to precisely control junction area, and it addresses most of the reproducibility issues. FeGaInSn junctions were successfully employed to characterize charge transport characteristics (rectification ratios) of chemically modified Si–C-bound monolayers, including novel alkyne–alkyne homocoupling reactions. We attempted, unsuccessfully, to use data obtained in static FeGaInSn-based junctions to make predictions on the tribocurrents (DC outputs under zero external bias) of sliding Schottky diodes (Pt–monolayers–Si TENGs). Finally, we found that iron particles present in the magnetic GaInSn led to poor C–V data repeatability. This is not the case for I–V measurements and points to the superior ability of impedance measurements in highlighting surface defects and changes to surface states. Overall, this research expands our understanding of the GaInSn scope and limitations in silicon-based molecular electronic research.

■ ASSOCIATED CONTENT

SI Supporting Information

The Supporting Information is available free of charge at <https://pubs.acs.org/doi/10.1021/acs.langmuir.3c02340>.

Additional experimental procedures and experimental setups; surface tension data; additional XPS and XRR data; additional electrochemical data; AFM topography and current maps; capacitance–voltage data (PDF)

■ AUTHOR INFORMATION

Corresponding Author

Simone Ciampi – School of Molecular and Life Sciences, Curtin University, Bentley, Western Australia 6102, Australia; orcid.org/0000-0002-8272-8454; Email: simone.ciampi@curtin.edu.au

Authors

Carlos Hurtado – School of Molecular and Life Sciences, Curtin University, Bentley, Western Australia 6102, Australia
Tony Andreoli – School of Molecular and Life Sciences, Curtin University, Bentley, Western Australia 6102, Australia
Anton P. Le Brun – Australian Centre for Neutron Scattering, Australian Nuclear Science and Technology Organization, Lucas Heights, New South Wales 2234, Australia; orcid.org/0000-0003-2431-6985
Melanie MacGregor – Flinders Institute for Nanoscale Science and Technology, Flinders University, Bedford Park, South Australia 5042, Australia; orcid.org/0000-0002-8671-181X
Nadim Darwish – School of Molecular and Life Sciences, Curtin University, Bentley, Western Australia 6102, Australia; orcid.org/0000-0002-6565-1723

Complete contact information is available at: <https://pubs.acs.org/doi/10.1021/acs.langmuir.3c02340>

Notes

The authors declare no competing financial interest.

■ ACKNOWLEDGMENTS

This work was financially supported by the Australian Research Council (Grants DP220100735, FT190100148, and

FT200100301). The authors acknowledge the instruments and expertise of Microscopy Australia at the Future Industries Institute, University of South Australia, enabled by NCRIS, university, and state government support.

■ REFERENCES

- (1) Vilan, A.; Cahen, D. Chemical Modification of Semiconductor Surfaces for Molecular Electronics. *Chem. Rev.* **2017**, *117*, 4624–4666.
- (2) Heath, J. R.; Ratner, M. A. Molecular electronics. *Phys. Today* **2003**, *56*, 43–49.
- (3) Maldonado, S.; Plass, K. E.; Knapp, D.; Lewis, N. S. Electrical Properties of Junctions between Hg and Si(111) Surfaces Functionalized with Short-Chain Alkyls. *J. Phys. Chem. C* **2007**, *111*, 17690–17699.
- (4) Yakuphanoglu, F.; Kandaz, M.; Senkal, B. F. Current–voltage and capacitance–voltage characteristics of Al/p-type silicon/organic semiconductor based on phthalocyanine rectifier contact. *Thin Solid Films* **2008**, *516*, 8793–8796.
- (5) Aswal, D.; Lenfant, S.; Guerin, D.; Yakhmi, J.; Vuillaume, D. Self assembled monolayers on silicon for molecular electronics. *Anal. Chim. Acta* **2006**, *568*, 84–108.
- (6) Aragonès, A. C.; Darwish, N.; Ciampi, S.; Sanz, F.; Gooding, J. J.; Díez-Pérez, I. Single-molecule electrical contacts on silicon electrodes under ambient conditions. *Nat. Commun.* **2017**, *8*, No. 15056.
- (7) Peiris, C. R.; Ciampi, S.; Dief, E. M.; Zhang, J.; Canfield, P. J.; Le Brun, A. P.; Kosov, D. S.; Reimers, J. R.; Darwish, N. Spontaneous S–Si bonding of alkanethiols to Si(111)-H: towards Si-molecule-Si circuits. *Chem. Sci.* **2020**, *11*, 5246–5256.
- (8) Peiris, C. R.; Vogel, Y. B.; Le Brun, A. P.; Aragonès, A. C.; Coote, M. L.; Díez-Pérez, I.; Ciampi, S.; Darwish, N. Metal–Single-Molecule–Semiconductor Junctions Formed by a Radical Reaction Bridging Gold and Silicon Electrodes. *J. Am. Chem. Soc.* **2019**, *141*, 14788–14797.
- (9) Zhang, S.; Ferrie, S.; Peiris, C. R.; Lyu, X.; Vogel, Y. B.; Darwish, N.; Ciampi, S. Common Background Signals in Voltammograms of Crystalline Silicon Electrodes are Reversible Silica–Silicon Redox Chemistry at Highly Conductive Surface Sites. *J. Am. Chem. Soc.* **2021**, *143*, 1267–1272.
- (10) Yaffe, O.; Scheres, L.; Segev, L.; Biller, A.; Ron, I.; Salomon, E.; Giesbers, M.; Kahn, A.; Kronik, L.; Zuilhof, H.; Vilan, A.; Cahen, D. Hg/Molecular Monolayer–Si Junctions: Electrical Interplay between Monolayer Properties and Semiconductor Doping Density. *J. Phys. Chem. C* **2010**, *114*, 10270–10279.
- (11) Zhang, G.-J.; Huang, M. J.; Ang, J. A. J.; Liu, E. T.; Desai, K. V. Self-assembled monolayer-assisted silicon nanowire biosensor for detection of protein–DNA interactions in nuclear extracts from breast cancer cell. *Biosens. Bioelectron.* **2011**, *26*, 3233–3239.
- (12) Peng, K.-Q.; Wang, X.; Li, L.; Hu, Y.; Lee, S.-T. Silicon nanowires for advanced energy conversion and storage. *Nano Today* **2013**, *8*, 75–97.
- (13) Ferrie, S.; Le Brun, A. P.; Krishnan, G.; Andersson, G. G.; Darwish, N.; Ciampi, S. Sliding silicon-based Schottky diodes: Maximizing triboelectricity with surface chemistry. *Nano Energy* **2022**, *93*, No. 106861.
- (14) Hurtado, C.; Lyu, X.; Ferrie, S.; Le Brun, A. P.; MacGregor, M.; Ciampi, S. Organic Monolayers on Si(211) for Triboelectricity Generation: Etching Optimization and Relationship between the Electrochemistry and Current Output. *ACS Appl. Nano Mater.* **2022**, *5*, 14263–14274.
- (15) Haick, H.; Ghabboun, J.; Cahen, D. Pd versus Au as evaporated metal contacts to molecules. *Appl. Phys. Lett.* **2005**, *86*, 042113–042113–3.
- (16) Haag, R.; Rampi, M. A.; Holmlin, R. E.; Whitesides, G. M. Electrical Breakdown of Aliphatic and Aromatic Self-Assembled Monolayers Used as Nanometer-Thick Organic Dielectrics. *J. Am. Chem. Soc.* **1999**, *121*, 7895–7906.

- (17) Shin, R. H.; Jo, W.; Kim, D. W.; Yun, J. H.; Ahn, S. Local current–voltage behaviors of preferentially and randomly textured Cu(In,Ga)Se₂ thin films investigated by conductive atomic force microscopy. *Appl. Phys. A: Mater. Sci. Process.* **2011**, *104*, 1189–1194.
- (18) Liu, Y.; Guo, J.; Zhu, E.; Liao, L.; Lee, S.-J.; Ding, M.; Shakir, I.; Gambin, V.; Huang, Y.; Duan, X. Approaching the Schottky–Mott limit in van der Waals metal–semiconductor junctions. *Nature* **2018**, *557*, 696–700.
- (19) Wang, Y.; Kim, J. C.; Wu, R. J.; Martinez, J.; Song, X.; Yang, J.; Zhao, F.; Mkhoyan, A.; Jeong, H. Y.; Chhowalla, M. Van der Waals contacts between three-dimensional metals and two-dimensional semiconductors. *Nature* **2019**, *568*, 70–74.
- (20) Liu, Y.-J.; Yu, H.-Z. Molecular Passivation of Mercury–Silicon (p-type) Diode Junctions: Alkylation, Oxidation, and Alkylsilation. *J. Phys. Chem. B* **2003**, *107*, 7803–7811.
- (21) Hiremath, R. K.; Mulimani, B.; Rabinal, M.; Khazi, I. Electrical characterization of a phenylacetylene-modified silicon surface via mercury probe. *J. Condens. Matter Phys.* **2007**, *19*, 446003.
- (22) Weiss, E. A.; Chiechi, R. C.; Kaufman, G. K.; Kriebel, J. K.; Li, Z.; Duati, M.; Rampi, M. A.; Whitesides, G. M. Influence of defects on the electrical characteristics of mercury-drop junctions: self-assembled monolayers of n-alkanethiolates on rough and smooth silver. *J. Am. Chem. Soc.* **2007**, *129*, 4336–4349.
- (23) Rice, K. M.; Walker, E. M., Jr; Wu, M.; Gillette, C.; Blough, E. R. Environmental mercury and its toxic effects. *J. Prev. Med. Public Health* **2014**, *47*, 74.
- (24) Langford, N.; Ferner, R. Toxicity of mercury. *J. Hum. Hypertens.* **1999**, *13*, 651–656.
- (25) Cheng, S.; Wu, Z. Microfluidic electronics. *Lab Chip* **2012**, *12*, 2782–2791.
- (26) Dickey, M. D.; Chiechi, R. C.; Larsen, R. J.; Weiss, E. A.; Weitz, D. A.; Whitesides, G. M. Eutectic Gallium-Indium (EGaIn): A Liquid Metal Alloy for the Formation of Stable Structures in Microchannels at Room Temperature. *Adv. Funct. Mater.* **2008**, *18*, 1097–1104.
- (27) Chen, Y.; Wagner, J. L.; Farias, P. A.; DeMauro, E. P.; Guildenbecher, D. R. Galinstan liquid metal breakup and droplet formation in a shock-induced cross-flow. *Int. J. Multiphase Flow* **2018**, *106*, 147–163.
- (28) Cheng, S.; Wu, Z. Microfluidic electronics. *Lab Chip* **2012**, *12*, 2782–2791.
- (29) Munirathinam, K.; Park, J.; Jeong, Y.-J.; Lee, D.-W. Galinstan-based flexible microfluidic device for wireless human-sensor applications. *Sens. Actuators, A* **2020**, *315*, 112344 DOI: [10.1016/j.sna.2020.112344](https://doi.org/10.1016/j.sna.2020.112344).
- (30) Yu, Y.; Miyako, E. Recent advances in liquid metal manipulation toward soft robotics and biotechnologies. *Eur. J. Chem.* **2018**, *24*, 9456–9462.
- (31) Yang, Y.; Sun, N.; Wen, Z.; Cheng, P.; Zheng, H.; Shao, H.; Xia, Y.; Chen, C.; Lan, H.; Xie, X.; et al. Liquid-metal-based superstretchable and structure-designable triboelectric nanogenerator for wearable electronics. *ACS Nano* **2018**, *12*, 2027–2034.
- (32) Sarfo, D. K.; Taylor, R. R.; O'Mullane, A. P. Investigating Liquid Metal Galinstan as a High Current Carrier and Its Interaction with Collector Electrodes. *ACS Appl. Electron. Mater.* **2020**, *2*, 2921–2928.
- (33) Chiechi, R. C.; Weiss, E. A.; Dickey, M. D.; Whitesides, G. M. Eutectic Gallium-Indium (EGaIn): A Moldable Liquid Metal for Electrical Characterization of Self-Assembled Monolayers. *Angew. Chem.* **2008**, *120*, 148–150.
- (34) Allioux, F.-M.; Han, J.; Tang, J.; Merhebi, S.; Cai, S.; Tang, J.; Abbasi, R.; Centurion, F.; Mousavi, M.; Zhang, C.; Xie, W.; Mayyas, M.; Rahim, M. A.; Ghasemian, M. B.; Kalantar-Zadeh, K. Nanotip Formation from Liquid Metals for Soft Electronic Junctions. *ACS Appl. Mater. Interfaces* **2021**, *13*, 43247–43257.
- (35) Nijhuis, C. A.; Reus, W. F.; Whitesides, G. M. Molecular Rectification in Metal–SAM–Metal Oxide–Metal Junctions. *J. Am. Chem. Soc.* **2009**, *131*, 17814–17827.
- (36) Lamport, Z. A.; Broadnax, A. D.; Scharmann, B.; Bradford, R. W., III; DelaCourt, A.; Meyer, N.; Li, H.; Geyer, S. M.; Thonhauser, T.; Welker, M. E.; Jurchescu, O. D. Molecular Rectifiers on Silicon: High Performance by Enhancing Top-Electrode/Molecule Coupling. *ACS Appl. Mater. Interfaces* **2019**, *11*, 18564–18570.
- (37) Ciampi, S.; Harper, J. B.; Gooding, J. J. Wet chemical routes to the assembly of organic monolayers on silicon surfaces via the formation of Si-C bonds: surface preparation, passivation and functionalization. *Chem. Soc. Rev.* **2010**, *39*, 2158–2183.
- (38) Zhang, S.; Ferrie, S.; Lyu, X.; Xia, Y.; Darwish, N.; Wang, Z.; Ciampi, S. Absence of a Relationship between Surface Conductivity and Electrochemical Rates: Redox-Active Monolayers on Si(211), Si(111), and Si(110). *J. Phys. Chem. C* **2021**, *125*, 18197–18203.
- (39) Lyu, X.; Ferrie, S.; Pivrikas, A.; MacGregor, M.; Ciampi, S. Sliding Schottky diode triboelectric nanogenerators with current output of 10⁹ A/m² by molecular engineering of Si(211) surfaces. *Nano Energy* **2022**, *102*, No. 107658.
- (40) Ciampi, S.; Le Saux, G.; Harper, J. B.; Gooding, J. J. Optimization of Click Chemistry of Ferrocene Derivatives on Acetylene-Functionalized Silicon(100) Surfaces. *Electroanalysis* **2008**, *20*, 1513–1519.
- (41) Zhou, W.; Liang, Q.; Chen, T. 3D Manipulation of Magnetic Liquid Metals. *Adv. Intell. Syst.* **2020**, *2*, 900170 DOI: [10.1002/aisy.201900170](https://doi.org/10.1002/aisy.201900170).
- (42) Vogel, Y. B.; Zhang, L.; Darwish, N.; Gonçalves, V. R.; Le Brun, A.; Gooding, J. J.; Molina, A.; Wallace, G. G.; Coote, M. L.; Gonzalez, J.; Ciampi, S. Reproducible flaws unveil electrostatic aspects of semiconductor electrochemistry. *Nat. Commun.* **2017**, *8*, No. 2066.
- (43) Colazzo, L.; Sedona, F.; Moretto, A.; Casarin, M.; Sambri, M. Metal-Free on-Surface Photochemical Homocoupling of Terminal Alkynes. *J. Am. Chem. Soc.* **2016**, *138*, 10151–10156.
- (44) Laviron, E. AC Polarography and faradaic impedance of strongly adsorbed electroactive species: Part III. Theoretical complex plane analysis for a surface redox reaction. *J. Electroanal. Chem.* **1979**, *105*, 35–42.
- (45) Ziegel, E. R. *Statistics and Chemometrics for Analytical Chemistry*; Taylor & Francis: Alexandria, 2004; Vol. 46, pp 498–499.
- (46) Schindelin, J.; Arganda-Carreras, I.; Frise, E.; Kaynig, V.; Longair, M.; Pietzsch, T.; Preibisch, S.; Rueden, C.; Saalfeld, S.; Schmid, B.; Tinevez, J.-Y.; White, D. J.; Hartenstein, V.; Elceiri, K.; Tomancak, P.; Cardona, A. Fiji: An open-source platform for biological-image analysis. *Nat. Methods* **2012**, *9*, 676–682.
- (47) Daerr, A.; Adrien, M. Pendent_Drop: An ImageJ Plugin to Measure the Surface Tension from an Image of a Pendent Drop. *J. Open Res. Softw.* **2016**, *4*, 3–e3.
- (48) Ciampi, S.; Böcking, T.; Kilian, K. A.; James, M.; Harper, J. B.; Gooding, J. J. Functionalization of acetylene-terminated monolayers on Si(100) surfaces: a click chemistry approach. *Langmuir* **2007**, *23*, 9320–9329.
- (49) Nelson, A. R. J.; Prescott, S. W. refnx: neutron and X-ray reflectometry analysis in Python. *J. Appl. Crystallogr.* **2019**, *52*, 193–200.
- (50) Du, J.; Wang, X.; Li, Y.; Min, Q. How an Oxide Layer Influences the Impact Dynamics of Galinstan Droplets on a Superhydrophobic Surface. *Langmuir* **2022**, *38*, 5645–5655.
- (51) Lorenz, M. R.; Woods, J. F.; Gambino, R. J. Some electrical properties of the semiconductor β Ga₂O₃. *J. Phys. Chem. Solids* **1967**, *28*, 403–404.
- (52) Sato, T.; Yamagishi, K.; Hashimoto, M.; Iwase, E. Method to Reduce the Contact Resistivity between Galinstan and a Copper Electrode for Electrical Connection in Flexible Devices. *ACS Appl. Mater. Interfaces* **2021**, *13*, 18247–18254.
- (53) Van der Linden, W.; Dieker, J. W. Glassy carbon as electrode material in electro-analytical chemistry. *Anal. Chim. Acta* **1980**, *119*, 1–24.
- (54) Lindsay, S. Molecular wires and devices: Advances and issues. *Faraday Discuss* **2006**, *131*, 403–409.
- (55) Downs, A. J. *Chemistry of Aluminium, Gallium, Indium and Thallium*; Springer Science & Business Media, 1993.

- (56) Dickey, M. D. Emerging Applications of Liquid Metals Featuring Surface Oxides. *ACS Appl. Mater. Interfaces* **2014**, *6*, 18369–18379.
- (57) Yaffe, O.; Scheres, L.; Puniredd, S. R.; Stein, N.; Biller, A.; Lavan, R. H.; Shpaisman, H.; Zuilhof, H.; Haick, H.; Cahen, D.; Vilan, A. Molecular Electronics at Metal/Semiconductor Junctions. Si Inversion by Sub-Nanometer Molecular Films. *Nano Lett.* **2009**, *9*, 2390–2394.
- (58) Handschuh-Wang, S.; Gan, T.; Wang, T.; Stadler, F. J.; Zhou, X. Surface Tension of the Oxide Skin of Gallium-Based Liquid Metals. *Langmuir* **2021**, *37*, 9017–9025.
- (59) Liu, T.; Sen, P.; Kim, C. J. *Characterization of Liquid-metal Galinstan for Droplet Applications*, 2010 IEEE 23rd International Conference on Micro Electro Mechanical Systems (MEMS), 2010; pp 560–563.
- (60) Gooding, J. J.; Ciampi, S. The molecular level modification of surfaces: from self-assembled monolayers to complex molecular assemblies. *Chem. Soc. Rev.* **2011**, *40*, 2704–2718.
- (61) Linford, M. R.; Chidsey, C. E. Alkyl monolayers covalently bonded to silicon surfaces. *J. Am. Chem. Soc.* **1993**, *115*, 12631–12632.
- (62) Ciampi, S.; Le Saux, G.; Harper, J. B.; Gooding, J. J. Optimization of Click Chemistry of Ferrocene Derivatives on Acetylene-Functionalized Silicon (100) Surfaces. *Electroanalysis* **2008**, *20*, 1513–1519.
- (63) Meldal, M.; Tornøe, C. W. Cu-catalyzed azide–alkyne cycloaddition. *Chem. Rev.* **2008**, *108*, 2952–3015.
- (64) Nijhuis, C. A.; Reus, W. F.; Barber, J. R.; Dickey, M. D.; Whitesides, G. M. Charge Transport and Rectification in Arrays of SAM-Based Tunneling Junctions. *Nano Lett.* **2010**, *10*, 3611–3619.
- (65) Wu, F.; Zhang, D.-W.; Wang, J.; Watkinson, M.; Krause, S. Copper Contamination of Self-Assembled Organic Monolayer Modified Silicon Surfaces Following a “Click” Reaction Characterized with LAPS and SPIM. *Langmuir* **2017**, *33*, 3170–3177.
- (66) Gonzalez, J.; Sequí-Castellano, J. A. Electrochemical determination of kinetic parameters of surface confined redox probes in presence of intermolecular interactions by means of Cyclic Voltammetry. Application to TEMPO monolayers in gold and platinum electrodes. *Electrochim. Acta* **2021**, *365*, No. 137331.
- (67) Zaroni, R.; Cattaruzza, F.; Coluzza, C.; Dalchiale, E. A.; Decker, F.; Di Santo, G.; Flamini, A.; Funari, L.; Marrani, A. G. An AFM, XPS and electrochemical study of molecular electroactive monolayers formed by wet chemistry functionalization of H-terminated Si(100) with vinylferrocene. *Surf. Sci.* **2005**, *575*, 260–272.
- (68) Rowe, G. K.; Creager, S. E. Redox and ion-pairing thermodynamics in self-assembled monolayers. *Langmuir* **1991**, *7*, 2307–2312.
- (69) Chidsey, C. E. D.; Bertozzi, C. R.; Putvinski, T. M.; Mujisce, A. M. Coadsorption of ferrocene-terminated and unsubstituted alkanethiols on gold: electroactive self-assembled monolayers. *J. Am. Chem. Soc.* **1990**, *112*, 4301–4306.
- (70) González, J.; Sequí, J.-A. Analysis of the Electrochemical Response of Surface-confined Bidirectional Molecular Electrocatalysts in the Presence of Intermolecular Interactions. *ChemCatChem* **2021**, *13*, 747–762.
- (71) Zhang, L.; Vogel, Y. B.; Noble, B. B.; Gonçalves, V. R.; Darwish, N.; Brun, A. L.; Gooding, J. J.; Wallace, G. G.; Coote, M. L.; Ciampi, S. TEMPO Monolayers on Si(100) Electrodes: Electrostatic Effects by the Electrolyte and Semiconductor Space-Charge on the Electroactivity of a Persistent Radical. *J. Am. Chem. Soc.* **2016**, *138*, 9611–9619.
- (72) Vogel, Y. B.; Molina, A.; Gonzalez, J.; Ciampi, S. Quantitative Analysis of Cyclic Voltammetry of Redox Monolayers Adsorbed on Semiconductors: Isolating Electrode Kinetics, Lateral Interactions, and Diode Currents. *Anal. Chem.* **2019**, *91*, 5929–5937.
- (73) Cerofolini, G. F.; Galati, C.; Renna, L. Accounting for anomalous oxidation states of silicon at the Si/SiO₂ interface. *Surf. Interface Anal.* **2002**, *33*, 583–590.
- (74) Ahmad, S. A. A.; Ciampi, S.; Parker, S. G.; Gonçalves, V. R.; Gooding, J. J. Forming Ferrocenyl Self-Assembled Monolayers on Si(100) Electrodes with Different Alkyl Chain Lengths for Electron Transfer Studies. *ChemElectroChem* **2019**, *6*, 211–220.
- (75) Böcking, T.; James, M.; Coster, H. G. L.; Chilcott, T. C.; Barrow, K. D. Structural Characterization of Organic Multilayers on Silicon(111) Formed by Immobilization of Molecular Films on Functionalized Si–C Linked Monolayers. *Langmuir* **2004**, *20*, 9227–9235.
- (76) Sieval, A. B.; Demirel, A. L.; Nissink, J. W. M.; Linford, M. R.; van der Maas, J. H.; de Jeu, W. H.; Zuilhof, H.; Sudhölter, E. J. R. Highly Stable Si–C Linked Functionalized Monolayers on the Silicon (100) Surface. *Langmuir* **1998**, *14*, 1759–1768.
- (77) Ferrie, S.; Darwish, N.; Gooding, J. J.; Ciampi, S. Harnessing silicon facet-dependent conductivity to enhance the direct-current produced by a sliding Schottky diode triboelectric nanogenerator. *Nano Energy* **2020**, *78*, 105210.
- (78) Hurtado, C.; Ciampi, S. Oxidative Damage during the Operation of Si(211)-Based Triboelectric Nanogenerators. *Surfaces* **2023**, *6*, 281–290.
- (79) Olson, K. P.; Mizzi, C. A.; Marks, L. D. Band Bending and Ratcheting Explain Triboelectricity in a Flexoelectric Contact Diode. *Nano Lett.* **2022**, *22*, 3914–3921.
- (80) Witte, G.; Weiss, K.; Jakob, P.; Braun, J.; Kostov, K. L.; Wöll, C. Damping of molecular motion on a solid substrate: Evidence for electron-hole pair creation. *Phys. Rev. Lett.* **1998**, *80*, 121–124.
- (81) Wilhelm, S. M.; Yun, K. S.; Ballenger, L. W.; Hackerman, N. Semiconductor Properties of Iron Oxide Electrodes. *J. Electrochem. Soc.* **1979**, *126*, 419–423.
- (82) Sivula, K. Mott–Schottky Analysis of Photoelectrodes: Sanity Checks Are Needed. *ACS Energy Lett.* **2021**, *6*, 2549–2551.
- (83) Zhang, X. G. *Electrochemistry of Silicon and Its Oxide*; Springer US: Boston, MA, 2001.
- (84) Girard, H. A.; Simon, N.; Ballutaud, D.; Etcheberry, A. Correlation between flat-band potential position and oxygenated termination nature on boron-doped diamond electrodes. *C. R. Chim.* **2008**, *11*, 1010–1015.

Chapter 5. Schottky diode leakage current fluctuations:
electrostatically induced flexoelectricity in silicon

Introduction to Chapter 5

Nearly four decades have passed since IBM scientists pioneered atomic force microscopy (AFM) by merging the principles of a scanning tunneling microscope with the features of a stylus profilometer. Today, electrical AFM modes are an indispensable asset within the semiconductor and nanotechnology industries, enabling the characterization and manipulation of electrical properties at the nanoscale. However, electrical AFM measurements suffer from reproducibility issues, caused for example by surface contaminations, Joule heating, and hard-to-minimize tip drift and tilt. In this context, **Chapter 5**, presented here as paper 4, explores the root cause of these irreproducibility issues. As we previously discussed in Chapter 4, the presence of large strain gradients plays a major role in the overall triboelectric phenomenon and is likely always present in the Pt–SAM–Si junction.

Results reveal that voltage-dependent adhesion forces lead to significant rotation of the AFM metal tip and that this electrostatics-driven tip rotation causes a strain gradient on the silicon surface, which in turn induces a flexoelectric reverse bias term.

This flexoelectric internal bias term adds to the external, instrumental, reverse bias, causing both an increased diode leakage as well as a shift of the diode knee voltage to larger forward biases. These findings are crucial in the design and characterization of silicon-based devices, especially those that are deliberately operated under large strain or shear, such as in emerging energy harvesting technologies such as Schottky-based triboelectric nanogenerators (TENGs).

Supporting information for **Chapter 5** can be found in *Appendix F*.

Schottky Diode Leakage Current Fluctuations: Electrostatically Induced Flexoelectricity in Silicon

Carlos Hurtado, Melanie MacGregor, Kai Chen, and Simone Ciampi*

Nearly four decades have passed since IBM scientists pioneered atomic force microscopy (AFM) by merging the principles of a scanning tunneling microscope with the features of a stylus profilometer. Today, electrical AFM modes are an indispensable asset within the semiconductor and nanotechnology industries, enabling the characterization and manipulation of electrical properties at the nanoscale. However, electrical AFM measurements suffer from reproducibility issues caused, for example, by surface contaminations, Joule heating, and hard-to-minimize tip drift and tilt. Using as experimental system nanoscale Schottky diodes assembled on oxide-free silicon crystals of precisely defined surface chemistry, it is revealed that voltage-dependent adhesion forces lead to significant rotation of the AFM platinum tip. The electrostatics-driven tip rotation causes a strain gradient on the silicon surface, which induces a flexoelectric reverse bias term. This directional flexoelectric internal-bias term adds to the external (instrumental) bias, causing both an increased diode leakage as well as a shift of the diode knee voltage to larger forward biases. These findings will aid the design and characterization of silicon-based devices, especially those that are deliberately operated under large strain or shear, such as in emerging energy harvesting technologies including Schottky-based triboelectric nanogenerators (TENGs).

While traditionally associated with certain data storage technologies and powering circuitry,^[3] Schottky diodes have also recently entered the field of energy generation.^[4,5] In a nanoscale metal–semiconductor Schottky diode, relative motion of the two materials leads to a measurable direct current (DC) output, even under zero external bias.^[6,7] Sliding diodes represent a significant category within the technology of triboelectric nanogenerators (TENGs).^[8–11] The process through which a DC-TENG based on a Schottky diode transforms mechanical energy into electrical energy is unclear, with the specific roles of friction,^[12] normal pressure,^[13] shear and strain,^[14] and their interactions, still being unclear. Specifically, what has recently emerged, is that surface polarization in response to bending—flexoelectricity—is not just limited to insulators, but occur also in semiconductors.^[15,16] For instance, in 2016 Catalan and co-workers demonstrated that in wide-bandgap semiconductor oxides, flexoelectricity is augmented, rather than diminished, by increasing the

material conductivity through doping.^[17]

The DC output of a sliding Schottky diode increases as the junction contact area decreases,^[18,19] hence nanoscale measurements, especially through atomic force microscopy (AFM), are ideally suited to study TENGs mechanisms and performances. The suitability of AFM-based measurements in TENG research is strengthened by the possibility of simultaneously probing, with high spatiotemporal resolution, DC outputs, mechanical and electronic aspects of the junction, such as normal force, friction, and adhesion, as well as detecting the presence or absence of electronic defects.^[20–22] However, AFM-based measurements, and not just in the context of TENGs but also within the broader realm of nanoscale electrical measurements, are often hindered by experimental factors that are hard to control or account for, such as tip-tilting and bias-dependent electrostatic interactions between probe and substrate.^[23,24]

Here we report experimental evidence of electrostatic forces between a conductive AFM tip and a silicon surface leading to mechanical instability of a nanoscale Schottky diode, and reveal that these forces account for a directional (relative to the diode's internal field) surface polarization. Regardless of the silicon doping type, the mechanically induced voltage term bears the direction of a reverse bias: it augments the external (operator-defined)

1. Introduction

Metal–semiconductor rectifying junctions—Schottky diodes—are a building block of many digital circuits and technologies.^[1,2]

C. Hurtado, S. Ciampi
School of Molecular and Life Sciences
Curtin University
Bentley, Western Australia 6102, Australia
E-mail: simone.ciampi@curtin.edu.au

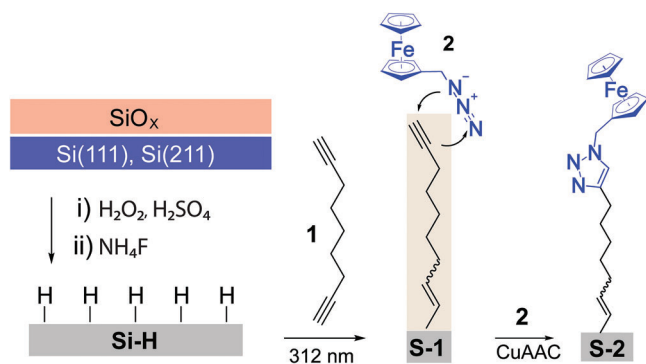
M. MacGregor
Flinders Institute for Nanoscale Science and Technology
Flinders University
Bedford Park, South Australia 5042, Australia

K. Chen
School of Molecular Sciences
The University of Western Australia
Crawley, Western Australia 6009, Australia

 The ORCID identification number(s) for the author(s) of this article can be found under <https://doi.org/10.1002/advs.202403524>

© 2024 The Author(s). Advanced Science published by Wiley-VCH GmbH. This is an open access article under the terms of the [Creative Commons Attribution License](#), which permits use, distribution and reproduction in any medium, provided the original work is properly cited.

DOI: 10.1002/advs.202403524



Scheme 1. Schematic representation of the wet chemistry process for the passivation and functionalization of an oxide-free Si(211) crystal. The removal of the native SiO_x layer, followed by the UV-assisted hydrosilylation of 1,8-nonadiyne (**1**) on hydrogen-terminated (Si–H) Si(211) and Si(111) yields a passivating (against anodic decomposition) but yet electrically conductive alkyne-terminated monolayer (**S-1**). The monolayer is further functionalized through a Cu-catalyzed alkyne–azide cycloaddition (CuAAC) reaction to yield a ferrocene-terminated monolayer (**S-2**).

reverse bias and diminishes the external forward bias. We show how to detect, account for, and minimize (or augment) this parasitic polarization.

2. Results and Discussion

Asymmetric attractive forces between a semiconductor and metal-like AFM tips have been reported before.^[25,26] However, residual electrostatic effects—residual in the sense that they persist even upon the flow of an electric current—are poorly discussed in the literature.^[27,28] A Schottky junction, just like any junction, has a certain ability to let charge through and to store charge.^[29,30] Electronic drag is likely to have a negligible mechanical effect on the adhesion of a biased junction,^[25] so, if any, residual attractive forces are most likely capacitive in origin.

Since the capacitance of a Schottky diode depends on the external bias, our first objective was therefore to explore the magnitude and directionality of adhesion forces in diodes that were deliberately biased into either accumulation or depletion. The main experimental platform is shown in **Scheme 1**, which depicts the chemical strategy used to passivate oxide-free silicon wafers. In brief, silicon surfaces were first etched to yield a hydrogen-terminated surface (Si–H), which has a low density of electrical defects but is unfortunately prone to oxidation (Figures **S1** and **S2**, Supporting Information).^[31] The chemical reactivity of the Si–H surface can however be turned into a technical advantage, as it can be chemically passivated through surface hydrosilylation reactions with 1-alkenes^[32] and 1-alkynes^[33] monolayer-forming molecules.^[34–36] The hydrosilylation of an α,ω -dialkyne molecule (1,8-nonadiyne, **1**, **Scheme 1**) on Si–H was used to prepare **S-1** surfaces,^[34] where the acetylene moiety at the **S-1** monolayer distal end also opens up the possibility of further chemical derivatization of the semiconductor surface. This option is here used to covalently tether ferrocene-terminated monolayers (**S-2**).^[37] The presence of a metallocene in the **S-2** monolayer allows access to electrochemical measurements, which do not involve diffusive reactants and are therefore an unambiguous analytical tool to assess the outcome of the silicon passivation procedure. Elec-

trochemical measurements done on **S-2** samples also served to demonstrate that the chemical passivation of the Si(211) oxide-free crystal does not preclude the flow of DC across the interface (Figure **S3**, Supporting Information).^[38,39] The electrochemically determined monolayer surface coverage for **S-2** samples is $\approx 2.2 \times 10^{-10} \text{ mol cm}^{-2}$, which is lower than the expected theoretical value for a closely packed ferrocene monolayer ($4.5 \times 10^{-10} \text{ mol cm}^{-2}$)^[40] but in line with literature data for two-step surface derivatization procedures.^[41–43] The full width at half-maximum (fwhm) of cyclic voltammetry traces was $\approx 90 \text{ mV}$. This fwhm value indicates negligible interactions between the adsorbate molecules.^[44,45] What is also evident in the voltammograms shown in Figure **S3** (Supporting Information) is a peak “inversion”: the anodic wave peaks at more cathodic voltages than the cathodic wave. This inversion is indicative of electrostatic interactions between the silicon space charge region and the molecular charges of the adsorbate.^[42]

After having validated the good quality of the semiconductor chemical derivatization, we then turned our attention to “dry” junctions. Data presented in **Figure 1a** show changes in the adhesion force between the silicon surface and a platinum AFM tip as a function of the Schottky junction external bias. The junction’s adhesion force was estimated by measuring the pull-off force in AFM force–distance (F – d) experiments (Figure **S4**, Supporting Information), over a range of sample’s bias voltages (from -1.5 to $+1.5 \text{ V}$) covering from silicon accumulation to silicon depletion. The adhesion force displayed a quadratic voltage-dependent characteristic, indicative of a capacitive behavior.^[23,46] However, this bias-dependent tip–sample electrostatic interaction does not follow a symmetric rise around the zero bias: for a given (absolute) value of voltage bias, adhesion forces are generally larger than when the diode is under reverse bias (grey region, Figure **1a**) rather than under accumulation (red region, Figure **1a**).

The original assumption of metal–silicon attractive forces being capacitive in nature is therefore in poor agreement with the data shown in Figure **1a**, since the experimentally determined adhesion is greater when the junction is depleted, that is, when the interface capacitance drops and its resistance increases due to the silicon space-charge region increasing in thickness.^[47] The observed tip–silicon attraction is greater when the Si(211) near-surface region contains a population of unbalanced, immobile ionized phosphorous dopant atoms and opposes the flow of current^[48] (Figure **1a**). If the thickness of this charged region is minimized by means of increasing the silicon doping level, the magnitude of the metal–silicon attraction also drops (Figure **S5**, Supporting Information).

One of the possible expected consequences of this bias-dependent tip–surface adhesion force—a lateral tip-tilt due to the likelihood of an asymmetric tip shape—is schematically depicted in Figure **1b**. Such tilting of the AFM tip may be detected by the instrument’s position-sensitive photodiode (PSPD) in the form of a change in the tracking laser deflection (vide infra). However, we first turned our attention to another plausible consequence of a mechanical movement caused by the observed tip–substrate attraction. It is not unlikely that an increase in the normal force would cause a local strain gradient in the silicon substrate. For many materials, the consequence of a strain gradient (bending) is the generation of flexoelectricity. The first report on flexoelectricity is likely to be a 1910 paper by

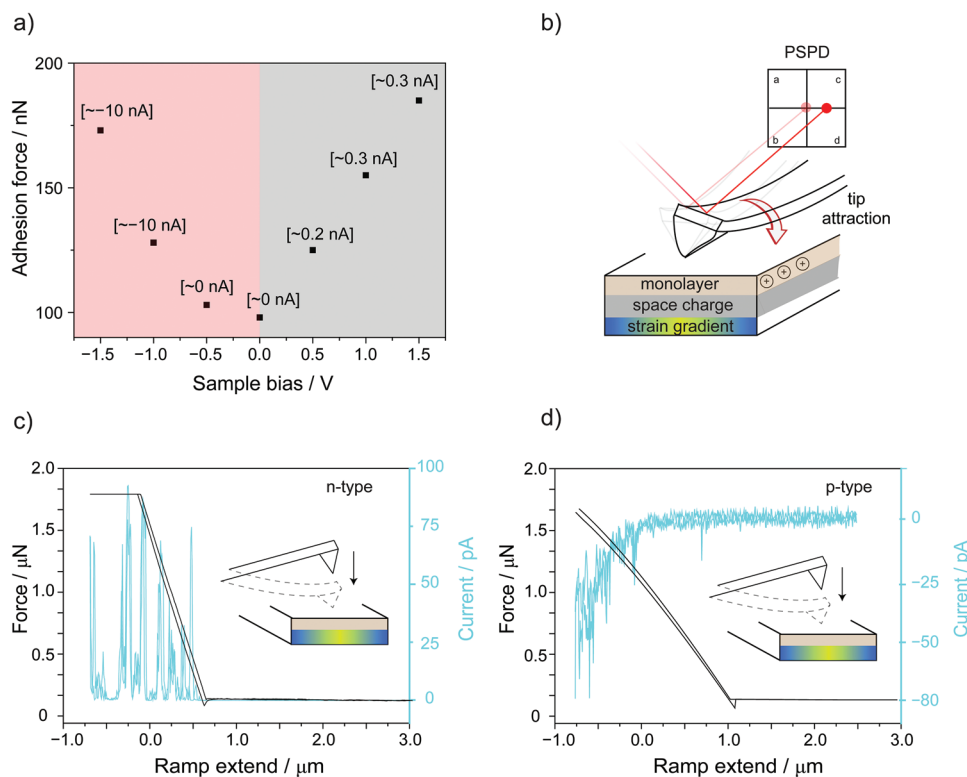


Figure 1. a) Tip-sample (Pt AFM tip-S-1 grafted on n-type Si(211)) adhesion force data as a function of the external semiconductor bias (−1.5 to +1.5 V). Shaded areas delimit the forward (red) and reverse bias (gray) regimes. Labels next to each adhesion force–sample bias data point are the corresponding current values. b) Schematics depiction of a geometrically imperfect tip tilting laterally in response to a normal attractive force. The near-surface positive charges of space-charge ionized phosphorous dopants are indicated as plus symbols, and the blue/green color gradient indicates the strain gradient. c,d) High-speed current capture data was acquired during AFM force–distance ($F-d$) measurements done on Si(211) S-1 monolayers prepared on either c) n-type, or d) p-type samples. The cyan traces represent the current flowing across the Schottky junction, under zero external bias, recorded as the platinum AFM tip is pressed down onto the silicon surface ($F-d$ data, black traces). The instrument routing is such that a current of the positive sign indicates a flow of electrons from tip to sample.

Walter Jamieson, who observed for celluloid sheets a curvature-dependent surface charging.^[49] Flexoelectricity has been since then verified or anticipated for several materials^[14,50–55] including semiconductors.^[15–17,56] For instance, Wu et al.^[53] have explored the modulation of device performance through flexoelectric effects in MoS₂-based metal–semiconductor field-effect transistors (MESFETs), and Sun et al.^[52] have developed new methods to measure flexoelectric coefficients of semiconductors. But while a flexoelectric effect is likely to occur in strained silicon,^[16,57] unfortunately the flexoelectric coefficient of silicon remains to be accurately determined. The reason for the lack of data on the magnitude and sign of the silicon flexoelectric coefficient is that a macroscopic strain–voltage measurement of such a brittle and hard material is hindered by the rapid formation of cracks.^[58,59] However, as shown recently for n-type SrTiO₃, a strain gradient may alter local band bending, and since the flexoelectric surface polarization can increase (or decrease) the height and width of the interface Schottky barrier, strain gradients will likely affect charge transport characteristics (Figure S6, Supporting Information).^[60]

To gain quantitative insights relevant to flexoelectricity in silicon we conducted $F-d$ experiments while rapidly sampling the zero-bias current. High-speed force–current data (ramp speed

300 nm s^{−1}) shown in Figure 1c and in Figure S7 (Supporting Information) show that, under no external bias, pressing down a platinum tip onto a Si(211) S-1 surface leads to a current response that bears the sign of the reverse current. It is not unlikely that pressure from the AFM tip (≈ 5 GPa) is causing a nonuniform strain near the tip–surface contact region^[61] and that surface polarization due to the strain gradient (flexoelectricity) is the cause of the current flow. We note that the large zero-bias current shown in Figure 1c is not an experimental artifact arising from the coupling of an increase in contact area (i.e., decrease in resistance) with a residual instrument “burden” voltage. As shown in Figure 1d, control force–current experiments performed on p-type silicon revealed that the effect is directional: the direction of the putative flexovoltage changes by switching from n- to p-substrate. These controls prove that the pressure-related zero-bias current is not caused by residual instrument burden voltage coupled to a drop in electrical resistance during the $F-d$ scan. It is also unlikely for this current to have a thermal origin, such as a Seebeck voltage in response to a temperature gradient. The silicon Seebeck coefficient is ≈ 0.4 mV K^{−1}, and to thermally generate currents such as those obtained in the $F-d$ experiments of Figure 1 would require a junction potential of ≈ 1.7 V, which

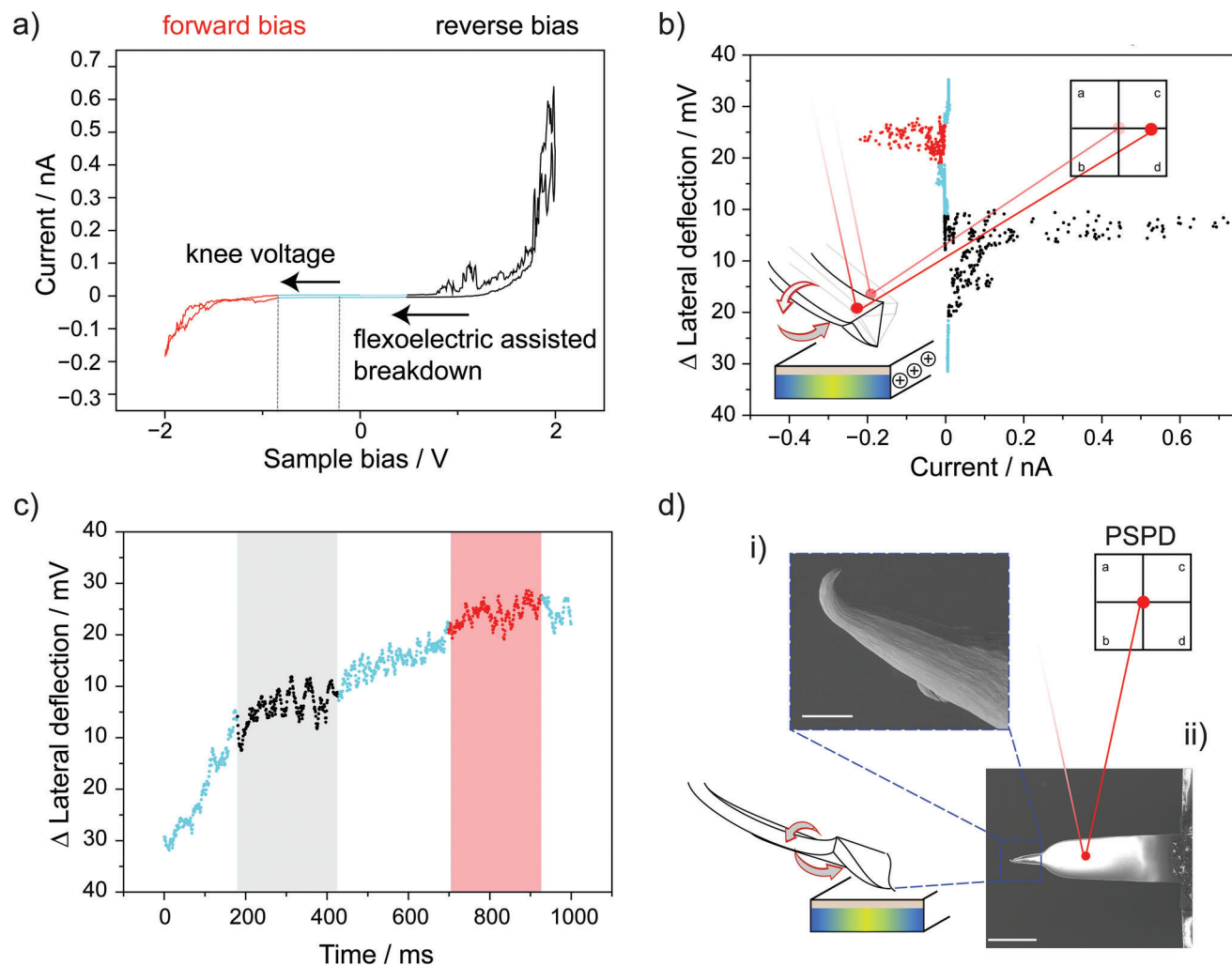


Figure 2. (a) Current–voltage (I – V) curves acquired at Pt AFM tip–n-type Si(211) S-1 junctions under an applied normal load of 100 nN at a voltage sweep rate of 8 V s^{-1} . The expected asymmetric diode I – V trace is “inverted,” with the reverse bias current (black lines) comparable to, or greater than, the forward current. (b) Lateral deflection–current plot revealing a substantial tip-tilting during the I – V experiment shown in (a). The inset depicts the detection through the PSPD signal of the lateral tilt of the tip. The near-surface positive charges of ionized phosphorous dopants in the space-charge are indicated as plus symbols, and the color gradient indicates qualitatively the silicon strain gradient. (c) Plot of the lateral deflection data shown in (b) as a function of time during the voltage ramp. Shaded areas indicate a “flatter” sections within the deflection curve which also correspond to maximum values of forward (gray) or reverse (red) current. (d) SEM images of the Pt AFM tip obtained after the AFM measurements. Scale bars are $10\ \mu\text{m}$ (i) and $100\ \mu\text{m}$ (ii).

would in turn arise from a temperature difference as large as $\approx 3000\text{ K}$.^[62]

How the zero-bias current output (Figure 1c,d) tracks the AFM tip force setpoint warrants a further discussion. Especially evident for junctions made on n-type substrates, but to a lesser degree also for the p-type systems, the flexoelectric current exhibits spike-like features. There are two possible explanations for these current spikes. The first is an intrinsic technical limitation: the contact force is inferred from the vertical position of the cantilever rather than from the actual position of the platinum tip contacting the silicon substrate. Consequently, mechanical deformations, shear, and irregularities or abrupt changes in the nanoscopic motion of actual contact cannot be ruled out. Notably, the observation that current spikes are much less frequent in the p-type system may also suggest an additional, although some-

what speculative, explanation, which is that in n-type silicon the flexoelectric coupling is not linear with strain gradient.^[63]

Having firstly demonstrated the presence of bias-dependent attractive forces (Figure 1a) and then of an “internal” reverse bias term due to mechanical forces (Figure 1c,d), we went back to the hypothesis schematically depicted in Figure 1b: the possibility of an electrostatically driven lateral tip tilting during a static (i.e., not the typical mapping^[6,12]) AFM electrical measurement.

With this in mind we performed current–voltage (I – V) measurements while monitoring the tip lateral deflection channel. We found that poorly performing Schottky junctions, that is, “leaky” diodes with a poor rectification ratio (RR at 1 V below ≈ 0.3 , Figure 2a), were generally mechanically unstable as indicated by data on the tip lateral deflection (Figure 2b). A large diode’s leakage, which we argue is the result of a flexoelectric

voltage pushing electrons from the tip to the n-type Si(211), was generally coupled to the presence of two discrete populations of tip-tilt angles. As the external bias is ramped between the forward vertex (-2 V, sample bias) to the reverse bias vertex ($+2$ V), the tip tilts laterally until it reaches a deflection plateau (Figure 2b,c; tilting plateaus in red and black symbols) when a large forward or backward current effectively nullifies the electrostatic tip–semiconductor interaction. Mechanical movements of the tip are greater in between, i.e., when the flow of current is minimal (e.g., cyan symbols in Figure 2b). As mentioned earlier, the reason why a normal force causes a lateral, rather than normal, deflection is rooted in the imperfect geometry of the AFM tip, as revealed by representative scanning electron microscopy (SEM) images in Figure 2d. SEM data of the tip also help answering another important question: the cause of a delay between the end of the tip tilting event (as measured by the deflection channel) and the onset of the putative flexovoltage (as measured by the onset of an unexpected large leakage current). In other words, although a large reverse current is flowing—larger than expected based on the externally applied bias—while the tip-tilt is “locked” in an apparent plateau, it is not unlikely that the end of the AFM tip (Figure 2d, inset-i), which is in contact with the sample and located beyond the cantilever region probed by the AFM PSPD (Figure 2d, inset-ii), is still rotating or sliding. We suggest that it is this “delayed” movement the cause of the flexoelectric surface polarization, which as shown by the current data acquired during F - d curves (Figure 1c) has the direction of a reverse bias. We note that this delayed movement is not affected by surface roughness. Control experiments done on Si(111) crystals, which are even smoother than the Si(211) substrates (rms roughness 0.3 nm vs 3 nm, Figure S8, Supporting Information) revealed similar tip lateral deflections and current outputs for the two platforms regardless of surface roughness (Figure S9, Supporting Information). Experiments with softer tips of the same radius (Figure S10, Supporting Information) showed larger zero-bias currents, tentatively associated with an increased probability of the tip tilting in response to the electrostatic tip-silicon attraction.

Regarding the nature of the electrical breakdown involved (i.e., the flexoelectric current has a direction of a leakage current), we attempted to elucidate whether the main mechanism is an avalanche or a Zener breakdown. For nominally static junctions biased externally (I - V curves), the leakage magnitude decreased with increasing temperature (Figure S11, Supporting Information) and for zero-bias F - d curves we observed an enhanced flexoelectric response as the silicon space-charge layer becomes thinner (i.e., higher dopant concentration) (Figure S12, Supporting Information). The effect of temperature and doping points towards a Zener rather than avalanche breakdown, where quantum tunnelling decreases as the depletion region widens.^[64] We also investigated the effect of changes to the normal load on the charge transport characteristics. I - V data in Figure S13 (Supporting Information) show that increasing the load increased both the leakage and the forward current: beyond a certain pressure threshold, the effect of an increased contact area overwrites any flexoelectric effect. Figures S14 and S15 (Supporting Information) show the C-AFM maps at either the nullifying voltage (i.e., the external voltage required to bring the leakage

current to noise level) or at zero-bias, respectively. The open circuit voltage (V_{OC}) and short-circuit current (I_{SC}) extracted from these maps scale with the applied load, ranging from 0.25 to 0.42 V, and from 0.2 to 1.0 nA (Table S1, Supporting Information).

To reinforce the role of electrostatics in causing mechanical instability (hence flexoelectricity) of the Schottky junctions, we conducted I - V measurements at a much lower scan rate (0.01 Hz), hence allowing additional time for the putative surface charges to dissipate. As shown in Figure S16 (Supporting Information), I - V inversion was rarely observed for slowly ramped junctions: only $\approx 1\%$ of the I - V curves showed a measurable leakage current. Importantly, a normal diode behavior (RR is well above 1000) was also observed for nanoscale junctions that despite being ramped at a faster voltage sweep rate were mechanically stable (Figure 3), as well as for macroscopic Schottky junctions under negligible normal force (Figure S17, Supporting Information). Also worth noting is the shift in knee voltage.^[65] The knee voltage of junctions that showed a lateral tip tilt (Figure 2a,b) was ≈ -0.8 V, hence significantly greater than the ≈ -0.3 to ≈ -0.5 V of static silicon-platinum junctions (Figure 3a,b). Such negative shift is the result of a flexoelectric voltage term, which has the polarity of a reverse bias and results from the silicon strain gradient caused by the electrostatic-driven tip rotation. Further mechanistic insights would be at this stage speculative as dynamic changes to the energy levels of a Schottky junction under a dynamic strain gradient remain poorly understood.^[60]

We then performed additional controls to further clarify both the delay between the flexoelectric effect and the tip-tilt, as well as the potential involvement of galvanic (corrosion) processes. Consecutive I - V scans recorded over the same sample location (Figure 4a) returned a progressive decay of the leakage current over successive scans along with an increase in forward current. This agrees with the flexoelectric term eventually disappearing as the movement subsides. It also suggests an unlikely role of corrosion, as the “oxidized” diode would not revert to a non-leaky status as it does. Further, if silicon corrosion was involved, such corrosion current should decrease over time as silicon oxide grows. This is not what the data indicates. Sequential trace and retrace AFM scans in Figure 4b show that sample locations characterized by a significant tribocurrent retain this characteristic over time. We further ruled out galvanic corrosion by observing that the direction of the galvanic voltage does not depend, unlike the flexovoltage (Figure 1c,d), on the silicon doping type. Both n- and p-type silicon samples immersed in an electrolytic solution, and then mechanically damaged to deliberately promote their corrosion, showed, as expected for a corroding substrate, a shift in open circuit potential towards more cathodic voltages, irrespective of the doping type (Figure S18, Supporting Information).

Finally, we tested our junctions when operated as a sliding TENG, with a representative zero-bias current map (C-AFM) shown in Figure S19 (Supporting Information). The tip slides along the S-1 surface generating a DC output that bears the sign of a reverse current, and with an average current density of $\approx 5.5 \times 10^6$ A m⁻². The performances of this TENG design are benchmarked in Table S1 (Supporting Information) against those of alternative TENG systems.

We conclude with a quantitative analysis (Figure 5) on the fraction of samples characterized by a simultaneous I - V inversion

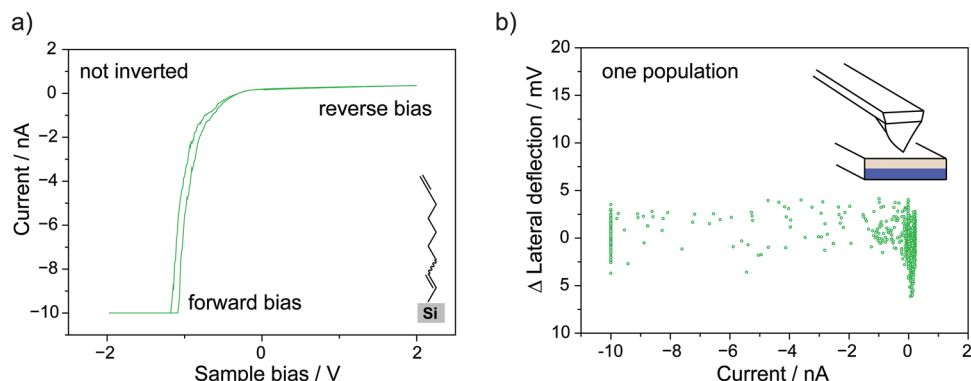


Figure 3. a) Representative I - V spectroscopy data acquired at a Pt AFM tip-n-type Si(211) S-1 junction under an applied normal load of 100 nN (voltage sweep rate of 8 V s^{-1}). b) Lateral deflection-current plot showing negligible lateral tilting during the bias ramping. The inset schematically depicts the Pt AFM tip in static contact with the silicon surface when no tip tilting is observed.

(RR below ≈ 0.3) and the presence of two discrete populations in the lateral tilt recorded during the I - V s. A remarkable 90% of the inverted I - V curves also showed two populations of lateral deflection. As discussed above, this mechanical tip instability causes a directional—additional reverse bias—parasitic flexovoltage. Furthermore, a compelling 92% of the samples with large RR (“not inverted” samples) were mechanically stable.

3. Conclusion

In this study we have revealed the presence of a directional “parasitic” reverse bias term in mechanically unstable Schottky junctions made between a platinum AFM tip and a monolayer-modified oxide-free silicon crystal. We have explained this additional reverse bias term as a silicon flexoelectric effect and assigned the origin of the mechanical instability to a semiconductor-to-metal electrostatic attraction, which surprisingly does not scale with the capacitance of the junction. The parasitic flexoelectric voltage adds to the external (instrumental) bias and leads to current fluctuations in current-voltage (I - V) mea-

surements. The silicon strain gradient that leads to the flexoelectric disturbance can be detected as it is immediately preceded by a lateral deflection of the AFM cantilever. Such deflection is found in most “leaky” nanoscopic junctions, and we bring evidence that it is cause, not effect, of such a large leakage current.

We show the additional “flexoelectric” term is doping type dependent (i.e., its direction changes from n- to p-type Si), it is linked to the electrostatic tip-substrate attraction, and it is not a corrosion or heating effect. The work deepens our understanding of Schottky diodes, explains a parasitic effect in electrical AFM measurements and will aid the design and characterization of devices based on out-of-equilibrium diodes such as DC-TENGs. We believe this work can aid in developing advanced sensing technologies and enhancing energy harvesting systems to fully leverage flexoelectric effects. Although large scale heterogeneous generators based on flexoelectricity are unlikely to be based on silicon, the reason being the availability of several materials with larger flexoelectric coefficients,^[66] the finding of this paper will be of value in nanoscale electrical measurements performed on silicon.

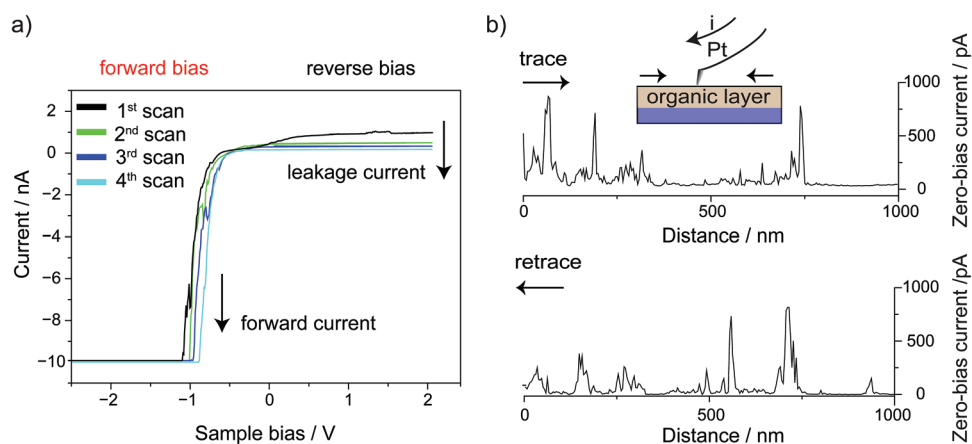


Figure 4. a) Consecutive color-coded I - V curves acquired at a Pt AFM tip-n-type Si(211) S-1 junction under an applied normal load of 100 nN and at a sweep rate of 8 V s^{-1} . b) Trace (left to right) and retrace (right to left) consecutive AFM scans acquired over the same sample location.

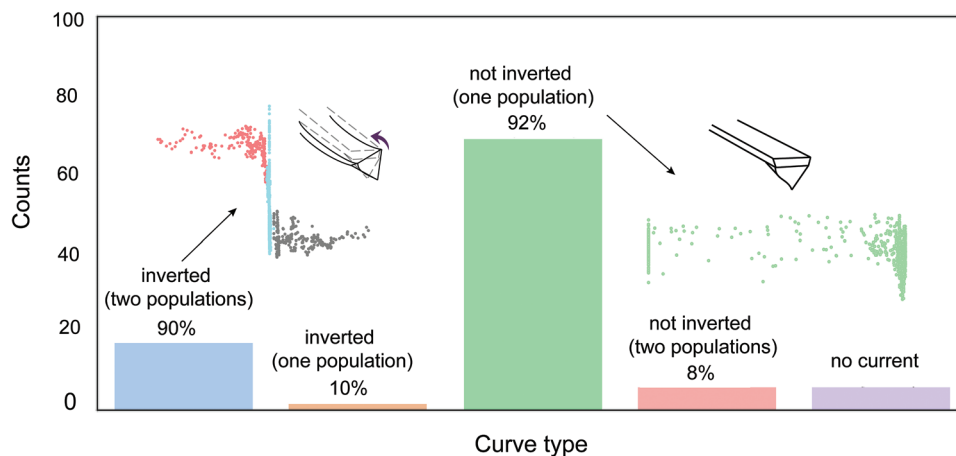


Figure 5. Analysis of 100 I - V curves recorded between a Pt AFM tip and n-type Si(211) S-1 samples (applied normal load of 100 nN, voltage sweep rate of 8 V s^{-1}).

4. Experimental Section

Chemicals and Materials: Redistilled dichloromethane (DCM), and Milli-Q water ($>18\text{ M}\Omega\text{ cm}$ resistivity) were used for substrate-cleaning and surface-modification procedures. Aqueous ammonium fluoride (40%, w/w), sulfuric acid (95–97%), and aqueous hydrogen peroxide (30% w/w) were of semiconductor grade and purchased from Honeywell. Methanol ($\geq 99.8\%$), ammonium sulfite monohydrate (92%), aqueous hydrochloric acid (HCl, 35–37%), and 1,8-nonadiyne (**1**, 98%) were purchased from Sigma–Aldrich. 2-Propanol ($>99.8\%$) was obtained from Ajax Finechem. Si(211) and Si(111) crystals, phosphorous-doped (n-type, $7\text{--}13\ \Omega\text{ cm}$, referred to as “lowly doped”) and boron-doped (p-type, $0.001\ \Omega\text{ cm}$, referred to as “highly doped”), prime grade, single-side polished Si(211) crystals phosphorous-doped (n-type, $0.007\text{--}0.013\ \Omega\text{ cm}$, referred to as “highly doped”) were of prime grade, single-side polished, with a mis-cut angle of $\pm 0.05^\circ$, $500\ \mu\text{m}$ in thickness and acquired from Silltronix, S.A.S (Archamps, France). Azidomethylferrocene (**2**) was prepared according to previously published procedures.^[38]

Silicon Surface Derivatization: Silicon wafers were cut into samples of either $10 \times 10\text{ mm}$ (for AFM, current–voltage, and XPS measurements) $15 \times 15\text{ mm}$ (electrochemical measurements), and then sequentially rinsed with DCM ($3 \times 50\text{ mL}$), 2-propanol ($3 \times 50\text{ mL}$), and water ($3 \times 50\text{ mL}$). Samples then underwent a 30-min wash in a heated ($100\text{ }^\circ\text{C}$) 3:1 mixture (v/v) of concentrated sulfuric acid (98%) and hydrogen peroxide (30%). Cautionary note: Piranha solution reacts violently with any organic material. Following the Piranha wash, samples were rinsed with water ($3 \times 50\text{ mL}$) and then etched (with the polished side facing upwards) for 13 min in either aqueous 40% ammonium fluoride under ambient light (fluorescent tubes, $\approx 4.1\text{ mW cm}^{-2}$) for highly doped Si(111) and Si(211) samples, or under dark in a mixture of MeOH and aqueous 40% NH_4F (1:10, v/v) for lowly doped Si(211) samples. The etching solutions had been previously deoxygenated by bubbling argon for 15 min ($>99.99\%$, Core-gas). Approximately 50 mg of ammonium sulfite was added to the etching bath as an oxygen scavenger. Hydrogen-terminated samples (Si–H) were then rinsed once with water, twice with DCM ($3 \times 50\text{ mL}$), and then blow-dried using a stream of nitrogen gas. The Si–H surfaces were promptly subjected to a reaction with a small amount of compound **1** (Scheme 1), following slight adjustments to a previously reported hydrosilylation procedure. Briefly, the liquid diyne **1** stock was purged with argon for at least 15 min, and approximately 0.1 mL of it was applied to cover the Si–H surface. The sample rested for 2 h under nitrogen, positioned $\approx 20\text{ cm}$ from a 312 nm light source (Vilber, VL-215.M, nominal power output of 30 W). A 1 mm thick quartz plate (part 01031-AB, SPI Supplies) covered the liquid sample surface to limit its evaporation. The reaction was terminated by removing the acetylene-terminated monolayer (S-1) from the UV chamber, followed by extensive rinsing with DCM.

S-1 samples were stored for 24 h under DCM at $+4\text{ }^\circ\text{C}$ before analysis.

S-1 samples were further derivatized through a CuAAC reaction to prepare a ferrocene-functionalized silicon surface (S-2). To this end, S-1 samples were rinsed with 2-propanol and then placed in a reaction tube containing 4 mL of **2** in 2-propanol ($0.5 \times 10^{-3}\text{ M}$), 1 mL of aqueous copper sulfate (20 mol % relative to **2**), and 1 mL of aqueous sodium ascorbate (100 mol% relative to **2**). The reaction tube was sealed, and the CuAAC reaction was conducted at room temperature with gentle agitation while shielded from ambient light. After 30 min, the ferrocene-modified electrode (S-2) was removed from the vial and thoroughly rinsed with 2-propanol, water, HCl (0.5 M), and DCM. Finally, the samples were dried under a stream of nitrogen gas before analysis.

Atomic Force Microscopy (AFM): AFM measurements were conducted using a Park NX10 instrument from Park Systems Corp., Korea. The instrument has a variable-enhanced conductive (VECA) probe holder for conductive AFM. The AFM tips were solid platinum tips (RMN-25Pt300B and RMN-12Pt300B, Rocky Mountain Nanotechnology, Holladay) with resonance frequency of 14 kHz and a spring constant of 18 N m^{-1} for the RMN-25Pt300B tips and resonance frequency of 9 kHz and a spring constant of 0.8 N m^{-1} for the RMN-12Pt300B tips. The tip radius was approximately 18.2 nm for both tips. All measurements were conducted at room temperature ($22 \pm 2\text{ }^\circ\text{C}$) in ambient air with a relative humidity of approximately 75% unless specified otherwise. Experiments conducted at higher temperatures ($40 \pm 2\text{ }^\circ\text{C}$) were conducted incorporating a Peltier plate (part number 174-3113, RS components, Australia). Electrical contact was ensured between the silicon sample and the metal sample stage/holder bypassing the Peltier plate with copper tape. A positive sign current indicates a tip-to-silicon electron flow. Samples were mounted on the AFM stage using carbon tape after scratching the silicon’s back with SiC emery paper and applying a small amount of gallium–indium eutectic (99.9% Alfa Aesar) on the abraded surface. Imaging parameters were set to a size of $5 \times 5\ \mu\text{m}$, a resolution of 256 points per line, a scan rate of 1.0 Hz, and an applied normal force of 360 nN. Data analysis was performed using XEI processing software (Park Systems), and the reported average and maximum current outputs are based on a minimum of three independent measurements. The vertical palette color legend (scale bar) for the AFM height does not cover the full scale; the scale bar maximum was chosen to better visualize lateral changes in the height images. The residual output (noise level) is approximately around 120 fA. Force–distance (F–d) measurements were employed to estimate adhesion forces and the flexoelectric response of the samples. The maximum deflection was set to 2000 nN, the ramp size to 300 nm and the ramp speed to 300 nm s^{-1} . The applied load on I - V measurements was 100 nN unless specified otherwise. To calculate the adhesion force, the curves were processed with OriginPro 9.0 (OriginLab Corp.).

Scanning Electron Microscopy (SEM): Samples were mounted onto the conductive copper tape and visualized using scanning electron microscopy (SEM). SEM images were captured on an FEI's Verios SEM using an Everhart–Thornley detector (ETD) with a voltage of 5 kV and a probe current of 100 pA.

Macroscopic Current–Voltage Electrical Measurements: Current–voltage (*I*–*V*) measurements were performed inside a grounded and light-proof Faraday cage using a source measure unit (SMU, B2902A, Keysight) and a FeGaInSn drop as the top contact. GaInSn alloy with a composition of 62% gallium, 22% indium, and 16% tin by weight was acquired from Thermo Fisher Scientific and was kept in conditions devoid of air exposure before its utilization. The process of creating magnetic GaInSn was adapted from the methodology described by Chen et al.^[67] In summary, 2 g of the GaInSn alloy were carefully blended with 200 mg of iron particles (approximately 0.5 μm in size, purity of 99.98%, sourced from Alfa Aesar) within a 150 ml Pyrex container. Following this, the resultant magnetic GaInSn composite was subjected to purification through five consecutive rinses with 20 mL of a 0.5 M hydrochloric acid solution, after which it was preserved away from light, and submerged in a 0.5 M HCl solution until needed. The drop of Fe-GaInSn was dispensed on the silicon sample using a threaded plunger syringe (Gilmont, model GS-1200A, 2 mL capacity, 0.002 mL graduation intervals, 24 G). A steel needle with a blunt tip (approximately 0.49 mm radius) was brought into contact with the GaInSn drop and connected to the SMU. The positioning of the needle in contact with GaInSn was controlled by a three-axis micromanipulator (three DTS25 linear translation stages, Thorlabs). For *I*–*V* measurements the junction voltage was cyclically ramped between –2.0 and 2.0 V in steps of 55 mV. The bias is applied from the sample to the GaInSn top contact, and the terminal was configured to be grounded internally (sensing type set to four wires).

Electrochemical Measurements: Cyclic voltammetry and open-circuit potentiometry experiments were performed with a CHI650D electrochemical workstation (CH Instruments) and a three-electrode, single-compartment poly(tetrafluoroethylene) cell. The working electrodes were monolayer-modified **S-2** surfaces (15 × 15 mm), a platinum coil served as the counter electrode, and Ag/AgCl (in a 3.0 M aqueous NaCl solution) was employed as the reference electrode. The geometric area of the working electrode was set to 0.28 cm² using a circular rectilinear cross-sectional Kalrez gasket. Electrical contact between the working electrode and a copper plate was established following the same procedure described for the conductive AFM experiments. The electrolyte was aqueous 1.0 M perchloric acid, and all measurements were conducted in air at room temperature (22 ± 2 °C) and under illumination (660 nm light-emitting diode, nominal power output 940 mW, Thorlabs part M660L4) coupled to a collimator adapter (SM1P25-A, Thorlabs). Illumination of the silicon electrode was through the electrolyte compartment, the collimator–sample distance was approximately 10 cm, and illuminance was measured using a meter from Amprobe (model IC-LM-200). The light intensity at the electrode surface was generally ≈0.12 mW cm⁻². Surface coverages of ferrocene molecules on **S-2** samples are reported in mol cm⁻². Coverage values were calculated from the cyclic voltammetry derived Faradaic charge, taken as the average of the anodic and cathodic scans background-subtracted integrated current. The 99% confidence limit of the mean coverage was calculated following literature procedures.^[68]

X-Ray Photoelectron Spectroscopy (XPS): XPS was employed to analyze the atomic composition and chemical state of elements in the monolayers. An AXIS Ultra DLD spectrometer (Kratos Analytical Inc., Manchester, UK) with monochromatic Al K α radiation (1486.6 eV) and a hemispherical analyzer (165 mm radius) was operated in fixed analyzer transmission mode at 2 × 10⁻⁸ Torr. The analysis area was 300 × 700 μm, and the photoelectron take-off angle was perpendicular to the sample. Survey spectra resulted from the accumulation of five scans using 160 eV pass energy over a 0–1100 eV range in 0.5 eV steps. High-resolution spectra (10 scan accumulations) were collected at a pass energy of 20 eV, with step sizes of 0.05 eV for Si 2p (96–108 eV) and 0.1 eV for C 1s (278–295 eV). The pass energy was set to 20 eV, the step size to 0.05 eV, and the dwell time

to 200 ms. The XPS data underwent processing using CasaXPS software. Spectra analysis involved background subtraction using the U2 Tougaard routine and Lorentzian-Asymmetric (LA, 1.53243) line shape. All reported energies are binding energies (eV) and are corrected by applying a rigid shift to bring the Si 2p_{3/2} emission to 99.5 eV.

Supporting Information

Supporting Information is available from the Wiley Online Library or from the author.

Acknowledgements

This work was financially supported by the Australian Research Council (Grants DP220100553, FT190100148, and FT200100301). The authors acknowledge the instruments and expertise of Microscopy Australia at the Future Industries Institute, University of South Australia, enabled by NCRIS, university, and state government support.

Open access publishing facilitated by Curtin University, as part of the Wiley - Curtin University agreement via the Council of Australian University Librarians.

Conflict of Interest

The authors declare no conflict of interest.

Data Availability Statement

The data that support the findings of this study are available from the corresponding author upon reasonable request.

Keywords

flexoelectricity, Schottky diodes, silicon, surface chemistry, triboelectricity

Received: April 4, 2024

Revised: July 17, 2024

Published online:

- [1] N. A. Al-Ahmadi, *Mater. Res. Express.* **2020**, *7*, 032001.
- [2] B. Ezhilmaran, A. Patra, S. Benny, M. Sreelakshmi, V. Akshay, S. V. Bhat, C. S. Rout, *J. Mater. Chem. C* **2021**, *9*, 6122.
- [3] J. H. Smits, S. C. Meskers, R. A. Janssen, A. W. Marsman, D. M. de Leeuw, *Adv. Mater.* **2005**, *17*, 1169.
- [4] S. Lin, Y. Lu, S. Feng, Z. Hao, Y. Yan, *Adv. Mater.* **2019**, *31*, 1804398.
- [5] H. Shao, J. Fang, H. Wang, H. Niu, H. Zhou, Y. Cao, F. Chen, S. Fu, T. Lin, *Nano Energy* **2019**, *62*, 171.
- [6] C. Hurtado, X. Lyu, S. Ferrie, A. P. Le Brun, M. MacGregor, S. Ciampi, *ACS Appl. Nano Mater.* **2022**, *5*, 14263.
- [7] S. Ferrie, A. P. Le Brun, G. Krishnan, G. G. Andersson, N. Darwish, S. Ciampi, *Nano Energy* **2022**, *93*, 106861.
- [8] D. Liu, L. Zhou, Z. L. Wang, J. Wang, *iScience* **2021**, *24*, 102018.
- [9] Y. Song, N. Wang, Y. Wang, R. Zhang, H. Olin, Y. Yang, *Adv. Energy Mater.* **2020**, *10*, 2002756.
- [10] Z. Lin, B. Zhang, Y. Xie, Z. Wu, J. Yang, Z. L. Wang, *Adv. Funct. Mater.* **2021**, *31*, 2105237.
- [11] J. H. Lee, S. Kim, T. Y. Kim, U. Khan, S.-W. Kim, *Nano Energy* **2019**, *58*, 579.
- [12] X. Lyu, M. MacGregor, J. Liu, N. Darwish, S. Ciampi, *Nano Energy* **2023**, *114*, 108627.

- [13] R. I. G. Dharmasena, J. H. Deane, S. R. P. Silva, *Adv. Energy Mater.* **2018**, *8*, 1802190.
- [14] X. Jiang, W. Huang, S. Zhang, *Nano Energy* **2013**, *2*, 1079.
- [15] P. V. Yudin, A. K. Tagantsev, *Nanotechnology* **2013**, *24*, 432001.
- [16] L. Wang, S. Liu, X. Feng, C. Zhang, L. Zhu, J. Zhai, Y. Qin, Z. L. Wang, *Nat. Nanotechnol.* **2020**, *15*, 661.
- [17] J. Narvaez, F. Vasquez-Sancho, G. Catalan, *Nature*. **2016**, *538*, 219.
- [18] J. Liu, A. Goswami, K. Jiang, F. Khan, S. Kim, R. McGee, Z. Li, Z. Hu, J. Lee, T. Thundat, *Nat. Nanotechnol.* **2018**, *13*, 112.
- [19] S. Ferrie, N. Darwish, J. J. Gooding, S. Ciampi, *Nano Energy* **2020**, *78*, 105210.
- [20] R. A. Oliver, *Rep. Prog. Phys.* **2008**, *71*, 076501.
- [21] A. Avila, B. Bhushan, *Crit. Rev. Solid State Mater. Sci.* **2010**, *35*, 38.
- [22] H.-J. Butt, B. Cappella, M. Kappl, *Surf. Sci. Rep.* **2005**, *59*, 1.
- [23] A. V. Tivanski, J. E. Bemis, B. B. Akhremitchev, H. Liu, G. C. Walker, *Langmuir* **2003**, *19*, 1929.
- [24] R. Garcia, R. Perez, *Surf. Sci. Rep.* **2002**, *47*, 197.
- [25] J. Y. Park, D. F. Ogletree, P. A. Thiel, M. Salmeron, *Science* **2006**, *313*, 186.
- [26] M. Lantz, S. O'Shea, M. Welland, *Phys. Rev. B* **1997**, *56*, 15345.
- [27] S. Jeffery, A. Oral, J. B. Pethica, *Appl. Surf. Sci.* **2000**, *157*, 280.
- [28] S. Hudlet, M. Saint Jean, B. Roulet, J. Berger, C. Guthmann, *J. Appl. Phys.* **1995**, *77*, 3308.
- [29] M. Lepselter, S. Sze, *Bell Syst. Tech. J.* **1968**, *47*, 195.
- [30] B. L. Sharma, *Metal-Semiconductor Schottky Barrier Junctions and Their Applications*, 1st ed., Springer, Berlin **1984**.
- [31] X. G. Zhang, *Electrochemistry of Silicon and Its Oxide*, 1st ed., Springer, New York **2001**.
- [32] M. R. Linford, P. Fenter, P. M. Eisenberger, C. E. D. Chidsey, *J. Am. Chem. Soc.* **1995**, *117*, 3145.
- [33] A. B. Sieval, R. Opitz, H. P. Maas, M. G. Schoeman, G. Meijer, F. J. Vergeldt, H. Zuilhof, E. J. Sudhölter, *Langmuir* **2000**, *16*, 10359.
- [34] S. Ciampi, J. B. Harper, J. J. Gooding, *Chem. Soc. Rev.* **2010**, *39*, 2158.
- [35] S. Ciampi, T. Böcking, K. A. Kilian, M. James, J. B. Harper, J. J. Gooding, *Langmuir* **2007**, *23*, 9320.
- [36] S. Ciampi, M. James, G. Le Saux, K. Gaus, J. J. Gooding, *J. Am. Chem. Soc.* **2012**, *134*, 844.
- [37] B. Fabre, *Chem. Rev.* **2016**, *116*, 4808.
- [38] S. Ciampi, G. Le Saux, J. B. Harper, J. J. Gooding, *Electroanalysis* **2008**, *20*, 1513.
- [39] D. Mandler, S. Kraus-Ophir, *J. Solid State Electrochem.* **2011**, *15*, 1535.
- [40] C. E. Chidsey, C. R. Bertozzi, T. Putvinski, A. Mujscce, *J. Am. Chem. Soc.* **1990**, *112*, 4301.
- [41] J. J. Gooding, S. Ciampi, *Chem. Soc. Rev.* **2011**, *40*, 2704.
- [42] Y. B. Vogel, L. Zhang, N. Darwish, V. R. Gonçalves, A. Le Brun, J. J. Gooding, A. Molina, G. G. Wallace, M. L. Coote, J. Gonzalez, *Nat. Commun.* **2017**, *8*, 2066.
- [43] L. Zhang, Y. B. Vogel, B. B. Noble, V. R. Goncales, N. Darwish, A. L. Brun, J. J. Gooding, G. G. Wallace, M. L. Coote, S. Ciampi, *J. Am. Chem. Soc.* **2016**, *138*, 9611.
- [44] Y. B. Vogel, A. Molina, J. Gonzalez, S. Ciampi, *Anal. Chem.* **2019**, *91*, 5929.
- [45] A. J. Bard, L. R. Faulkner, *Electrochemical Methods: Fundamentals and Applications*, 2nd ed., John Wiley & Sons, New York **2001**.
- [46] A. Mukherjee, A. D. Craciun, J. L. Gallani, M. V. Rastei, *Faraday Discuss* **2017**, *199*, 323.
- [47] C. Hurtado, T. Andreoli, A. P. Le Brun, M. MacGregor, N. Darwish, S. Ciampi, *Langmuir* **2024**, *40*, 201.
- [48] K. Nieuwesteeg, M. Van Der Veen, T. Vink, J. Shannon, *J. Appl. Phys.* **1993**, *74*, 2581.
- [49] W. Jamieson, *Nature* **1910**, *83*, 189.
- [50] F. Vasquez-Sancho, A. Abdollahi, D. Damjanovic, G. Catalan, *Adv. Mater.* **2018**, *30*, 1705316.
- [51] Q. Deng, L. Liu, P. Sharma, *J. Mech. Phys. Solids*. **2014**, *62*, 209.
- [52] L. Sun, L. Zhu, C. Zhang, W. Chen, Z. Wang, *Nano Energy* **2021**, *83*, 105855.
- [53] J. Wu, C. Wu, W. Zhang, C. Zhang, W. Chen, *Nano Energy* **2024**, *123*, 109415.
- [54] B. Javvaji, B. Mortazavi, X. Zhuang, T. Rabczuk, *Carbon*. **2021**, *185*, 558.
- [55] K. M. Hamdia, H. Ghasemi, X. Zhuang, N. Alajlan, T. Rabczuk, *Comput. Methods Appl. Mech. Eng.* **2018**, *337*, 95.
- [56] Y.-X. Wang, J.-G. Li, G. Seifert, K. Chang, D.-B. Zhang, *Nano Lett.* **2024**, *24*, 411.
- [57] U. K. Bhaskar, N. Banerjee, A. Abdollahi, Z. Wang, D. G. Schlom, G. Rijnders, G. Catalan, *Nat. Nanotechnol.* **2016**, *11*, 263.
- [58] S. Garcia-Manyes, A. G. Güell, P. Gorostiza, F. Sanz, *J. Chem. Phys.* **2005**, *123*, 11.
- [59] L. Zhang, I. Zarudi, *Int. J. Mech. Sci.* **2001**, *43*, 1985.
- [60] K. P. Olson, C. A. Mizzi, L. D. Marks, *Nano Lett.* **2022**, *22*, 3914.
- [61] T. Namazu, Y. Isono, T. Tanaka, *J. Microelectromech. Syst.* **2002**, *11*, 125.
- [62] H. Ikeda, F. Salleh, *Appl. Phys. Lett.* **2010**, *96*, 012106.
- [63] Z. Wang, R. Song, Z. Shen, W. Huang, C. Li, S. Ke, L. Shu, *Appl. Phys. Lett.* **2019**, *115*, 252905.
- [64] S. M. Sze, *Semiconductor Devices: Physics and Technology*, 2nd ed., John Wiley & Sons, New York **2001**.
- [65] P. Kinget, C. Vezyrtzis, E. Chiang, B. Hung, T. L. Li, in *2008 IEEE Custom Integrated Circuits Conf.*, IEEE, Piscataway, NJ, **2008**, pp. 715–720.
- [66] Y. Xia, W. Qian, Y. Yang, *ACS Appl. Mater. Interfaces*. **2024**, *16*, 9597.
- [67] W. Zhou, Q. Liang, T. Chen, *Adv. Intell. Syst.* **2020**, *2*, 1900170.
- [68] J. Miller, J. C. Miller, *Statistics and Chemometrics for Analytical Chemistry*, 7th ed., Coronet Books Inc., London **2018**.

Chapter 6. Summary and future outlook

6.1 Summary

This thesis presents an experimental and comprehensive exploration of the relationship between apparently separated fields such as surface chemistry, mechanical motion, and current generation in monolayer-functionalized electrodes. I have investigated how mechanical motion (i.e., sliding and pressing events) have the potential to produce clean energy in the form of current output. Silicon, a primary and low-cost semiconductor in industry, has been proposed as an electrode platform.

Chapter 1 introduced SC physics' fundamental concepts, including a comprehensive overview of the band diagram theory. A brief description of the band energetics on silicon–electrolyte and silicon–metal contact based on the equalization of the E_F , is also provided. Given the relevance of the surface properties control on the overall current-generation phenomena, concepts of silicon surface chemistry were also introduced. Chemical etching methods to remove the native oxide layer and surface functionalization pathways were subsequently considered and presented. The main techniques, including working principles and history, were presented to characterize and test the system (namely, silicon–monolayer functionalized surfaces).

Chapter 2 focused on the role of crystal orientation and surface conductivity in current output generation when silicon performs as a TENG. Surfaces bearing higher conductivity (namely Si(211)) returned greater current output compared to less conductive cuts (namely, Si(111)). Remarkably, predicting the TENG performance of the system by a simple electrochemistry approach (i.e., CV shape analysis) was explored and proposed as a straightforward diagnostic

tool. The chapter concludes with an analysis of how the introduction of surface defects (namely, oxide) transiently enhances current output.

The current generation mechanism—the sliding of the AFM tip along the silicon surface—induces surface damage, limiting the longevity of the device. **Chapter 3** addressed the root cause of surface damage during device operation. Results demonstrated that this damage, driven primarily by mechanical pressure, leads to a reduction in current output. Interestingly, the current drop caused by surface damage occurs with a slight delay, as successive trace and retrace scans produced comparable output. A closer examination of line scans revealed that the spots with the highest current output correspond to locations where mechanical pressure is greatest.

Prompted by conclusions dragged on Chapter 3, the motivation focused on replacing the hard metal contact (i.e., Pt tip) with a softer metal contact (i.e., Galinstan). **Figure 1** shows the vibration set-up designed to emulate the sliding events happening in the Schottky junction on AFM. Although the junction was stable, unlike on AFM, the contact pressure was negligible and so was the tribocurrent generated.

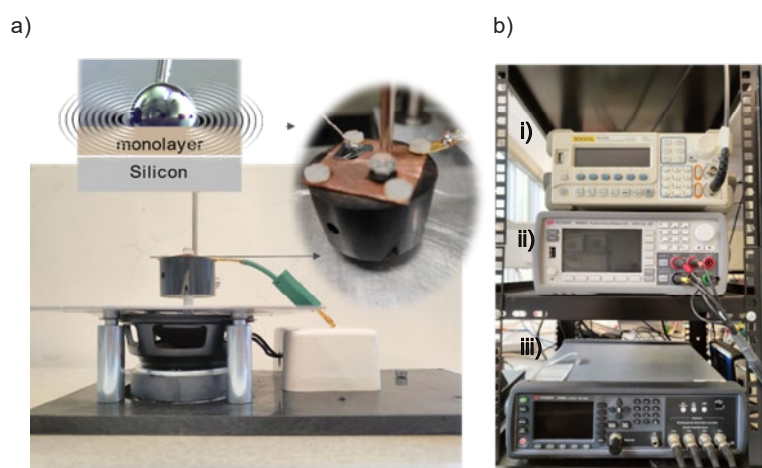


Figure 1. (a) Experimental vibration set-up designed to produce vibrations emulating the sliding events happening on a conventional C-AFM experiment. Insets show the silicon–SAM–Galinstan junction in ohmic contact with a copper plate previously polished. (b) Shows the instruments used to perform the experiment. (i) Function generator, model DG-1022 to control the vibrations. (ii) SMU, model B2902A to collect current output and (iii) LCR meter, model E4980A, to collect capacitance data.

Although this lack of pressure turned out to be detrimental for Galinstan to be implemented on a hypothetical TENG set-up, in **Chapter 4** its role as a macroscopic probe was explored. The goal was to use Galinstan top contacts on Si-SAMs systems to track shifts in the leakage current, and to predict with these changes the DC output when the electrode forms part of a TENG. Since results showed that the junction stability was controlled by the surface-to-volume ratio, the chapter explores a chemical strategy (i.e., iron particle addition) to increase the surface tension of the Galinstan probe. This increase in surface tension was crucial to enhancing the reproducibility and repeatability of the I–V measurements but had a negative impact on the capacitance measurements. Galinstan top contact was finally used to explore the electrical characteristics of silicon electrodes functionalized via a novel alkyne–alkyne homocoupling reaction.

While I–Vs collected with Galinstan contacts (namely, macroscopic junctions) were close to ideal, I–Vs collected on AFM (namely, nanoscopic junction) returned more often than not, non-ideal behavior characterized by an anomalous high reverse current (i.e., inverted I–V curves). To explain this effect, **Chapter 5** starts with an analysis of the adhesion force under bias (–1.5 to +1.5) between the tip and the sample showing that adhesion was greater when the junction was depleted. This instability triggers tip-tilting which translates into an induced strain gradient in the silicon sample. Therefore, Chapter 5 focused on the role of strain gradients occurring on the tip–silicon junction and the subsequent surface electric polarization (i.e., flexoelectric effect). The consequence of this so-called flexoelectric effect is that an additional ‘parasitic’ reverse bias term is added to the instrumental (external) bias, shifting the turn-on voltage and increasing the leakage current.

6.2 Future outlook

Although tremendous effort has been made to account for the main factors governing the triboelectric and flexoelectric phenomena, there is still some degree of uncertainty regarding the working mechanism of devices that convert mechanical motion into electricity. For instance, results in **Chapter 5** indicate that the influence of temperature and doping points to the Zener breakdown mechanism being more probable than avalanche breakdown, regarding the nature of the electrical breakdown involved. This is based on the fact that quantum tunnelling decreases with the widening of the depletion region. Nevertheless, further research into triboelectric and flexoelectric phenomena under varying environmental conditions is needed for a deeper understanding and development of this class of technologies.

Additionally, while this thesis has focused on single-contact asperity (i.e., Pt tip contacting the electrode surface) further research on multi asperity contacts warrants further attention. Recent advances in tribology have started to highlight the role of surface chemistry governing macroscopic friction phenomena. It seems that van der Waals interactions, along with interfacial bond networks, including covalent and hydrogen bonds, play a critical role in influencing stick-slips events. Despite these insights, the exact correlation between the number of interfacial bonds and the friction force at the microscopic level is still not fully understood. Furthermore, it remains unclear whether the bonding mechanisms driving nanoscale friction are also responsible for friction at larger, application-relevant scales.

An important open question concerns the impact and extent of the flexoelectric effect, and whether it can be optimized to increase current output. Even though **Chapter 5** has provided significant insights into the role of strain gradient at the tip–electrode junction, the magnitude of the silicon flexoelectric coefficient remains experimentally undetermined. More quantitative studies are needed to investigate how zero-bias current reacts to material deformation when strain is applied, which would help clarify the role of flexoelectricity in the zero-bias

performance of TENGs. This can be examined using soft materials, like silicon thin films, where both the current and the material's deformation are recorded at the same time.

The implications of these findings open up new avenues for future research in enhancing the durability and current generation of silicon-based TENGs. Developing strategies to mitigate oxidative damage, while preserving the beneficial effects of surface defects will be critical for advancing the practical application of these devices. Furthermore, the insights gained from this research extend beyond silicon, suggesting that similar approaches could be applied to other semiconductor materials, potentially leading to the discovery of new, more efficient energy-harvesting technologies.

Appendix A. Rights and permissions

Figure 6 is reprinted from the book “Electrochemistry of silicon and its oxides”

Xiagoe Gregory Zhang

Under the terms of the terms and conditions provided by Springer Nature and Copyright Clearance Center.

Etching of Oxides
Publication: Springer eBook
Publisher: Springer Nature
Date: Jan 1, 2004
Copyright © 2004, Kluwer Academic Publishers

Order Completed

Thank you for your order.

This Agreement between Carlos Hurtado ("You") and Springer Nature ("Springer Nature") consists of your license details and the terms and conditions provided by Springer Nature and Copyright Clearance Center.

Your confirmation email will contain your order number for future reference.

License Number	5852301089599	Printable Details
License date	Aug 19, 2024	

Figure 7 is reprinted from the work Galinstan Liquid Metal Electrical Contacts for Monolayer-Modified Silicon Surfaces, Jan 1, 2024, American Chemical Society

Carlos Hurtado, Tony Andreoli, Anton P. Le Brun, et al

Galinstan Liquid Metal Electrical Contacts for Monolayer-Modified Silicon Surfaces

Author: Carlos Hurtado, Tony Andreoli, Anton P. Le Brun, et al
Publication: Langmuir
Publisher: American Chemical Society
Date: Jan 1, 2024
Copyright © 2024, American Chemical Society

PERMISSION/LICENSE IS GRANTED FOR YOUR ORDER AT NO CHARGE

This type of permission/license, instead of the standard Terms and Conditions, is sent to you because no fee is being charged for your order. Please note the following:

- Permission is granted for your request in both print and electronic formats, and translations.
- If figures and/or tables were requested, they may be adapted or used in part.
- Please print this page for your records and send a copy of it to your publisher/graduate school.
- Appropriate credit for the requested material should be given as follows: "Reprinted (adapted) with permission from (COMPLETE REFERENCE CITATION). Copyright (YEAR) American Chemical Society." Insert appropriate information in place of the capitalized words.
- One-time permission is granted only for the use specified in your RightsLink request. No additional uses are granted (such as derivative works or other editions). For any uses, please submit a new request.


If credit is given to another source for the material you requested from RightsLink, permission must be obtained from that source.

[BACK](#) [CLOSE WINDOW](#)

Figure 9 is reprinted Non-Ideal Cyclic Voltammetry of Redox Monolayers on Silicon Electrodes: Peak Splitting is Caused by Heterogeneous Photocurrents and Not by Molecular Disorder Jan 1, 2022 American Chemical Society

Song Zhang, Xin Lyu, Carlos Hurtado Torres, et al

Langmuir

 ACS Publications
Most Trusted. Most Cited. Most Read.

Non-Ideal Cyclic Voltammetry of Redox Monolayers on Silicon Electrodes: Peak Splitting is Caused by Heterogeneous Photocurrents and Not by Molecular Disorder
Author: Song Zhang, Xin Lyu, Carlos Hurtado Torres, et al
Publication: Langmuir
Publisher: American Chemical Society
Date: Jan 1, 2022
Copyright © 2022, American Chemical Society

PERMISSION/LICENSE IS GRANTED FOR YOUR ORDER AT NO CHARGE

This type of permission/license, instead of the standard Terms and Conditions, is sent to you because no fee is being charged for your order. Please note the following:

- Permission is granted for your request in both print and electronic formats, and translations.
- If figures and/or tables were requested, they may be adapted or used in part.
- Please print this page for your records and send a copy of it to your publisher/graduate school.
- Appropriate credit for the requested material should be given as follows: "Reprinted (adapted) with permission from {COMPLETE REFERENCE CITATION}. Copyright {YEAR} American Chemical Society." Insert appropriate information in place of the capitalized words.
- One-time permission is granted only for the use specified in your RightsLink request. No additional uses are granted (such as derivative works or other editions). For any uses, please submit a new request.

If credit is given to another source for the material you requested from RightsLink, permission must be obtained from that source.

[BACK](#) [CLOSE WINDOW](#)

Figure 14 is reprinted with permission granted by AAAS MATERIAL:

Figure 1 from Park et al., *SCIENCE*, 14 Jul 2006 Vol 313, Issue 5784, pp. 186,

Jeong Young Park, D. F. Ogletree, P. A. Thiel, and M. Salmeron

AAAS MATERIAL:

Figure 1 from Park et al., *SCIENCE*, 14 Jul 2006
Vol 313, Issue 5784, pp. 186, DOI: 10.1126/science.1125017

YOUR RE-USE: THESIS/DISSERTATION

Title: Harvesting DC current from friction and pressure on silicon-based diodes: from micro to macro devices
Publication date: December 1, 2024

Dear Carlos:

Thank you very much for your interest in the AAAS material identified in your request.

We are pleased to have you include this material in your thesis or dissertation subject to the following guidelines. These guidelines also appear on our website: <https://www.science.org/content/page/reprints-and-permissions> under the heading 'Using AAAS material in a thesis or dissertation'.

REPRODUCING AAAS MATERIAL IN YOUR THESIS OR DISSERTATION

AAAS permits the use of content published in its journals but only provided the following criteria are met:

1. If you are using figures/tables, permission is granted for use in print and electronic versions of your dissertation or thesis.
2. A full text article may be used only in print versions of a dissertation or thesis. AAAS does not permit the reproduction of full text articles in electronic versions of theses or dissertations.
3. The following credit line must be printed along with the AAAS material: "From [Insert Full Reference Citation]/ Reprinted with permission from AAAS".
4. All required credit lines and notices must be visible any time a user accesses any part of the AAAS material and must appear on any printed copies that an authorized user might make.
5. The AAAS material may not be modified or altered except that figures and tables may be modified with permission from the author. Author permission for any such changes must be secured prior to your use.
6. AAAS must publish the full paper prior to your use of any of its text or figures.
7. If the AAAS material covered by this permission was published in *Science* during the years 1974-1994, you must also obtain permission from the author, who may grant or withhold permission, and who may or may not charge a fee if permission is granted. See original article for author's address. This condition does not apply to the news articles published in *Science*.
8. Permission covers the distribution of your dissertation or thesis on demand by a third-party distributor (e.g. ProQuest/UMI), provided the AAAS material covered by this permission remains in situ and is not distributed by that third party outside of the context of your thesis/dissertation.
9. Permission does not apply to figures/photos/artwork or any other content or material included in your work that are credited to non-AAAS sources. If the requested material is sourced to or references non-AAAS sources, you must obtain authorization from that source as well before using that material. You agree to hold harmless and indemnify AAAS against any claims arising from your use of any content in your work that is credited to non-AAAS sources.
10. By using the AAAS Material identified in your request, you agree to abide by all the terms & conditions herein.
11. AAAS makes no representations or warranties as to the accuracy of any information contained in the AAAS material covered by this permission, including any warranties of merchantability or fitness for a particular purpose.

If how you wish to use the content falls outside of these guidelines or if you have any questions, please let me know.

Kind regards,

Figure 15a is reprinted with permission from the work Flexoelectronics of centrosymmetric semiconductors, *Nat. Nanotechnol.* **15**, 661–667 (2020).

Wang, L., Liu, S., Feng, X. *et al.*

Flexoelectronics of centrosymmetric semiconductors

Author: Longfei Wang et al
 Publication: Nature Nanotechnology
 Publisher: Springer Nature
 Date: Jun 22, 2020

Copyright © 2020, The Author(s), under exclusive licence to Springer Nature Limited

Order Completed

Thank you for your order.

This Agreement between Carlos Hurtado ("You") and Springer Nature ("Springer Nature") consists of your license details and the terms and conditions provided by Springer Nature and Copyright Clearance Center.

Your confirmation email will contain your order number for future reference.

License Number: 5836251191784 [Printable Details](#)

License date: Jul 25, 2024

Licensed Content		Order Details	
Licensed Content Publisher	Springer Nature	Type of Use	Thesis/Dissertation
Licensed Content Publication	Nature Nanotechnology	Requestor type	non-commercial (non-profit)
Licensed Content Title	Flexoelectronics of centrosymmetric semiconductors	Format	print and electronic
Licensed Content Author	Longfei Wang et al	Portion	figures/tables/illustrations
Licensed Content Date	Jun 22, 2020	Number of figures/tables/illustrations	1
		Would you like a high resolution image with your order?	no
		Will you be translating?	no
		Circulation/distribution	1 - 29
		Author of this Springer Nature content	no

Figure 15b is reprinted with permission from the work Band Bending and Ratcheting Explain Triboelectricity in a Flexoelectric Contact Diode. Nano Letters Vol 22. Issue 10

Karl P. Olson Christopher A. Mizzi and Laurence D. Marks

Band Bending and Ratcheting Explain Triboelectricity in a Flexoelectric Contact Diode
Author: Karl P. Olson, Christopher A. Mizzi, Laurence D. Marks
Publication: Nano Letters
Publisher: American Chemical Society
Date: May 1, 2022
Copyright © 2022, American Chemical Society

PERMISSION/LICENSE IS GRANTED FOR YOUR ORDER AT NO CHARGE

This type of permission/license, instead of the standard Terms and Conditions, is sent to you because no fee is being charged for your order. Please note the following:

- Permission is granted for your request in both print and electronic formats, and translations.
- If figures and/or tables were requested, they may be adapted or used in part.
- Please print this page for your records and send a copy of it to your publisher/graduate school.
- Appropriate credit for the requested material should be given as follows: "Reprinted (adapted) with permission from (COMPLETE REFERENCE CITATION). Copyright (YEAR) American Chemical Society." Insert appropriate information in place of the capitalized words.
- One-time permission is granted only for the use specified in your RightsLink request. No additional uses are granted (such as derivative works or other editions). For any uses, please submit a new request.

If credit is given to another source for the material you requested from RightsLink, permission must be obtained from that source.

[BACK](#) [CLOSE WINDOW](#)

Figure 16 is reprinted with permission from the work Flexible Triboelectric generator Nano Energy March 2012 provided by Elsevier and Copyright Clearance Center

Feng-Ru Fan,Zhong-Qun Tian,Zhong Lin Wang



Flexible triboelectric generator

Author: Feng-Ru Fan,Zhong-Qun Tian,Zhong Lin Wang

Publication: Nano Energy

Publisher: Elsevier

Date: March 2012

Copyright © 2012 Elsevier Ltd. All rights reserved.

Order Completed

Thank you for your order.

This Agreement between Carlos Hurtado ("You") and Elsevier ("Elsevier") consists of your license details and the terms and conditions provided by Elsevier and Copyright Clearance Center.

Your confirmation email will contain your order number for future reference.

License Number 5852321002001

[Printable Details](#)

License date Aug 19, 2024

Licensed Content

Licensed Content Publisher	Elsevier
Licensed Content Publication	Nano Energy
Licensed Content Title	Flexible triboelectric generator
Licensed Content Author	Feng-Ru Fan,Zhong-Qun Tian,Zhong Lin Wang
Licensed Content Date	Mar 1, 2012
Licensed Content Volume	1
Licensed Content Issue	2
Licensed Content Pages	7

Order Details

Type of Use	reuse in a thesis/dissertation
Portion	figures/tables/illustrations
Number of figures/tables/illustrations	1
Format	both print and electronic
Are you the author of this Elsevier article?	No
Will you be translating?	No

About Your Work

Title of new work	Harvesting DC current from friction and pressure on silicon-based diodes: from micro to macro devices
Institution name	Curtin Uniersity
Expected presentation date	Nov 2024

Additional Data

Portions	1
The Requesting Person / Organization to Appear on the License	Carlos Hurtado

Organic Monolayers on Si(211) for Triboelectricity Generation: Etching Optimization and Relationship between the Electrochemistry and Current Output



Author: Carlos Hurtado, Xin Lyu, Stuart Ferrie, et al

Publication: ACS Applied Nano Materials

Publisher: American Chemical Society

Date: Oct 1, 2022

Copyright © 2022, American Chemical Society

PERMISSION/LICENSE IS GRANTED FOR YOUR ORDER AT NO CHARGE

This type of permission/license, instead of the standard Terms and Conditions, is sent to you because no fee is being charged for your order. Please note the following:




- Permission is granted for your request in both print and electronic formats, and translations.
- If figures and/or tables were requested, they may be adapted or used in part.
- Please print this page for your records and send a copy of it to your publisher/graduate school.
- Appropriate credit for the requested material should be given as follows: "Reprinted (adapted) with permission from {COMPLETE REFERENCE CITATION}. Copyright {YEAR} American Chemical Society." Insert appropriate information in place of the capitalized words.
- One-time permission is granted only for the use specified in your RightsLink request. No additional uses are granted (such as derivative works or other editions). For any uses, please submit a new request.

If credit is given to another source for the material you requested from RightsLink, permission must be obtained from that source.

[BACK](#)

[CLOSE WINDOW](#)

Oxidative Damage during the Operation of Si(211)-Based Triboelectric Nanogenerators

by Carlos Hurtado  and Simone Ciampi *  

School of Molecular and Life Sciences, Curtin University, Bentley, WA 6102, Australia

* Author to whom correspondence should be addressed.

Surfaces **2023**, *6*(3), 281-290; <https://doi.org/10.3390/surfaces6030020>

Submission received: 23 July 2023 / Revised: 16 August 2023 / Accepted: 18 August 2023 /

Published: 21 August 2023

Dear Carlos,

Thank you for your email.

No special permission is required to reuse all or part of an article published by MDPI, including figures and tables. For articles published under an open-access Creative Common CC BY license, any part of the article may be reused without permission, provided that **the original article is cited**. Reuse of an article does not imply endorsement by the authors or MDPI.

Please Note: Some articles (especially Reviews) may contain figures, tables, or text taken from other publications, for which MDPI does not hold the copyright or the right to re-license the published material. Please note that you should speak with the original copyright holder (usually the original publisher or authors), to enquire about whether or not this material can be re-used.

Please let us know if you have any further questions.

Kind regards,
Support team

Galinstan Liquid Metal Electrical Contacts for Monolayer-Modified Silicon Surfaces



Author: Carlos Hurtado, Tony Andreoli, Anton P. Le Brun, et al

Publication: Langmuir

Publisher: American Chemical Society

Date: Jan 1, 2024

Copyright © 2024, American Chemical Society

PERMISSION/LICENSE IS GRANTED FOR YOUR ORDER AT NO CHARGE

This type of permission/license, instead of the standard Terms and Conditions, is sent to you because no fee is being charged for your order. Please note the following:

- Permission is granted for your request in both print and electronic formats, and translations.
- If figures and/or tables were requested, they may be adapted or used in part.
- Please print this page for your records and send a copy of it to your publisher/graduate school.
- Appropriate credit for the requested material should be given as follows: "Reprinted (adapted) with permission from {COMPLETE REFERENCE CITATION}. Copyright {YEAR} American Chemical Society." Insert appropriate information in place of the capitalized words.
- One-time permission is granted only for the use specified in your RightsLink request. No additional uses are granted (such as derivative works or other editions). For any uses, please submit a new request.

If credit is given to another source for the material you requested from RightsLink, permission must be obtained from that source.

BACK

CLOSE WINDOW

Schottky Diode Leakage Current Fluctuations: Electrostatically Induced Flexoelectricity in Silicon

Carlos Hurtado, Melanie MacGregor, Kai Chen, Simone Ciampi

First published: 09 August 2024 | <https://doi.org/10.1002/adv.202403524>



CC BY 4.0

ATTRIBUTION 4.0 INTERNATIONAL

Deed

Canonical URL: <https://creativecommons.org/licenses/by/4.0/>

[See the legal code](#)

You are free to:

Share — copy and redistribute the material in any medium or format for any purpose, even commercially.

Adapt — remix, transform, and build upon the material for any purpose, even commercially.

The licensor cannot revoke these freedoms as long as you follow the license terms.

Under the following terms:

Attribution — You must give [appropriate credit](#), provide a link to the license, and [indicate if changes were made](#). You may do so in any reasonable manner,

Appendix B. Statement of contributions to others

Statement of contributions for:

Hurtado, C.; Lyu, X.; Ferrie, S.; Le Brun, A. P.; MacGregor, M.; Ciampi, S. Organic Monolayers on Si(211) for Triboelectricity Generation: Etching Optimization and Relationship between the Electrochemistry and Current Output. *ACS Appl. Nano Mater.* 2022, 5, 14263–14274. Included in **Chapter 2**.

I, Carlos Hurtado, as the first author conducted surface functionalization experiments, electrochemical measurements, and AFM tests, collected and analyzed relevant data, drafted the first version, and prepared the necessary figures and schematics for the paper, except for the contributions of co-authors as specified below.

Stuart Ferrie and Xin Lyu helped with AFM data using related software.

Melanie MacGregor performed XPS analysis.

Anton P. Le Brun performed XRR analysis.

Simone Ciampi designed the project, supervised the project, interpreted the data and co-wrote the manuscript.

Co-author signatures:


Stuart Ferrie



Melanie MacGregor

Melanie MacGregor Digitally signed by Melanie MacGregor
Date: 2024.09.03 14:29:34 +09'30'

Anton P. Le Brun 


Xin Lyu

Simone Ciampi 

Statement of contributions for:

Hurtado, C.; Ciampi, S. Oxidative Damage during the Operation of Si(211)-Based Triboelectric Nanogenerators. *Surfaces 2023*, 6, 281– 290. Included in Chapter 3

I, Carlos Hurtado, as the first author conducted surface functionalization experiments, electrochemical measurements, and AFM tests, collected and analyzed relevant data, drafted the first version, and prepared the necessary figures and schematics for the paper, except for the contributions of co-authors as specified below.

Simone Ciampi supervised the project, interpreted the data, and co-wrote the manuscript.

Co-author signatures:

Simone Ciampi

A handwritten signature in black ink, appearing to read 'Simone Ciampi', written in a cursive style.

Statement of contributions for:

Hurtado, C.; Andreoli, T.; Le Brun, A. P.; MacGregor, M.; Darwish, N.; Ciampi, S. Galinstan Liquid Metal Electrical Contacts for Monolayer-Modified Silicon Surfaces. *Langmuir* 2024, 40, 201-210. Included in **Chapter 4**

I, Carlos Hurtado, as the first author conducted surface functionalization experiments, Galinstan synthesis, electrochemical and electrical measurements, and AFM tests, collected and analyzed relevant data, drafted the first version, and prepared the necessary figures and schematics for the paper, except for the contributions of co-authors as specified below.

Tony Andreoli helped with some of the electrochemical measurements.

Melanie MacGregor performed XPS analysis.

Anton P. Le Brun performed XRR analysis.

Nadim Darwish supervised the project.

Simone Ciampi designed the project, supervised the project, interpreted the data, and co-wrote the manuscript.

Co-author signatures:

Tony andreoli



Melanie MacGregor

Melanie MacGregor Digitally signed by Melanie MacGregor
Date: 2024.09.03 14:29:34 +09'30"

Anton P. Le Brun



Simone Ciampi



Nadim Darwish



Statement of contributions for:

Hurtado, C.; Kai. Chen. Melanie MacGregor, Ciampi, S. Leaky Schottky Diodes: Electrostatically Induced Flexoelectricity in Silicon *Adv. Sci, 2024* Included in Chapter 4

I, Carlos Hurtado, as the first author conducted surface functionalization experiments, , electrochemical and electrical measurements, and AFM tests, collected and analyzed relevant data, drafted the first version, and prepared the necessary figures and schematics for the paper, except for the contributions of co-authors as specified below.

Kai Chen performed SEM analysis

Melanie MacGregor performed XPS analysis.

Simone Ciampi designed the project, supervised the project, interpreted the data, and co-wrote the manuscript.

Co-author signatures:

Kai Chen



Melanie MacGregor

Melanie MacGregor

Digitally signed by Melanie MacGregor
Date: 2024.09.03 14:29:34 +09'30'

Simone Ciampi



Appendix C. Supplementary material of Chapter 2

Organic Monolayers on Si(211) for Triboelectricity Generation: Etching Optimization and Relationship between the Electrochemistry and Current Output

Carlos Hurtado,^a Xin Lyu,^a Stuart Ferrie,^a Anton P. Le Brun,^b Melanie MacGregor,^c Simone Ciampi,^{a,*}

^aSchool of Molecular and Life Sciences, Curtin University, Bentley, Western Australia 6102, Australia

^bAustralian Centre for Neutron Scattering, Australian Nuclear Science and Technology Organization, Lucas Heights, New South Wales 2234, Australia

^cFlinders Institute for Nanoscale Science and Technology, Flinders University, Bedford Park, South Australia 5042, Australia

Correspondence: simone.ciampi@curtin.edu.au

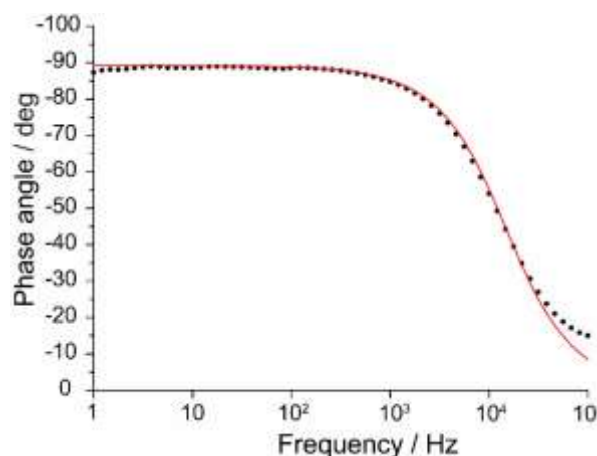


Figure S1. Representative EIS phase angle versus frequency plot for a **S-1** sample on Si(111). The E_{dc} was set to -0.5 V. Black dots are the experimental values, and the red line is the best fit (Chi-squared = 0.01). The equivalent circuit used in the fitting is shown in Section S2. Refined values of R_{film} , and C_{dl} where $6.2 \times 10^6 \Omega$ and 0.1×10^{-6} F respectively.

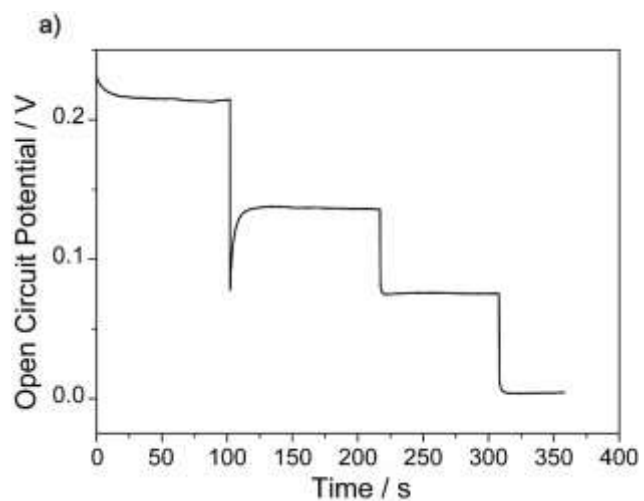


Figure S2. Progressive cathodic shift of the open circuit potential for a Si(111) S-2 sample (photoanode) as a function of its illumination intensity. The electrode was irradiated with a red LED and progressively increasing the light intensity from dark (0 – 100 s), to 1.0 mW cm^{-2} (100 – 200 s), 1.7 mW cm^{-2} (200 – 300 s) and reaching 3.4 mW cm^{-2} (after 300 s).

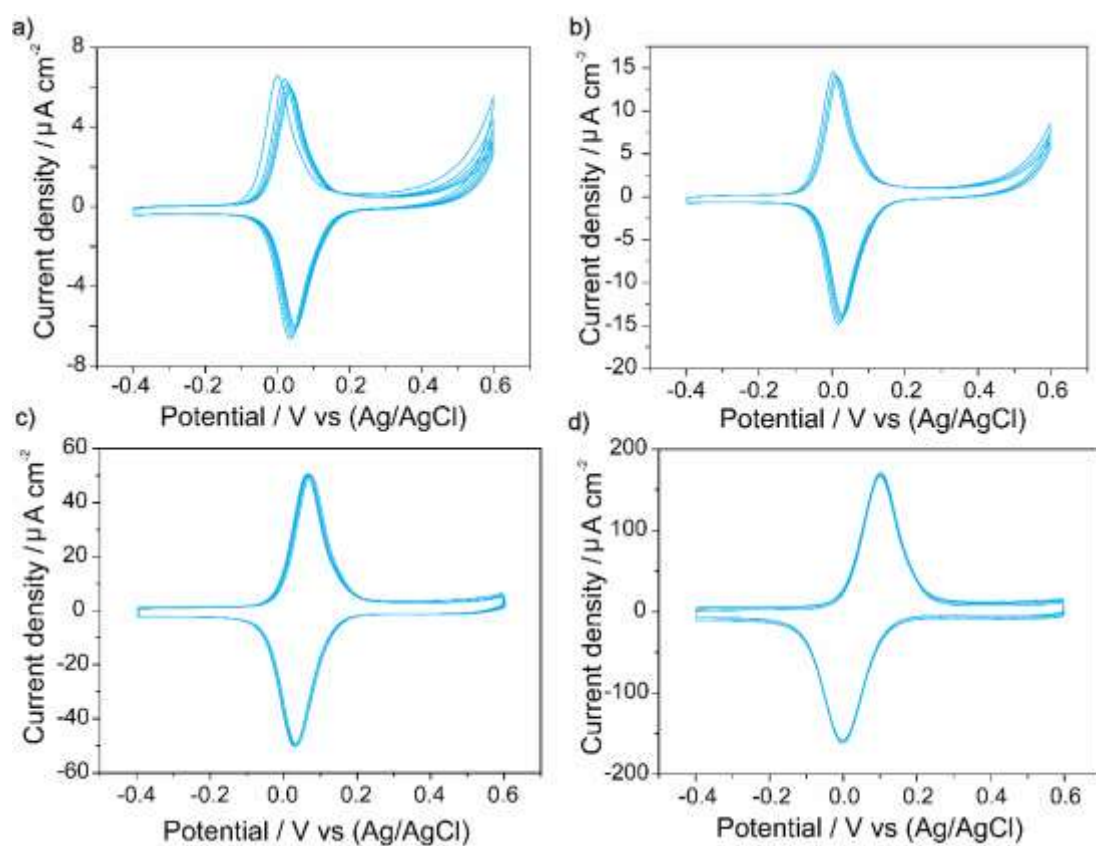


Figure S3. Representative cyclic voltammograms (CVs) for a S-2 Si(111) photoanode. The electrode was illuminated at a light intensity of 1.7 mW cm^{-2} . The scan rate was (a) 50 mV/s, (b) 100 mV/s, (c) 500 mV/s and (d) 2000 mV/s.

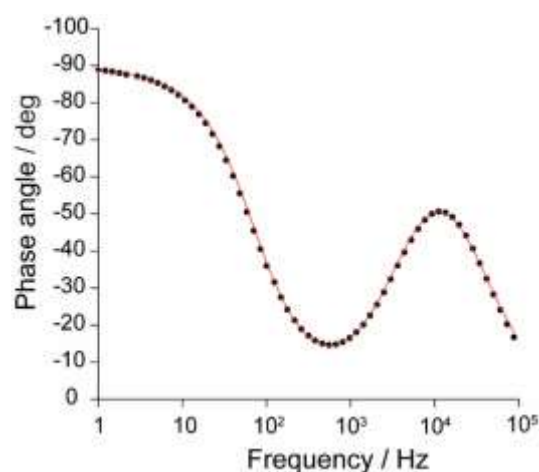


Figure S4. Representative EIS phase angle versus frequency plot for a **S-2** sample on Si(111). The E_{dc} was set to 0.1 V. The electrode was illuminated at a light intensity of 1.7 mW cm^{-2} . Black dots are the experimental values and the red line is the best fit (Chi-squared = 0.01). The equivalent circuit model used in the fitting is shown in Section S2. The refined k_{et} was $(3.6 \pm 1.4) \times 10^2 \text{ s}^{-1}$. Values of R_{et} , C_{ads} , and C_{dl} were $50.1 \text{ } \Omega$, $4.2 \times 10^{-5} \text{ F}$ and $1.1 \times 10^{-6} \text{ F}$, respectively. Capacitors were modelled as CPEs with power modifiers of 0.98 for C_{dl} and 0.99 for C_{ads} .

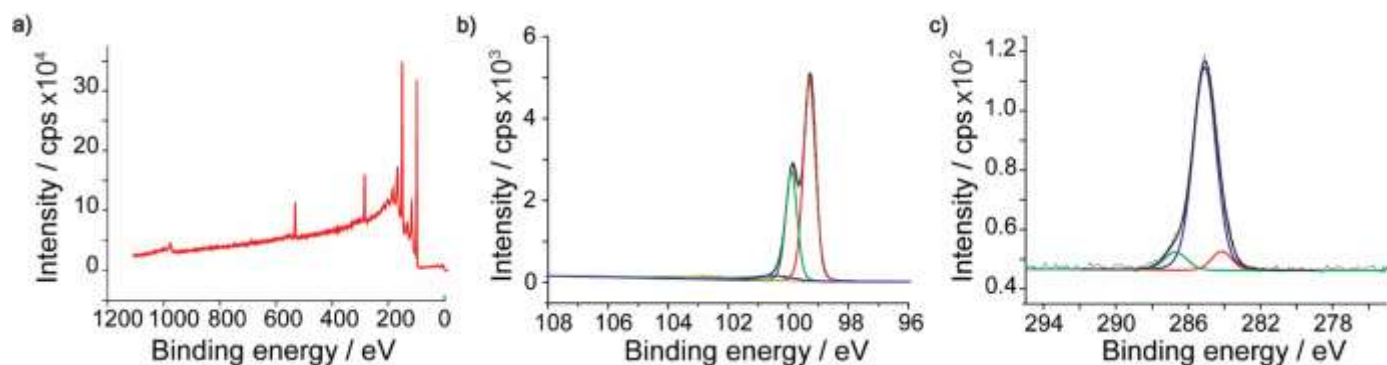


Figure S5. XPS spectra for **S-1** samples on Si(211). The etching time was 13 min [40% aqueous NH_4F under ambient light (0.2 mW cm^{-2})]. (a) XPS survey spectrum. (b) Narrow scan of the Si 2p region. The Si $2p_{3/2}$ peak was 99.5 eV. The high binding energy shoulder (0.40 eV higher than Si $2p_{1/2}$) is tentatively attributed to photoelectrons from Si-H species.² In the 101.5–104 eV region, photoelectrons from $\text{Si}^{(2)}$, $\text{Si}^{(3)}$ and $\text{Si}^{(4)}$ oxides merge into a single band. (c) Narrow scan of the C 1s region. The signal was deconvoluted into a main C–C peak (carbon bound to carbon) at 284.9 eV, a C–Si (carbon bound to silicon) at 284.0 eV, and a contribution at 286.9 eV ascribed to C≡C and/or C–OH.³

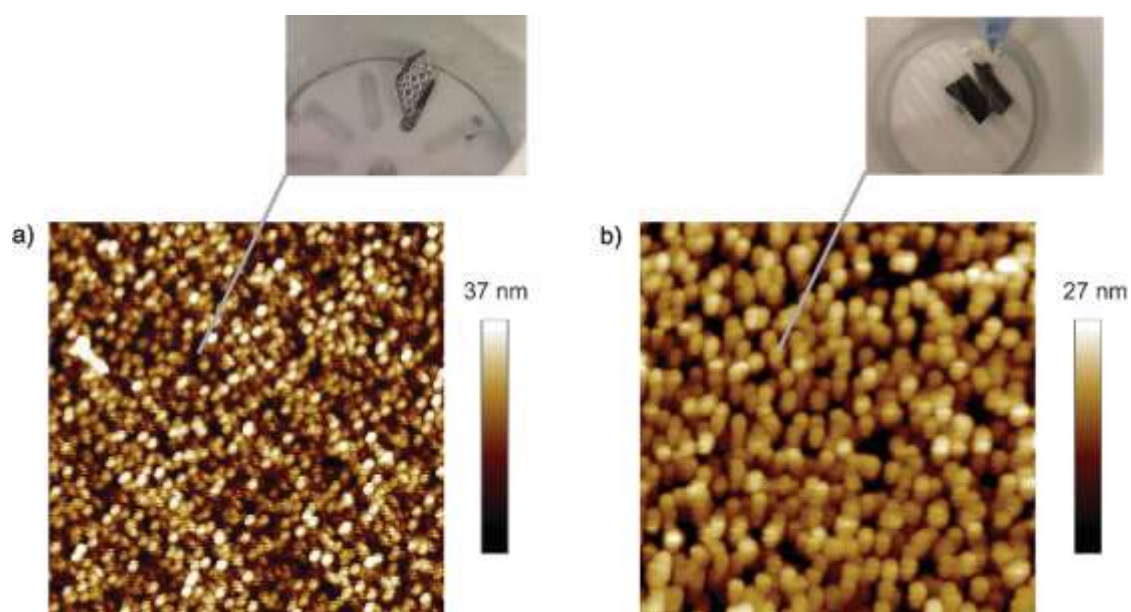


Figure S6. (a) AFM topography image of a **S-1** sample grafted on a Si(211) wafer etched for 13 min in aqueous 40% NH_4F under ambient light and in the absence of methanol. The sample roughness was 8.6 nm. The photograph shown in (a) above the AFM map shows the wafer while being etched. (b) AFM topography image of a representative **S-1** sample grafted on a Si(211) wafer etched for 13 min in a mixture of MeOH and 40% NH_4F (1:10) under ambient light. The sample roughness was 3.1 nm. The photograph shown in (b) above the AFM map shows the wafer while being etched.

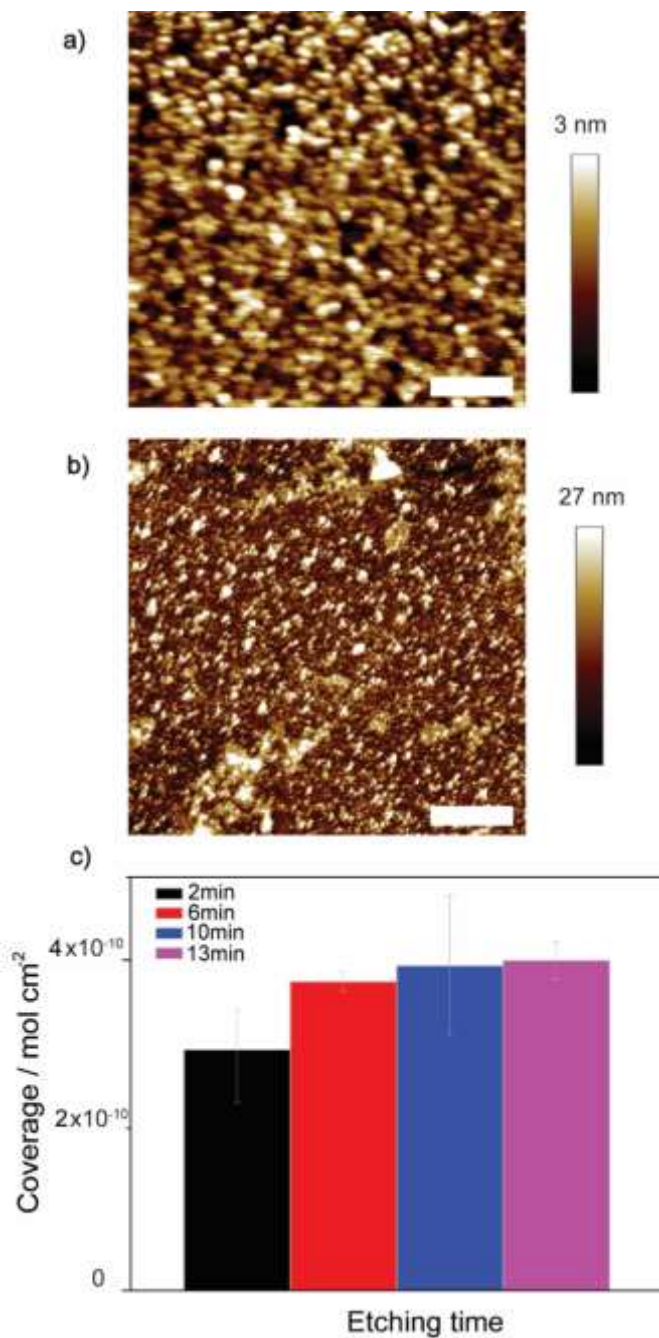


Figure S7. (a) AFM topography image of a representative **S-1** sample on Si(211). The wafer was etched for 2 min in a mixture of MeOH and 40% NH₄F (1:10), under ambient light (0.2 mW cm⁻²). The sample roughness was 1.0 nm. (b) AFM topography image of a representative **S-1** sample grafted on Si(211) etched for 13 min in a mixture of MeOH and 40% NH₄F (1:10) under ambient light. Roughness value for the sample shown in panel was 3.4 nm. (c) Bar plot showing the evolution of the ferrocene coverage for **S-2** samples prepared from the **S-1** samples of (a) and (b) as well as on samples prepared via intermediate etching times. The etching time is shown in figure, and the error bars represent the standard deviation from the mean coverage value.

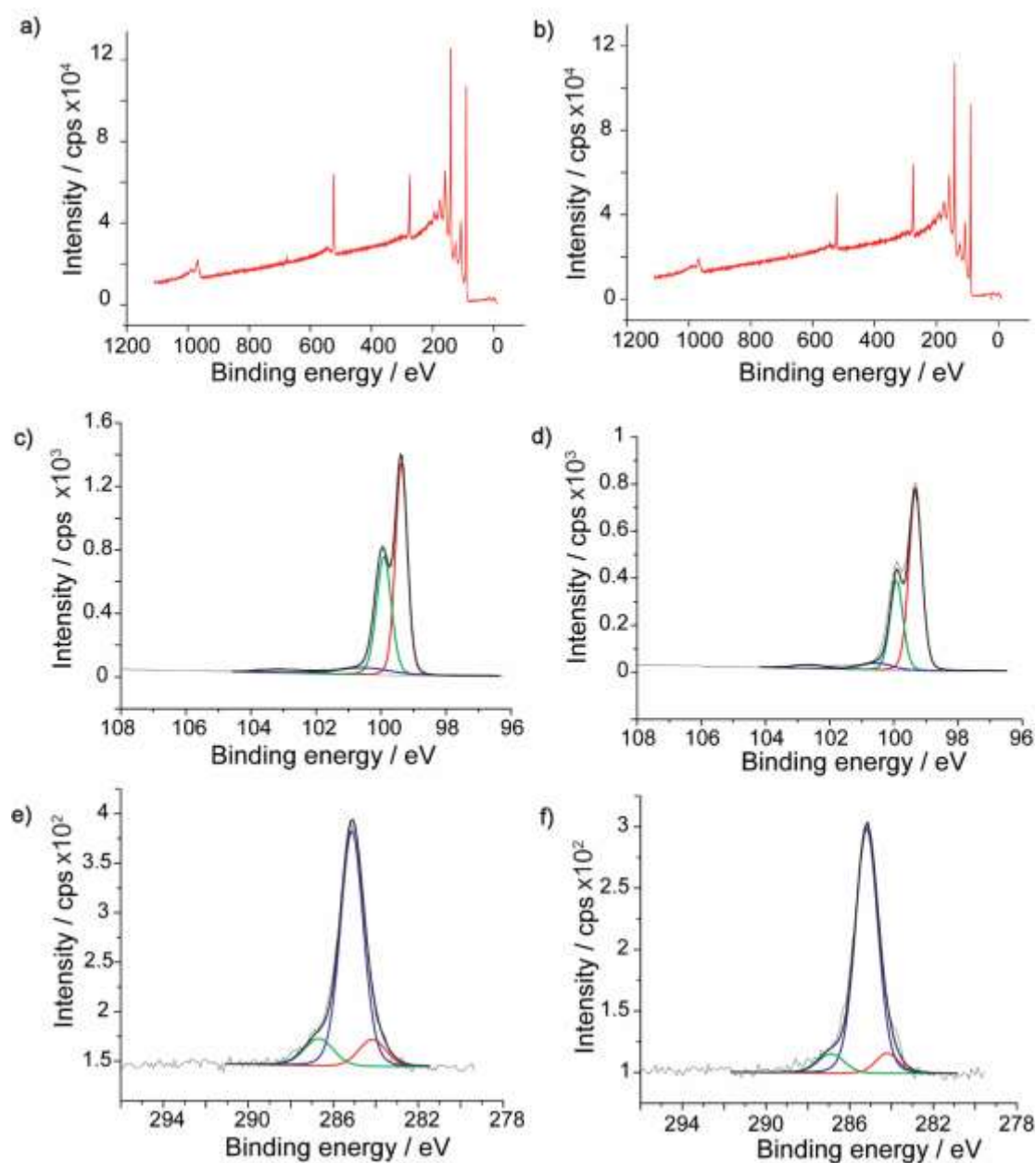


Figure S8. XPS data for **S-1** samples grafted on Si(211). The Si(211) substrates were etched for 2 min (a, c, e) and for 13 min (b, d, f), in a mixture of MeOH and 40% NH_4F (1:10) under ambient light (0.2 mW cm^{-2}). (a, b) XPS survey spectra. (c, d) Narrow scans of the Si 2p region. The Si $2p_{3/2}$ peak was at 99.5 eV. The high binding energy shoulder (0.40 eV from Si $2p_{1/2}$) is tentatively attributed to Si-H species.² In the 101.6–104 eV region, photoelectrons from $\text{Si}^{(2)}$ $\text{Si}^{(3)}$ and $\text{Si}^{(4)}$ oxides merge into a single band (2 min etch). Photoelectron from $\text{Si}^{(2)}$ and $\text{Si}^{(3)}$ and $\text{Si}^{(4)}$ oxides, are attributed to the signal at 101.5–103.7 eV (13 min etch). (e, f) Narrow scans of the C 1s region. The spectra were deconvoluted into a main C-C signal (carbon bound to carbon) at 284.9 eV, a C-Si (carbon bound to silicon) shifted at 284.0 eV, and a third contribution at 286.9 eV, ascribed to $\text{C}\equiv\text{C}$ and/or C-OH.³

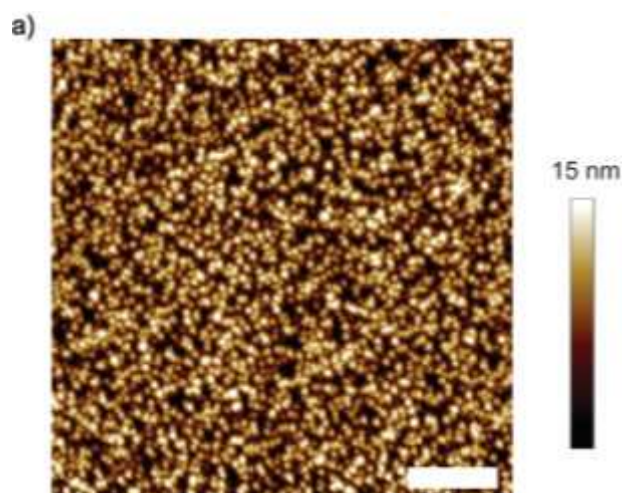


Figure S9. (a) AFM topography image of a representative **S-1** sample prepared on Si(211). The Si(211) substrate was etched for 13 min in a mixture of MeOH and 40% NH_4F (1:10) in dark. The roughness value for the sample shown in figure is 2.6 nm.

Table S1. Surface roughness (AFM data) for **S-1** samples on Si(211) as function of solvent, etchant, etching time and illumination levels

Solvent	Etching time (min)	Illumination (mWcm ⁻²)	Roughness (RMS, nm)
Aqueous 40% NH ₄ F	2	0.2	0.4 ± 0.1
MeOH 10%, 40% NH ₄ F (1:10, v/v)	2	0.2	0.9 ± 0.1
MeOH 10%, 40% NH ₄ F (1:10, v/v)	2	dark	0.7 ± 0.4
Aqueous 40% NH ₄ F	13	0.2	7.8 ± 3.2
MeOH 10%, 40% NH ₄ F (1:10, v/v)	13	0.2	3.2 ± 0.3
MeOH 10%, 40% NH ₄ F (1:10, v/v)	13	dark	2.6 ± 0.1

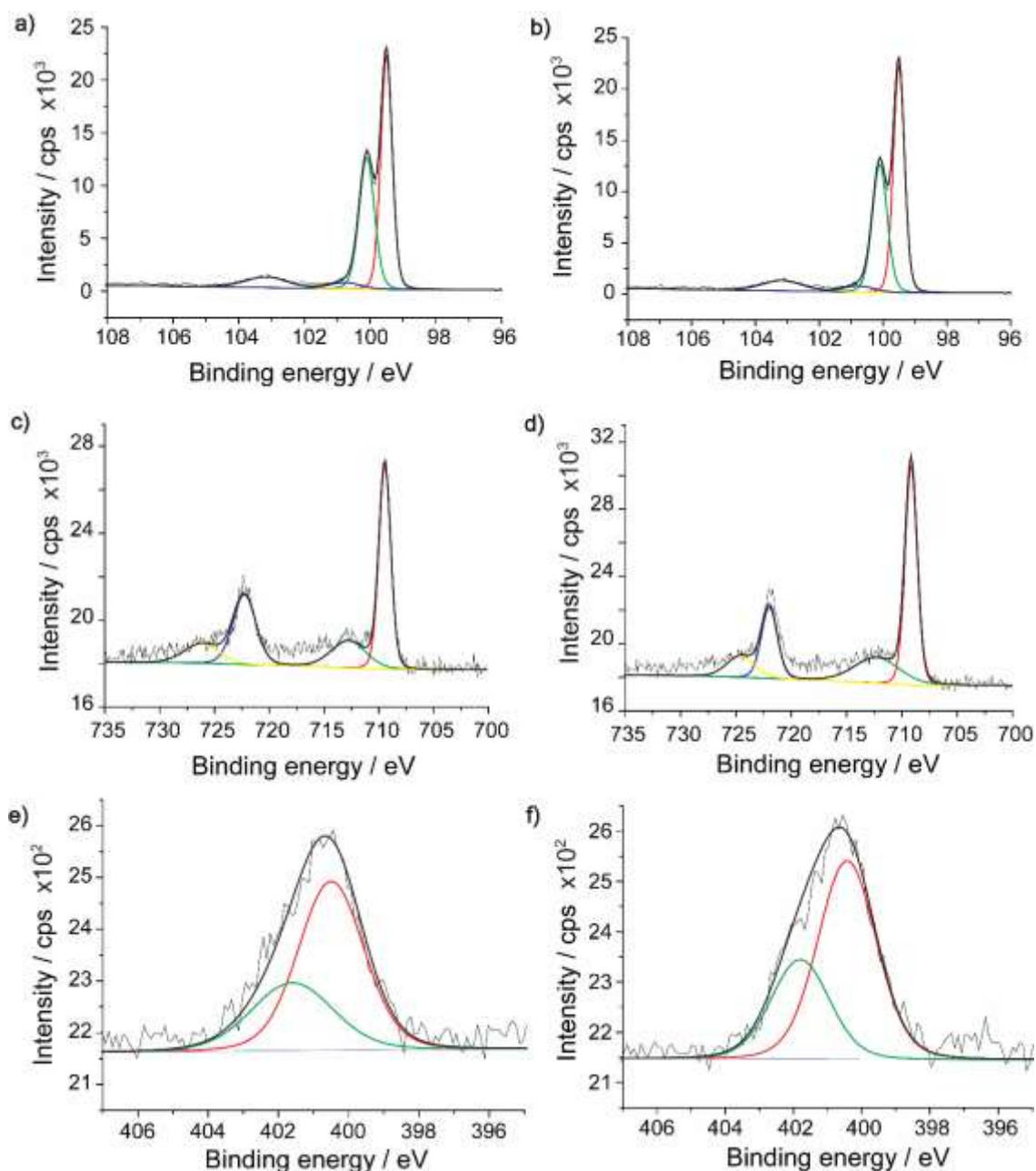


Figure S10. XPS data for S-2 samples grafted on Si(111) (a, c, e), and on Si(211) (b, d, f). The Si(211) substrates were etched for 13 min in a mixture of MeOH and 40% NH_4F (1:10) under ambient light (0.2 mW cm^{-2}). (a, b) Narrow scans of the Si 2p region. The Si $2p_{3/2}$ peak was at 99.5 eV. The high binding energy shoulder (0.40 eV from the Si $2p_{1/2}$) is tentatively ascribed to Si-H species. In the 102–104 eV region, photoelectrons from $\text{Si}^{(2)}$, $\text{Si}^{(3)}$ and $\text{Si}^{(4)}$ oxides merge into a single band (2 min etch). Photoelectron from $\text{Si}^{(3)}$ and $\text{Si}^{(4)}$ oxides, are attributed to the signal at 102–104 eV (13 min etch). (c, d) Narrow scans of the Fe 2p region showing refined Fe $2p_{3/2}$ [708.6 eV for Fe(II)] and Fe $2p_{1/2}$ (721.5 eV for Fe(II)) spin–orbit-split signals. High binding energy shoulders are Fe(III) signals from ferricenium species. (e, f) Narrow scans of the N 1s region.

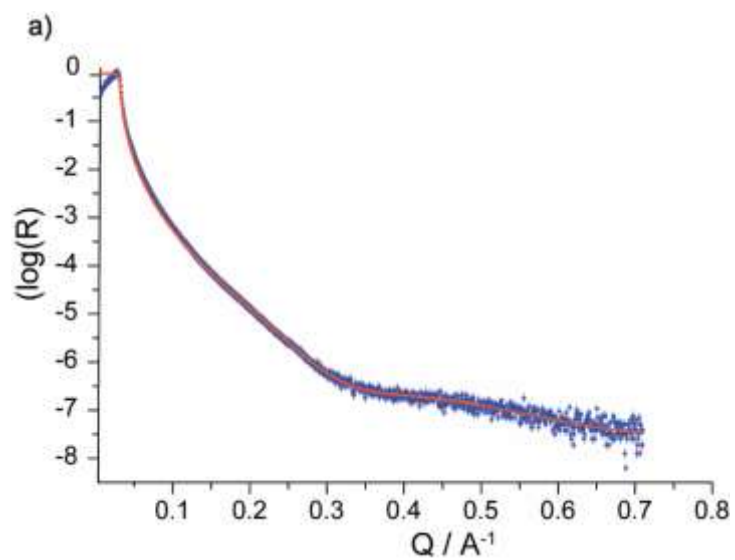


Figure S11. XRR profile for a **S-1** film on Si(111) surfaces. The refined model (red line) is shown over the experimental data (solid blue symbols, $\chi^2 \sim 10$). The etching time was 13 min [40% aqueous NH_4F under ambient light (0.2 mW cm^{-2})]

Table S2. XRR Refined Structural Parameters for **S-1** films on Si(111) and Si(211)

	Si(111)	Si(211)
SLD (\AA^{-2})	1.3×10^{-5}	1.0×10^{-5}
Roughness monolayer–air interface (\AA)	2.9	3.1
Roughness monolayer–silicon interface (\AA)	3.2	8.2
Organic film thickness (\AA)	9.5	10

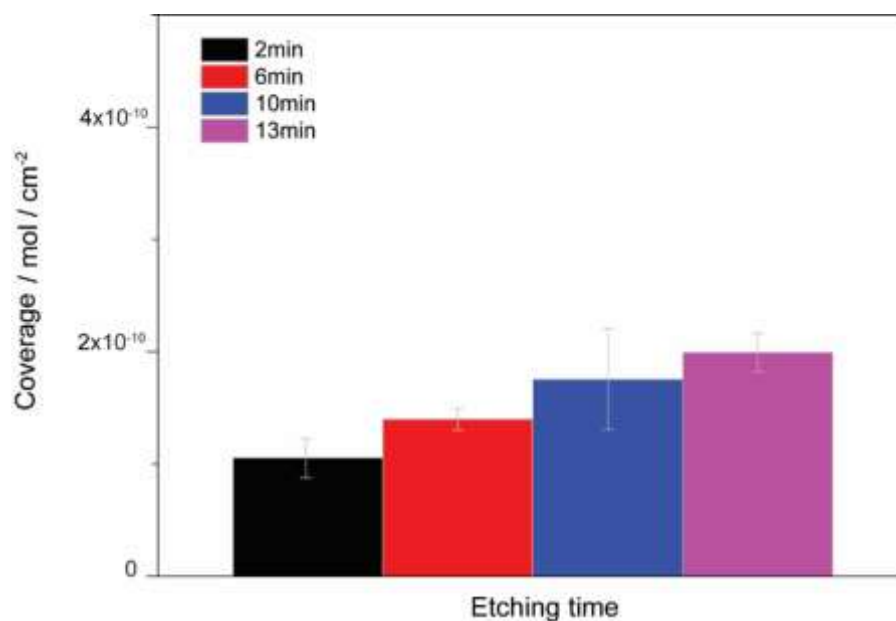


Figure S12. Evolution of the ferrocene surface coverage for **S-2** samples prepared on Si(211) with etching time. Si(211) substrates were etched in dark in a mixture of MeOH and 40% NH₄F (1:10). The etching time varied between 2 and 13 min and is specified in figure [(black) 2 min; (red) 6 min; (blue) 10 min; (pink) 13 min]. The error bar represents the standard deviation from the mean coverage value.

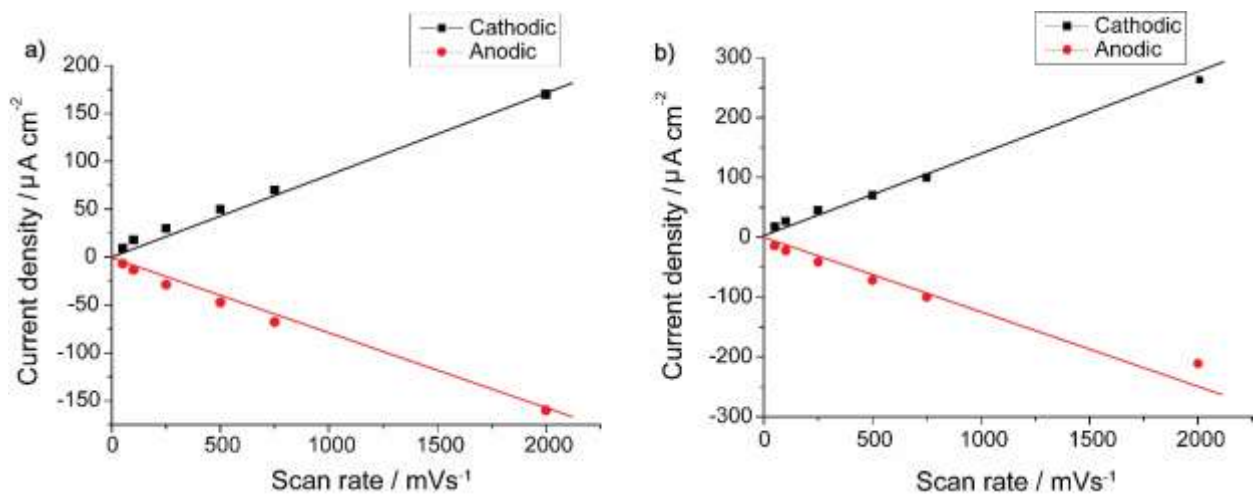


Figure S13. Cathodic and anodic peak heights (current density) as function of the voltage scan rate (mV/s) for S-2 samples made on (a) Si(111) and (b) Si(211). The electrodes were illuminated at a light intensity of 1.7 mW cm^{-2} . Si(211) samples were etched in a mixture of MeOH and aqueous 40% NH_4F (1:10, v/v) in dark.

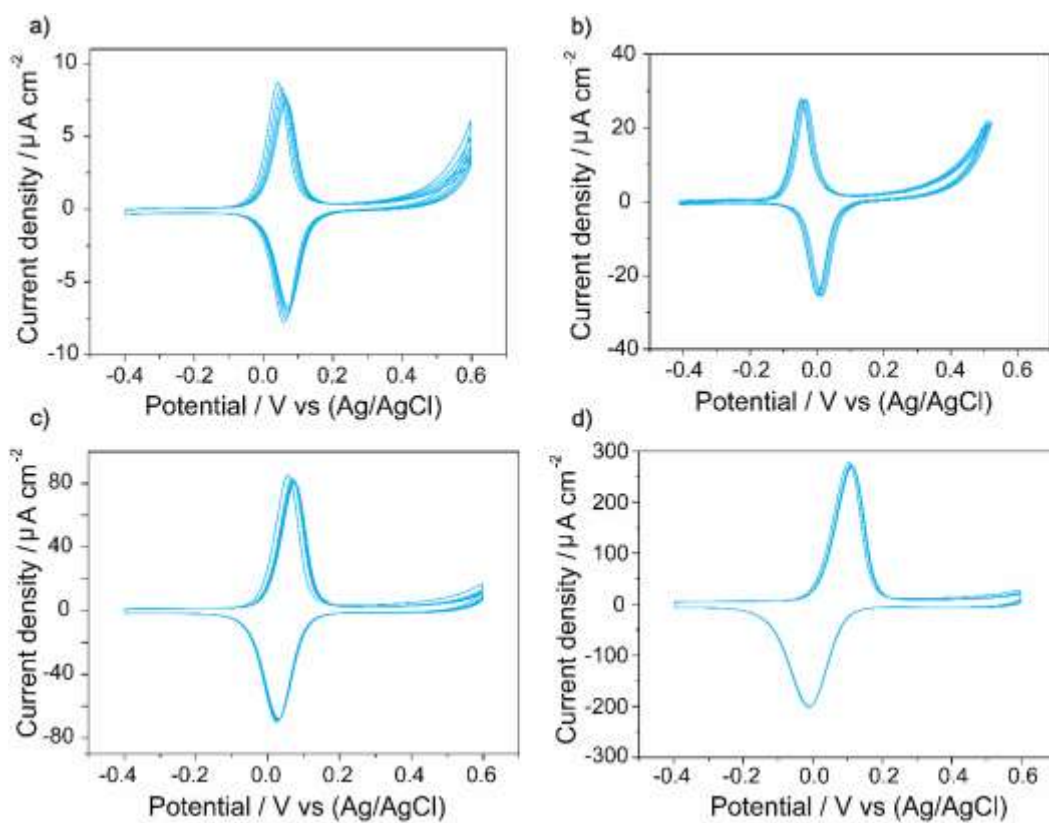


Figure S14. Representative cyclic voltammograms (CVs) for a S-2 Si(211) photoanode. The electrode was illuminated at a light intensity of 1.7 mW cm^{-2} . The voltage scan rate was (a) 50 mV/s, (b) 100 mV/s, (c) 500 mV/s, and (d) 2000 mV/s. Samples were etched in a mixture of MeOH and aqueous 40% NH_4F (1:10, v/v) in dark.

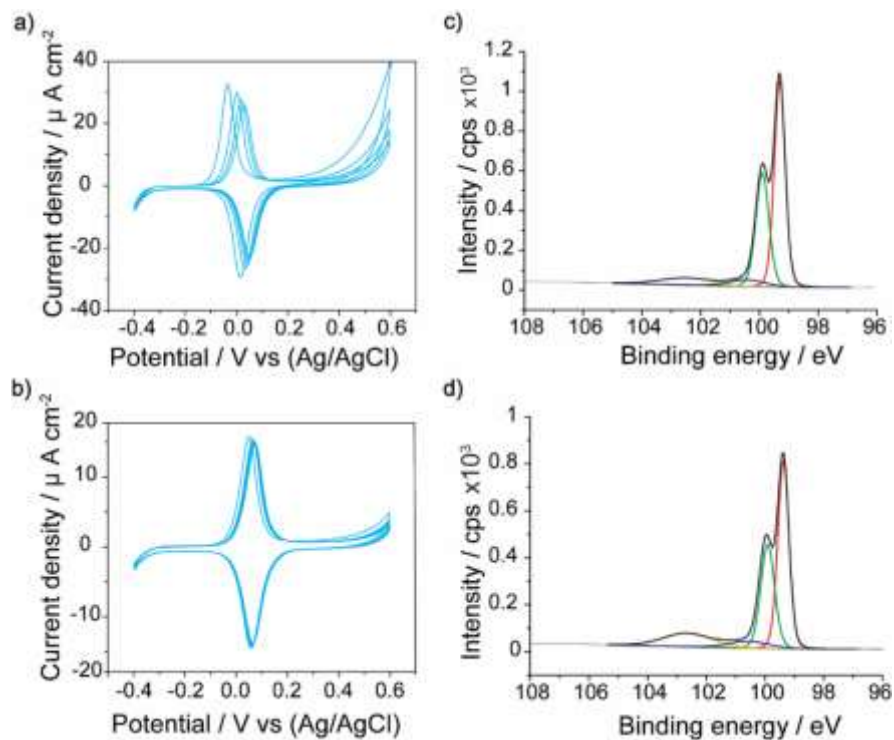


Figure S15. Representative CVs (100 mV/s, 1.0 M HClO₄) for S-2 samples made on Si(211). The Si(211) substrate was etched in a mixture of MeOH and aqueous 40% NH₄F (1:10, v/v) in absence of light. The CVs in figure were recorded after either (a) 10 CV cycles or (b) 40 cycles. Cycles were in the -0.4 to 0.6 V range (100 mV/s, 1.0 M HClO₄). The electrodes were illuminated at a light intensity of 1.7 mW cm⁻². (c, d) XPS high-resolution Si 2p spectra for the samples analyzed by CVs in (a, b). A broad 100–104 eV signal is the result of photoelectrons from Si⁽¹⁾, Si⁽²⁾, Si⁽³⁾ and Si⁽⁴⁾ oxides.

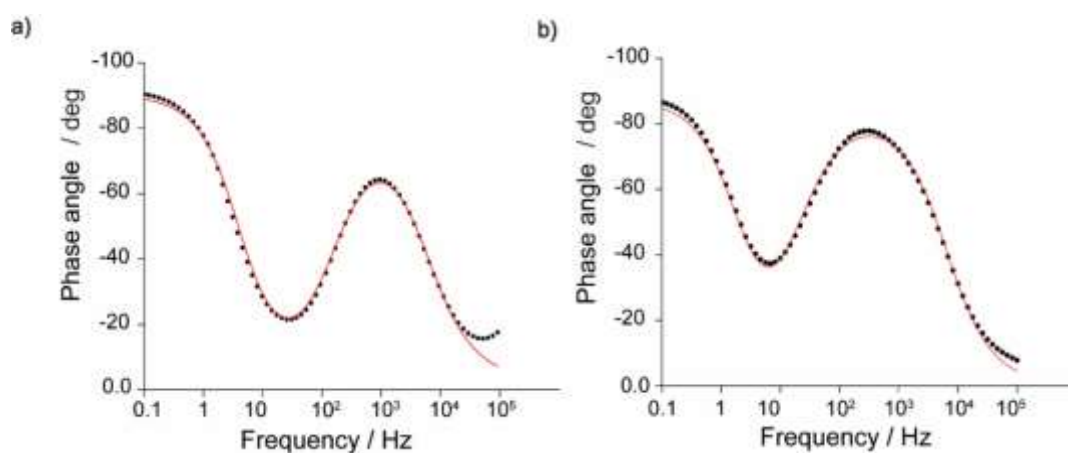


Figure S16. Representative EIS phase angle versus frequency plots for **S-2** samples on Si(211). Samples were anodically damaged by means of 10 and 40 cycles ((a) and (b) respectively) prior to the EIS experiments. The E_{dc} was set to 0.1 V. Black dots are the experimental values and the red lines the best fits. The equivalent circuit used in the fitting is shown in Section S2. Refined values of R_{et} , C_{ads} , and C_{dl} were 696.2 Ω , 5.5×10^{-5} F and 2.7×10^{-6} F for samples subjected to 10 CV cycles, and 7170 Ω , 1.2×10^{-5} F and 1.8×10^{-6} F for samples subjected to 40 cycles (yielding k_{et} of 12.9 s^{-1} and 5.9 s^{-1} respectively). Experimental data are solid points and the fits solid lines ((a) Chi-squared = 0.01, (b) Chi-squared = 0.02)). The substrate was Si(211) etched in a mixture of MeOH and aqueous 40% NH_4F (1:10, v/v) in dark.

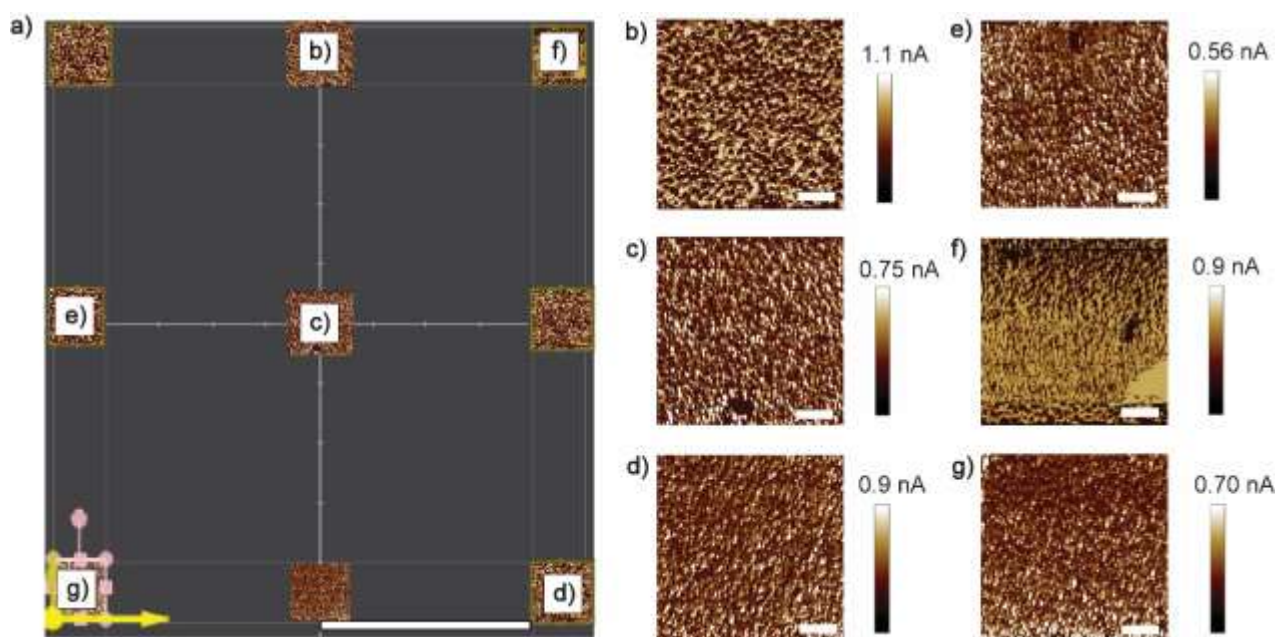


Figure S17. (a) Location of nine separate sampling regions across a Si(211) S-1 surface. The horizontal scale bar is 2.5 mm, and the size of the AFM micrographs, indicating the actual sampling locations, is not up to scale. (b–g) Representative C-AFM maps for S-1 Si(211) samples etched for 13 min in 1:10 v/v MeOH/NH₄F 40% while shielded from ambient light. Horizontal scale bars in (b–g) are 1 μm. The mean current output value for the different locations were (b) 241 pA, (c) 347 pA, (d) 293 pA, (e) 429 pA, (f) 371 pA, and (g) 434 pA.

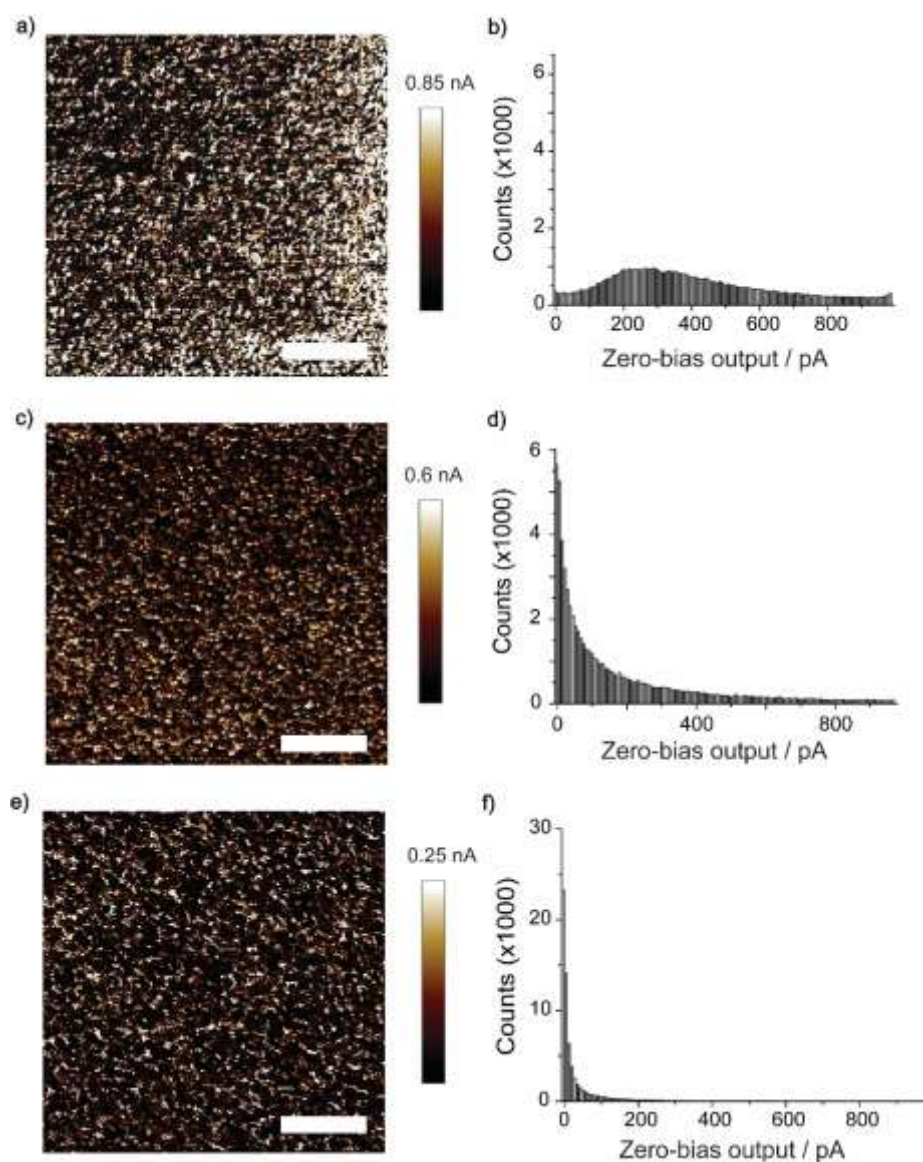


Figure S18. Zero-bias C-AFM maps for **S-1** samples etched under dark for 13 min in a mixture of MeOH and aqueous 40% NH_4F (1:10, v/v). Panels (a, c, e) are current maps recorded after 1 (mean of current output value of 352 pA), 2 (mean of current output value of 187 pA) and 3 (mean of current output value of 47 pA) successive scan cycles under 50 nN of normal force. Panels (b, d, f) show histograms of the current output in the C-AFM maps. The histograms' y-axis counts indicate the number of pixels (sample locations) of a given current magnitude, with a total of $\sim 65\text{k}$ pixels making up a C-AFM map. Horizontal scale bars in panels (a, c, e) are 1 μm .

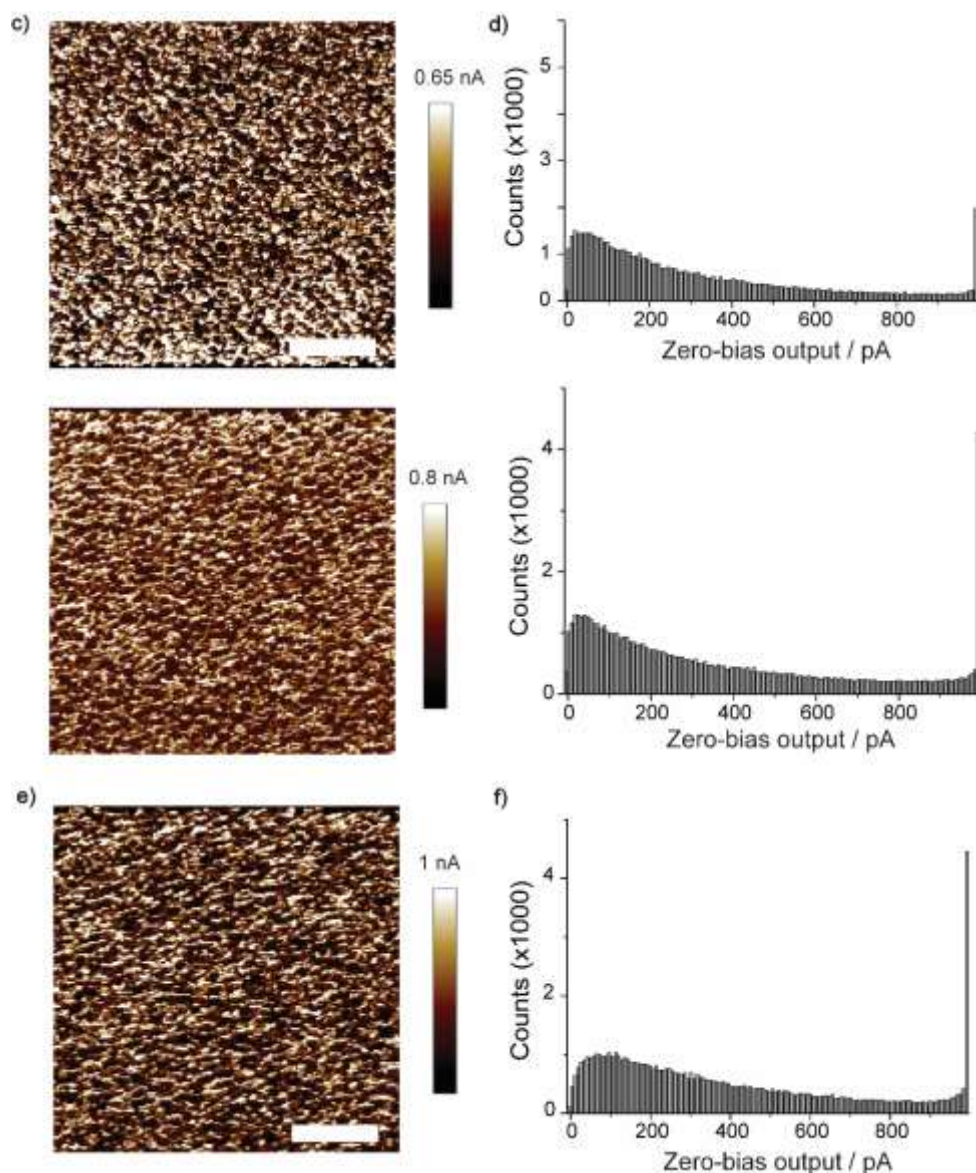


Figure S19. Zero-bias C-AFM maps acquired on S-1 at different scan rates. Samples were etched under dark for 13 min in a mixture of MeOH and aqueous 40% NH_4F (1:10, v/v). Panels (a, c, e) are current maps recorded at 5 Hz (mean of current value of 295 pA), 7 Hz (mean of current value of 372 pA), and 11 Hz (mean of current value of 397 pA), under 360 nN of normal force. Panels (b, d, f) show histograms of the current output obtained from the C-AFM maps. The histograms y-axis counts indicate the number of pixels (sample locations) of a given current magnitude, with a total of $\sim 65\text{k}$ pixels making up a C-AFM map. Horizontal scale bars in panels (a, c, e) are 1 μm .

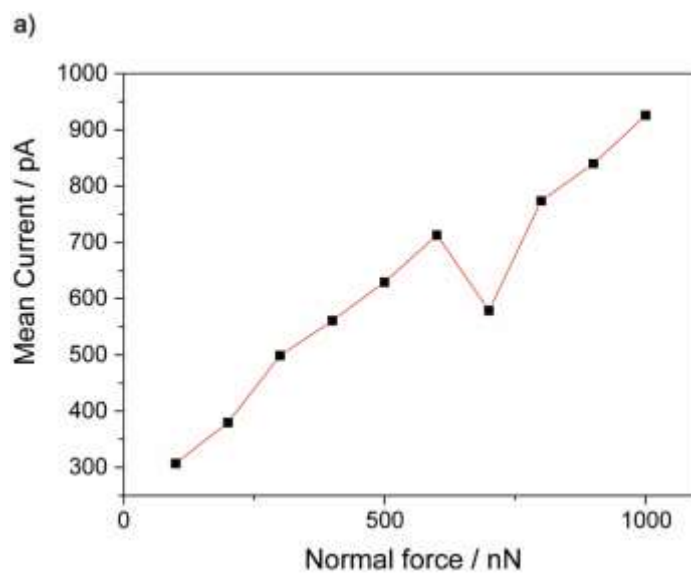


Figure S20. Dependence of the mean zero-bias current output on normal force. Sliding diode C-AFM data obtained on Si(211) **S-1** samples. The substrates were etched for 13 min in a mixture of MeOH and aqueous 40% NH_4F (1:10, v/v) under dark.

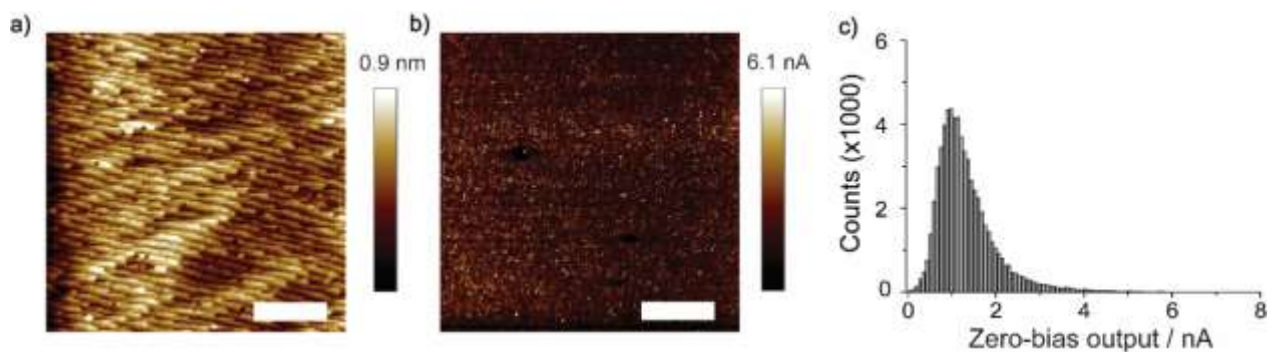


Figure S21. (a) AFM topography image of a **S-2** sample made on Si(111). (b) Zero bias C-AFM map of a **S-2** sample–platinum junction on Si(111). Horizontal scale bars in (a, b) are 1 μm . (c) Histogram plot of the current output of data in (b). Counts indicate the number of pixels of a given current bin, with a total of $\sim 65\text{k}$ pixels being sampled in a single C-AFM map. The current average output was 1.4 nA.

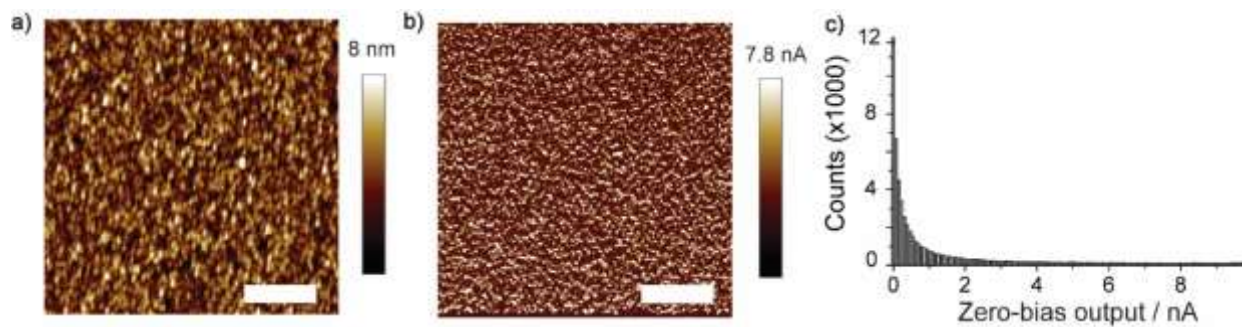


Figure S22. (a) AFM topography image of a **S-2** sample made on Si(211) (b) Zero bias C-AFM map of a **S-2** sample–platinum junction. Horizontal scale bars in (a, b) are 1 μm . (c) Histogram plot of the current output of data in (b). Counts indicate the number of pixels of a given current bin, with a total of $\sim 65\text{k}$ pixels being sampled in a single C-AFM map. Data in figure are for Si(211) wafers etched for 13 min in 1:10 v/v MeOH/NH₄F 40% and shielded from ambient light. The current average output was 2.3 nA.

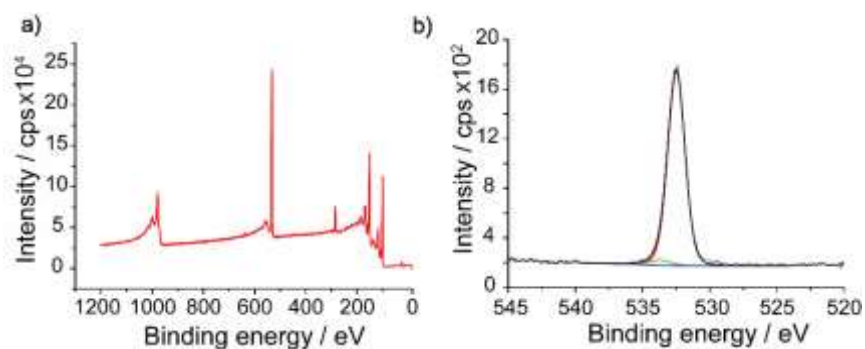


Figure S23. XPS data for **S-1** samples grafted on Si(211). Samples were subjected to 40 CV cycles from -0.4 to 0.6 V, 100 mV/s, 1.0 M HClO_4 , 1.7 mW cm^{-2} red light electrode illumination. The Si(211) substrates were etched for 13 min in a mixture of MeOH and 40% NH_4F (1:10), shielded from ambient light. (a) XPS survey spectra. (b) Narrow scan of the O 1s region. The spectra were deconvoluted into a main O–Si signal (oxygen bound to Si) at 533 eV, and a second peak signal at higher binding energy attributed to water adsorption to satisfy the fitting.⁴

Section S1

Determination of AFM tip–sample contact area

We estimated the tip–silicon contact area for current density calculations in C-AFM. Calculations were made following the DMT (Derjaguin–Muller–Toporov) model.^{5,6} The contact area is defined by:

$$A = \pi \left\{ \frac{R}{K} (L + 2\pi R\gamma) \right\}^{\frac{2}{3}}$$

Where:

- R is the tip radius,
- K is the reduced Young's modulus,

(K) is given by:

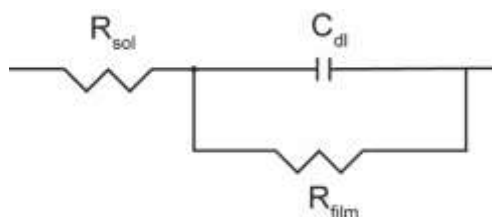
$$\frac{1}{K} = \frac{4}{3} \left(\frac{1 - \nu_1^2}{E_1} + \frac{1 - \nu_2^2}{E_2} \right)$$

where E is Young's modulus and ν denotes the Poisson ratio. For silicon and platinum Poisson ratios are 0.222 and 0.395, respectively, and the Young's modulus are 162.9 GPa and 177.3 GPa, respectively.⁷ The reduced Young's modulus is therefore 70.78 GPa.

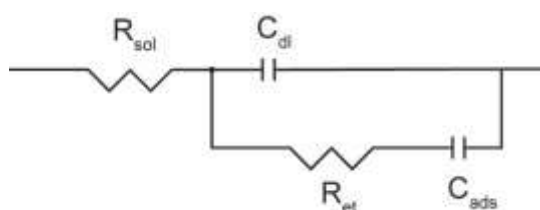
- L is the Set point (normal applied force)

And $2\pi R\gamma$ is the adhesion force, obtained as the average of 10 force–distance curves. The adhesion force is obtained by averaging data from multiple F–D (force–distance) curves.

Section S2



Equivalent electrical circuit used to fit the EIS data acquired at a DC offset (E_{dc}) sufficiently different from ferrocene apparent formal potential. The capacitor was treated as a constant phase element (CPE).



Equivalent electrical circuit used to fit the EIS data acquired at a DC offset (E_{dc}) equal to ferrocene apparent formal potential. Both capacitors were treated as a constant phase element (CPE).

REFERENCES

1. Ciampi, S.; Choudhury, M. H.; Ahmad, S. A. B. A.; Darwish, N.; Brun, A. L.; Gooding, J. J. The impact of surface coverage on the kinetics of electron transfer through redox monolayers on a silicon electrode surface. *Electrochim. Acta.* **2015**, *186*, 216-222.
2. Cerofolini, G. F.; Galati, C.; Renna, L. Accounting for anomalous oxidation states of silicon at the Si/SiO₂ interface. *Surf. Interf. Anal.* **2002**, *33*, 583-590.
3. Scheres, L.; Arafat, A.; Zuilhof, H. Self-Assembly of High-Quality Covalently Bound Organic Monolayers onto Silicon. *Langmuir* **2007**, *23*, 8343-8346.
4. Alam, A. U.; Howlader, M. M. R.; Deen, M. J. Oxygen Plasma and Humidity Dependent Surface Analysis of Silicon, Silicon Dioxide and Glass for Direct Wafer Bonding. *ECS J Solid State Sci. Technol.* **2013**, *2*, 515-523
5. Theiler, P. M.; Ritz, C.; Stemmer, A. Shortcomings of the Derjaguin–Muller–Toporov model in dynamic atomic force microscopy. *J. Appl. Phys.* **2021**, *130*,
6. Park, J. Y.; Salmeron, M. Fundamental aspects of energy dissipation in friction. *Chem. Rev.* **2014**, *114*, 677-711.
7. Hassel Ledbetter, S. K., Monocrystal elastic constants and derived properties of the cubic and the hexagonal elements. In *Handbook of elastic properties of solids, liquids and gases*, M. Levy, H. E. B., R.R. Stern, L. Furr, V. Keppens, Ed. Academic Press.: San Diego, 2001; pp 97-106.

Appendix D. Supplementary material of Chapter 3

Oxidative Damage during the Operation of Si(211)-Based Triboelectric Nanogenerators

Carlos Hurtado and Simone Ciampi *

School of Molecular and Life Sciences, Curtin University, Bentley, WA 6102, Australia;
c.hurtadotorres@curtin.edu.au

* Correspondence: simone.ciampi@curtin.edu.au

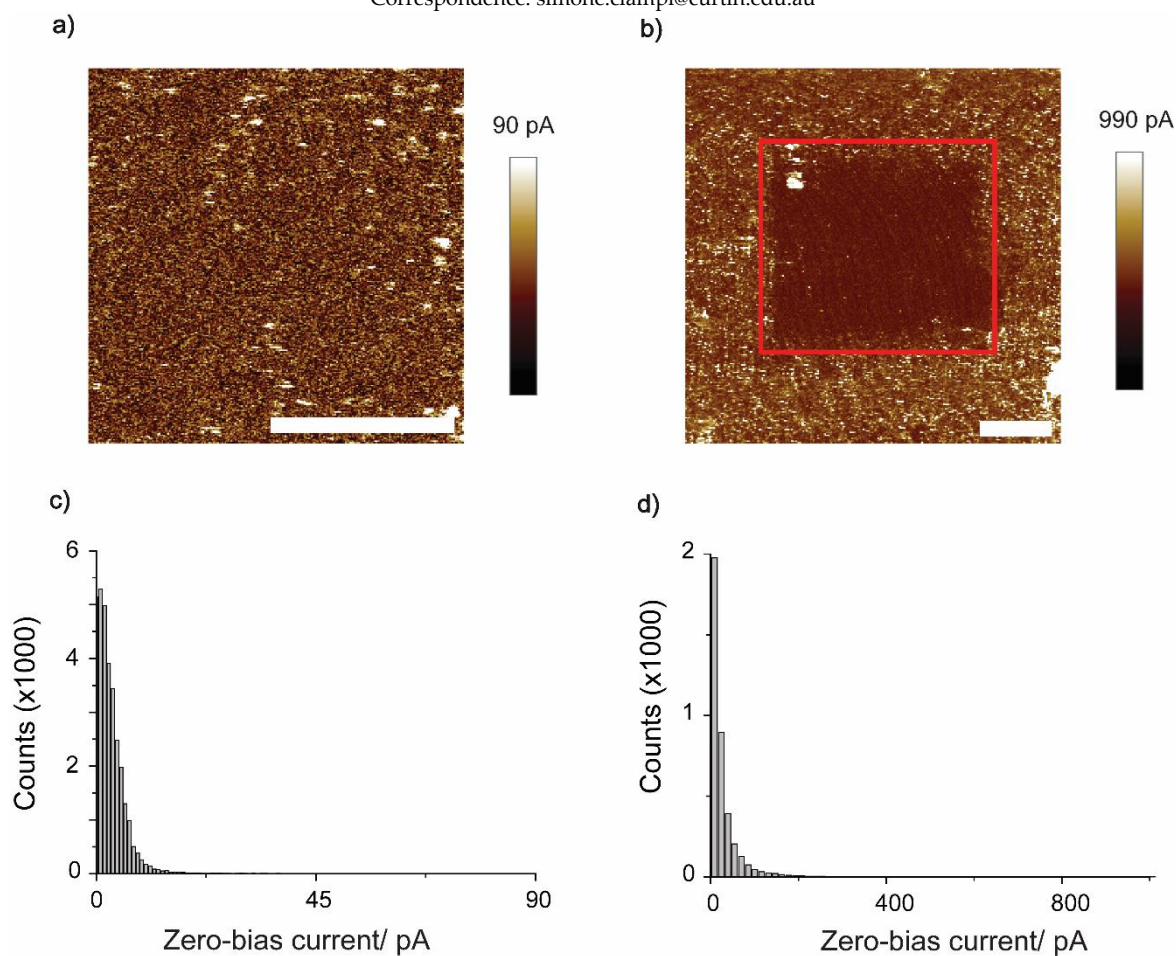


Figure S1. (a, b) Sequential C-AFM images ($2 \times 2 \mu\text{m}$ (a), $5 \times 5 \mu\text{m}$ (b)) recorded at zero-voltage bias on a Si(211) S-1 sample. The first map ($2 \times 2 \mu\text{m}$ (a)) was recorded setting a normal force set point of 50 nN. The corresponding histogram plot for the current output is shown in panel (c). The second map ($5 \times 5 \mu\text{m}$ (b)) covered the sample area imaged in (a) and was acquired under a normal force of 360 nN. The specific area highlighted by a red square coincides with the region scanned in panel (a). The current histogram associated with the region marked by the red square within this broader C-AFM map is depicted in panel (d). It is important to note that the histogram counts represent the quantity of pixels (sample locations) falling within each current value/bin. The complete C-AFM map ($5 \times 5 \mu\text{m}$) comprises a total of approximately 65,000 pixels. Horizontal scale bars indicating $1 \mu\text{m}$ are provided in panels (a) and (b).

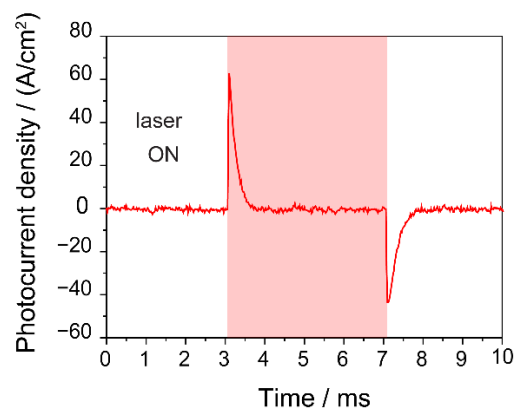


Figure S2. Example of a “capacitor-like” PCM transient trace.

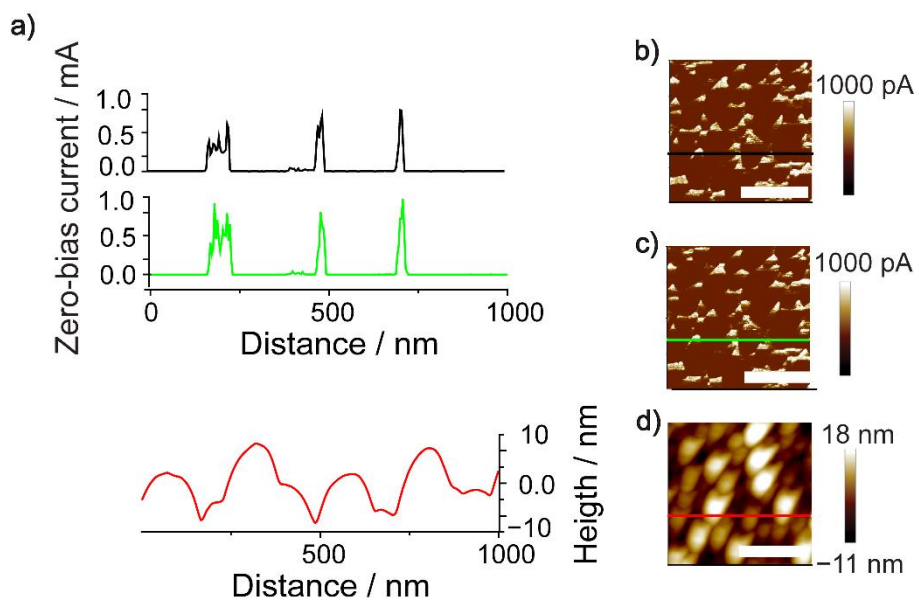


Figure S3. (a) Zero-bias DC current and topography profiles obtained during C-AFM experiments. The green and black color coding indicates the direction of the scan: first a trace (green, left to right) and then a retrace (black, right to left) over the same line. The topographic (height) profile is indicated by the red trace. (c–e) C-AFM and topography maps indicating the location of the line along which the current trace (green), current retrace (black) and topography (red) data of panel (a) were acquired.

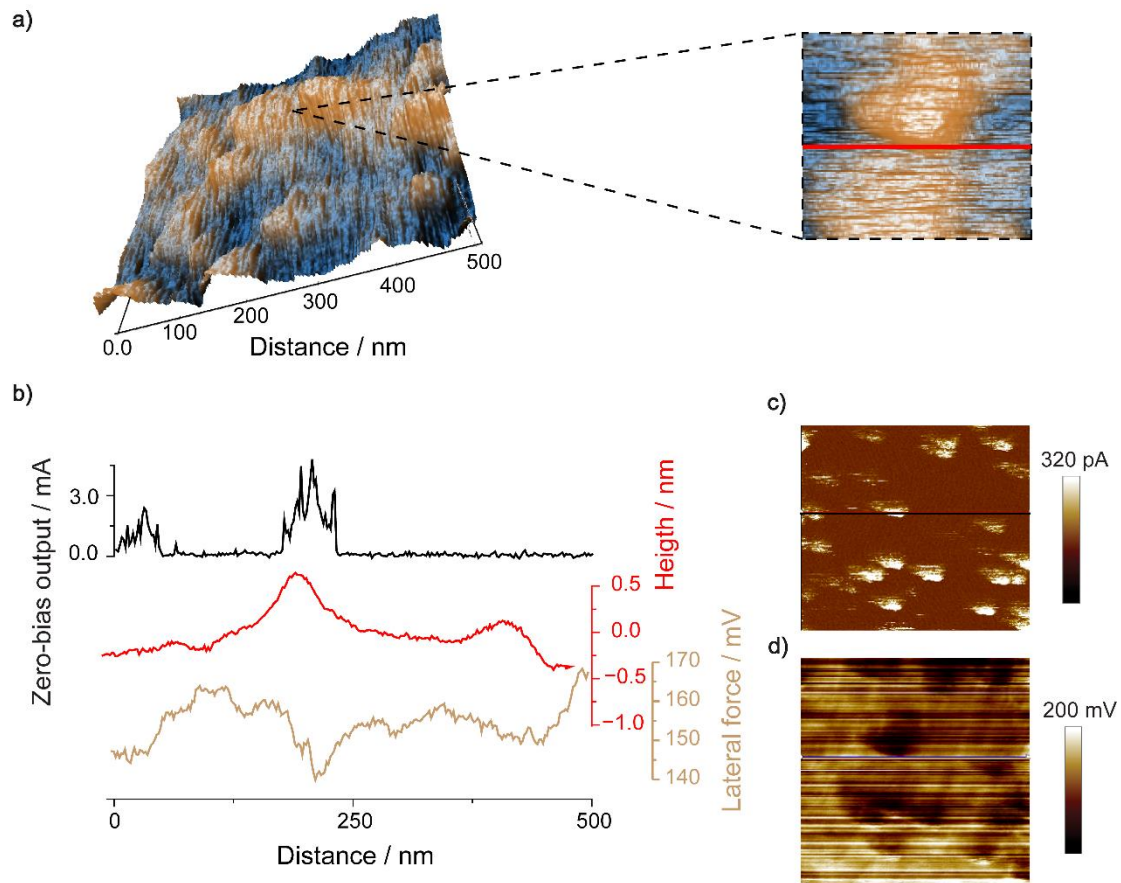


Figure S4. (a) 3D topography scan image of a Si(211) S-1 surface. (b) Zero-bias DC current, topography and lateral force profiles obtained during C-AFM experiments. The black color indicate the current profile output (trace direction). The height profile is indicated by the red trace. The brown color profile represents the lateral force data. (c) Zero-bias current map. (d) Lateral force (tip deflection) map.

Contact area (Pt AFM tip–S1 sample) determination

The DMT (Derjaguin–Muller–Toporov) model is a widely used approach for studying solid adhesion in materials, particularly applicable to hard and weakly adhesive substances such as silicon. The model's equation for estimating the contact area (A) is expressed as follows:

$$A = \pi \left\{ \frac{R}{K} (L + 2\pi R\gamma) \right\}^{\frac{2}{3}}$$

Here:

R refers to the tip radius,

K represents the reduced Young's modulus,

L is the normal applied force, and $2\pi R\gamma$ denotes the adhesion force.

The adhesion force is determined by averaging data from multiple F–D (force–distance) curves. Meanwhile, the reduced Young's modulus (K) can be calculated using the formula:

$$\frac{1}{K} = \frac{4}{3} \left(\frac{1 - \nu_1^2}{E_1} + \frac{1 - \nu_2^2}{E_2} \right)$$

where E represents the Young's modulus and ν represents the Poisson ratio. For silicon and platinum, the Poisson ratios are 0.222 and 0.395, respectively, with Young's modulus values of 162.9 GPa and 177.3 GPa, respectively. Thus, the reduced Young's modulus for these materials is determined to be 70.78 GPa. Experimental contact area have been observed to be 80 nm² on average.

Appendix E. Supplementary material of Chapter 4

Galinstan Liquid Metal Electrical Contacts for Monolayer-Modified Silicon Surfaces

Carlos Hurtado,^a Tony Andreoli,^a Anton P. Le Brun,^b Melanie MacGregor,^c Nadim Darwish,^a Simone Ciampi^{a,*}

^aSchool of Molecular and Life Sciences, Curtin University, Bentley, Western Australia 6102, Australia

^bAustralian Centre for Neutron Scattering, Australian Nuclear Science and Technology Organization, Lucas Heights, New South Wales 2234, Australia

^cFlinders Institute for Nanoscale Science and Technology, Flinders University, Bedford Park, South Australia 5042, Australia

*Email: simone.ciampi@curtin.edu.au

Supporting Information Table of Contents

Figure S1. Schematic depiction of the single-compartment three-electrode custom polytetrafluoroethylene cell used for the electrochemical experiments.	S2
Figure S2. Instrument rack for the J–V and C–V measurements.	S3
Figure S3. Experimental setup used for J–V and C–V experiments.	S4
Figure S4. Optical images of FeGaInSn.	S5
Figure S5. Experimental setup for pendant drop experiments used to estimate surface tension data.	S6
Table S1. Refined experimental surface tension data.	S7
Figure S6. AFM topography images of S-1 surfaces.	S8
Figure S7. AFM topography images of S-2 and S-3 surfaces.	S9
Figure S8. Voltammetric current peak as function of the scan rate for S-2 and S-3 samples.	S10
Figure S9. Broadening of voltammetric fwhm with scan rate.	S11
Figure S10. Prolonged cycling (50 consecutive cyclic voltammetry cycles) of S-3 samples grafted on Si(211) surface.	S12
Figure S11. Progressive masking by kinetic factors of the electrostatic-based peak inversion.	S13
Figure S12. XPS and XRR characterization of S-3 samples.	S14
Figure S13. Additional XPS data for S-3 surfaces.	S15
Figure S14. Representative EIS phase angle versus frequency plots for S-2 and S-3 samples.	S16
Figure S15. Zero-voltage bias C-AFM maps of S-3 samples.	S17

Figure S16. Mott–Schottky plots.

S18

Section S2. Equivalent electrical circuit used to fit the EIS data.

S19

References.

S20

Section S1

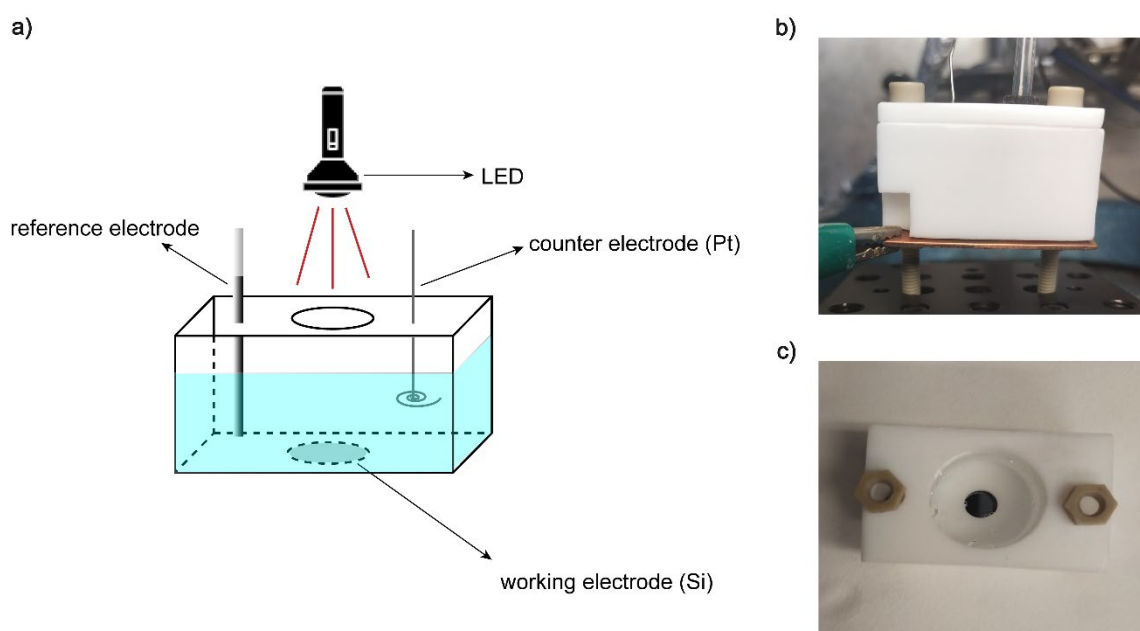


Figure S1. (a) Schematic depiction of the single-compartment three-electrode custom polytetrafluoroethylene cell used for the electrochemical experiments. (b) Front and (c) top view optical images of the actual cell.



Figure S2. Instrument rack for the J–V and C–V measurements. **(1)** Function generator, model DG-1022, from RIGOL, **(2)** SMU, model B2902A, from Keysight, and **(3)** LCR meter, model E4980A, from Keysight.

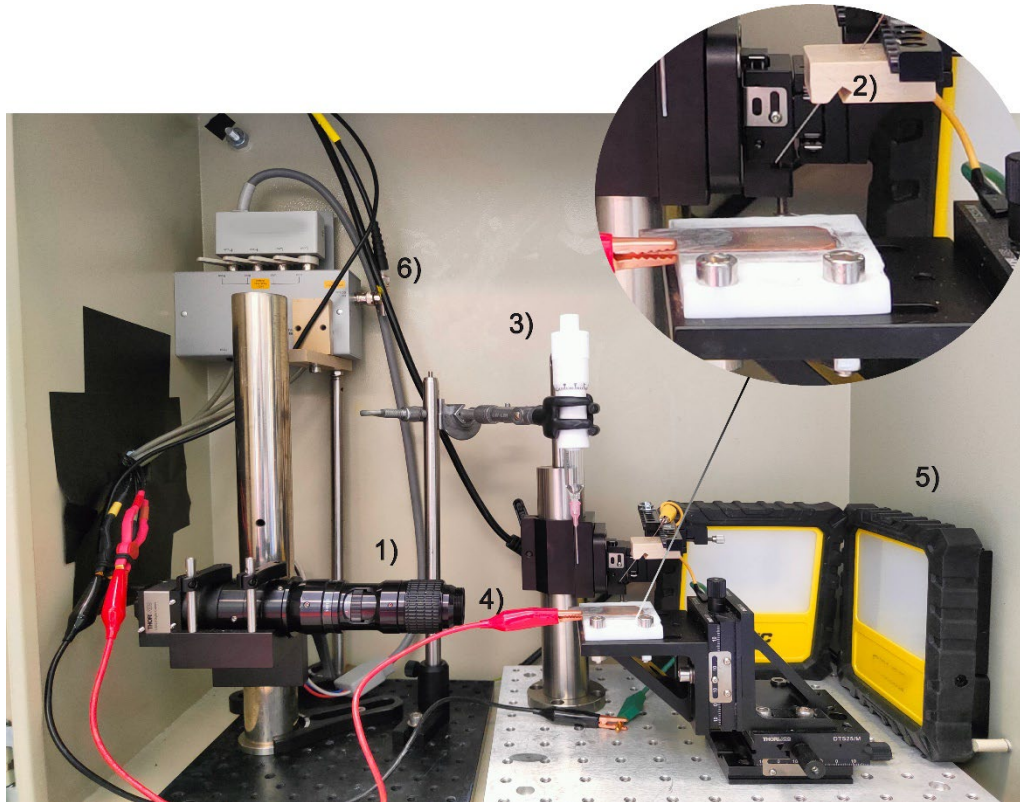
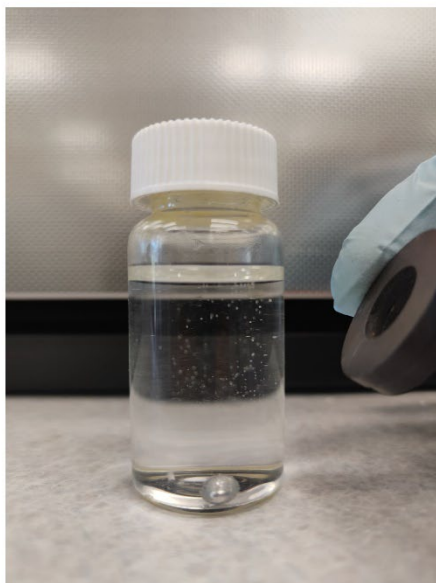


Figure S3. Experimental setup used for J–V and C–V experiments. (1) A camera (model DCC1240C, Thorlabs) fitted with a machine-vision lens (model MVL133A and 1.5 \times lens attachment, Thorlabs), was used to measure the Galinstan drop size. Control of the top-contact deposition was achieved via a (2) x-y-z positioning stage (made up by three DTS25 linear translation stages, Thorlabs) holding the stainless steel metal contact and a (3) threaded plunger syringe to dispense the liquid alloy. (4) Bottom electrode connection and sample holder plate. (5) Illumination system (used only during the capture of the Galinstan droplet optical images). All measurements were carried out in dark, inside a grounded Faraday cage. (6) External bias adapter (16065C, Keysight) used to couple the LCR with the SMU.

a)



b)

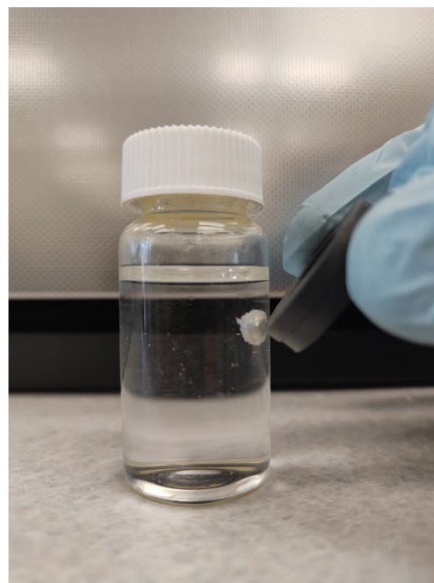


Figure S4. Optical images of the synthesized FeGaInSn, immersed in an acid bath solution (aqueous 0.5 M HCl), showing its attraction to a magnet. (a) FeGaInSn sample away from the magnet, and (b) movement of the sample towards the magnet (part number 13020, AMF magnetics).

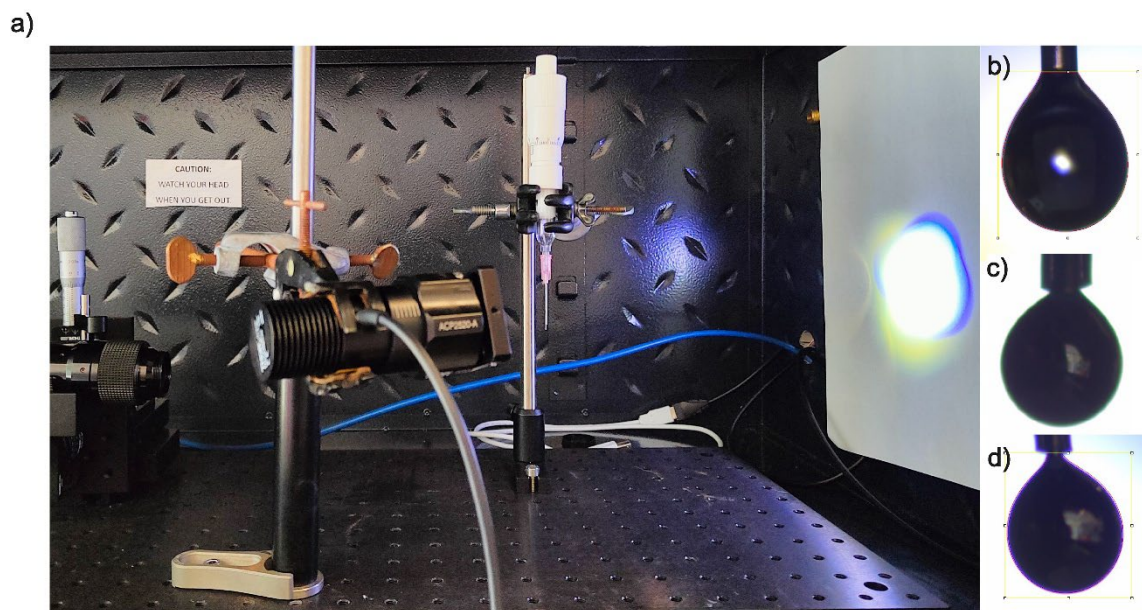


Figure S5. (a) Experimental setup for pendant drop experiments used to estimate surface tension data. Data were analyzed with the image processing software ImageJ (pendent drop analysis, results presented in Table S1). (b) Representative water surface tension experiment used for calibration (water surface tension = 72.00 ± 0.01 mN/m). (c) GaInSn drop, surface tension = 0.47 ± 0.03 N/m and (d) FeGaInSn drop, surface tension = 0.56 ± 0.02 N/m.

Table S1. obtained from the “drop-shape” (Image J^{1,2}) analysis of pendant drops micrographs of water, GaInSn and FeGaInSn samples in air. In ImageJ, "px" represents pixels, the basic unit of measurement in digital images, used for analysis and measurements.

	Surface tension / mN/m	RMS fitting / px
Water	72.0	0.8
	72.1	0.9
	72.1	0.8
	71.8	0.9
GaInSn	504.6	1.0
	462.2	0.9
	473.8	1.1
	445.8	0.9
FeGaInSn	588.2	0.9
	475.2	0.9
	600.6	1.2
	565.20	1.0

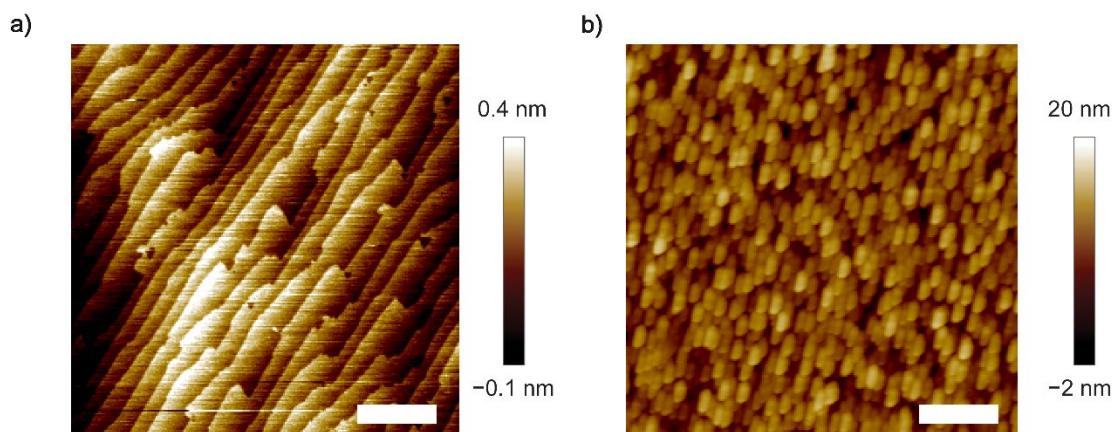


Figure S6. AFM topography images of **S-1** surfaces. (a) Data for Si(111) crystals showing a terraced structure (rms = 0.1 nm) steps are on average ~ 0.2 nm. (b) Data for Si(211) samples indicating a relatively rougher surface (rms = 1.2 nm). Scale bar in panels (a) and (b) is 1 μm .

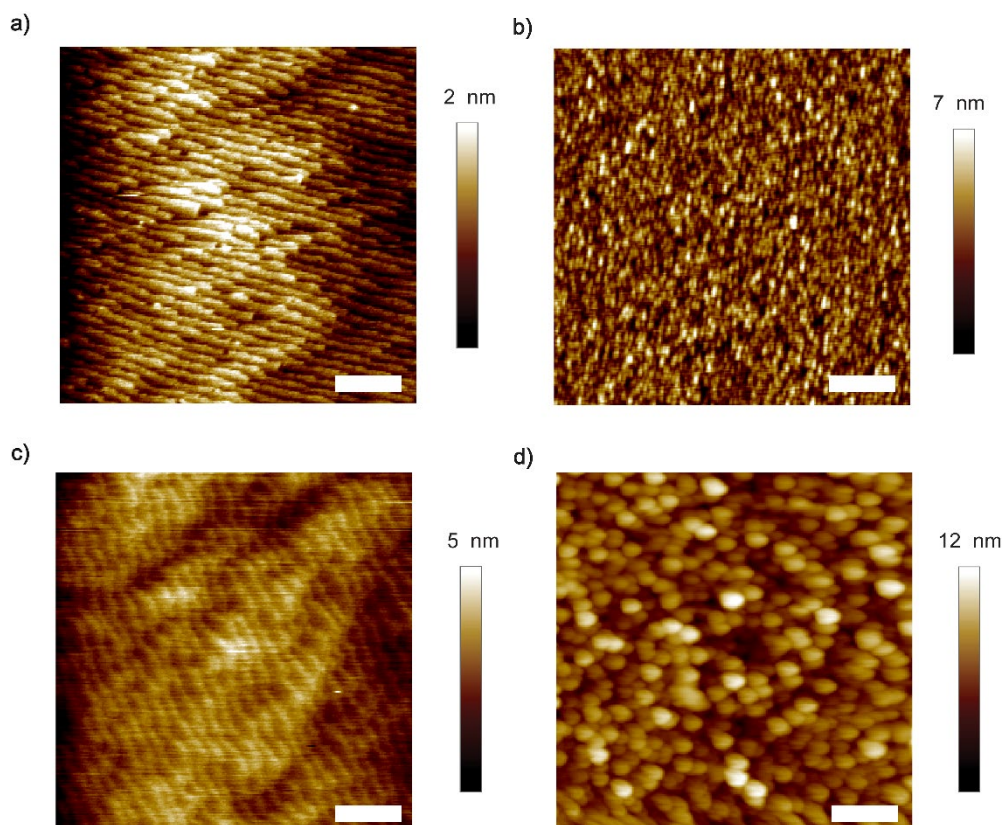


Figure S7. AFM topography images of **S-2** (a, b) and **S-3** (c, d) surfaces. (a, c) The terraced Si(111) structure remains evident after monolayer derivatization (conversion of **S-1** into **S-2** and **S-3**). (b, d) Evidence of a rougher (relatively to the Si(111) samples) Si(211) surface. Roughness values are 0.2 nm and 1.4 nm for Si(111) and Si(211) **S-2** surfaces respectively, and 1.6 nm and 3.4 nm for Si(111) and Si(211) **S-3** surfaces, respectively. Scale bars are 1 μm .

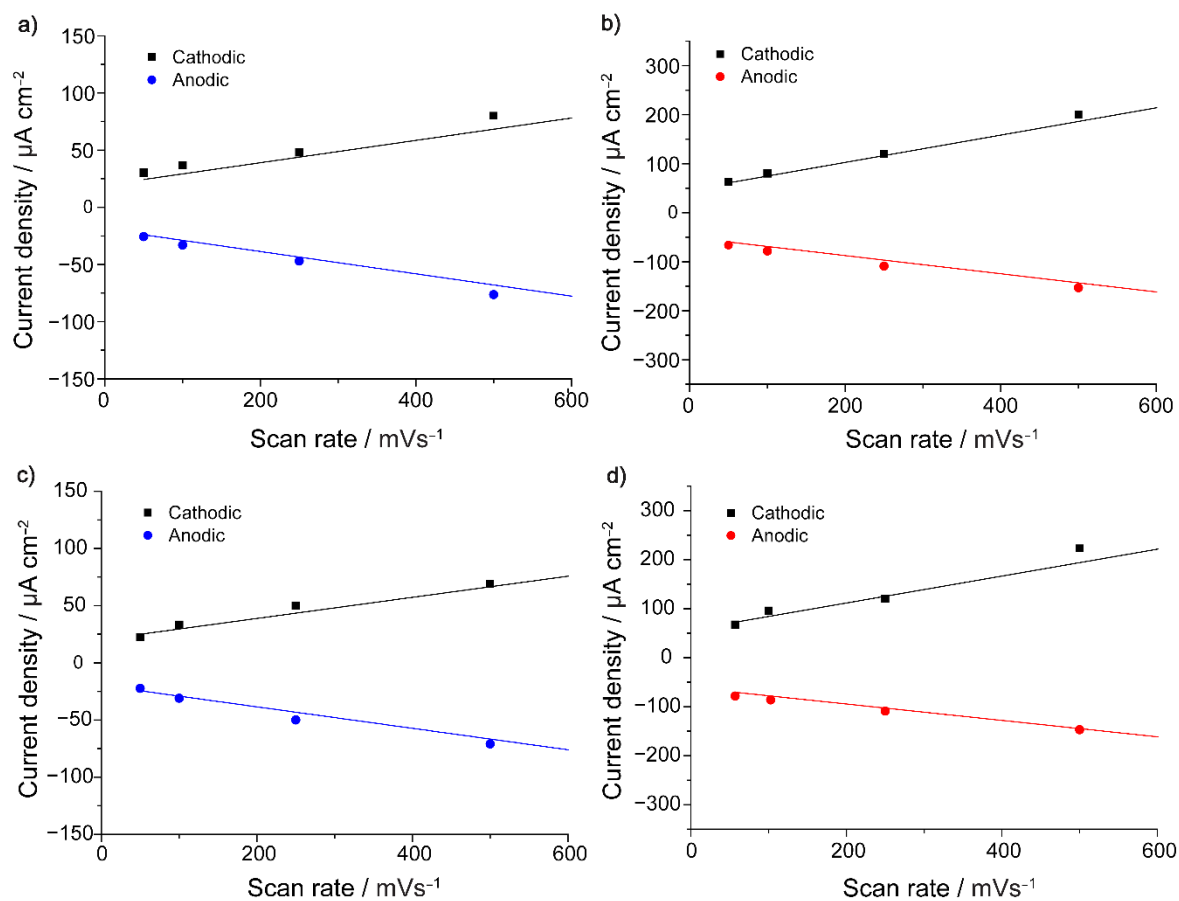


Figure S8. Voltammetric current peak as function of the scan rate for **S-2** and **S-3** samples prepared on Si(111) (a, b) (slope: 0.087, -0.097 and 0.278, -0.185) and on Si(211) (c, d) electrodes (slope: 0.094, -0.093 and 0.274, -0.167). During the experiments the electrodes were illuminated with a red light of 0.12 mW cm⁻² intensity. The electrolyte is aqueous 1.0 M HClO₄.

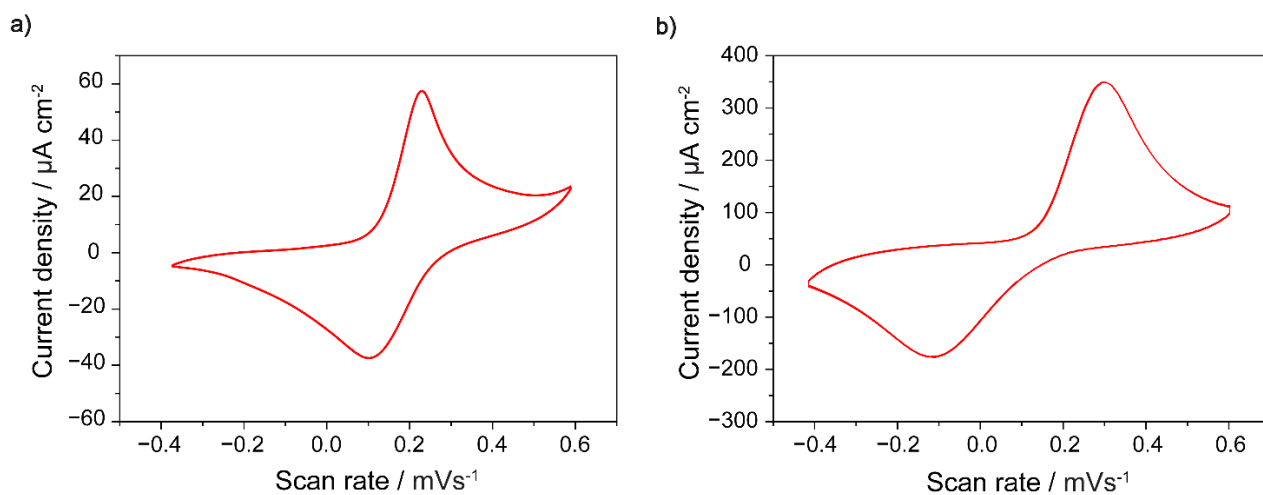


Figure S9. (a–b) Broadening of fwhm with scan rate. Representative cyclic voltammograms (CVs) for **S-3** surfaces (a, b) grafted on Si(211). The electrode was illuminated at a light intensity of 0.12 mW cm^{-2} . The voltage scan rate was 50 mV/s (a), and 1000 mV/s (b). The electrolyte is aqueous 1.0 M HClO_4 .

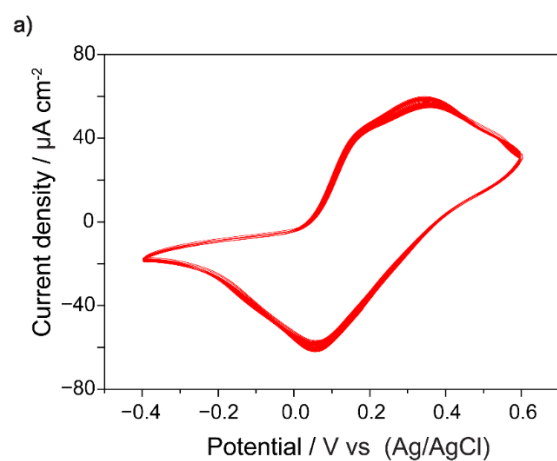


Figure S10. Prolonged cycling (50 consecutive cyclic voltammetry cycles) of **S-3** samples grafted on a Si(211) surface. The electrode was illuminated at a light intensity of 0.12 mW cm^{-2} . The voltage scan rate was 100 mV/s, and the coverage dropped only from $\sim 7.2 \times 10^{-10}$ to $6.4 \times 10^{-10} \text{ mol cm}^{-2}$ (first and last cycle, respectively).

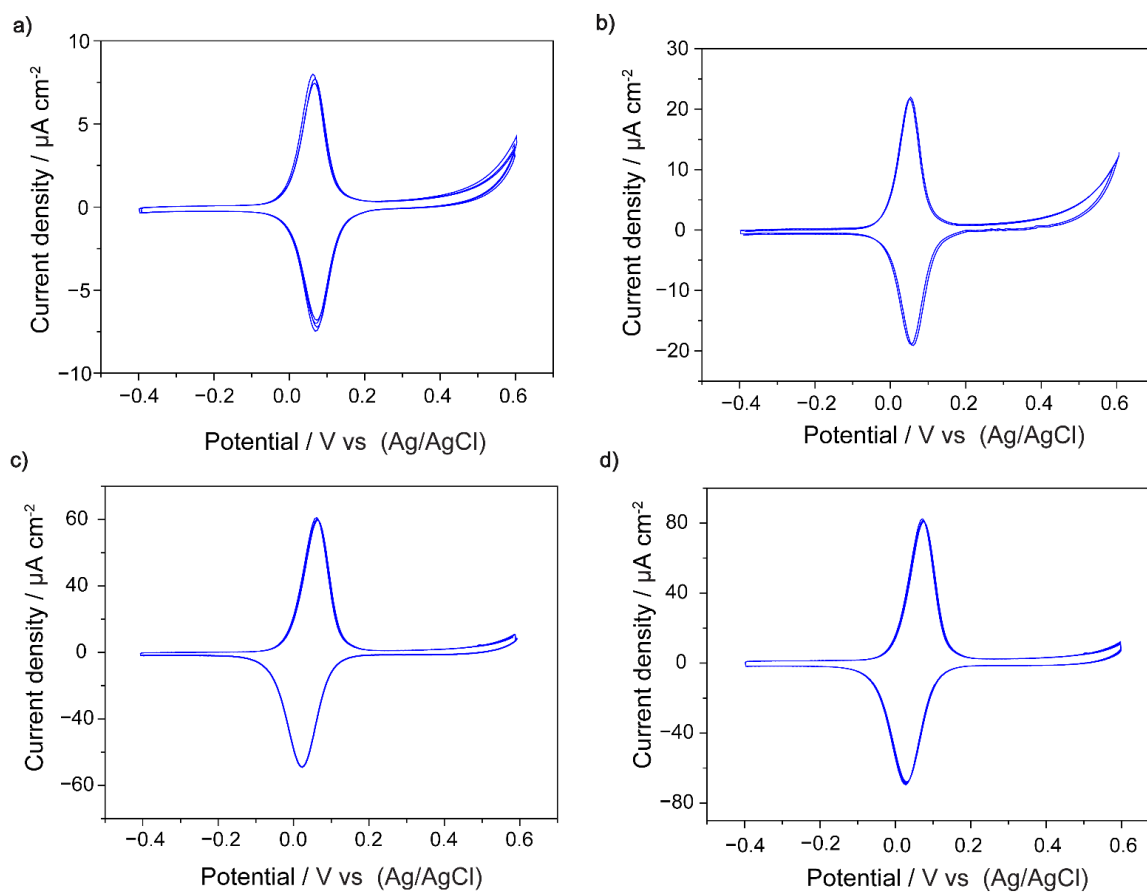


Figure S11. (a–d) Progressive masking by kinetic factors of the electrostatic-based peak inversion.^{3,4} Representative cyclic voltammograms (CVs) for S-2 surfaces made on Si(211) and recorded at different voltage sweep rates. The electrode was illuminated at a light intensity of 0.12 mW cm^{-2} . The voltage scan rate was 50 mV/s (a), 100 mV/s (b), 250 mV/s (c), and 500 mV/s (d).

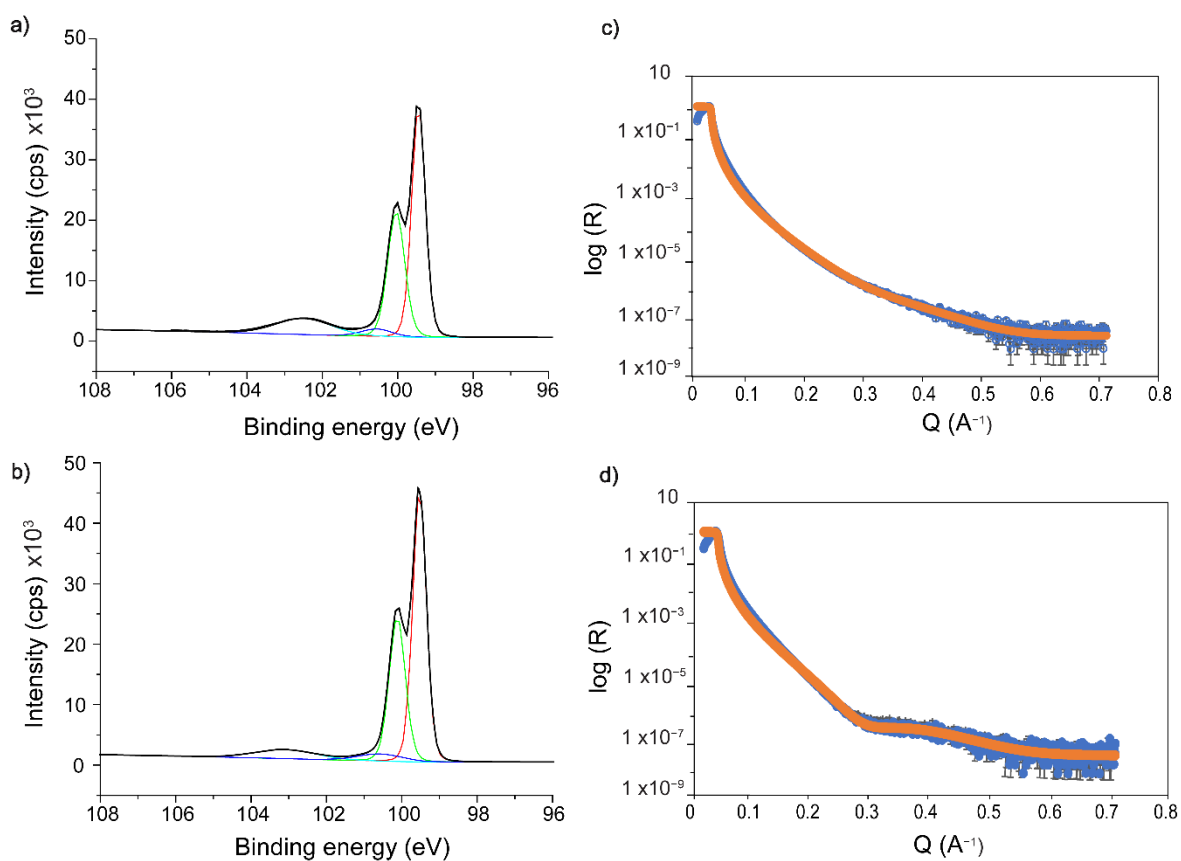


Figure S12. (a, b) Narrow scans of the Si 2p region of **S-3** surfaces grafted on Si(111) (a) and on Si(211) (b). The Si 2p_{3/2} peak is located at 99.5 eV. The high binding energy shoulder at 0.4 eV from the Si 2p_{1/2} emission is attributed to Si–H species.⁵ Photoelectrons from Si(2) Si(3) and Si(4) oxides merge into a single band (101–104 eV). (c, d) XRR profiles for **S-3** films made on Si(111) (c), and on Si(211) (d) crystals. The refined XRR trace is plotted in orange over the experimental data (solid blue symbols).

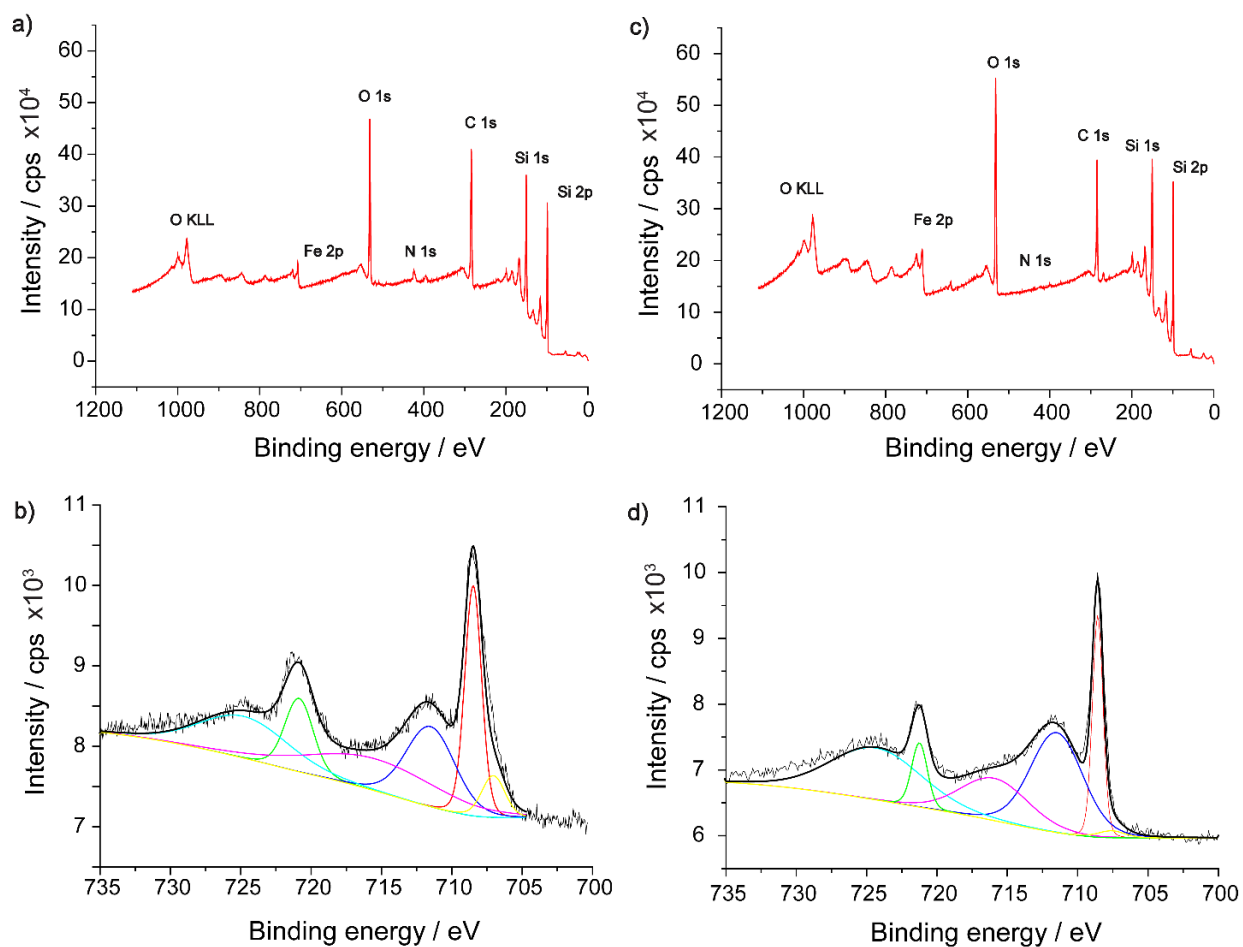


Figure S13. XPS data for **S-3** surfaces grafted on Si(111) (a, b) and on Si(211) (c, d). (a, c) XPS survey spectra. (b, d) Narrow scans of the Fe 2p region. The reduced iron (ferrocene) Fe 2p_{3/2} peak was centred at 708.5 eV and the Fe 2p_{1/2} peak felt at 721.5 eV. Signals from the oxidized iron of ferrocenium moieties appear as high binding energy shoulders. The signal at ~717 eV is a commonly observed satellite iron peak.⁶

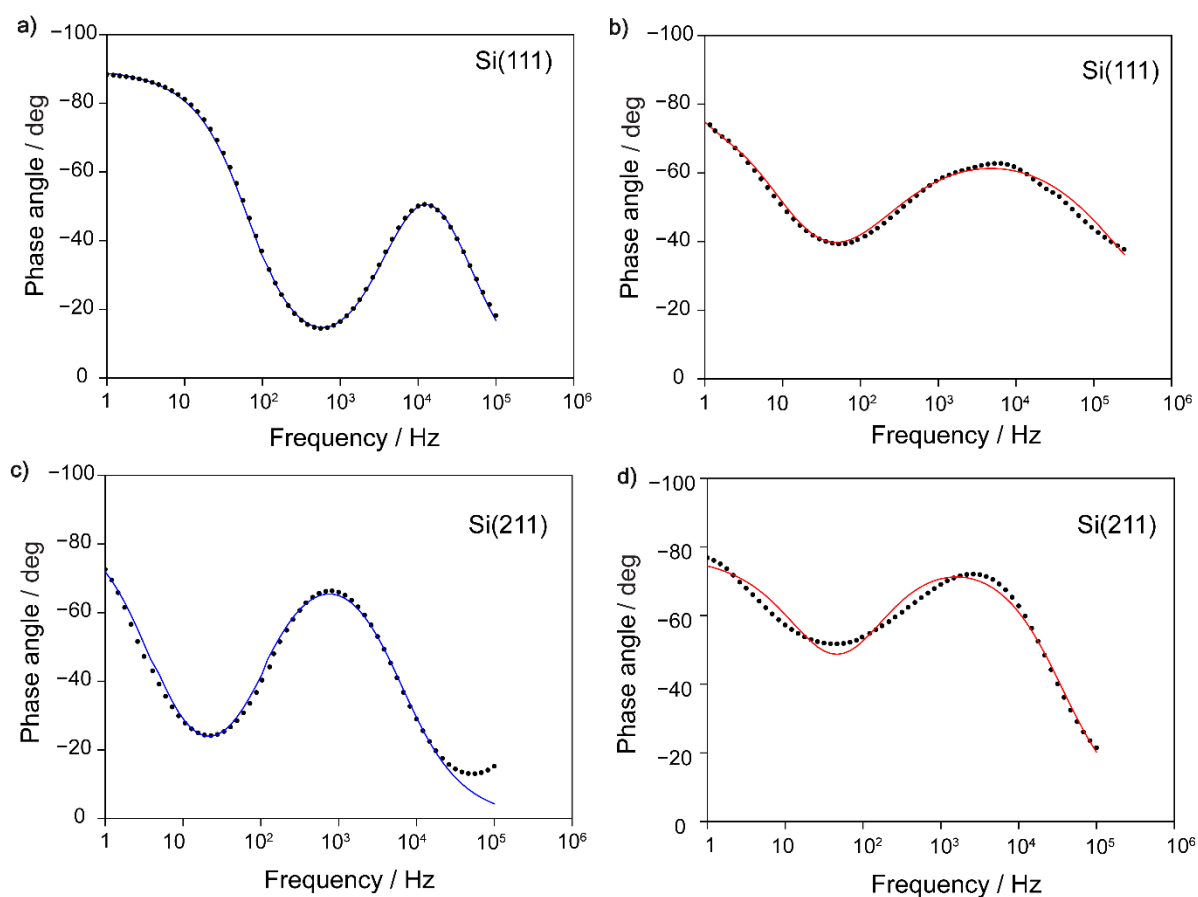


Figure S14. Representative EIS phase angle versus frequency plots obtained for **S-2** and **S-3** samples grafted on Si(111) (a, b) and on Si(211) (c, d) electrodes. During the EIS measurement the electrodes were illuminated at a light intensity of 1.7 mW cm^{-2} . Black symbols are the experimental data, while the blue and red solid lines are the best fits (**S-2** and **S-3** surfaces, respectively). The fittings chi-squared was $\sim 1 \times 10^{-6}$. The E_{dc} was set to 0.1 V. The equivalent circuit model used in the fitting is shown in Section S1. The refined k_{et} values were: $2.18 \times 10^2 \text{ s}^{-1}$ (a); $5.01 \times 10^1 \text{ s}^{-1}$ (b); $5.89 \times 10^1 \text{ s}^{-1}$ (c); $3.29 \times 10^1 \text{ s}^{-1}$ (d).⁷

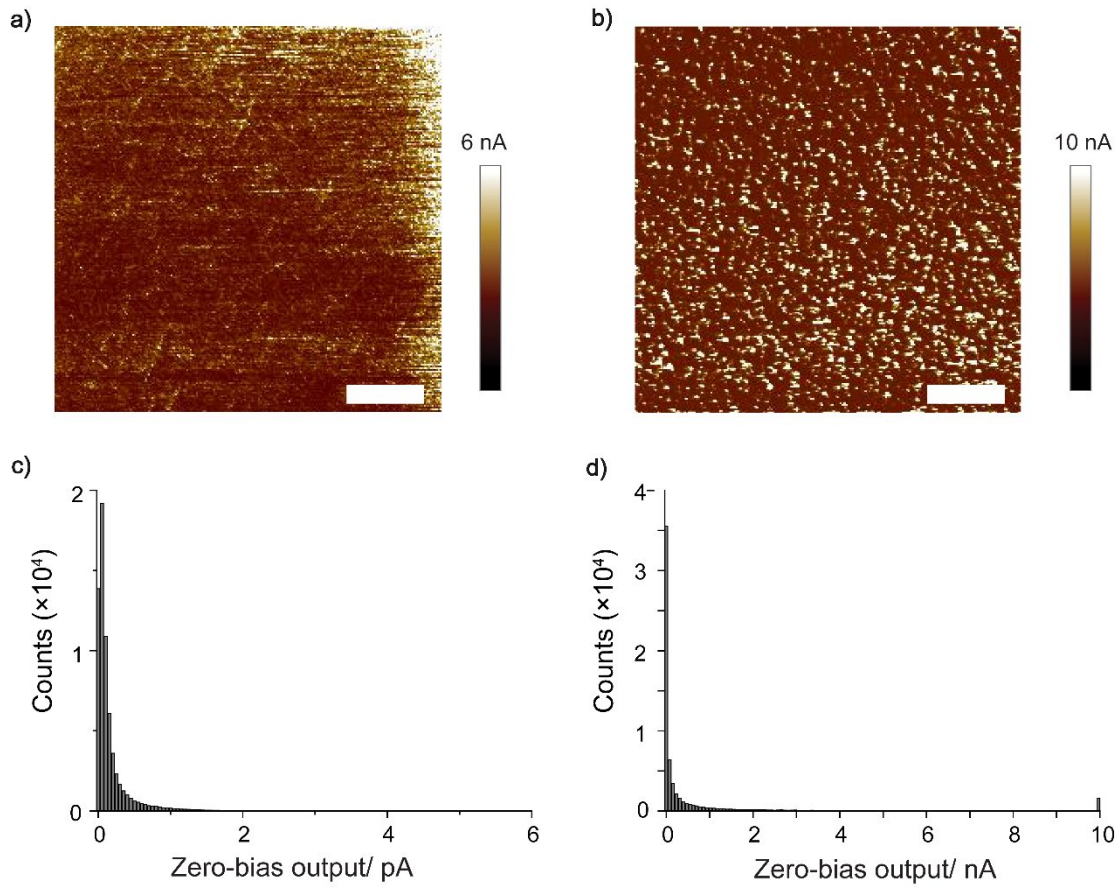


Figure S15. Zero-voltage bias C-AFM maps of **S-3** samples prepared on (a) Si(111) and (b) Si(211). Panels (c) and (d) are the histograms of the zero-bias output extracted from the C-AFM experiments shown in (a) and (b) respectively. The 99th percentile of the DC output is 1.3 nA and 9.6 nA and average current density values are 0.2 and 2.2 nA for Si(111) and Si(211) respectively. The area of the scan was $5 \times 5 \mu\text{m}$ and the applied normal load was 360 nN. Scale bars in panel (a) and panel (b) are $1 \mu\text{m}$. The C-AFM bias routing is such that positive currents have the direction of a leakage current (electrons flowing from the platinum AFM tip to the n-type silicon substrate).

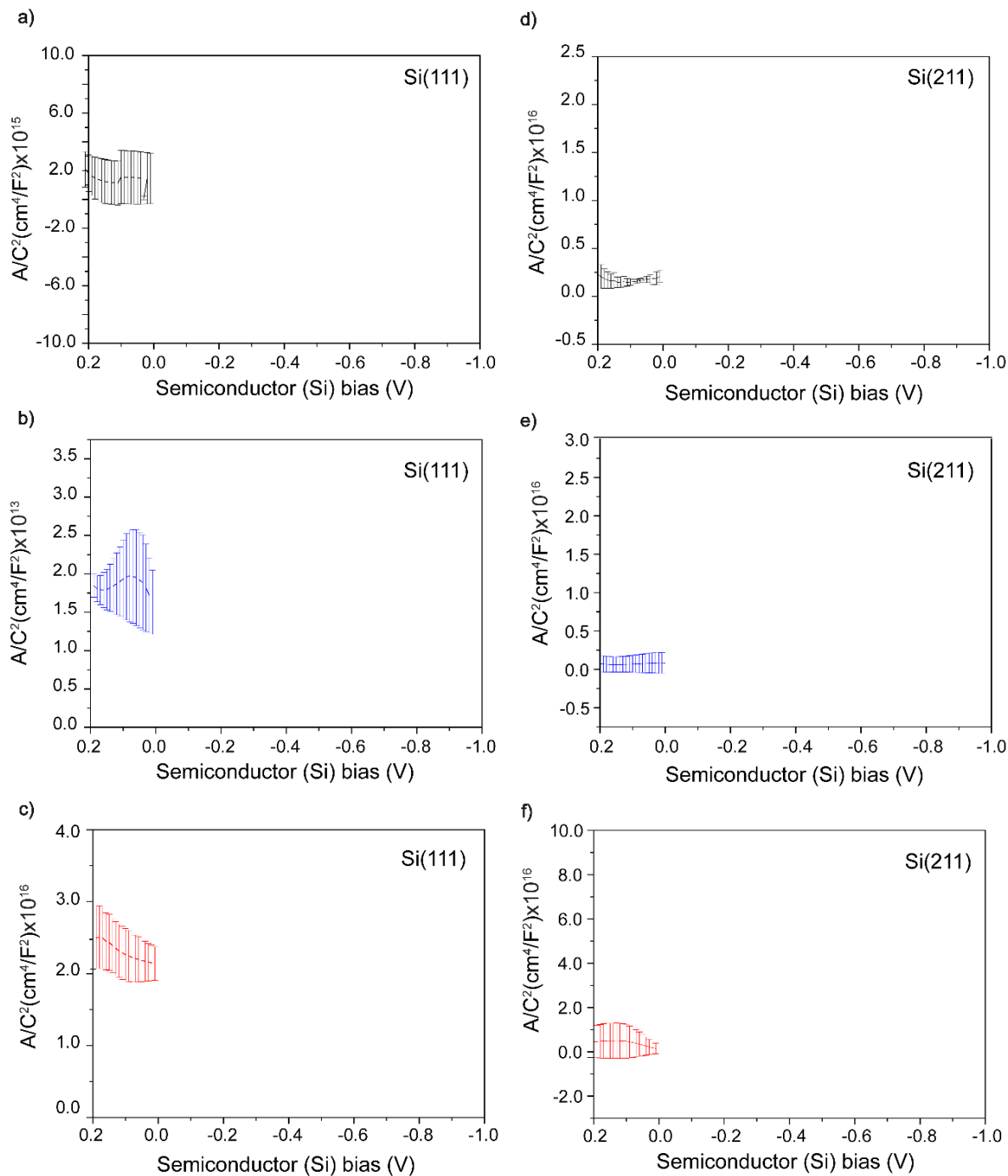
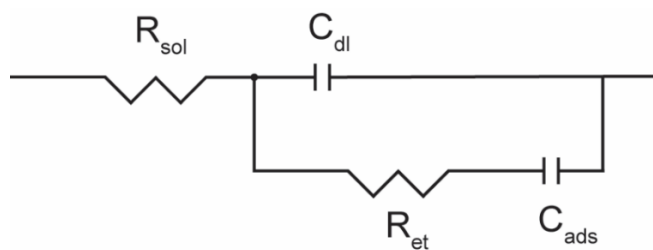


Figure S16. Mott-Schottky plots of capacitance–voltage data acquired at an AC frequency of 1 KHz on moderately doped (a, b, c) Si(111), and (d, e, f) Si(211)/FeGaInSn junctions. The surface chemistries were **S-1** (a, d), **S-2** (b, e), and **S-3** (c, f). Capacitance data are plotted as $1/C^2$ against the silicon bias. Curves were recorded at three different samples where the dashed central line is the calculated mean, and the error bars indicate the standard deviation.

Section S1

Equivalent electrical circuit used to fit the EIS data acquired at a DC offset (E_{dc}) of 0.1 V (equal to the ferrocene apparent formal potential, cyclic voltammetry data). The capacitor was treated as a constant phase element (CPE).



References

1. Adrian, D.; Adrien, M. Pendent_Drop: An ImageJ Plugin to Measure the Surface Tension from an Image of a Pendent Drop. *J. Open Res. Softw.* **2016**, *4*, 3–e3.
2. Schindelin, J.; Arganda-Carreras, I.; Frise, E.; Kaynig, V.; Longair, M.; Pietzsch, T.; Preibisch, S.; Rueden, C.; Saalfeld, S.; Schmid, B.; Tinevez, J.-Y.; White, D. J.; Hartenstein, V.; Eliceiri, K.; Tomancak, P.; Cardona, A. Fiji: An open-source platform for biological-image analysis. *Nat. Methods* **2012**, *9*, 676–682.
3. Vogel, Y. B.; Zhang, L.; Darwish, N.; Gonçalves, V. R.; Le Brun, A.; Gooding, J. J.; Molina, A.; Wallace, G. G.; Coote, M. L.; Gonzalez, J.; Ciampi, S. Reproducible flaws unveil electrostatic aspects of semiconductor electrochemistry. *Nat. Commun.* **2017**, *8*, 2066–9.
4. Vogel, Y. B.; Molina, A.; Gonzalez, J.; Ciampi, S. Quantitative Analysis of Cyclic Voltammetry of Redox Monolayers Adsorbed on Semiconductors: Isolating Electrode Kinetics, Lateral Interactions, and Diode Currents. *Anal. Chem.* **2019**, *91*, 5929–5937.
5. Cerofolini, G.; Galati, C.; Renna, L. Accounting for anomalous oxidation states of silicon at the Si/SiO₂ interface. *Surf. Interface Anal.* **2002**, *33*, 583–590.
6. Li, P.; Xuan, Y.; Jiang, B.; Zhang, S.; Xia, C. Hollow La_{0.6}Sr_{0.4}Ni_{0.2}Fe_{0.75}Mo_{0.05}O_{3-δ} electrodes with exsolved FeNi₃ in quasi-symmetrical solid oxide electrolysis cells for direct CO₂ electrolysis. *Electrochem. commun.* **2022**, *134*, 107188.
7. Ciampi, S.; Choudhury, M. H.; Ahmad, S. A. B. A.; Darwish, N.; Brun, A. L.; Gooding, J. J. The impact of surface coverage on the kinetics of electron transfer through redox monolayers on a silicon electrode surface. *Electrochim. Acta* **2015**, *186*, 216–222.

Appendix F. Supplementary material of Chapter 5

Schottky Diode Leakage Current Fluctuations: Electrostatically Induced Flexoelectricity in Silicon

Carlos Hurtado^a, Melanie MacGregor^b, Kai Chen^c and Simone Ciampi^{a,}*

^aSchool of Molecular and Life Sciences, Curtin University, Bentley, Western Australia 6102, Australia

^bFlinders Institute for Nanoscale Science and Technology, Flinders University, Bedford Park, South Australia 5042, Australia

^cSchool of Molecular Sciences, The University of Western Australia, Crawley, Western Australia 6009, Australia

*Email: simone.ciampi@curtin.edu.au

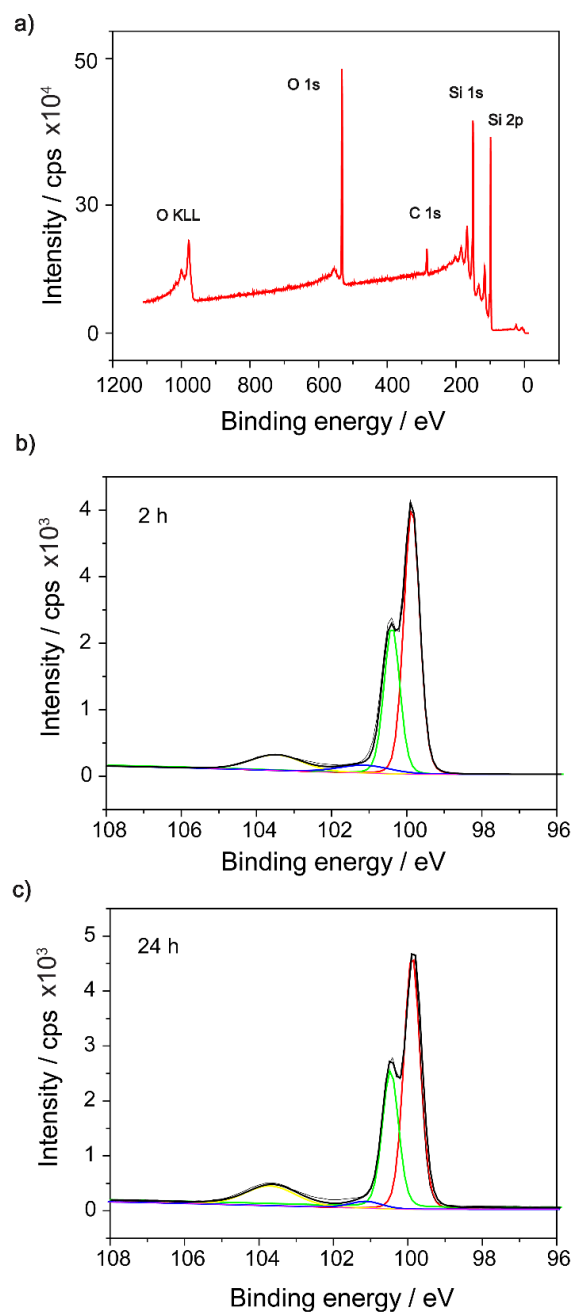


Figure S1. XPS data for Si-H samples made on n-type, lowly doped Si(211) crystals. The substrates were etched for 13 min in a mixture of MeOH and 40% NH_4F (1:10) under dark. (a) XPS survey spectra. (b, c) Narrow scans of the Si 2p region conducted on the Si-H terminated samples exposed to ambient air for either (b) 2 h, or (c) 24 h. The Si $2p_{3/2}$ emission is at 99.5 eV. A noticeable high binding energy shoulder (0.40 eV from the Si $2p_{1/2}$ emission), is ascribed to Si-H species. Evident in the 102–105 eV region are photoelectrons originating from $\text{Si}^{(2)}$, $\text{Si}^{(3)}$, and $\text{Si}^{(4)}$ oxides, which coalesce into a single band.

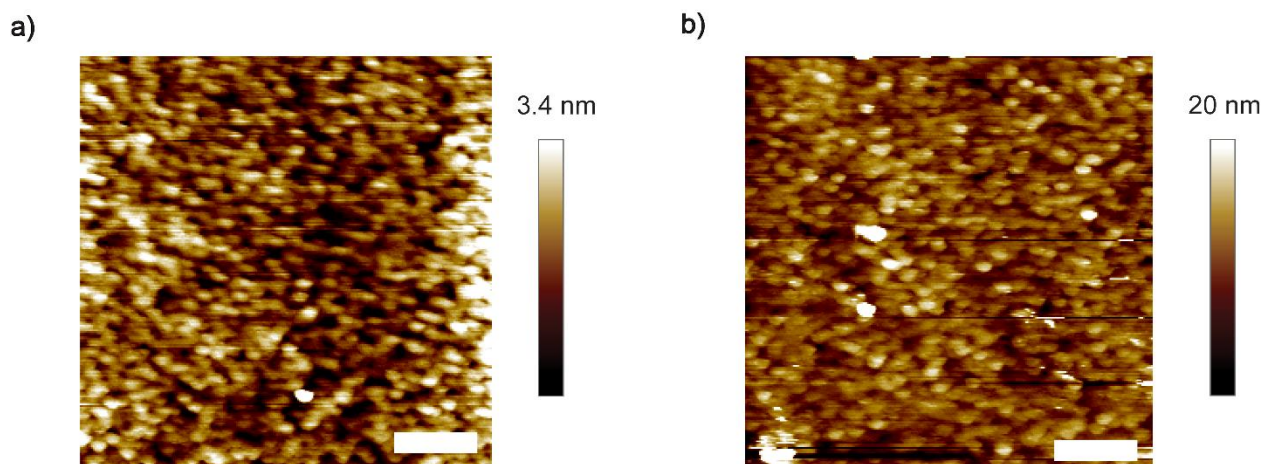


Figure S2. AFM topography images of Si-H terminated surfaces (n-type, lowly doped, Si(211) crystals) exposed to air for 2 h (a) and 24 h (b). Rounded topographical features (white dots) are attributed to oxidized surface sites. Scale bars in panels (a) and (b) are 1 μm .

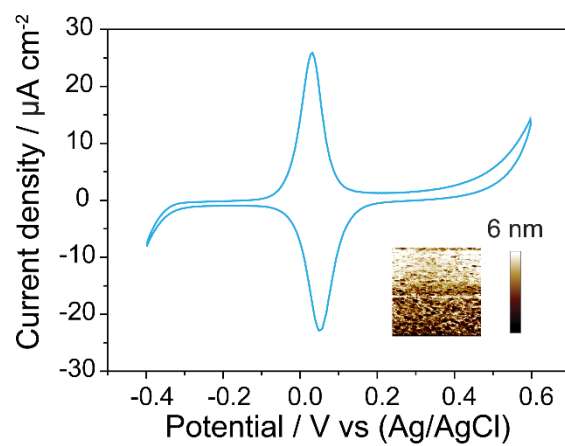


Figure S3. Representative cyclic voltammogram for a **S-2** sample made on a Si(211) and run as photoanode (n-type, lowly doped, 100 mV s^{-1} , 1.0 M HClO_4 , red light illumination). The sample was etched in a mixture of MeOH and aqueous 40% NH_4F (1:10, v/v) in the dark. The inset displays AFM topography image of the **S-1** sample (rms = $\sim 3 \text{ nm}$).

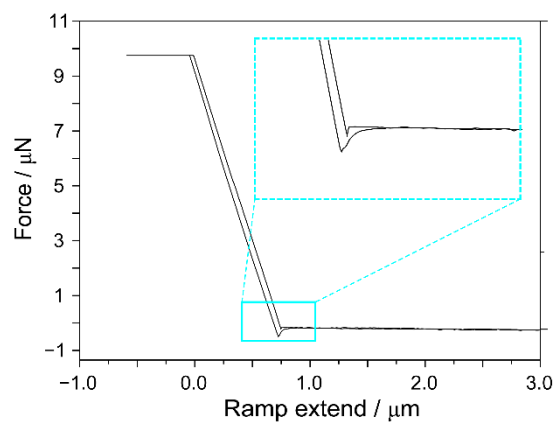


Figure S4. (a) A representative force–distance (F–d) AFM curve part of an adhesion force measurement. The inset shows the section of the curve used to estimate the adhesion force.

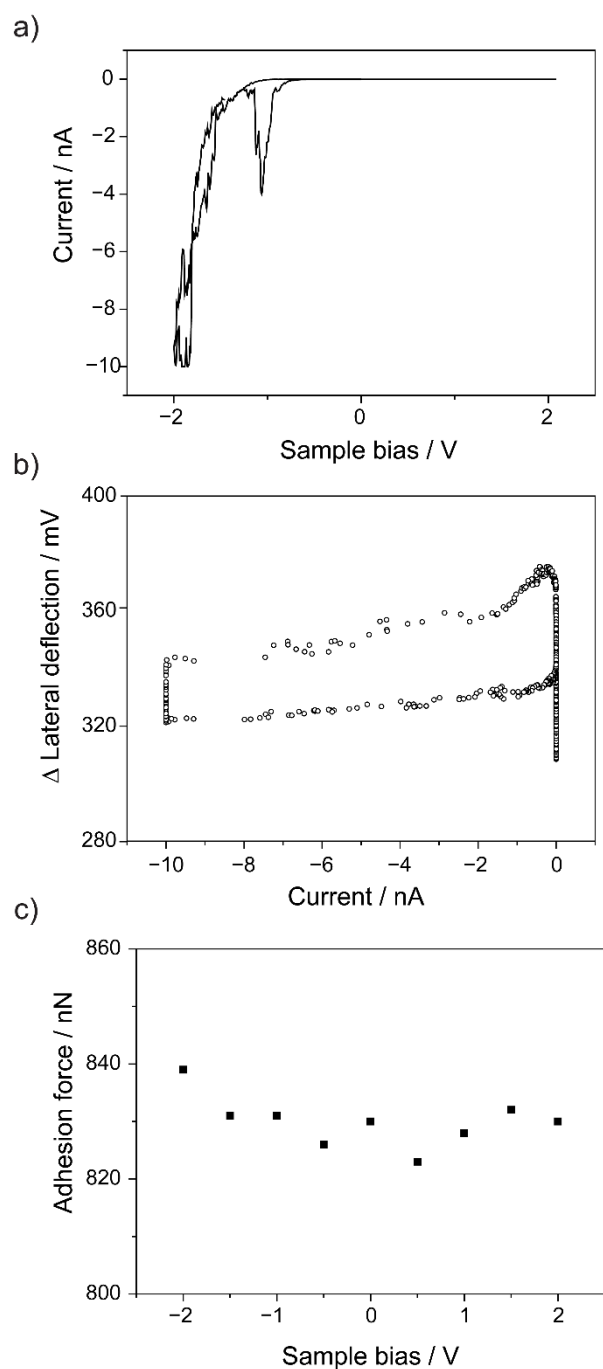


Figure S5. (a) Current–voltage (I–V) spectroscopy data acquired on a **S-1** sample grafted on highly doped Si(211). The force setpoint was of 100 nN, and the voltage sweep rate 8 V/s. The applied bias ranged from –2 V to +2 V. (b) Tip tilting–current plot corresponding to the experiment shown in (a), showing the lateral tip movement as function of the current crossing the Pt–silicon junction. The lateral deflection data suggest only a small tip deflection. (c) Tip–sample adhesion force as function of the externally applied bias (–2 V to +2 V).

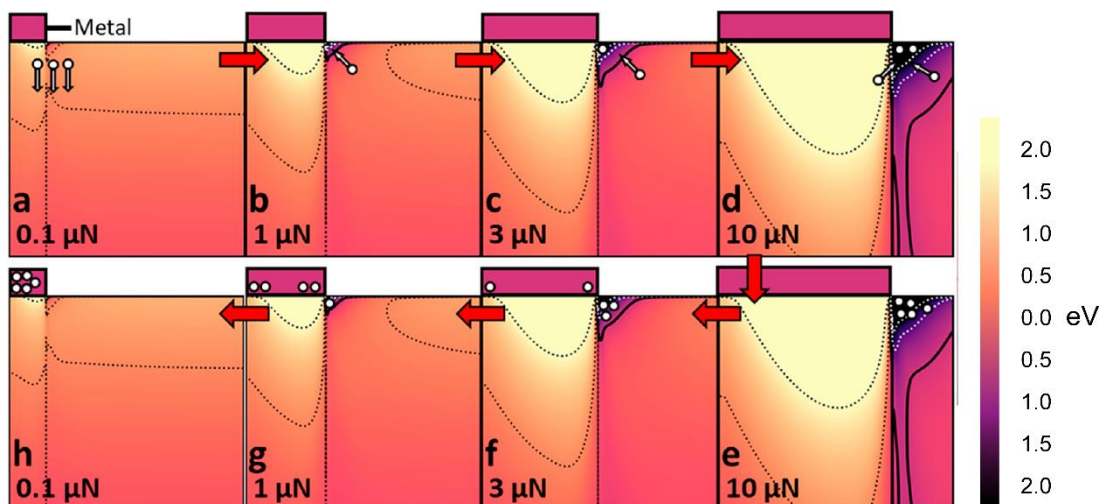


Figure S6. Proposed ratcheting mechanism for charge transfer in a PtIr-STO system. Reprinted (adapted) with permission from Nano Lett. 2022, 22, 10, 3914–3921. Copyright 2022 American Chemical Society. (a) At minimal applied force, the depletion potential is predominant. (b–d) As the force rises, electrons (illustrated as white circles with arrows) shift from areas with an increasing potential to areas with a decreasing potential. (e–g) Once the applied force diminishes, the quantity of available states within the potential well is reduced. This forces some electrons to move into the metal instead of crossing back over the barrier into the semiconductor (h).

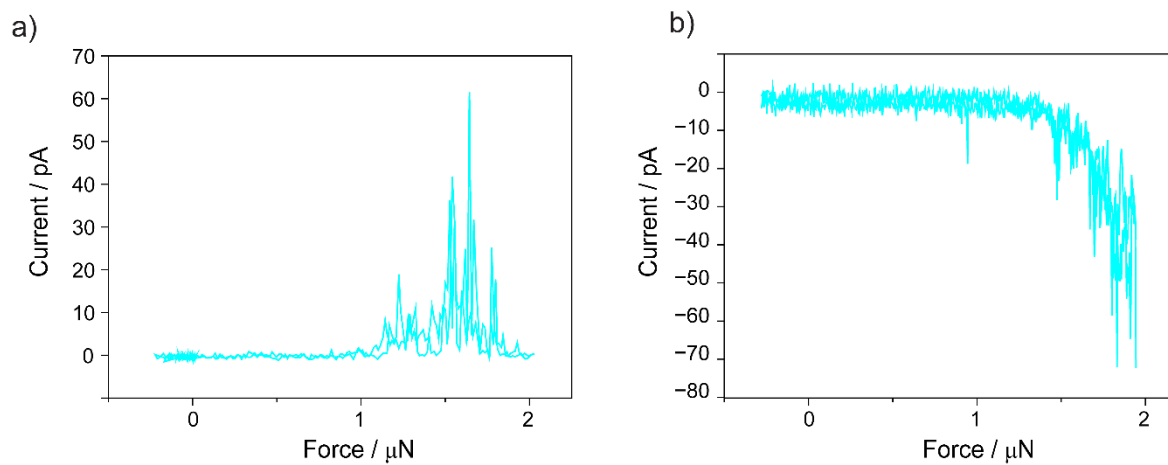


Figure S7. Current–force data acquired during AFM force–distance (F–d) measurements on Si(211) **S-1** monolayers prepared on either n-type (a), or p-type (b) Si(211) substrates. The F–d traces were acquired under zero external bias. The instrument routing is such that a current with a positive sign indicates a flow of electrons from the tip to the sample.

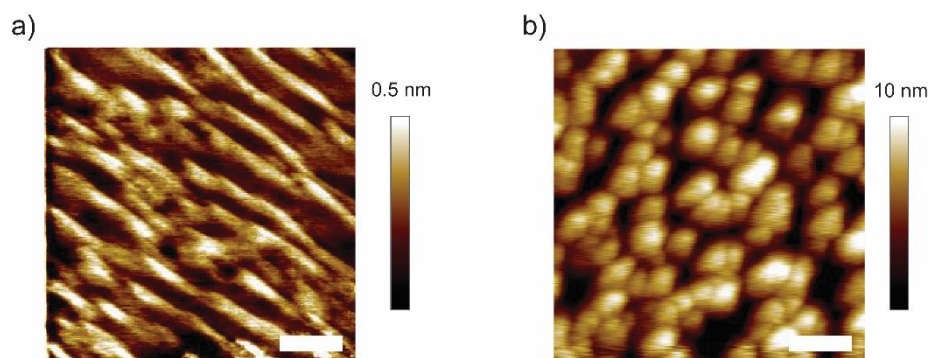


Figure S8. AFM topography images for **S-1** monolayers grafted on (a) Si(111) and on (b) Si(211) crystals, both n-type and lowly doped. The root-mean-square (rms) roughness of the Si(111) sample is ~ 0.3 nm. The rms value of the Si(211) sample is ~ 3 nm. The horizontal scale bars in panels (a) and (b) are $1 \mu\text{m}$.

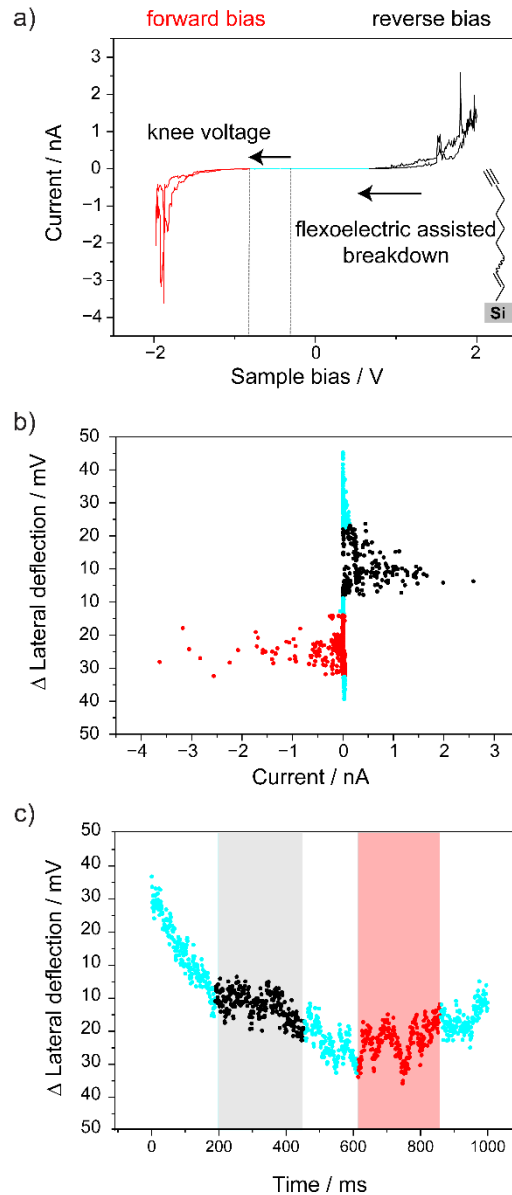


Figure S9. (a) A representative I–V curve acquired for a Pt AFM tip–n-type Si(111) S-1 junction under an applied normal load of 100 nN, and at a voltage sweep rate of 8 V/s. The two vertical dashed lines indicate the conventional knee voltage for a Si/Pt junction (generally located between ~ -0.3 and ~ -0.5 V), and the “shifted” knee voltage (~ -0.8 V) experimentally observed when a putative flexoelectric voltage term is present. Analogously, this flexoelectric term shifts the reverse breakdown voltage towards smaller applied reverse voltages. (b) Lateral deflection–current plot indicating a substantial tip-tilt during the I–V experiment shown in (a). (c) Plot of the lateral deflection data shown in (b) as a function of time during the voltage ramp. Shaded areas indicate regions with a less pronounced rate of deflection change (i.e. tilting less over time) corresponding to forward regions where knee voltage shifts negative (red) and reverse regions where the breakdown voltage shifts towards zero (black).

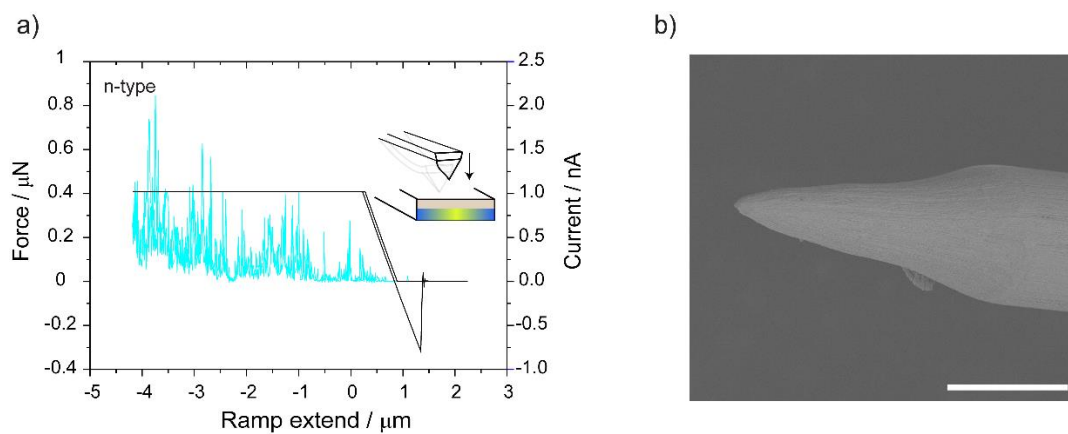


Figure S10. (a) High-speed capture current data acquired during AFM F-d measurements performed on **S-1** samples prepared on n-type Si(211). Experiments conducted with soft RMN-12Pt300B tips (spring constant of 0.8 N/m for the RMN-12Pt300B tips, versus 18 N/m of the RMN-25Pt300B). (b) SEM image of an RMN-12Pt300B tip. The scale bar is 10 μm .

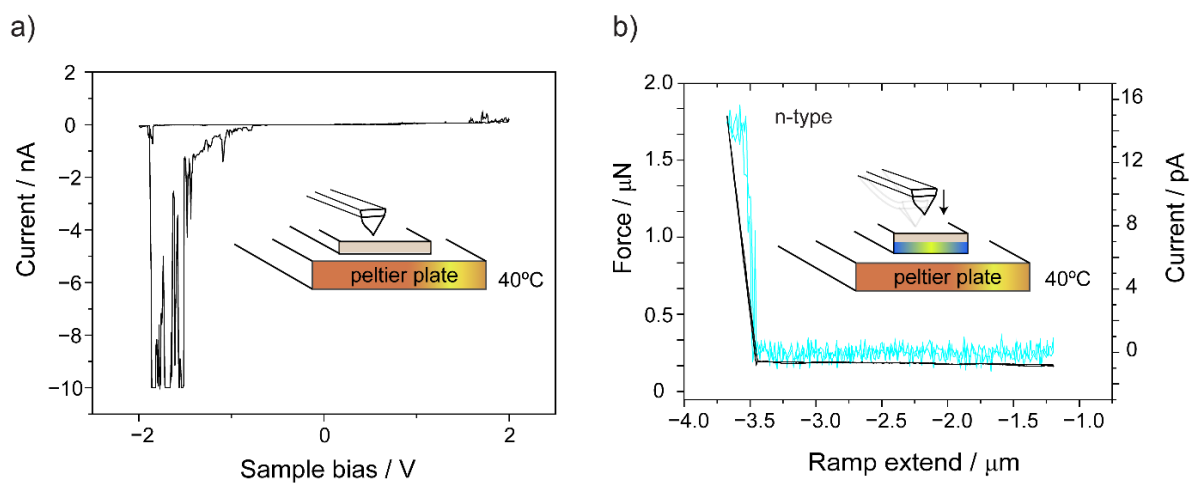


Figure S11. (a) Representative I–V curve acquired on Pt AFM tip–n-type Si(211) S-1 junctions under an applied normal load of 100 nN at a voltage sweep rate of 8 V/s. (b) F–d measurements conducted on Si(211) S-1 n-type. A Peltier plate schematically depicted in the inset, was used to increase the sample temperature to 40 ± 2 °C. Electrical contact between the back of the silicon sample and the metal AFM sample stage/holder (not shown in figure) was realised by copper tape bypassing the Peltier plate.

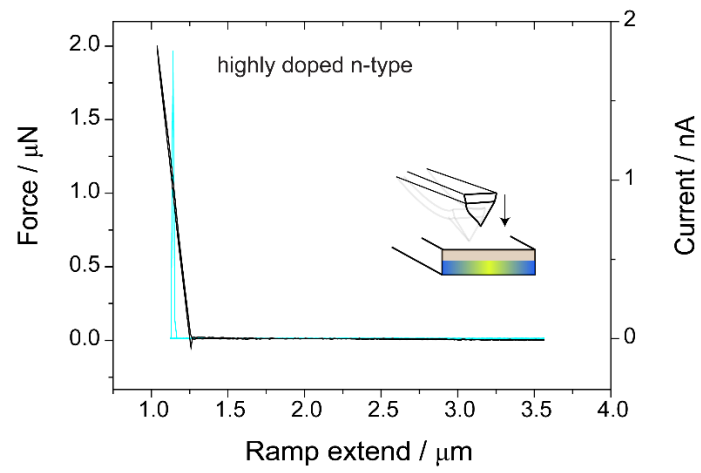


Figure S12. Representative AFM-based F-d measurement performed on a S-1 sample prepared on highly doped Si(211) n-type.

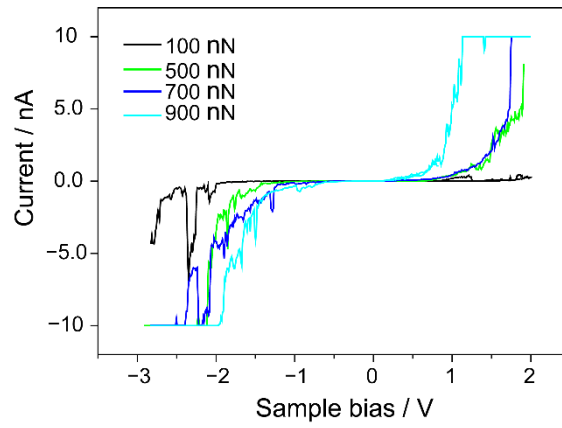


Figure S13. I–V measurements conducted on lowly doped Si(211) **S-1** n-type samples at a voltage sweep rate of 8 V/s. The normal load applied to the cantilever was varied as specified by the labels in figure.

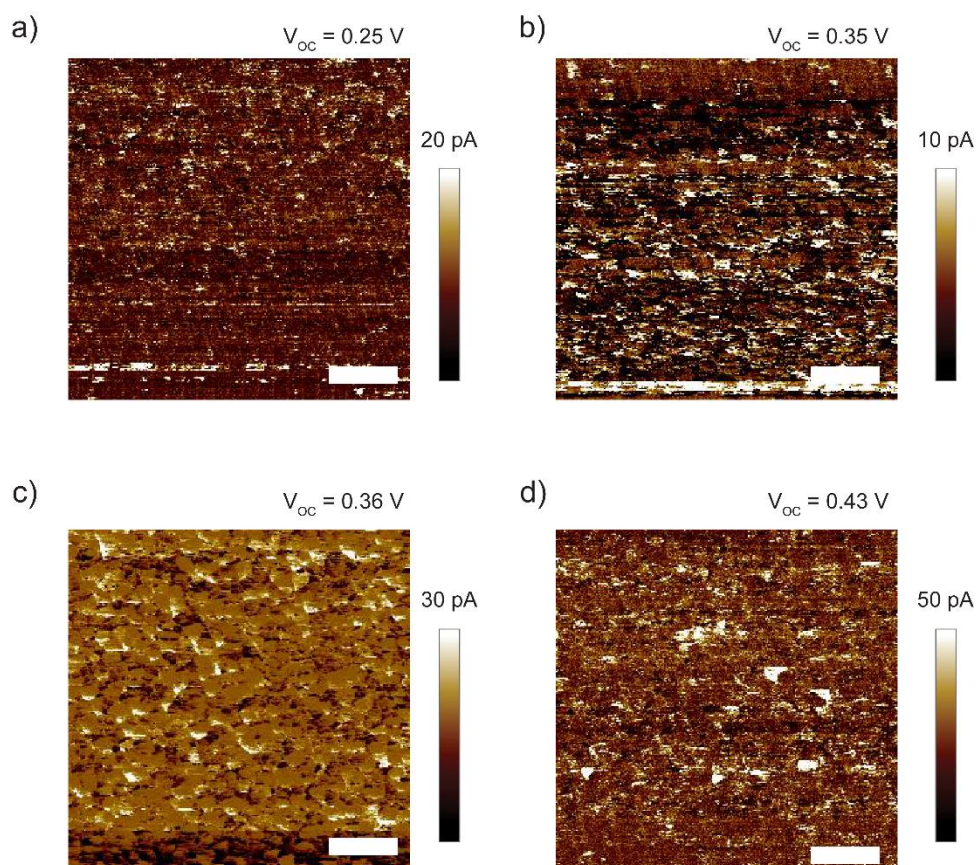


Figure S14. Experimentally determined open-circuit voltage (V_{oc}) on Si(211) S-1 surfaces. (a–d) C-AFM maps recorded on S-1 samples with the platinum AFM tip moving along the surface at 1 Hz. The force setpoint was 100, 500, 700, and 900 nN for panels (a–d), respectively. The bias applied to the silicon sample corresponds to the voltage required to bring the current output to noise level at each force setpoint.

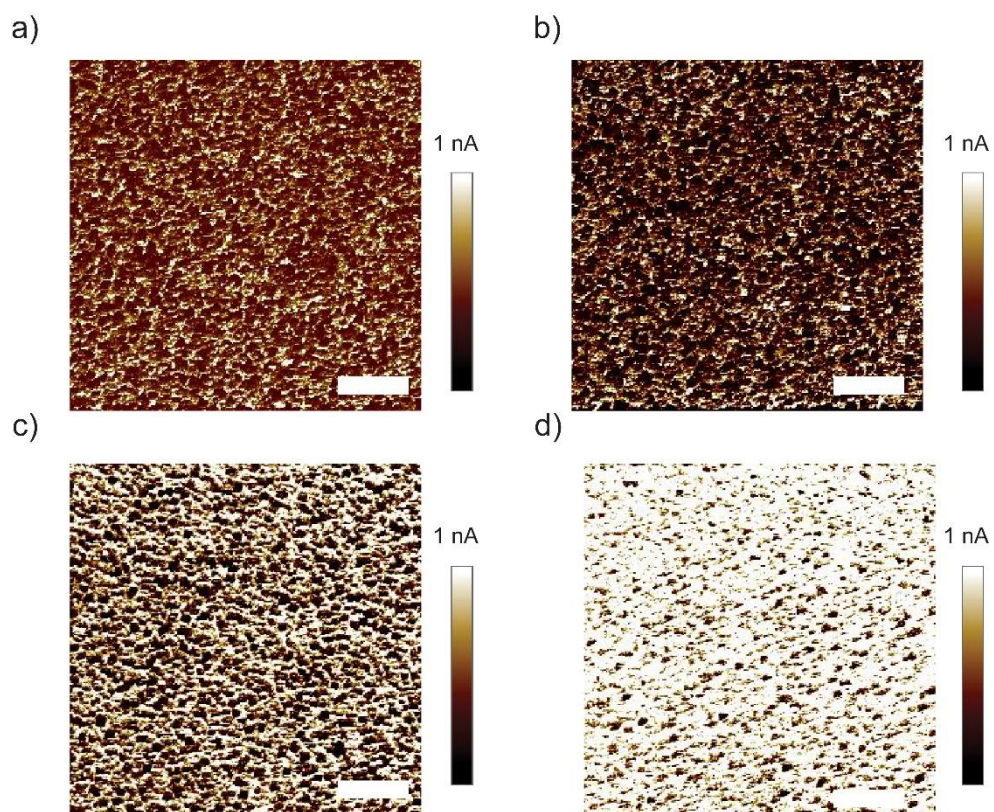


Figure S15. Experimentally determined short-circuit current (I_{SC}) for Si(211) **S-1** surfaces. (a–d) Zero-bias C-AFM maps recorded on **S-1** samples with the platinum AFM tip moving along the surface at 1 Hz. The force setpoint was 100, 500, 700, and 900 nN, panels (a–d), respectively.

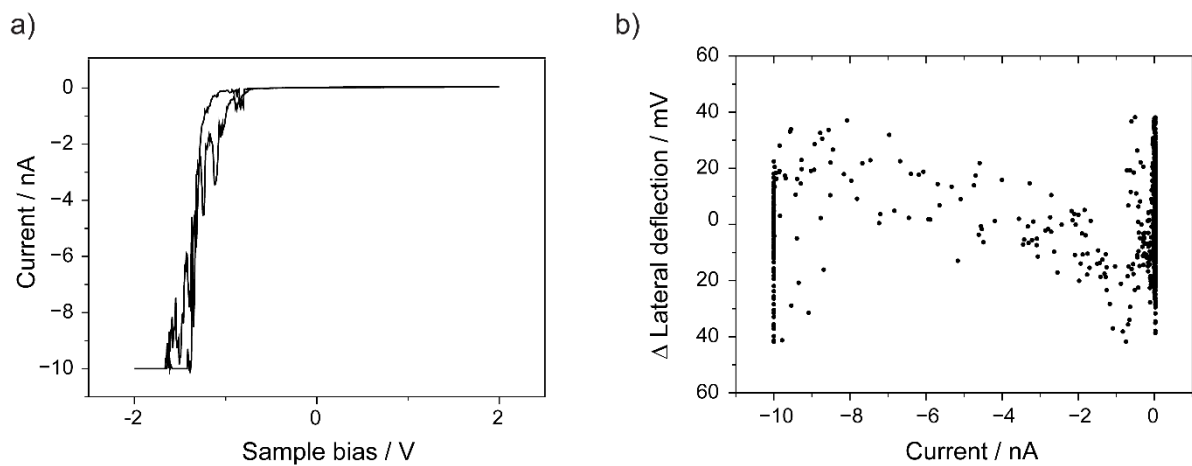


Figure S16. (a) Experimental current–voltage (I–V) spectroscopy data acquired on **S-1** lowly-doped n-type functionalized Si(211) surfaces with an applied load of 100 nN, at 0.01Hz (0.08 V/ s sweep rate) and an applied bias which ranged from –2 V to +2 V. (b) Tip tilting–current plot corresponding to the experiment in (a), tracking the lateral tip displacement as a function of the current crossing the junction. Lateral force values indicate low or negligible lateral tip displacement.

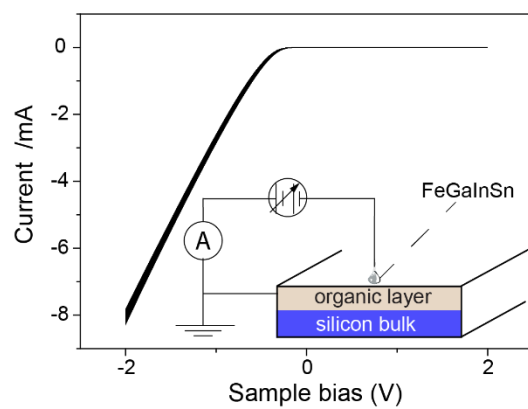


Figure S17. Evolution of current–voltage (I–V) curves over 50 continuous voltage cycles (~ 1.5 h of sampling time, -2 V to $+2$ V) recorded on a **S-1** Si(211) surface with FeGaInSn top contact, in ambient air at a voltage sweep rate of 55 mV/s. The inset represents the scheme of the measurement circuit.

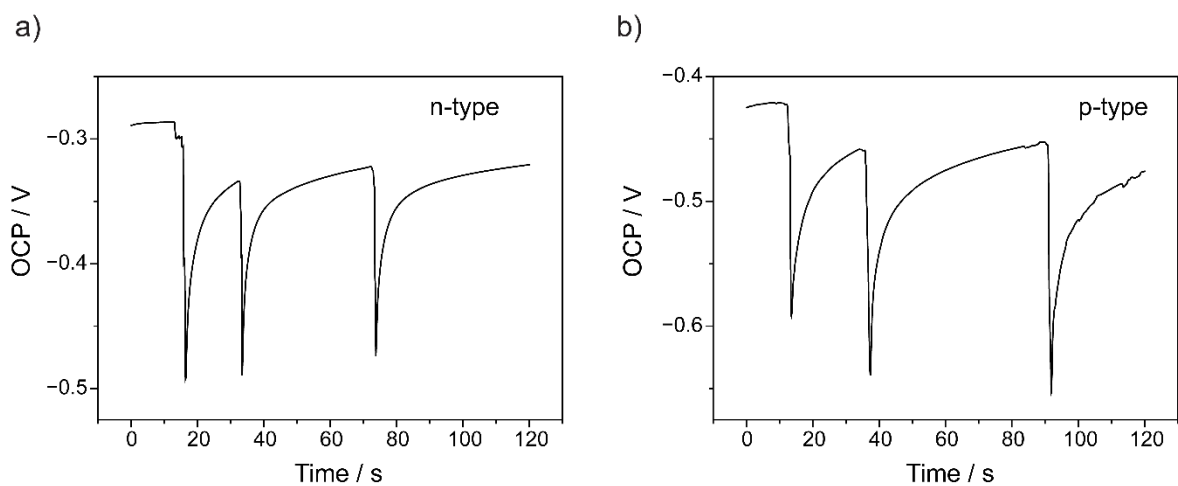


Figure S18. (a) Evolution of the open-circuit potential (OCP, working vs reference electrode) over time of a Si(211) lowly-dope n-type (a), and of a lowly-doped p-type (b) electrodes. In both panels, three cathodic OCP spikes indicate the build-up of an open-circuit electronic “pressure” following the in-situ mechanically induced (surface scribing with a diamond scribe) oxidation of the freshly exposed silicon surface. Samples are immersed in aqueous 1.0 M HClO_4 electrolyte.

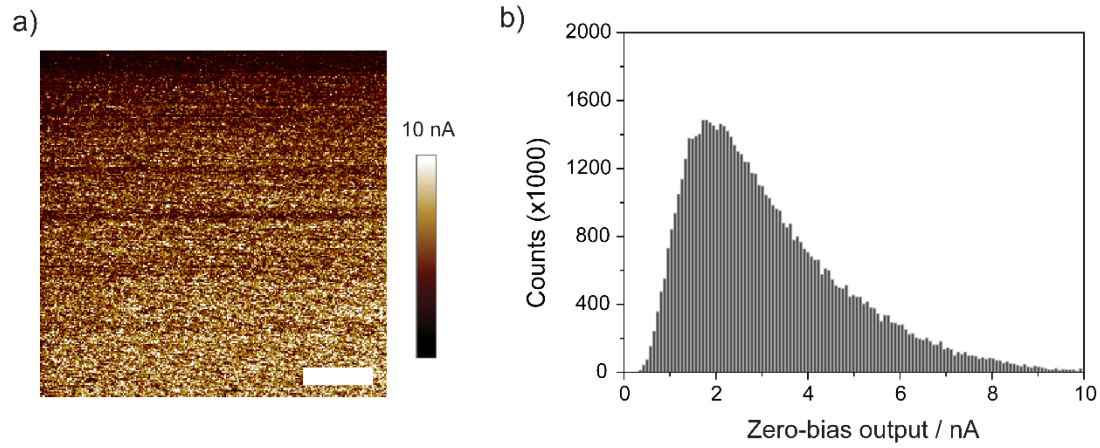


Figure S19. C-AFM map recorded on a **S-1** sample, at zero-voltage bias, and with the platinum AFM tip moving along the surface at 1 Hz (force setpoint of 360 nN). The horizontal scale bar in panel (a) represents 1 μm . (b) Histogram plot of the current output for the C-AFM map shown in panel (a). Counts indicate the number of pixels of a given current bin (x-axis), with a total of $\sim 65\text{K}$ pixels being sampled in a single C-AFM map.

Table S1. Performances of various TENGs designs.

Material junction	Surface treatment	Operation mode	I_{sc} (nA)	Load (nN)	V_{oc} (V)	$J_{avg.}$ (A/m^2)	ϕ_B (eV)	Ideality factor	Ref
Si(111) and Si(100)/ [Pt]	SAMs functionalized (1,8-nonadiyne)	Sliding				2.9×10^5	0.3		[1]
Si(111)/ [Pt]	SAMs & CuAAC ($-\text{NH}_2$, $-\text{OH}$, $-\text{CH}_3$)	Sliding				4.6×10^6			[2]
Si(211)/ [Pt]	SAMs functionalized ($-\text{CH}_3$, $-\text{OH}$, $-\text{C}\equiv\text{CH}$)	Sliding				4.9×10^9			[3]
Si(211)/ [Pt]	SAMs functionalized (1,8-nonadiyne)	Static		100				6.8	This work ^e
Si(211)/ [Pt]	SAMs functionalized (1,8-nonadiyne)	Static		500				8.2	This work ^e
Si(211)/ [Pt]	SAMs functionalized (1,8-nonadiyne)	Static		700				12.5	This work ^e
Si(211)/ [Pt]	SAMs functionalized (1,8-nonadiyne)	Static		900				19.0	This work ^e
Si(211)/ [Pt]	SAMs functionalized (1,8-nonadiyne)	Sliding		100	0.25	–	–	–	This work ^b
Si(211)/ [Pt]	SAMs functionalized (1,8-nonadiyne)	Sliding		500	0.35	–	–	–	This work ^b
Si(211)/ [Pt]	SAMs functionalized (1,8-nonadiyne)	Sliding		700	0.37	–	–	–	This work ^b
Si(211)/ [Pt]	SAMs functionalized (1,8-nonadiyne)	Sliding		900	0.42	–	–	–	This work ^b
Si(211)/ [Pt]	SAMs functionalized (1,8-nonadiyne)	Sliding	0.2 ^a	100	–	4×10^6	0.24		This work ^{c, d}
Si(211)/ [Pt]	SAMs functionalized (1,8-nonadiyne)	Sliding	0.6 ^a	500	–	5×10^6	0.22		This work ^{c, d}
Si(211)/ [Pt]	SAMs functionalized (1,8-nonadiyne)	Sliding	0.8 ^a	700	–	6×10^6	0.20		This work ^{c, d}
Si(211)/ [Pt]	SAMs functionalized (1,8-nonadiyne)	Sliding	1.0 ^a	900	–	7×10^6	0.19		This work ^{c, d}

PTFE/ [Cu]	Pre-charged PTFE	Sliding	200	50		[4]
Si/ [graphene]	HF etched	Sliding			40.0	[5]
Si(100)/ [graphite]	Buffered oxide etched	Sliding			210	[6]
p-type Si/ [n-type Si]	HF etched	Sliding	50			[7]
Si/ [black phosphorus]	Deposition (AlN, HfO ₂ , Al ₂ O ₃)	Sliding		6.1	124	[8]
n-type Si/ [n-type Si]	HF etched	Sliding		0.35	214	[9]
p-type Si(111)/ [diamond coated Si tip]	Molecular beam epitaxy (InP)	Sliding		15×10^{-3}	2×10^4	[10]

- I_{SC} , short-circuit current. Represents the average current at zero bias (under sliding at different set point).
- V_{OC} , open-circuit voltage. Represents the nullifying voltage (under sliding at different force set point) to bring the leakage current to noise level.
- $J_{avg.}$, Average current density calculated by estimating the tip-sample contact area using the Derjaguin-Muller-Toporov (DMT) model.
- ϕ_B , Schottky barrier height calculated by applying the thermionic emission equation, using a the average current density (C-AFM) calculated at different setpoint forces.
- Ideality factor calculated from the slope of the linear region of the natural logarithm of the forward current density versus voltage plot.

References

- [1] S. Ferrie, N. Darwish, J. J. Gooding, S. Ciampi, *Nano Energy* **2020**, *78*, 105210.
- [2] S. Ferrie, A. P. Le Brun, G. Krishnan, G. G. Andersson, N. Darwish, S. Ciampi, *Nano Energy* **2022**, *93*, 106861.
- [3] X. Lyu, S. Ferrie, A. Pivrikas, M. MacGregor, S. Ciampi, *Nano Energy* **2022**, 107658.
- [4] Z. You, S. Wang, Z. Li, Y. Zou, T. Lu, F. Wang, B. Hu, X. Wang, L. Li, W. Fang, Y. Liu, *Nano Energy* **2022**, *91*, 106667.
- [5] S. Chen, D. Liu, L. Zhou, S. Li, Z. Zhao, S. Cui, Y. Gao, Y. Li, Z. L. Wang, J. Wang, *Adv. Mater. Technol.* **2021**, *6*, 2100195.
- [6] S. Lin, Y. Lu, S. Feng, Z. Hao, Y. Yan, *Adv. Mater.* **2018**, *31*, 1804398.
- [7] X. Huang, X. Xiang, J. Nie, D. Peng, F. Yang, Z. Wu, H. Jiang, Z. Xu, Q. Zheng, *Nat. Commun.* **2021**, *12*, 2268.
- [8] R. Xu, Q. Zhang, J. Y. Wang, D. Liu, J. Wang, Z. L. Wang, *Nano Energy* **2019**, *66*, 104185.
- [9] Y. Lu, S. Feng, R. Shen, Y. Xu, Z. Hao, Y. Yan, H. Zheng, X. Yu, Q. Gao, P. Zhang, S. Lin, *Research* **2019**, *2019*, 5832382.
- [10] Y. Lu, Q. Gao, X. Yu, H. Zheng, R. Shen, Z. Hao, Y. Yan, P. Zhang, Y. Wen, G. Yang, S. Lin, *Research* **2020**, *2020*, 5714754.
- [11] V. A. Sharov, P. A. Alekseev, B. R. Borodin, M. S. Dunaevskiy, R. R. Reznik, G. E. Cirilin, *ACS Appl. Energy Mater.* **2019**, *2*, 4395.

